SPATIAL MEASUREMENT WITH CONSUMER GRADE DIGITAL CAMERAS

René Wackrow

Department of Civil and Building Engineering

Loughborough University

A Doctoral Thesis Submitted for the Degree of

Doctor of Philosophy

October 2008

Abstract

Key words: photogrammetry, camera calibration, digital camera, camera stability, image configuration, spatial measurement, digital elevation model, lens distortion

This thesis develops the potential of consumer-grade digital cameras for accurate spatial measurement. These cameras are generally considered unstable but their uncertain geometry can be partially resolved by calibration. The validity of calibration data over time should be carefully assessed before subsequent photogrammetric measurement. The use of such digital cameras for photogrammetric measurement is increasingly accepted in many industrial fields but also in a diverse range of fields including medical and forensic science and architectural work. However, the stability of these cameras is less frequently reported in the literature, which can be attributed to the absence of standards for quantitative analyses of camera stability.

The approach used to assess camera stability in this study is based on comparing the accuracy in the reconstructed object space, achieved using sets of interior orientation parameters of a sensor, derived in different calibration sessions. This technique was successfully applied to assess the temporal stability and manufacturing consistency of seven identical Nikon Coolpix 5400 digital cameras. These cameras demonstrated remarkable potential to maintain their internal geometry over a 1-year period. This study also identified residual systematic error surfaces, discernable in digital elevation models (DEMS) derived from image pairs. These 'domes' are caused by slightly inaccurately estimated lens distortion parameters.

A methodology that uses a mildly convergent image configuration removes the systematic error sources. This result is significant for DEM generation using low-cost digital cameras and a series of case studies demonstrated that this methodology can reduce the need for an accurate lens model and effectively increase the accuracy achievable with non-metric digital sensors.

Acknowledgements

I have really enjoyed the three years of research at Loughborough University. However, the production of this thesis would not have been possible without the support and assistance of so many people.

First of all, I would like to thank my supervisor Jim H. Chandler for his expert guidance in the field of Photogrammetry, constant encouragement and for always being accessible, despite other obligations. I also appreciated the help by Paul Bryan (English Heritage) for allowing access to their digital cameras. Special thanks go to Tobi, Nick and Xin for helping to conduct the case studies of a simulated river bed in London, Ontario and a small river in Loughborough.

Thanks to all the people I have had the pleasure of working with over my three years in RL.0.17 and RL.0.18, including Uli, Jan, Colin, Masoud, Tingting, Keyur, Ben and Fiona.

Also thanks to all members of the Loughborough Academicals and the "Friday Evening Football Team" for many hours of enjoyable football, probably not at the highest standard but at a very competitive level.

My time in Loughborough would never have been so enjoyable without the many great friends that I met in this town, including Jan and Jan, Paul, Kate, Lora, Chris, Richard, Gaiva, Nils, Abi and Lee, Patricia, my housemates from 75 Westfield Drive and many, many others. Thanks for many great nights out and an unforgettable time.

My final thanks are to my family, particularly my parents, without their consideration and support I would have not got this far.

Thanks to Loughborough University and the Engineering and Physical Sciences Research Council for funding the project.

Contents

List of Tables

List of Figures

Nomenclature

Greek Symbols

Δr	Radial lens distortion
$\Delta x, \Delta y$	Lens distortion parameters
γ_{SS^1}	Coefficient to model variation of radial distortion within depth of field
κ	Rotation about z-axis
λ	Scale factor
μ	Scalar greater than zero
ω	Rotation about x-axis
φ	Rotation about y-axis
φ_{LSE}	Sum of squares of residuals of measured parameters

Other Symbols

A	Partial differentials of a functional model with respect to all estimated parameters
b	Length of photo base
c	Principal distance
$C_{\hat{l}}$	Covariance matrix of the measured parameters

$C_{\hat{x}}$	Covariance matrix of the estimated parameters
f	Focal length
h	Camera-to-object distance
K_i	Radial distortion coefficients
$k^{'}, k^{''}$	Epipolar lines
l	Vector of observed minus computed observations
O	Perspective centre
P	Point in the object space
P_i	Tangential distortion coefficients
$Q_{\hat{l}}$	Cofactor matrix of the measured parameters
Q_{ll}	Cofactor matrix of observations
$Q_{\hat{x}}$	Cofactor matrix of the estimated parameters
r	Radial distance
r_{ij}	Elements of rotation matrix
R	Rotation matrix
S	Camera-object distance
σ_0^2	Variance factor
$s_{px'}$	Image precision
s_Z	Accuracy in camera direction
v	Vector of photo-coordinate residuals

W	Weight matrix
X	x - Coordinate in object space
x	x - Coordinate in image space
$\hat{x}$	Vector of parameters to be estimated
x_P	Principal point offset in x
Y	y - Coordinate in object space
y	y - Coordinate in image space
y_P	Principal point offset in y
Z	z - Coordinate in object space
z	z - Coordinate in image space

Abbreviations and Acronyms

2D	Two-Dimensional
3D	Three-Dimensional
AOI	Area of Interest
ATE	Automatic Terrain Extraction
CCD	Charge-coupled device
DEM	Digital elevation model
DSLR	Digital single-reflex camera
EDM	Electromagnetic Distance Measurement
EOP	Exterior Orientation Parameters

GAP	General Adjustment Program
GIS	Geographic Information System
IO	Interior Orientation
IOP	Interior Orientation Parameters
ISPRS	International Society for Photogrammetry and Remote Sensing
LPS	Leica Photogrammetry Suite
LSE	Least Squares Estimation
MDF	Medium density fibreboard
PRO	Professional
RGB	Red Green Blue
RMS	Root mean square
STARS	Simultaneous Triangulation and Resection System
TIN	Triangular Irregular Network
VMS	Vision Measurement System

CHAPTER 1

Introduction

Photogrammetry, particularly close range photogrammetry, is the main focus of this thesis. Photogrammetry can be defined as:

> *'the science, and art, of determining the size and shape of objects as a consequence of analysing images recorded on film or electronic media. The word science is important, as it implies the laws of mathematics, physics and chemistry and a knowledge of their practical application'*, (Fryer, 2001b).

Digital single-reflex (DSLR) cameras and compact digital cameras can be described as consumer-grade digital cameras. An automatic moving mirror system is used by DSLR cameras to direct light from the lens through the viewfinder so that the user recognises exactly what will be reproduced by the digital imaging system. Compact digital cameras use two separate light paths, one path through the lens to the imaging system, and another slightly offset path through the viewfinder. The area recognised by the user viewing through the viewfinder can be significantly different from what is reproduced by the imaging system. The viewfinder parallax is of particular importance to close range application.

Deriving **accurate** spatial data from a series of digital images remains an enduring quest in photogrammetry and is particularly important since consumer-grade digital cameras are becoming increasingly used. The main advantages of

these cameras are their convenience, portability and low cost. However, consumer-grade digital cameras have not been traditionally designed for use for photogrammetric measurement and are generally considered unstable. Although their uncertain geometry can be partially resolved by calibration, their temporal stability and manufacturing consistency often remain unknown. The validity of calibration data over time is questionable and should be carefully assessed to provide accurate spatial data for reconstructing the object space.

The quality of derived spatial data can be defined as a function of precision, accuracy and reliability with respect to random, gross and systematic errors (Cooper and Cross, 1988). The accuracy of photogrammetric data has the most significance for most users and is related to the eradication of systematic effects. These are more difficult to detect than random and gross errors. Calibrating the instruments, for example consumer-grade digital cameras, can help to minimise the systematic errors, but accounting explicitly for all of them can be difficult because of high correlation between calibration parameters.

This thesis attempts to assess the geometric stability of consumer-grade digital cameras and detect and eradicate remaining systematic errors in the reconstructed object space. This approach can increase the accuracy achievable using non-metric digital cameras.

1.1 Aims and Objectives

The initial project aim was formulated as follows; *'assess the temporal stability and manufacturing consistency of consumer-grade digital cameras'*. Whilst conducting research to accomplish this aim, another significant issue with respect to the use of consumer-grade digital cameras for accurate spatial measurement was identified. This led to the specification of an additional aim: *'investigate, clarify and minimise remaining residual systematic error surfaces in digital elevation models (DEMs)'*. Both aims were accomplished through achieving five main objectives:

- Review photogrammetric techniques currently reported and available, with particular focus on camera calibration, camera stability and data quality issues.

An extensive literature review of photogrammetric techniques was carried out to achieve this objective. Key elements were identified, required for camera calibration, stability analysis of non-metric digital cameras and quality analysis of photogrammetric data.

- Development of an appropriate methodology to assess the temporal stability and manufacturing consistency of consumer-grade digital cameras.

The aim of stability analysis is to determine the degree of similarity between sets of interior orientation parameters for a camera. An appropriate methodology was identified in this study that establishes the stability of a camera by evaluating the accuracy in the object space achieved using sets of interior orientation parameters determined in various calibration sessions. Comparing these achieved accuracies reveals the degree of similarity between sets of interior orientation parameters determined for a sensor over a 1-year period. This approach was used to assess the temporal stability and manufacturing consistency of consumer-grade digital cameras, demonstrated using a sample of seven identical Nikon Coolpix 5400 compact digital cameras.

- Confirm the theory that attributes residual systematic error surfaces (domes) in digital elevation models (DEMs) to inaccurately estimated lens distortion parameters.

Residual systematic error surfaces or domes, discernable in DEMs, were identified through conducting research to evaluate camera stability and have also been reported in past work (Section 2.6.1). A theoretical proof that attributes these to inaccurate radial lens distortion parameters was developed by Fryer and Mitchell (1987). In achieving this objective, various parameters describing interior and exterior orientation of a camera had to be controlled independently. The variability

and uncertainties, caused using real data, continuously prevented this. The use of simulated data was judged to be a more productive method of confirming this theoretical proof and provided a basis for seeking for an approach to minimise the systematic effects.

- Develop an approach to minimise residual systematic error surfaces, recognisable in DEMs.

This objective comprised the investigation of different approaches to minimise residual systematic error surfaces in DEMs, caused by inaccurately estimated lens distortion parameters. Various camera calibration methods were analysed to improve the estimation of lens distortion parameters but expected results failed to appear. The simulation approach identified in the previous objective was used to investigate the hypothesis that a specific image configuration can minimise these systematic effects. Various image configurations were systematically tested, identifying the potential of a mildly convergent image configuration to eradicate systematic effects in DEMs.

- Conduct case studies to verify the findings and demonstrate the significance of the developed methodology in real applications.

Two case studies were conducted to verify the methodology, developed in this research project, that minimises residual systematic error surfaces. A laboratory flume situated in London, Ontario, which represents the topography of a river bed surface was identified as being suitable for the first case study. The second was conducted on a small river in Loughborough, measuring the topographic surface of a running river. Both confirmed the finding described in the previous objective.

1.2 Contribution to Knowledge

The contribution to knowledge of this thesis is in two areas:

- The geometric stability over a 1-year period was explored using a sample of seven identical Nikon Coolpix 5400 digital cameras. This demonstrated the potential of such cameras to maintain their inner geometry and extract accurate spatial information. It is demonstrated that radial lens distortion is the main source of disturbing systematic effects of spatial data derived with non-metric digital cameras, a feature that is recognised in the literature.

- This study identifies a methodology to minimise residual systematic error surfaces in digital elevation models (DEMs), caused by significantly inaccurate lens distortion parameters. The accuracy of derived photogrammetric data is related to uncorrected systematic errors and can be estimated with respect to an external reference or standard. Eradicating these systematic effects effectively increases the accuracy achievable with consumer-grade digital cameras and is essential to exploit their complete potential for accurate spatial measurement. Additionally, the potential and flexibility of the developed methodology are explored and verified. The development of this technique, suitable to minimise residual systematic effects in digital surface representations, will further extend the value of consumer-grade digital cameras for accurate spatial measurements, by increasing the number of both potential applications and users.

1.3 Structure of Thesis

The structure of this thesis corresponds closely with the chronological order of the work conducted during the project. The thesis is divided into seven chapters, includes references and appendices A and B.

- *Chapter 1* introduces the aims and objectives of this research and presents the structure of this thesis.

- *Chapter 2* reviews briefly the evolution of photogrammetry science, explains the main principles used in photogrammetry, particularly focusing on the

fundamentals of camera calibration, stability analysis of non-metric digital cameras and quality issues associated with digital photogrammetric data sets.

- *Chapter 3* identifies and justifies strategies and workflows that were developed to achieve the aims and objectives of this research. Methodologies developed to accomplish satisfactory solutions for the difficulties, which arose in the course of work, are also presented.

- *Chapter 4* presents the results of stability analysis using seven identical consumer-grade digital cameras. It also accounts for findings that were achieved by investigating the criticality of interior orientation parameters of a digital sensor and developing a methodology to minimise residual systematic error surfaces in digital elevation models. Finally, a practical test conducted to verify this methodology is described.

- *Chapter 5* introduces two case studies that were selected to verify the convergent imaging methodology. The study sites are described and problems associated with acquiring data and assessing accuracy are discussed.

- *Chapter 6* reviews the results and findings of this research. Any problems that were identified are discussed and further tests are presented, which were conducted to clarify these. As a result of these tests, possibilities for future research were identified and an overview is provided that tentatively explores the relationship between costs and accuracies of various non-metric digital cameras.

- *Chapter 7* outlines the achievements of this research project and suggests recommendations for future work.

- *Appendix A* provides a MATLAB code that was developed in this research and automatically detects, extracts and measures object features in multiple digital images.

- *Appendix B* contains two journal publications, significant outcomes of this research, which have been published already.

CHAPTER 2

Review of Relevant Literature

Photogrammetry is the science of determining indirectly the size and shape of any object by analysing one or more images recorded on film or electronic media (Fryer, 2001b). The photogrammetric process can be used in any application where a measuring object can be photographically recorded and evaluated. The primary objective of photogrammetric measurement is the three-dimensional (3D) geometrical reconstruction of an object (Luhmann *et al.*, 2006).

A review of relevant research literature and technologies is provided in this chapter. After reviewing briefly the evolution of photogrammetric science, the main principles are explained, including mathematical models used in photogrammetry, fundamentals and methods of camera calibration, stability analysis of non-metric digital cameras and quality analysis. Finally, this chapter will finish with a short summary.

2.1 Brief Overview of the History of Photogrammetry

The history of photogrammetry is crucially influenced by applications at close range. A few years after Niepce and Daguerre (1839) invented photography, the Frenchman Laussedat (1851) and the German Meydenbauer (1858) independently

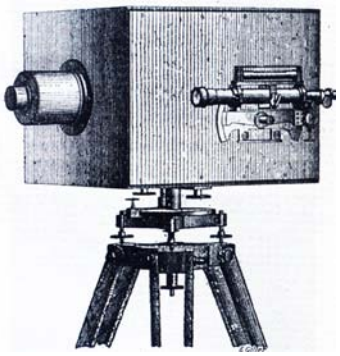

Figure 2.1: Camera from Brunner (1859) in Luhmann *et al.* (2006)

developed methods to extract geometric information from photographs using a basic camera (Figure 2.1). Meydenbauer designed his own camera to record important architectural monuments. Around 16,000 images were captured between 1885 and 1909, representing many features, most of which have subsequently disappeared (Luhmann *et al.*, 2006).

Photogrammetry was used as a technique for gait analysis by the American physician Holmes after the American Civil War in 1863. These analyses helped to fit prosthetic devices to limbless soldiers with increased precision. The measurement of the size and shape of body parts and changes in their form with time has since been called *biostereometrics* (Fryer, 2001b).

Pulfrich (1901), at the Zeiss company in Jena, designed the first stereocomparator instrument necessary to measure the coordinates of an image point from both photographs simultaneously. The comparator improved the identification of identical or conjugate image points (Fryer, 2001b; Luhmann *et al.*, 2006).

Between the two world wars, developments of instruments to evaluate image pairs progressed rapidly. These systems were mostly developed for map production by aerial photogrammetry. This period saw the development of what is now referred to as *analogue photogrammetry* (Luhmann *et al.*, 2006).

With the development of computer technology in the 1950s, the era of *analytical*

photogrammetry commenced but did not become established until mass produced computer processors became available in the early 1980's. Based on the collinearity equations, mono- and stereo-comparator instruments were developed and used to measure image coordinates very accurately. Furthermore, analytical stereoplotters were developed, which quickly led to the definition of the spatial location and orientation of a camera. As the model is scanned visually, the operator can enjoy three dimensional viewing (Fryer, 2001b).

In the 1960s and 1970s, bundle adjustment programs (Ackermann *et al.*, 1970; Brown, 1976) were developed. No restrictions on the positions or the orientations of the cameras are imposed. Furthermore, there is no necessity to limit the imaging system to a central projection. However, the main advantage of the method is that the interior orientation parameters (IOP) of all cameras can be included as unknowns in the solution. This feature of the bundle adjustment was significant, as it provided the opportunity to calibrate non-metric cameras and begin to use them for photogrammetric measurement tasks. The orientation of images, captured in close range applications, has been implemented using the bundle adjustment method since the 1980s (Granshaw, 1980; Luhmann *et al.*, 2006).

In the early 1980's, a shift in technology from analytical to digital photogrammetry was observed (Gruen, 2001a). Digital data were acquired directly by a digital sensor, such as a charge-couple device (CCD) array camera with a resolution (500×500 pixel) for close range photogrammetry or alternatively using digitised aerial photographs (Dowman, 2001; Gugan, 1989). Early digital systems had largely prototype status and were rarely used in real applications. However, these systems proved valuable as a basis for further research and developments (Gruen, 2001a). Digital cameras with useable resolution (640×480 pixel) were constructed in the early 1990's. Writers of software like the Simultaneous Triangulation and Resection System (STARS) (Fraser and Brown, 1986) developed more user-friendly packages and digital image processing could be performed on personal computers (Fryer, 2001b).

2.2 Mathematical Models in Photogrammetry

It is assumed that the reader is familiar with basic statistics as well as matrix and vector algebra. Coordinate transformations represent an important concept in photogrammetry, which establishes the mathematical relationship between object coordinates, photo coordinates and camera parameters. A functional model (central perspective projection) and its extension, universally adopted for close range photogrammetry are explained in the subsequent sections.

2.2.1 Coordinate Transformations

The exact position of a point may be defined and described using a 3D cartesian coordinate system with an arbitrary definition of its origin, scale and orientation often known as a datum (Cooper and Robson, 2001). The datum descriptions of coordinate systems used in photogrammetry are often different and it is possible to convert between them, using a 3D similarity transformation known as *The Helmert Transformation* (Luhmann *et al.*, 2006). The Helmert Transformation requires the specification of 7 datum elements, including scale change along the axes, translation of axes and three independent sequential rotations of axes.

The position of a point in a primary coordinate system may be represented by the vector $\mathbf{X} = [X\ Y\ Z]^t$ and its position in a secondary coordinate system by the vector $\mathbf{x} = [x\ y\ z]^t$. The vector equation $\mathbf{x} = \lambda\mathbf{X}$ may describe a scale change λ along each of the axes. A translation of axes can be represented by the vector $\mathbf{x} = \mathbf{X} - \mathbf{X}_0$, where the origin of the secondary coordinate system relative to the primary is described by the position vector $\mathbf{X}_0 = [X_0\ Y_0\ Z_0]^t$.

The three independent sequential rotations of orthogonal axes in 3D space are represented in Figure 2.2. The clockwise rotation ω of Point A with coordinates (x, y, z) relative to the $(x\ y\ z)$ system about the positive x-axis is represented in Figure 2.2a. The vector equation $[x_\omega y_\omega z_\omega]^t = \mathbf{R}_\omega[x\ y\ z]^t$ may represent the

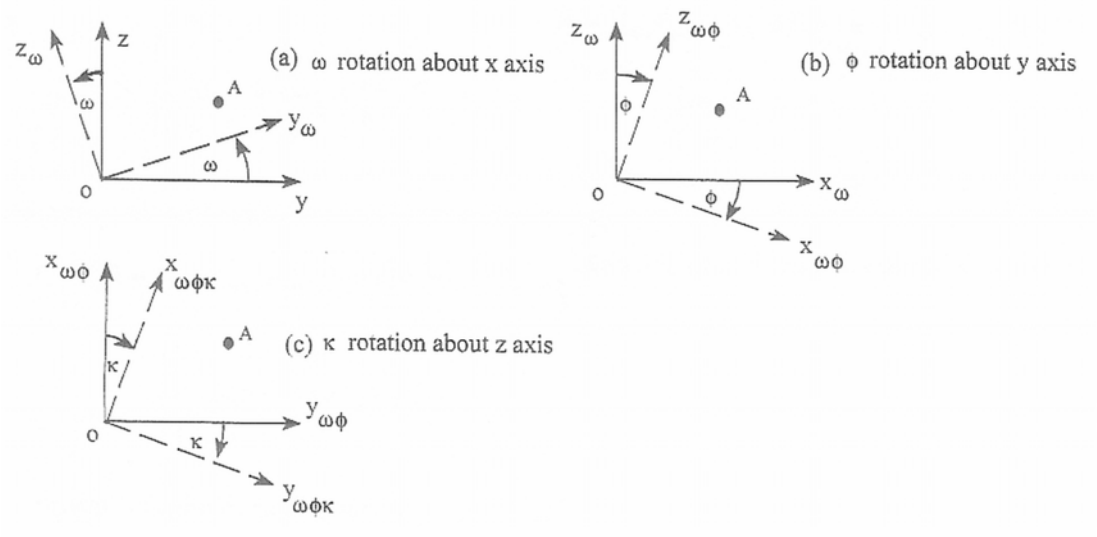

Figure 2.2: Sequential rotations of axes in three dimensional space (Cooper and Robson, 2001)

position vector of A in the rotated system $(x_\omega y_\omega z_\omega)$, where

$$\mathbf{R}_\omega = \begin{bmatrix} 1 & 0 & 0 \\ 0 & \cos\omega & \sin\omega \\ 0 & -\sin\omega & \cos\omega \end{bmatrix}. \tag{2.1}$$

After applying a clockwise rotation φ about the y_φ-axis (Figure 2.2b) the coordinates of A in the $(x_{\omega\varphi} y_{\omega\varphi} z_{\omega\varphi})$ system are represented by $[x_{\omega\varphi} y_{\omega\varphi} z_{\omega\varphi}]^t = \mathbf{R}_\varphi \mathbf{R}_\omega [x\ y\ z]^t$, where

$$\mathbf{R}_\varphi = \begin{bmatrix} \cos\varphi & 0 & -\sin\varphi \\ 0 & 1 & 0 \\ \sin\varphi & 0 & \cos\varphi \end{bmatrix}. \tag{2.2}$$

If the axes are finally given a rotation κ, clockwise about the $z_{\omega\varphi}$-axis (Figure 2.2c), the coordinates of point A in the $(x_{\omega\varphi\kappa} y_{\omega\varphi\kappa} z_{\omega\varphi\kappa})$ system are described by $[x_{\omega\varphi\kappa} y_{\omega\varphi\kappa} z_{\omega\varphi\kappa}]^t = \mathbf{R}_\kappa \mathbf{R}_\varphi \mathbf{R}_\omega [x\ y\ z]^t$, where

$$\mathbf{R}_\kappa = \begin{bmatrix} \cos\kappa & \sin\kappa & 0 \\ -\sin\kappa & \cos\kappa & 0 \\ 0 & 0 & 1 \end{bmatrix}. \tag{2.3}$$

The rotation matrix $\mathbf{R}_{\omega\varphi\kappa}$ is the matrix product $\mathbf{R}_\kappa\mathbf{R}_\varphi\mathbf{R}_\omega$ corresponding to primary rotation ω, secondary rotation φ and tertiary rotation κ and is in full:

$$\mathbf{R}_{\omega\varphi\kappa} = \mathbf{R}_\kappa\mathbf{R}_\varphi\mathbf{R}_\omega = \begin{bmatrix} \cos\varphi\cos\kappa & \sin\omega\sin\varphi\cos\kappa + \cos\omega\sin\kappa & -\cos\omega\sin\varphi\cos\kappa + \sin\omega\sin\kappa \\ -\cos\varphi\sin\kappa & -\sin\omega\sin\varphi\sin\kappa + \cos\omega\cos\kappa & \cos\omega\sin\varphi\sin\kappa + \sin\omega\cos\kappa \\ \sin\varphi & -\sin\omega\cos\varphi & \cos\omega\cos\varphi \end{bmatrix}$$

or

$$\mathbf{R} = \begin{bmatrix} r_{11} & r_{12} & r_{13} \\ r_{21} & r_{22} & r_{23} \\ r_{31} & r_{32} & r_{33} \end{bmatrix}. \tag{2.4}$$

Using the rotation matrix $\mathbf{R}$, primary coordinates $(X\ Y\ Z)$ can be transformed to secondary coordinates $(x\ y\ z)$ as follows:

$$\begin{bmatrix} x \\ y \\ z \end{bmatrix} = \begin{bmatrix} r_{11} & r_{12} & r_{13} \\ r_{21} & r_{22} & r_{23} \\ r_{31} & r_{32} & r_{33} \end{bmatrix} \begin{bmatrix} X \\ Y \\ Z \end{bmatrix}. \tag{2.5}$$

The rotation matrix $\mathbf{R}$ is an orthogonal matrix. The reverse transformation is therefore:

$$\begin{bmatrix} X \\ Y \\ Z \end{bmatrix} = \begin{bmatrix} r_{11} & r_{12} & r_{13} \\ r_{21} & r_{22} & r_{23} \\ r_{31} & r_{32} & r_{33} \end{bmatrix} \begin{bmatrix} x \\ y \\ z \end{bmatrix}. \tag{2.6}$$

The rotation matrix $\mathbf{R}$ will be used in equations in the subsequent sections.

2.2.2 Collinearity Equations

Two specific coordinate systems (Figure 2.3) are normally identified in photogrammetry. A frame of reference for the camera is defined by the secondary image coordinate system $(x\ y\ z)$. It is orthogonal to the projection plane and its x and y axes are parallel to the image plane or plane of projection. Its origin is commonly defined at the perspective centre O and the z axis is orientated along the perspective axis. The principal point is defined as the intersection between the perspective axis and the plane of projection (Cooper and Robson, 2001). The

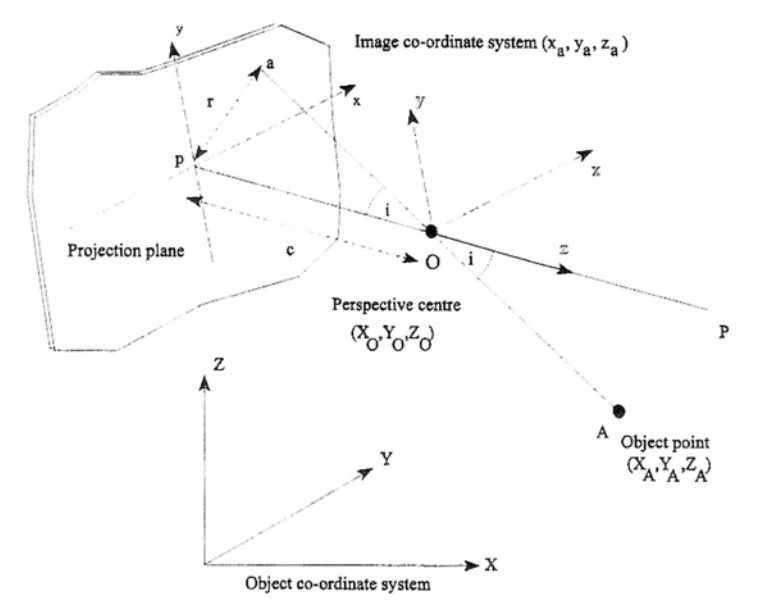

Figure 2.3: Central perspective projection (Cooper and Robson, 2001)

distance from the principal point to the origin of the coordinate system is usually known as the principal distance c.

The object coordinate system ($X\ Y\ Z$) is the primary system and its origin is arbitrarily defined. The position of the perspective centre in the primary coordinate system can be described by the 3D coordinates (X_O, Y_O, Z_O) and the position of an object point A can be described similarly by the coordinates (X_A, Y_A, Z_A). The straight line (Figure 2.3) from A passing through the perspective centre projects the object point A onto the plane of projection. The 3D coordinates of point A in the secondary image coordinate system are $(x_a, y_a, -c)$. Vectors can be written relative to the primary coordinate system. $X_A = X_O + S$ where S is the position vector of point A relative to the projective centre and collinear to x_a, but of opposite direction and can be represented in the vector equation $X_A = X_O - \mu \mathbf{R}^t x_a$ or

$$\begin{bmatrix} X_A \\ Y_A \\ Z_A \end{bmatrix} = \begin{bmatrix} X_O \\ Y_O \\ Z_O \end{bmatrix} - \mu \begin{bmatrix} r_{11} & r_{21} & r_{31} \\ r_{12} & r_{22} & r_{32} \\ r_{13} & r_{23} & r_{33} \end{bmatrix} \begin{bmatrix} x_a \\ y_a \\ -c \end{bmatrix}, \tag{2.7}$$

where the rotation matrix $\mathbf{R}$ is described by Equation 2.4 and μ is a scalar greater than zero. The transformation of a object point A from the primary to the secondary coordinate system is consequently $x_a = \mu^{-1}\mathbf{R}(X_O - X_A)$ or

$$\begin{bmatrix} x_a \\ y_a \\ -c \end{bmatrix} = \mu^{-1} \begin{bmatrix} r_{11} & r_{12} & r_{13} \\ r_{21} & r_{22} & r_{23} \\ r_{31} & r_{32} & r_{33} \end{bmatrix} \begin{bmatrix} X_O - X_A \\ Y_O - Y_A \\ Z_O - Z_A \end{bmatrix} \tag{2.8}$$

The third line in Equation 2.8 can be written explicitly in μ^{-1} and substituted into the first and second line in Equation 2.8. The unknown scalar μ is consequently eliminated and the final collinearity equations can be represented by:

$$\begin{aligned} x_a &= \frac{-c[r_{11}(X_O - X_A) + r_{12}(Y_O - Y_A) + r_{13}(Z_O - Z_A)]}{[r_{31}(X_O - X_A) + r_{32}(Y_O - Y_A) + r_{33}(Z_O - Z_A)]} \\ y_a &= \frac{-c[r_{21}(X_O - X_A) + r_{22}(Y_O - Y_A) + r_{23}(Z_O - Z_A)]}{[r_{31}(X_O - X_A) + r_{32}(Y_O - Y_A) + r_{33}(Z_O - Z_A)]} \end{aligned} \tag{2.9}$$

The negative sign of c becomes positive if the projection plane lies on the same side of the perspective centre as point A (Cooper and Robson, 2001).

2.2.3 Extended Collinearity Equations

The collinearity Equations 2.9 are suitable for pin-hole and metric cameras, designed for photogrammetry and used traditionally for analogue and analytical photogrammetry. The theory assumes that the coordinate reference system used to define the origin of the photo coordinate system is referenced directly to the true principal point and the camera lens is free of distortion. Digital cameras do not normally fulfill these collinearity conditions and the mathematical model needs to be extended. If the origin of the two-dimensional (2D) image coordinate system is offset, the coordinates (x_P, y_P) representing the position of the

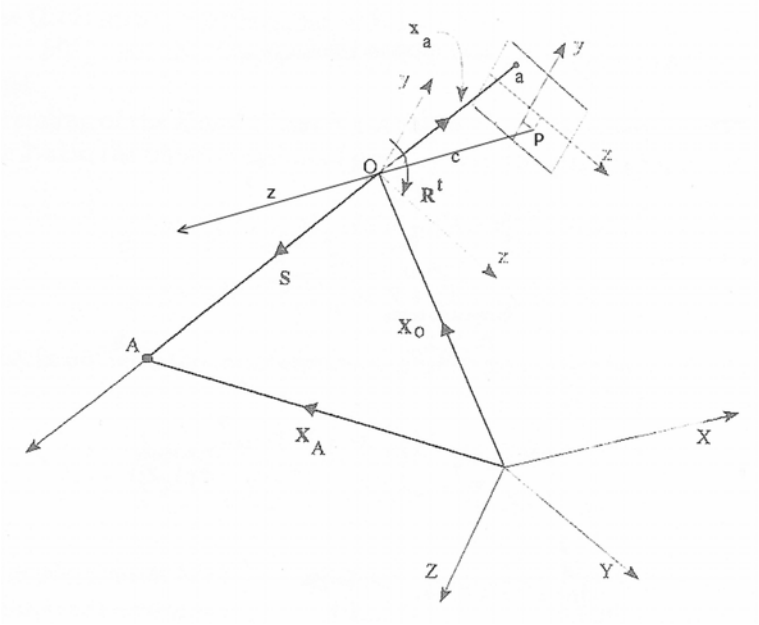

Figure 2.4: Extended collinearity condition (Cooper and Robson, 2001)

principal point can be included as two additional parameters (Figure 2.4). The collinearity equation also can be further extended by parameters $(\Delta x, \Delta y)$ to model lens distortion and the extended collinearity equations can be represented by $x_a - x_P - \Delta x = \mu^{-1}\mathbf{R}(X_O - X_A)$ or

$$\begin{aligned} x_a &= x_P - c \cdot \frac{[r_{11}(X_O - X_A) + r_{12}(Y_O - Y_A) + r_{13}(Z_O - Z_A)]}{[r_{31}(X_O - X_A) + r_{32}(Y_O - Y_A) + r_{33}(Z_O - Z_A)]} + \Delta x \\ y_a &= y_P - c \cdot \frac{[r_{21}(X_O - X_A) + r_{22}(Y_O - Y_A) + r_{23}(Z_O - Z_A)]}{[r_{31}(X_O - X_A) + r_{32}(Y_O - Y_A) + r_{33}(Z_O - Z_A)]} + \Delta y. \end{aligned} \tag{2.10}$$

These equations are fundamental to digital photogrammetry and describe a transformation of object coordinates (X, Y, Z) in corresponding photo coordinates (x, y) with knowledge of the interior orientation parameters (IOP) $(x_P, y_P, c, \Delta x, \Delta y)$ of a single camera and exterior orientation parameters (EOP) $(X_O, Y_O, Z_O, \omega, \varphi, \kappa)$ of a single image. The image coordinates are formulated as a function of the unknown parameters on the right side of the equation. An over-determined least

square estimation (LSE) can be used to determine the IOP and EOP, this is especially important if a non-metric digital camera has been used, because calibration parameters for these cameras are generally unavailable. These equations also represent mathematical fundamentals for analytical stereo plotters (Luhmann *et al.*, 2006).

2.3 Fundamentals of Camera Calibration

The term *interior orientation* summarises the set of parameters, which describe the internal geometry of a camera and lens system. The parameters defining the interior orientation are the principal distance c, the principal point offset x_P, y_P and the total lens distortion $\Delta x, \Delta y$ that will be described in more detail in the following sections. These parameters represent deviations from the central perspective projection (Section 2.2.2), caused by imperfectly constructed lenses or complex lens systems (Fryer, 2001a).

Whether the sensor is an analogue film-based or a digital camera using a charge-coupled device (CCD), the parameters of interior orientation are similar. However, a major difference is the definition of the coordinate system used to define the position of points in the image. The origin of the photo coordinate system in an ideal metric analogue camera is defined by pairs of fiducial marks or a Reseau grid (Figure 2.5), which ideally define the principal point. In reality, an offset (x_P, y_P) can be added to the photo coordinates to reduce them to the principal point (Section 2.2.3). The unit used in the photo coordinate system defined by fiducial marks or a Reseau grid is normally millimetres in the x and y directions. Manufacturers of metric cameras provide a calibration certificate that includes the parameters of the interior orientation but these vary with camera usage and regular re-calibration is recommended (Cooper and Robson, 2001).

The image coordinate system used for digital sensors is commonly a pixel coordinate system with rows and columns related to its origin in the upper left corner of the CCD device (Figure 2.5), the number of columns and rows depending

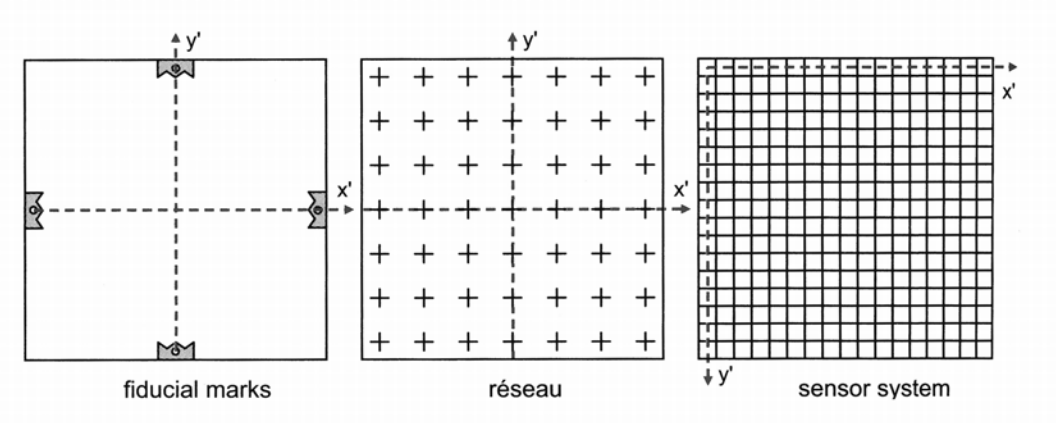

Figure 2.5: Image coordinate systems (Luhmann *et al.*, 2006)

on the resolution and sensor size of the camera. The principal point should usually coincide with the centre of the CCD device for an ideal digital camera, but the principal point is normally offset and the image coordinates must be reduced to the principal point. This procedure has also been adopted for analogue cameras. In contrast to metric cameras, parameters representing the interior orientation are rarely available for non-metric digital cameras. Consequently, camera calibration is necessary to ascertain these critical parameters for accurate spatial measurement.

2.3.1 Radial Lens Distortion

The collinearity Equations (2.9) assume that light rays passing through the camera lens are perfect collinear rays, which do not deviate from their original path. Variations in angles of refraction of lenses are responsible for deviations from the perfect collinear ray and are commonly interpreted as lens distortion. The distortion of a lens can be separated into two components: radial and tangential distortion (Section 2.3.2). For good quality lenses, the radial distortion is usually 10 times more significant than the tangential distortion (Luhmann *et al.*, 2006).

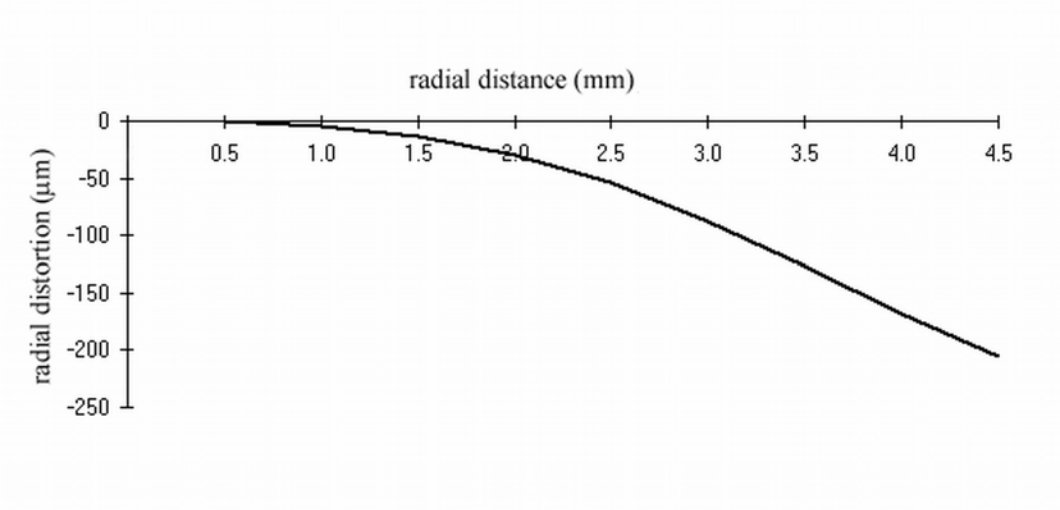

Figure 2.6: Radial distortion curve for Nikon Coolpix 5400 digital camera

The magnitude of the radial distortion (Δr) depends on the radial distance, illustrated in Figure 2.6, and focus settings of the lens. The distortion curve is usually expressed in a formula, derived from the Seidel aberrations:

$$\Delta r = K_1 r^3 + K_2 r^5 + K_3 r^7 + ... \tag{2.11}$$

where K_1 to K_n are the distortion coefficients corresponding to infinity focus and $r^2 = (x - x_P)^2 + (y - y_P)^2$ (Brown, 1971). The distortion parameters represented in Equation 2.11 are numerically correlated with the principal distance and image scale. Therefore, a linear part of the distortion function is separated and can be expressed in the form:

$$\Delta r = K_0 r + K_1 r^3 + K_2 r^5 + K_3 r^7 + ... \tag{2.12}$$

where $K_0 r$ is a constant term, which describes the angle of axial tilt to achieve the desired mathematical condition. The Equation 2.12 is known as *balanced radial distortion* (Fryer, 2001a). The total amount of radial distortion can be separated into its Δx_{rad} and Δy_{rad} components:

$$\Delta x_{rad} = \frac{(x - x_P)}{r}\Delta r \qquad \Delta y_{rad} = \frac{(y - y_P)}{r}\Delta r. \tag{2.13}$$

The K_0 and K_1 term is sufficient to model the radial lens distortion to micrometre level for most lenses fitted on non-metric digital cameras (Fryer, 2001a). For more complex lens systems, like wide angle lenses or lenses manufactured for metric cameras, the K_2 and even the K_3 term may be necessary to model the radial lens distortion accurately (Fryer, 2001a).

The radial distortion is also affected by the focus settings of the lens and the photographic depth of the field. Strictly speaking, the basic mathematical approach introduced is only valid for object points that are positioned in the same object plane on which the lens is focussed. Light rays of object points situated outside this object plane pass through the lens system on another path and other distortion values are strictly required. The formulae:

$$\begin{aligned} K_{1S^1} &= \left(1-\frac{c}{S^1}\right)^3 \left[\frac{\alpha_{S^1}}{\left(1-\frac{c}{S_1}\right)^3}\cdot K_{1S_1} + \frac{(1-\alpha_{S^1})}{\left(1-\frac{c}{S_2}\right)^3}\cdot K_{1S_2}\right] \\ K_{2S^1} &= \left(1-\frac{c}{S^1}\right)^5 \left[\frac{\alpha_{S^1}}{\left(1-\frac{c}{S_1}\right)^5}\cdot K_{2S_1} + \frac{(1-\alpha_{S^1})}{\left(1-\frac{c}{S_2}\right)^5}\cdot K_{2S_2}\right] \end{aligned} \tag{2.14}$$

developed by Magill (1955) and subsequently modified by Brown (1972) allow the calculation of the radial distortion terms for any focus setting of a lens. The radial distortion coefficients have to be determined at two focus settings, normally at infinity and another position close to the camera. S^1 is the actual focus distance of the lens, K_{1S^1} and K_{2S^1} are the unknown radial distortion parameters for the desired distance S^1; S_1 and S_2 are the camera to object distances used for calibration, K_{1S_1}, K_{1S_2} and K_{2S_1}, K_{2S_2} are the distortion coefficients determined at the distances S_1, S_2. The symbol for the principal distance is c and

$$\alpha_{S^1} = \frac{S_2 - S^1}{S_2 - S_1}\cdot\frac{S_1 - c}{S^1 - c}. \tag{2.15}$$

Fryer and Brown (1986) evaluated a further coefficient to model the variation of radial distortion within the depth of field:

$$\gamma_{SS^1} = \frac{S - c}{S^1 - c}\cdot\frac{S^1}{S} \tag{2.16}$$

where S refers to the distance of the plane of focus from the camera and S^1 is the distance to the object point. Hence the final mathematical form of the radial distortion Δr_{SS^1} is according to Fryer (2001a):

$$\Delta r_{SS^1} = \gamma^2_{SS^1} K_{1S^1} r^3 + \gamma^4_{SS^1} K_{2S^1} r^5 + \gamma^6_{SS^1} K_{3S^1} r^7 + \ldots \quad . \tag{2.17}$$

The depth of field distortions are usually smaller than 1 μm at the maximum radial distance of the sensor. Therefore, it is only necessary for high accuracy measurements using analogue metric cameras, although some high resolution cameras may have the accuracy potential for less than 1 μm and the depth of field effect should be considered (Luhmann *et al.*, 2006).

Fryer and Mitchell (1987) discussed the effect of radial lens distortion on close range stereophotogrammetry and presented an overview with a mathematical derivation. A detailed analysis showing the amount of x-parallax across a stereomodel, which are introduced by the distortion and that remain uncompensated during relative orientation is provided. These remaining uncompensated systematic errors cause a flat object to appear curved.

2.3.2 Tangential or Decentring Lens Distortion

Another component of distortion is the tangential or decentring distortion, mainly caused by decentring and misalignment of individual lens elements. The function developed by Brown (1971) can be used to compensate for this effect:

$$\begin{aligned} \Delta x &= P_1 \cdot (r^2 + 2(x - x_P)^2 + 2P_2 \cdot (x - x_P) \cdot (y - y_P) \\ \Delta y &= P_2 \cdot (r^2 + 2(y - y_P)^2 + 2P_1 \cdot (x - x_P) \cdot (y - y_P). \end{aligned} \tag{2.18}$$

Δx and Δy represent the tangential distortion at an image point (x, y) and r is again the radial distance. P_1 and P_2 are the coefficients for the tangential distortion. Fryer and Brown (1986) refined this model to calculate variations of

tangential distortion for different focus settings. The final form of this model can be represented by the equations:

$$\begin{aligned} \Delta x_S &= \left(1 - \frac{c}{S}\right) \left[P_1 \cdot (r^2 + 2(x - x_P)^2 + 2P_2 \cdot (x - x_P) \cdot (y - y_P)\right] \\ \Delta y_S &= \left(1 - \frac{c}{S}\right) \left[P_2 \cdot (r^2 + 2(y - y_P)^2 + 2P_1 \cdot (x - x_P) \cdot (y - y_P)\right]. \end{aligned} \tag{2.19}$$

If an object is positioned at the distance S^1 from the lens, the Equation 2.19 has to be multiplied by the factor γ_{SS^1} (Equation 2.16) according to Fryer (2001a). The impact of tangential distortion is less significant than the radial distortion. However, camera lenses should be tested to assess the significance of tangential distortion.

2.3.3 Affinity and Shear

Deviations of the image coordinate system with respect to orthogonality and uniform scale of the coordinate axes are described by affinity and shear. The following function provides an appropriate correction:

$$\begin{aligned} \Delta x_{aff} &= C_1 x' + C_2 y' \\ \Delta y_{aff} &= 0. \end{aligned} \tag{2.20}$$

These effects can be compensated for by means of an affine transformation based upon measurements of fiducial marks or a reseau grid (Figure 2.5) for analogue cameras. Digital imaging systems can produce these effects if the sensor has light sensitive elements that are rectangular rather than square (Luhmann *et al.*, 2006). Camera systems used for spatial measurements should be tested to assess the significance of affinity and shear.

2.3.4 Least Squares Estimation (LSE)

Least squares estimation can be described as a mathematical optimisation method to evaluate unknown parameters of a geometrical-physical model for a series of measurements according to the Gauss-Markov-Model. The aim of this approach is to conform the definite model with measurements and their unavoidable small residuals in the best possible way. It is widely used in geodesy, engineering surveying, photogrammetry and other disciplines where an over-determined system of equations is available (Cooper and Robson, 2001).

The bundle adjustment implements LSE for a special case involving photo and object coordinates. It is the most powerful tool and accurate method of image orientation and point determination in photogrammetry, because all observed values of different kinds and weights and all unknown elements are taken into account within one simultaneous calculation (Luhmann *et al.*, 2006). In order to meet criteria relating to precision, reliability and accuracy, it is possible to calculate standard deviations of object points and orientation parameters, residuals of image points, correlation between parameters and reliability numbers, which assists in the detection of gross errors. In addition, groups of parameters can be left out or others included. These characteristics of the bundle adjustment indicate the flexibility of this technique, which is particularly useful in close range photogrammetry since almost every measurement task has unique features (Cooper and Robson, 2001). Generation of approximate values for the unknowns, caused by the non-linear nature of the functional model and detection and elimination of gross errors, are known as practical disadvantages. However, an automatic estimation of starting parameters has been reported by Zheng and Wang (1992). Despite these disadvantages, the bundle adjustment has often demonstrated its ability to handle almost arbitrary image configurations with few restrictions on the image acquisition system (Luhmann *et al.*, 2006).

The roots of the bundle adjustment approach are to be found in the USA. Brown (1956) developed an analytical self-calibration method to recover the in-

terior orientation parameters simultaneously, whilst determining the exterior orientation of a ballistic camera (Kenefick *et al.*, 1972). The bundle adjustment has been modified and further developed by a variety of authors and is often known as the *self-calibrating bundle adjustment*. Ackermann *et al.* (1970) developed *PAT-B (PAT-M)*, a bundle adjustment package for aerial applications. Brown (1976) introduced the bundle adjustment for close-range use and also reviewed its evolution, application and potential. Further developments were closely related to increases in computing power and many different application packages for close range photogrammetry entered the market. STARS (Brown, 1982) is such an all-inclusive self-calibrating bundle adjustment package that has been further modified by Fraser and Brown (1986). The bundle adjustment has been accepted in all areas of photogrammetry since the early 1980s (Luhmann *et al.*, 2006).

The functional model of the bundle adjustment is based on the extended collinearity Equation 2.10. The photo coordinates (observed values) can be formulated as a function of all unknowns in the photogrammetric imaging process. If linearised at approximate values, these equations can be used directly as observation equations for least squares adjustment according to the Gauss-Markov model. A Taylor series expansion with approximate values for all unknowns is used to linearise the non-linear Equation 2.10, which involves deriving the differential coefficients of the function with respect to each parameter. The standard form is best represented using matrix notation:

$$l + v = A\hat{x} \; ; \; Q_{ll} \tag{2.21}$$

where

l	:	vector of observed minus computed photo-coordinates
v	:	vector of photo-coordinate residuals
A	:	partial differentials of extended collinearity equations with respect to all estimated parameters

$\hat{x}$: vector of parameters to be estimated

Q_{ll} : cofactor matrix of photo-coordinates.

The normal equation is:

$$A^T Q_{ll}^{-1} A = A^T Q_{ll}^{-1} l. \tag{2.22}$$

Finally, the solution vector is estimated in iteration:

$$\hat{x} = (A^T Q_{ll}^{-1} A)^{-1} A^T Q_{ll}^{-1} l. \tag{2.23}$$

The vital importance of the bundle adjustment for close range photogrammetry was described in this section. In particular, the possibility to include the parameters of interior orientation of all cameras in the solution demonstrates the significance of this technique for camera calibration procedures.

2.4 Camera Calibration Methods

Determination of the geometric relationships of a camera, defined by the interior orientation parameters, is known as *camera calibration*. Through the development of computer controlled techniques and the use of non-metric digital cameras for photogrammetry, methods of camera calibration have evolved rapidly over the last few decades. Different techniques of camera calibration will be discussed in this section.

2.4.1 Laboratory Calibration

The laboratory calibration approach has been traditionally adopted for calibrating aerial metric film-based cameras. The IOP is determined using a goniometer or collimator to measure the directions or angles of light rays passing through the lens of the camera. Instruments used for this calibration method are expensive

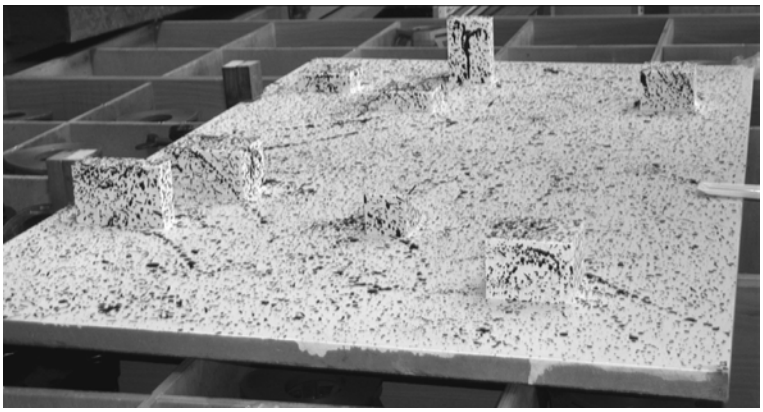

Figure 2.7: Camera calibration test field comprising flat fibre board with added square blocks and target points

and the execution is laborious and therefore, this approach is not popular for close range photogrammetry (Luhmann *et al.*, 2006).

With the availability of low cost computer power and the flexibility of the self-calibrating bundle adjustment, test fields containing hundreds of photogrammetric target points can be found in photogrammetric laboratories (Fryer, 2001a). These target points are normally coordinated to a few tenths of a millimetre through theodolite intersection. One image of a test field with photogrammetric target points, recorded from a single known position, provides a solution for camera calibration. A more robust and reliable solution can be provided using a combination of multiple images, recorded from several camera stations, with convergent arrangements (Granshaw, 1980). Such an optimum network design is provided in Fraser *et al.* (2005). Figure 2.7 represents an example for an indoor test field used for camera calibration in the research described in this project. The exterior orientation parameters $(X_O, Y_O, Z_O, \omega, \varphi, \kappa)$ and the familiar eight-parameter physical model, reported in Kenefick *et al.* (1972) and describing the interior orientation of a camera, are determined using a self-calibrating bundle adjustment. An $x,\ y$ observation for each of seven target points would provide a unique solution for the 14 unknowns (IOP + EOP). However, 3D observation of

50 or more targets, which are distributed across the entire format of a camera, provide a more reliable solution through redundancy (Fryer, 2001a).

Rotated images of 90 degrees about the camera axis are particularly significant to determine the principal point offset (Luhmann *et al.*, 2006). Using a known geometric distance, a solid test field or oblique images, the focal length of a camera lens system can be determined. It should be considered that the test field used for laboratory camera calibration should cover the entire image format and the location and number of target points can be critical for precise estimation of distortion parameters.

2.4.2 On-the-job Calibration

On-the-job-calibration can be regarded as a special case of test field calibration, where estimation of camera parameters and object recording are conducted at the same time (Fryer, 2001a). This approach is particularly suitable if the object, e.g. a patient's head, can not provide appropriate structures to identify discrete target points that can be used for self-calibration. This calibration method is especially efficient if the IOP of the camera used is considered unstable and has to be re-calibrated for each application or a change of focussing is needed for each recording session.

A simple setup can be described where a frame of levelling staves, is placed in the field of view and exposed simultaneously with the object. This procedure is widely used to capture large objects. This frame can also be used to provide absolute control to the image. Fryer (2001a) described a likely scenario used for close range applications. A frame with pre-coordinated targets, e.g. a cube made from lightweight aluminium bars, is placed over the object prior to photography. This of course implies that the object is not too large, say up to the size of a motor car. The object and the targeted frame are exposed simultaneously such that control information are available on each image, which provide appropriate data

to estimate the unknown camera parameters and can also be used for provision of control for the imagery.

2.4.3 Self-calibration

After Brown (1956) conceived the bundle adjustment and following further developments by Kenefick *et al.* (1972), the unknown parameters of a camera and the 3D coordinates of target points could be determined simultaneously. This technique is especially strong since all image observations, from various camera stations, are used to estimate the IOP and became known as self-calibration (Clarke and Fryer, 1998).

The data required for both object point determination and estimation of interior orientation parameters of the camera are provided by the observations of discrete targeted points on the object. The extended collinearity equations (2.10) are solved simultaneously using the bundle adjustment technique. The precision of object coordinates and IOP of the cameras are significantly influenced by geometrical arrangements of the cameras and the number and distribution of target points on the object (Section 2.4.1).

Kenefick *et al.* (1972) reported an eight-parameter model for the bundle adjustment, which includes parameters for: principal distance, principal point offset and correction coefficients to model radial and tangential distortion. In 1980, E. Kilpela presented how a Working Group of the International Society for Photogrammetry and Remote Sensing (ISPRS) assessed different sets of parameters that were added as additional parameters to a self-calibrating bundle adjustment (Clarke and Fryer, 1998). High correlation between certain parameters, orientations and locations of the cameras was recognised initially by Brown (1972). However, Granshaw (1980) and Fraser (1982) also identified the danger of potential 'overparameterization' of the bundle adjustment method. Including insignificant additional parameters in a bundle adjustment approach can actually weaken the solution and reduce the accuracy of derived parameters. Therefore,

all additional parameters included in the solution have to be examined to assess whether or not they are significant. Although a statistical test can be employed, a useful simplification is to compare the estimated additional parameters with their stochastical properties. These parameters are insignificant when their estimated values are smaller than their estimated standard deviation. This is a result of correlations amongst estimated parameters and attributable to weak network geometry (Chandler and Padfield, 1996; Cooper and Robson, 2001). The insignificant parameters have to be removed and remaining parameters re-estimated.

In summary, the main advantages of the self-calibration technique are its flexibility and that the IOP of the cameras involved can be estimated simultaneously with object recording using all available imagery, providing an optimal solution for object reconstruction (Luhmann *et al.*, 2006).

2.4.4 Plumb-line Calibration

The plumb-line calibration technique was originally developed by Brown (1971). This approach is based on the condition that a straight line in the object space is projected as a straight line in the image space, which is the case if perfect collinearity is achieved . Any deviations from linearity must be attributed to lens distortion. By measuring these deviations in the image space, parameters for radial and tangential distortion can be extracted. Estimated parameters to model lens distortion are uncorrelated to further parameters of IOP and EOP, which is the main advantage of the plumb-line method.

Various researchers (e.g. Brown (1971), Fryer and Fraser (1986), Clarke *et al.* (1998)) demonstrated that the principal point offset is highly correlated with the parameters of tangential distortion. More recently, Lerma and Cabrelles (2007) report that large offsets of the principal point can cause significant difficulties when attempting to recover accurate lens distortion parameters through plumb-line calibration. Using lenses with very large distortions (e.g. fish-eye-lenses), the

laboratory or self-calibration technique is required to estimate the offset of the principal point (Clarke and Fryer, 1998).

Initially, the plumb-line calibration method was developed as a laboratory calibration based approach used to calibrate cameras involved in close range photogrammetry. A laboratory test field, comprised of vertical hanging wires often achieved using plumb bobs, which gave the rise to the name of this approach, provided suitable lines. Alternatively, appropriate straight lines provided by natural structures, like features on buildings (close and medium range photogrammetry) or streets (aerial photogrammetry), have been used for camera calibration using the plumb-line technique (Fryer, 2001a; Luhmann *et al.*, 2006). Although these lines are indeed straight, they are not plumb. However, the photogrammetric theory stipulates that lines need only to be straight and not strictly vertical.

In the era of digital photogrammetry, automatic line following software was developed. Using these automatic line following routines, a high density sample of points on each line can be achieved and consequently, a large number of data points are available to estimate the lens distortion parameters with appropriate reliability.

Lens distortion parameters, determined using the plumb-line calibration approach, can be used as an independent check on lens models derived by self-calibration or, as an alternative to estimate lens distortion coefficients prior to a bundle adjustment (Fryer, 2001a).

2.5 Survey of Calibration Software

This section provides an overview of available commercial and non-commercial calibration software for digital cameras, which were identified using the world wide web. An overview of these software is represented in Table 2.1. Testing and describing all of these calibration programs was almost impossible. Therefore, only a small selection is described in this section, ranging from the professional software package of ERDAS IMAGINE to the freely available Camera Calibration

Table 2.1: List of camera calibration software

Software package	*Availability*
Leica Photogrammetry Suite LPS	commercial
Topcon PI-3000	commercial
OMC-Camera Calibration Software	commercial
PhotoModeler	commercial
A Calibration Toolbox for Matlab	freeware
Microsoft Easy Camera Calibration	freeware
Tsai Camera Calibration Software	freeware
Multi-Camera Self-Calibration	freeware
TELE 2	freeware

Toolbox for Matlab. Additionally, the external bundle adjustment program GAP, used for camera calibration in this study, which is neither commercially nor freely available, is introduced.

2.5.1 Leica Photogrammetry Suite (LPS) PRO

The ERDAS IMAGINE LPS Pro software provides opportunities for camera calibration but is not freely available. It can be used for triangulation and orthorectification of images collected from various types of sensors. LPS offers the opportunity to choose between a variety of geometric camera models that includes frame cameras, digital cameras, non-metric cameras etc. (Erdas Inc., 2003). The software uses a bundle adjustment approach (Section 2.3.4) to establish a mathematical relationship between images, IOP and EOP. If the IOP of a camera is known, these parameters can be incorporated manually or automatically using an LPS calibration file. If the digital camera option is selected, parameters include focal length, principal point coordinates, pixel size in the x and y directions of the CCD and parameters to model radial distortion, which can be fed into the software. Entering the values for focal length, principal point and size of the CCD is straightforward, but to establish the radial distortion of a camera, distortion values for a range of radial distances are required. However, LPS also comes with a self-calibration option in case the IOP of the camera is unknown. The pixel size

of the CCD and an initial estimate of the focal length have to be provided prior to self-calibration. Various predefined sets of additional parameters to model the camera geometry are provided, which range from two parameters modelling radial lens distortion up to a '14 parameter Brown model'. This model arises from a parameter set, identified by Zhizhuo (1990) using 29 additional parameters and attributed to Brown (1972). Reducing this model to the 14 parameters, which were most significant, should ideally provide most users with the capability to calibrate non-metric cameras (Chandler *et al.*, 2005). However, performing a self-calibration where just one radial distortion parameter is to be estimated is not possible and identifies a critical weakness of the software. Fryer (2001a) suggests that the radial distortion coefficient K_1 alone is significant to model the distortion of simple lens systems used in consumer-grade digital cameras.

This software package appropriates an easy-to-use environment for DEM generation (Section 2.7) and some possibilities for camera calibration if K_1 and K_2 are required and the image geometry is sufficient for their recovery.

2.5.2 A Camera Calibration Toolbox for Matlab

The camera calibration toolbox for Matlab (Bouguet, 2000) is an open source software for calibrating digital sensors. The computer operating system can be any system that supports a software version of Matlab from 5.x to 6.x. A planar pattern (Figure 2.8) is required that has to be observed in different orientations. The camera and this pattern can be freely moved and neither an *a priori* knowledge of the motion nor a specific camera model is required. After providing the calibration images, the user is asked to identify manually the four outer corner points in each of the images. Subsequently, the calibration process is automatically performed. Determined intrinsic camera parameters (focal length, principal point coordinates, a skew coefficient defining the angle between the x and y pixel axes, radial and tangential distortion parameters) as well as the extrinsic parameters (rotations and translations) are represented in the output file. These parameters

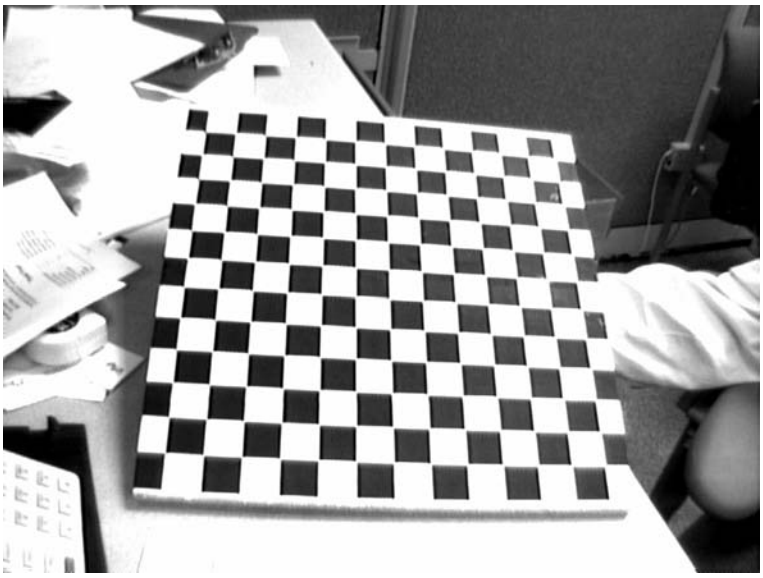

Figure 2.8: Planar pattern for Matlab calibration toolbox

are estimated by using a bundle adjustment that is similar to Heikkilä and Silvén (1997). Setting variables 'on' or 'off' in the program code provides the opportunity to specify, which of the IOP parameters are estimated. This approach is a powerful camera calibration tool for digital cameras, characterised particularly because it can be run on different computer operation systems. Tests were conducted using calibration sheets of various dimensions to calibrate a camera at distances, which were appropriate for this research. However, these tests revealed that satisfactory camera parameters could not always be derived using this software package.

2.5.3 PI-3000 Software (trial version)

The TOPCON camera calibration software (Topcon, 2007) provides opportunities to calibrate digital sensors but only a 30 day trial version is freely available. An exclusive calibration sheet (Figure 2.9) is included in the software that is available in different dimensions ranging from A4 to A0. After printing this cal-

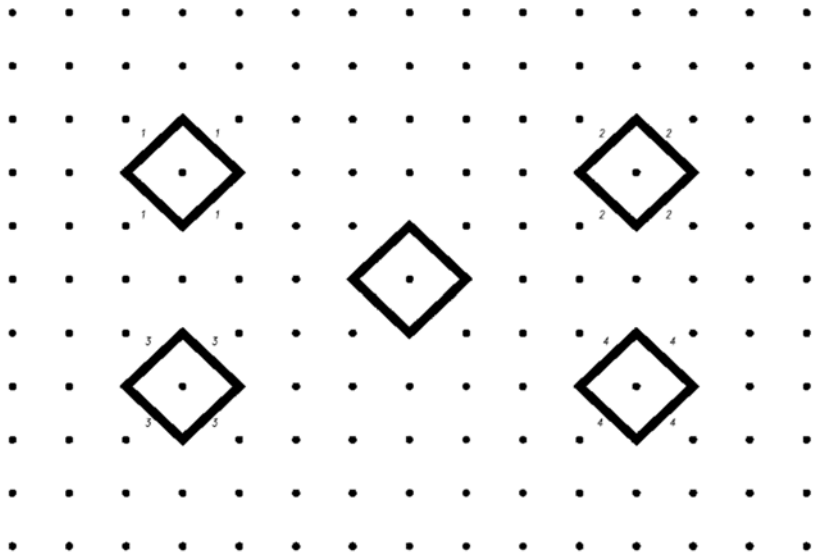

Figure 2.9: Calibration sheet for PI-3000

ibration sheet and attaching it on a flat surface, 5 images from different angles (Direct Front, Upper location, Lower location, Left side and Right side) have to be captured. These images are imported in the calibration software and an initial estimate for the focal length has to be set. In order to perform camera calibration, the centre of dot marks, positioned in 4 peripheral squares, except the centre square, have to be measured semi-automatically in each image. Remaining dot marks in each image are measured fully automatically. After all dot marks in each image are detected and measured, the software uses a bundle adjustment to compute the camera parameters, including focal length, principal point coordinates, two parameters to model radial lens distortion and two parameters to model tangential lens distortion. However, it is not possible to exclude parameters to be estimated, which again reveals a weakness of the software. Furthermore, the output report, created by the software, only includes the estimated camera parameters. Stochastical values like standard deviations for estimated camera parameters or number of iterations are not accessible, which

makes it difficult to evaluate the results. This software provides an easy-to-use calibration tool but estimated camera parameters would normally be carefully examined prior to their use for 3D measurement tasks.

2.5.4 General Adjustment Program (GAP)

The general adjustment program GAP, developed by Clark (Chandler and Clark, 1992), can be classified as a self-calibrating bundle adjustment and has successfully been used for camera calibration (Chandler *et al.*, 2001, 2003, 2005). The interior orientation parameters (focal length, principal point offset, scale factor in x direction, affine distortion, three parameters to model the radial distortion and two parameters modelling the tangential distortion) can be included into self-calibration in two ways. The first approach uses a block-variant solution, which assumes that each image was obtained with a different camera. An alternative approach, the block-invariant solution, assumes that all images were obtained with the same camera. These features, the fact that the interior orientation parameters are fully selective and the possibility to use this software with various operating systems (Unix, DOS, Windows) demonstrate its flexibility. In addition, a substantial output report is generated that summarises all results and contains following information:

- list of input files and control parameters, data, project description
- list of image measurements including corrections and reliability numbers
- list of adjusted object points with standard deviations
- mean standard deviations of image and object coordinates
- maximum corrections with identifiers of corresponding points
- parameters of interior and exterior orientation with standard deviations.

The datum for the bundle adjustment can be defined by a series of previously estimated or derived coordinates, constrained by their standard deviations.

In conclusion, GAP has proved to be flexible and reliable tool for self-calibration and has therefore been adopted for camera calibration tasks and simulation tests in this research.

A plumb-line calibration approach was also used in this study to estimate lens distortion parameters for a sensor. The development of test objects and software codes for this approach is described in Section 3.1.2.

2.6 Stability analysis of Consumer-grade Digital Cameras

The use of non-metric digital sensors for close range photogrammetry has been reported in many industrial applications (Fryer *et al.*, 2007) but also in diverse fields ranging from medical science, via forensic science to architectural work (Fryer, 2001b). This section summarises approaches that demonstrate the photogrammetric potential of non-metric digital cameras for close range measurements. Additionally, analytical methods later used to demonstrate the stability of such cameras will be introduced.

2.6.1 Photogrammetric Capabilities of Consumer-grade Digital Cameras

Over the last decade, several researchers have assessed the photogrammetric potential of non-metric digital sensors. The Kodak DCS420 and DCS460 cameras are widely reported in photogrammetric applications (Beyer, 1995; Brown and Dold, 1995; Dold and Peipe, 1995; Fraser *et al.*, 1995; Miyatsuka, 1996; Peipe, 1996; Schneider, 1996; Shortis *et al.*, 1998) and the use of similar cameras such as the Kodak DC40 has been described by Miyatsuka (1996) and Lichti and Chapman (1997).

Ahmad and Chandler (1999) discussed the impact of sensor size and resolution of the Kodak DC40 (756 × 504 pixel), DCS420 (1524 × 1012 pixel) and DCS460 (3060 × 2036 pixel) cameras upon the accuracy and precision of 3D data, derived using photogrammetry. A self-calibrating bundle adjustment (Section 2.3.4, 2.4.3) was used to estimate the IOP of the cameras. Images of a 3D test range with retro-reflective targets were acquired and the centre of these target points were measured automatically using two different image processing operators: centre of gravity and weighted mean. As expected, it concluded that an increase in sensor resolution is followed by a commensurate increase in precision. The DCS420 and DCS460 cameras demonstrated their potential for photogrammetric measurement applications where high accuracy is required whilst the low resolution DC40 camera was perhaps suitable for measurements that require medium accuracy.

The suitability of the Kodak DCS Pro Back for close range measurements in conjunction with the Mamiya body is reported in Mills *et al.* (2003). Several IOP parameters (principal distance, principal point offset, lens distortion and the effect of an removable infrared filter) were investigated in a series of self-calibrations. The camera is found to be suitable for photogrammetric measurement applications of low to medium accuracy, when re-calibration on a regular basis is executed. However, if using the camera for high precision metrology, modifications to minimise the body-back movements would be required.

The accuracy in close range surface measurement between three low-cost consumer-grade digital cameras (Sony DSC-P10, Olympus C3030, Nikon Coolpix 3100) and the Kodak DCS460 was compared in Chandler *et al.* (2005). The IMAGINE OrthoBase Pro software (now LPS) (Section 2.5.1) and an independent self-calibrating bundle adjustment (GAP) (Section 2.5.4) were employed to acquire interior and exterior orientation parameters for the cameras and digital elevation models (DEM) were extracted. This approach has proven to be efficient and effective to obtain camera calibration data suitable for close range surface

measurement. Tests have demonstrated that these consumer-grade digital cameras are capable of close range surface measurements. Achieved accuracies are comparable with the proven Kodak DCS460. However, the authors reported that sensor resolution is important and at the time of writing a 5 mega-pixel camera should be used to extract useful data. This research also identified residual systematic error surfaces or domes, visible in DEMs and probably arising from slightly inaccurately estimated radial distortion parameters (Fryer and Mitchell, 1987). This issue provides a major focus for the research described in this thesis.

2.6.2 Stability of Non-metric Digital Cameras

Analogue and digital metric cameras are designed to fulfill and maintain the collinearity condition (Section 2.2.2) and are ideally suited for photogrammetric measurements. Additionally, manufacturers of metric cameras provide a calibration certificate that includes the camera parameters for each sensor. Such cameras are capable of maintaining their interior orientation over a long time period, normally proven by substantive long term testing. Stability analysis, which investigate the stability of non-metric digital cameras, have rarely been reported. Habib and Morgan (2005) attribute this lack of literature to the absence of standards for quantitative analyses of camera stability. Hence, these scientists recommend and outline the incorporation of straight lines in a bundle adjustment procedure for camera calibration. An approach based on statistical testing between two sets of IOP of the same camera, derived from two different calibration sessions, is presented. It was identified that statistical testing would not yield reliable measures of the stability of the IOP of the camera used. Therefore, a new methodology for stability analysis, based on evaluating the degree of similarity between the reconstructed bundles, using two sets of IOP, was introduced. The author's expected high correlations between IOP and EOP and additional measures, for comparing the bundles in terms of their fit at the given object space, had to be developed. Consequently, a more relaxed measure could be derived.

The camera used was calibrated in various calibration sessions, which were conducted over a long time period. Through analysis of the determined sets of IOP, by means of the introduced methodologies, this camera revealed its stability.

Three approaches were used to evaluate the stability of off-the-shelf digital cameras by Habib *et al.* (2006). The strategy is based on investigating the degree of similarity between the reconstructed bundles, using two sets of IOP, derived in two calibration sessions (Habib and Morgan, 2005). This method imposed constraints regarding the EOP of the compared bundles. Each of these is applicable to a specific geo-referencing technique that describe the position and orientation of the images relative to a reference frame. The Kodak Pro DCS-14n digital camera, used in an aerial mapping project, was calibrated using a traditional 2D test field to evaluate the stability over a period of six months to prove these methodologies.

The stability of the Olympus C-5050 non-metric digital camera was analysed by Bosch *et al.* (2005). This camera was calibrated using a laboratory test range and the software package Pictran. Sets of IOP, derived in various calibration sessions over a three moth period, were evaluated for similarity. In addition, a test using real data was conducted to prove that the camera is suitable for keeping photogrammetric records of historical buildings. The author's concluded that the Olympus C-5050 camera seems to be stable and could be used for photogrammetric documentation of historical buildings.

2.7 DEM Extraction using LPS

A software package for DEM generation was needed to conduct stability analysis for the seven Nikon Coolpix 5400 digital cameras (Section 3.3). A routine for DEM generation, using a feature-based matching method and orthophoto generation is provided by the LPS software. This DEM extraction process can be split into three clearly defined steps: digital image matching, ground point coordinate determination and DEM construction.

The first step, digital image matching, forms the basis for automatic tie point generation and automatic DEM extraction in LPS (Erdas Inc., 2003). Digital image matching methods can be categorised into three general techniques; area based, feature based and hybrid techniques. Digital numbers in small sub-arrays from each image are numerically compared to perform the image match using the area based method. Extraction of features is involved in the feature based method and it is therefore more complicated than the area based method. The features to be extracted comprise edges at different scales, with subsequent comparison, based on feature characteristics such as size and shape. This is known as the feature based matching technique. A combination of the first two is the hybrid method. Typically, the left and right image are processed to highlight features. These identified features are then matched by the area based method (Wolf and Dewitt, 2000).

LPS uses a hierarchical hybrid based technique to perform digital image matching. Feature points are identified in each image using an interest operator. The centre of a template window that exhibits sufficient grey level and contrast variations describes a potential feature point. When a feature point has been successfully identified in the first image, LPS estimates the approximate position on the neighbouring overlapping image and searches for the corresponding feature point in an rectangular window around that approximate position. The rectangular window is known as the search window with dimensions $x \times y$. The x direction of the search window defines the search length along the epipolar line k'' (Figure 2.10) whilst y defines the search area across this epipolar line. Figure 2.10 represents the epipolar geometry for the photogrammetric normal case and convergent images. P'' in the right image, corresponding to P' in the left image, must lie on the epipolar line k'', assuming an error-free ray intersection. For images with accurate triangulation results, the epipolar line can be computed accurately enough that 1 to 3 pixels for the y direction and 7 pixels for the x direction for the search window size is sufficient (Erdas Inc., 2003). This is important for image matching since the search space for corresponding feature points

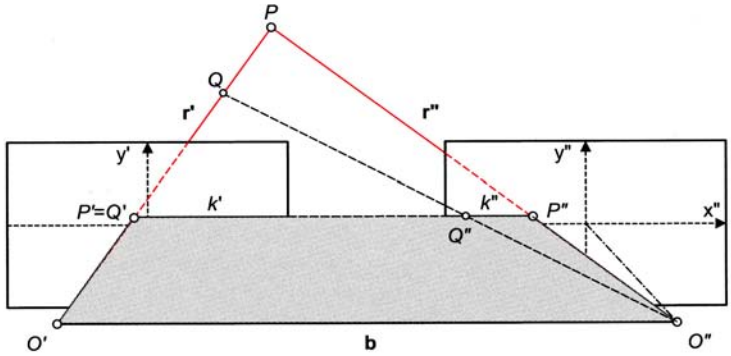

(a) Epipolar plane for normal case

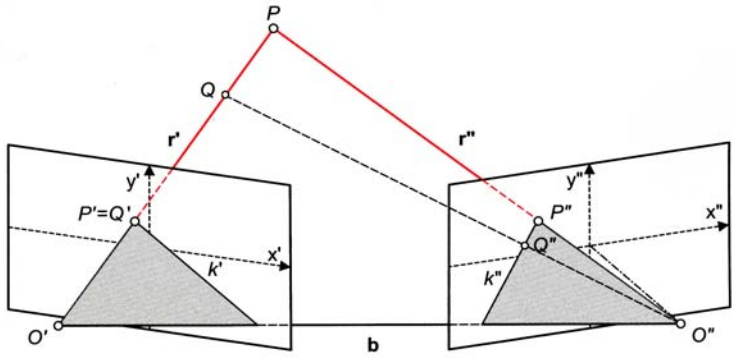

(b) Epipolar plane for convergent case

Figure 2.10: Epipolar Geometry (Luhmann *et al.*, 2006)

can be reduced significantly (Luhmann *et al.*, 2006). However, using a search windows size of more than 7 pixels for the x direction may be more adequate in close range applications.

The size of the window used to compute the correlation coefficient between feature points on multiple overlapping images is defined by the parameters $(x \times y)$ of the correlation window size. A correlation window size of 9×9 pixels or greater can be used for areas containing minimal variations in topographic relief, grey level or colour intensity whilst a smaller correlation window size of e.g. 5×5 pixels is recommended for areas containing large degrees of topographic relief, grey level or colour intensity variations (Erdas Inc., 2003). LPS computes a cor-

relation coefficient for each set of possible feature points. The similarity between a set of feature points appearing within the overlapping area of an image pair, is measured using these correlation coefficients. A lower correlation coefficient value statistically indicates that the set of feature points is less similar than a set with has a larger correlation coefficient value.

Another important parameter that influences the point matching process is the correlation coefficient limit. This defines the correlation coefficient threshold, which is used to determine whether or not two identified feature points are considered to be a possible match. The correlation limit is compared to the correlation coefficient that has been computed for two feature points appearing on two frames. These two points are to be considered as a match, if the correlation coefficient value is larger than the value of the correlation coefficient limit.

The second step of the DEM extraction process is the computation of the 3D ground coordinates of the successfully matched feature points using the method of space forward intersection using the known IOP, EOP and collinearity Equations 2.10. These computed points with known 3D coordinates are used as reference points for surface generation.

The third step comprises the task of surface generation. LPS uses the reference points to interpolate elevation values in order to obtain various surface representation outputs including: TerraModel TIN, ESPRI Shape file, ASCII file and raster DEM (Erdas Inc., 2003). The raster DEM output was adopted in this study since these could be compared with the "Truth", which is explained in Section 3.2.1, 3.2.2 and 3.2.3. Methods for interpolation can be divided into two groups, including global methods and local deterministic methods. All available data are used by global interpolators to provide predictions for the whole area of interest. Global interpolators are not considered here since they are not commonly used for direct interpolation. Local interpolators use only data in the immediate neighbourhood of a point to compute estimates (Burrough and Goodchild, 1998). The local deterministic methods of interpolation, which are briefly discussed in

this section include: nearest neighbours interpolation, inverse distance weighted interpolation, splines interpolation and Delaunay Triangulation.

The nearest neighbour interpolation uses Voronoi polygons or Thiessen regions whereby the prediction of the pixel value is provided by the nearest single data point. The region is divided by the Voronoi polygons in a way that is totally determined by the configuration of the data points. Therefore, this method is not appropriate for gradually varying phenomena, unless there are many observations available. The technique is often used in Geographic Information Systems (GIS) and geographical analysis as a quick technique relating point data to space (Burrough and Goodchild, 1998).

The inverse distance weighted technique is a two dimensional interpolation function for irregularly spaced data, developed by Shepard (1968). An average value is computed from neighbouring data points, and weighted according to distances between the set of neighbouring data points and the point to be predicted. This is the simplest form of the inverse distance weighted method, which uses an linear interpolator. Several shortcomings were identified for this simple method and various modifications and correction terms had to be developed to improve the weighting function (Shepard, 1968). However, inverse distance weighted interpolation is commonly used to create regular grid data.

Another method used for surface fitting is the spline interpolation. A polynomial function is fitted exactly to a small number of data points. Ensuring that the joins between one part of the curve and another are continuous, a smooth surface representation can be achieved. In contrast to weighted functions, splines are able to retain small-scale features. A disadvantage of the spline interpolation approach may be that thin plate splines provide a view of reality that is unrealistically smooth (Burrough and Goodchild, 1998).

Due to the problems identified for the described methods, an alternative technique for surface fitting has been developed, which is based on a triangulation of data sets. The most widely known triangulation method is the Delaunay Triangulation (Petrie and Kennie, 1990). The scattered reference points are meshed to

form a set of triangles. Once the triangulation process is completed, points can be interpolated using these triangles to create a raster DEM. This method is the one adopted by LPS for surface fitting (Erdas Inc., 2003) used during DEM generation (Section 3.2.2) and in creating a surface from XYZ data (Section 3.2.1).

In conclusion, the LPS software package provides an easy-to-use environment for DEM generation and orthophoto generation. This DEM generation routine was used in this study to provide appropriate surface representations used to assess the quality of photogrammetric data (Section 3.2).

2.8 Photogrammetric Data Quality

Data sets in photogrammetry generally consist of measured elements and estimated elements, normally referred to as parameters. Measured elements include image coordinates and coordinates of control points whilst the estimated elements consist of coordinates of object points and interior and exterior orientation parameters. Errors of measured values are divided into three groups: random, gross and systematic. Random errors can be described as variations of measured values obtained under the same conditions. These are impossible to eradicate and must be accepted as a feature of any measurement procedure. Gross errors are mistakes or 'blunders', made by operators, malfunctioning equipment or automatic measuring systems. Systematic errors arise from any biasing effect, in the environment, method of observation or instruments used or from the selection of incorrect or incomplete functional models (Cooper and Cross, 1988). All three types of error control the quality of derived data, which must be assessed. When photographs on film or glass were measured by an operator, the photogrammetrist was able to monitor the data fairly closely and correct or remeasure data that were clearly gross in nature. In digital photogrammetry, automated processes widely replaced human activity and these automatically generated data must be automatically assessed (Cooper and Robson, 2001).

Cooper and Cross (1988) define the quality of derived data as a function of precision, accuracy and reliability with respect to the three error types. The terms precision and reliability are used to describe the quality of data with respect to random and gross errors, whilst accuracy describes the quality of data with respect to systematic errors.

2.8.1 Precision

Measures of precision are commonly computed from the covariance matrices of the parameters. The covariance matrices $C_{\hat{x}}$ and $C_{\hat{l}}$, in case of a self-calibrating bundle adjustment, are:

$$Q_{\hat{x}} = (A^T Q_{ll}^{-1} A)^{-1} \tag{2.24}$$

$$C_{\hat{x}} = \sigma_0^2 Q_{\hat{x}} \tag{2.25}$$

$$Q_{\hat{l}} = A(A^T Q_{ll}^{-1} A)^{-1} A^T \tag{2.26}$$

$$C_{\hat{l}} = \sigma_0^2 Q_{\hat{l}} \tag{2.27}$$

where

$C_{\hat{x}}$	:	covariance matrix of the estimated parameters
$Q_{\hat{x}}$	:	cofactor matrix of the estimated parameters
$C_{\hat{l}}$	:	covariance matrix of the measured parameters
$Q_{\hat{l}}$	:	cofactor matrix of the measured parameters
σ_0^2	:	variance factor.

These covariance matrices can be used to compute various measurements of precision, including the standard deviation of measured and estimated parameters, error ellipses and ellipsoids, eigenvalues and eigenvectors and variances of derived quantities (Cooper and Cross, 1988).

The standard deviation of measured or estimated parameters by LSE is an indication of their precision since these parameters are generally correlated through

the LSE processes that are used to evaluate them. By increasing the number of measurements, the precision of the mean value of a measurement will always improve (Cooper and Robson, 2001).

Major controlling factors on the final precision of all estimated parameters are the precision, number and distribution of control points. The precision of control points is defined by their standard deviation. Poor precision, inconsistency or a minimal number of control points can degrade the final precision of estimated parameters. Additionally, poorly designed control targets, which cannot be accurately identified in the image, will lead to less precise measurements (Chandler, 1989).

The precision of measured image coordinates should be similar in x and y directions and is defined by their standard deviations. Different values for the standard deviation in x and y implicate that the measuring device or camera generates systematic errors. Different weighting for separate groups of observations (e.g. measured image coordinates, measured distances) can be integrated in most bundle adjustment programs, allowing processing according to their importance or precision. The precision of adjusted image points can be computed from the covariance matrix $C_{\hat{l}}$ (Equation 2.27) (Luhmann *et al.*, 2006).

For analysing the precision of a bundle adjustment, the precision of adjusted object points is of importance. Two criteria should be considered:

- Root mean square error (RMS) of all estimated coordinates
  The general precision level of the adjustment can be evaluated using the RMS.

- Maximum standard deviation of single points
  Loss of precision is indicated by maximum residuals, which are identified by maximum standard deviations.

The maximum standard deviation should stay within specific limits, if object coordinates are to be used for further calculations or analyses (Luhmann *et al.*, 2006).

```
#  Camera parameter data file and standard errors
#
#  Results from GAP (v8.00) run on Wednesday, 14/6/106 at 9:52 by PC user
#
#  Input files:
#  Target data      : E:\programs\GAF/report.tar.dat
#  Photo data       : E:\programs\GAF/report.phots.dat
#  Photo obs. data  : E:\programs\GAF/report.pobs.dat
#  Camera data      : E:\programs\GAF/report.cam.dat
#
# Camera X-shift Y-shift DeltaF  XScale Affine Rad1    Rad2        Rad3    Tan1   Tan2
#
  5.9569  0.0835  0.0018  0.000  1.000  1.000 -3930.01 89478251.4   0.0    0.000   0.000\
          0.0000  0.0000  0.000 -1.000 -1.000  0.000   0.000       -1.000 -1.00   -1.00
# s.e.'s  0.0024  0.0024  0.013  fixed  fixed  33.03   2135438.1    fixed  fixed   fixed
# Focal length changed by 0.1569mm
# XScale factor of: 1.00000000 and an Affine distortion of: 1.00000000
```

Figure 2.11: Results of a self-calibration (GAP output)

The precision of interior orientation parameters and their correlations should be carefully examined if estimated by self-calibration and extracted for use in further calculations or photogrammetric projects. Standard deviations for these parameters can be calculated from their covariance matrix $C_{\hat{x}}$ (Equation 2.25). An appropriate precision for focal length and principal point is achieved if their standard deviations are in the order of the image measuring accuracy (Luhmann *et al.*, 2006). Parameters to model radial distortion are usually the most effective additional parameters and their related standard deviations should be much smaller (approximately 100× for k_1, 10× for k_2) than the parameters themselves (Figure 2.11) (Luhmann *et al.*, 2006).

Another important factor affecting the precision is the overall network geometry used for self-calibration, and especially the camera station configuration (Remondino and Fraser, 2006). A weak network geometry will degrade the precision of estimated parameters, especially the interior orientation parameters. Consequently, a highly convergent imaging configuration, the incorporation of orthogonal camera roll angles and the use of four or more images can be considered as a minimum configuration appropriate for self-calibration (Fraser, 1997).

2.8.2 Reliability

Reliability is related to gross errors and are genuine mistakes or blunders, arising during photogrammetric measurements (Cooper and Cross, 1988). These author's also distinguish between internal and external reliability. The internal reliability of a single measurement is the size of a marginally detectable error whilst the external reliability refers to the effect of an undetected gross error on the parameters or data derived from them. Fortunately, a limited number of gross errors are easy to detect because of their size. However, the detection of gross errors in LSE is difficult because the target function $\varphi_{LSE} = v^T W v$ is minimised according to the Gauss-Markov-Model. If multiple measurements have gross errors this does not imply that computed estimates for these measurements through LSE have correspondingly large residual or correction. In order to minimise φ_{LSE}, the error will spread out amongst many measurements (Cooper and Robson, 2001). Probably the most widely used test to detect such outliers is the τ-test and is often included in bundle adjustment programs (Cooper and Cross, 1988). Hottier (1976) states that gross errors can be detected and eliminated by increasing the redundancy of the measurements, which increases the internal reliability of data sets. So if the network is strong, it is easier to detect gross errors.

2.8.3 Accuracy

Accuracy is related to uncorrected systematic errors that generally have a limiting effect on the quality of derived data. These errors are much more difficult to detect than gross or random errors. Systematic errors can arise from different sources including lens distortion, film deformation, un-flatness of the CCD array or poorly distributed control points. Calibrating all instruments can assist, removing the systematic errors before the measurements are used in an estimation algorithm. However, accounting explicitly for all systematic errors in a self-calibrating bundle adjustment is impossible because of high correlations between additional parameters (Section 2.4.3) or a particular systematic error, which is not estimable from

the measurements. The functional model can be extended, with additional parameters to model any suspected systematic error but these parameters have to be carefully examined in order to avoid over-parameterisation. Consequently, standard deviations for each additional parameter need to be computed so that the significance of parameters can be assessed. Insignificant additional parameters have to be removed from the functional model because these degrade the quality of measurements and hence of the estimated parameters (Cooper and Cross, 1988; Granshaw, 1980).

The stability of a camera can be derived from the degree of similarity between two sets of IOP. The degree of similarity can be reliably established by analysing the impact of varying IOP on accuracy in the object space (DEMs). A widely used measure in experimental and theoretical analyses of DEM accuracy is the RMS error of checkpoints. However, Li (1988) pointed out that this measure for DEM accuracy is not always appropriate in a statistical sense. Following Li (1988), using mean error and standard deviation of error is more appropriate. The mean error reflects remaining systematic errors, whilst the standard deviation is related to random errors.

2.9 Summary

The current literature reveal that the main mathematical principles used in photogrammetry are embodied by the collinearity conditions. By implementing and extending this simple geometric condition within a self-calibrating bundle adjustment, unknown camera parameters can be estimated simultaneously using all image observations. Additionally, this powerful technique provides an established theoretical framework to minimise errors and offers the possibility to include additional camera parameters to be estimated. Measurements of different parameter groups with varying quality can be combined in a rigorous way because of the use of both a functional and stochastical model. A variety of commercial and non-commercial software for camera calibration can be found on the market.

The literature identified that non-metric digital sensors are capable of maintaining their interior orientation over long time periods but the required stability analysis to support this have been rarely reported. This lack in literature is attributed to the absence of standards for stability analysis. It is suggested that approaches have to be developed to assess stability and conformation of digital sensors before they can be used routinely for measurement over long time periods.

Evaluating the quality of photogrammetric data is essential but often ignored, particularly through assessing the impact in the object space. The quality of acquired data is a function of precision, reliability and accuracy in respect to gross, random and systematic errors. Systematic errors are particularly difficult to detect and eliminate. These undetected systematic errors provide a limiting constraint on the quality of derived data. The functional model of a bundle adjustment can be extended with additional parameters to model systematic errors but these parameters have to be carefully analysed. Further studies are needed to develop techniques that minimise the effect of remaining systematic errors.

CHAPTER 3

Methodology

This chapter identifies and verifies the strategies and workflows developed to achieve the aims and objectives (Section 1.1) of this research. Difficulties that arose in the course of work, and the methodologies that were developed to accomplish satisfactory solutions for these, are illustrated. The structure of this chapter mirrors the order of the aims and objectives (Section 1.1) and concludes with a short summary.

3.1 Photogrammetric Processing

Photogrammetric processing describes the workflow, necessary to establish the relationship between images and control points, represented by interior and exterior orientation parameters. The process is also known as camera calibration, which was a key issue in this research. The Leica Photogrammetric Suite software LPS (Section 2.5.1) and the General Adjustment Program GAP (Section 2.5.4) were used for most of the photogrammetric processing carried out.

3.1.1 External Self-calibrating Bundle Adjustment GAP

The potential applications for rapidly evolving digital camera technology are particularly wide for very close range activities (Fryer *et al.*, 2007). It is for this

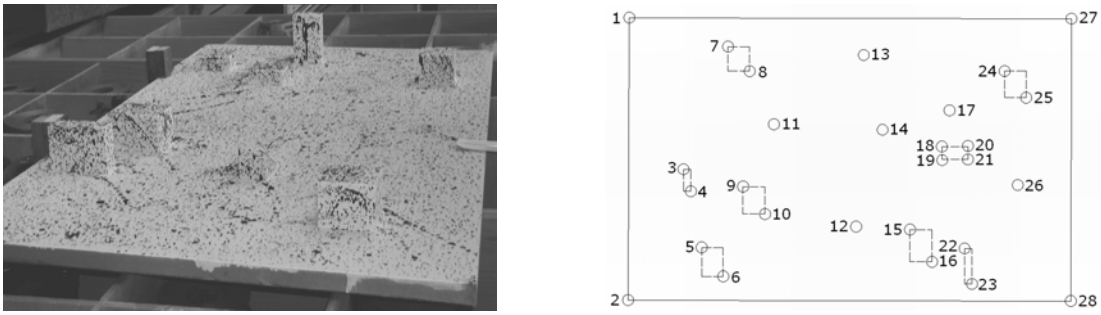

(a) Overview of the test field

(b) Photogrammetric target points

Figure 3.1: Test field used for camera calibration

reason that the cameras involved in this study would mainly be used at a camera-object distance of between 1.5m to 8.0m. Therefore, techniques and utilities were developed and constructed to be used for camera calibration at these distances.

A 3D and planar test field was specifically constructed to allow cameras to be calibrated at the distances specified previously. It is an enhancement of the test field used in Chandler *et al.* (2005) and consists of a medium density fibreboard (MDF) (1.2m × 0.9m). Eight square blocks of various shapes and heights were added (Figure 3.1a). These blocks replicate physical structures such as buildings found in normal vertical aerial photography. To provide an appropriate texture for automated image-matching algorithms, such as those provided by the LPS software, the MDF board was painted white and finally splattered with red and blue paint. This test object provides the opportunity to derive thousands of object measurements using fully automated methods. By comparing derived elevations with their known values, a similar number of check points can be achieved. This allows the accuracy in the object space to be determined with good statistical reliability. In addition, 28 photogrammetric target points were distributed over the test field (Figure 3.1b) and coordinated by theodolite intersection using a Leica TC1010 total station (June 2005). The measurements, both horizontal and vertical angles and the distance between the two theodolite stations were initially computed using basic intersection formulae. The estimates of the coordinates

of these target points, the measurements derived using the total station and a subset of distances measured with a steel band, were then combined in a least squares 'variation of coordinates' adjustment to determine the best estimates for the photogrammetric target points (RMS x=0.0006m, y=0.0007m, z=0.0002m). These coordinates were used to create a digital elevation model at 1mm resolution by interpolation using the surface generation tool of LPS. The derived surface representation is known as the 'Truth DEM'. This DEM represents the real geometry of the test field and is significant to assess the achieved accuracy of a camera in the object space. The importance of the 'Truth DEM' in this research is further discussed in Section 3.2. This procedure was repeated in May 2006 and includes distances measured to all targets using a reflectorless electromagnetic distance measurement (EDM) device. Thus a second set of coordinates for the photogrammetric target points was derived. Both coordinate sets were compared using a 3D similarity transformation and the results are presented in Section 4.1 (Table 4.2). This demonstrates that the geometry of the test field was stable over time. The stability of the MDF board over time was a crucial constraint to assess the stability of the cameras, since any discrepancies in the estimated accuracy statistics can be attributed to variations between sets of IOPs of the camera and are not caused by instability of the MDF board. It was judged that only 11 of the 28 target points were needed to provide appropriate control for the photogrammetry.

Six frames, representing the whole test object, were captured using the camera to be calibrated (Figure 3.2). Two frames were rotated by 90 degrees about the camera axis for the purpose of determining the principal point offset. This image configuration was used to provide a simple camera calibration method, which is suitable for non experts. These six calibration images and the coordinates of 11 photogrammetric target points were established in LPS. In addition, prior to performing image restitution using LPS, the primary orientation of the sensor had to be defined. The readily accessible http://www.dpreview.com website was used to identify the physical size of the sensor and consequently the physical size

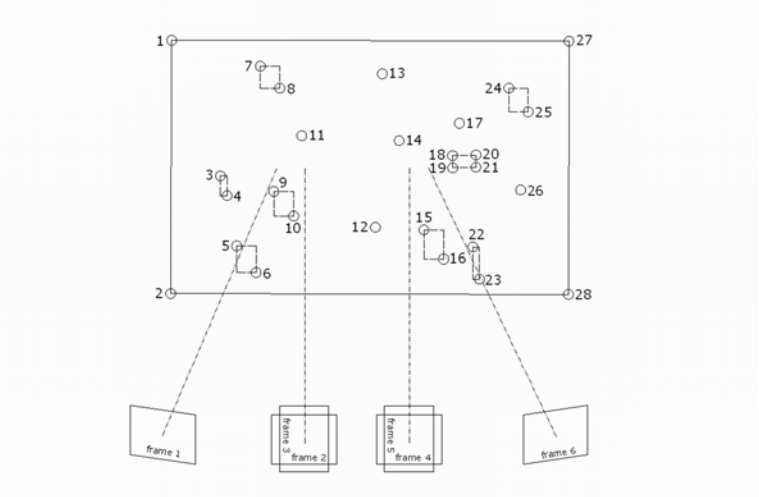

Figure 3.2: Image geometry used for self-calibration

of each pixel of the CCD array in the x and y directions. Once the pixel size and an approximate focal length were defined, the point measurement tool of LPS was used to measure the photogrammetric target points manually. Then, hundreds of tie points were measured using the tie point generation tool of LPS (Section 3.2.2), which is a fully automated process. These tie points provided an appropriate number of check points, which was significant to access the quality of the photogrammetric data, discussed in Section 3.2. Once these steps had been completed, the LPS triangulation process could be performed and initial estimates for the interior and exterior orientation parameters determined.

The weakness of LPS that a self-calibration cannot be performed, where just one radial distortion parameter is to be estimated, was identified as a key problem (Section 2.5.1). The flexibility of GAP, particularly the fact that the IOP are fully selective, was a crucial advantage in adopting this software to determine interior camera parameters (Section 2.5.4). The selectivity of the IOP provided the opportunity to assess whether the determined interior orientation parameters were significant or not. A suitable set of parameters that described the inner camera geometry could be determined. In addition, previous work conducted by

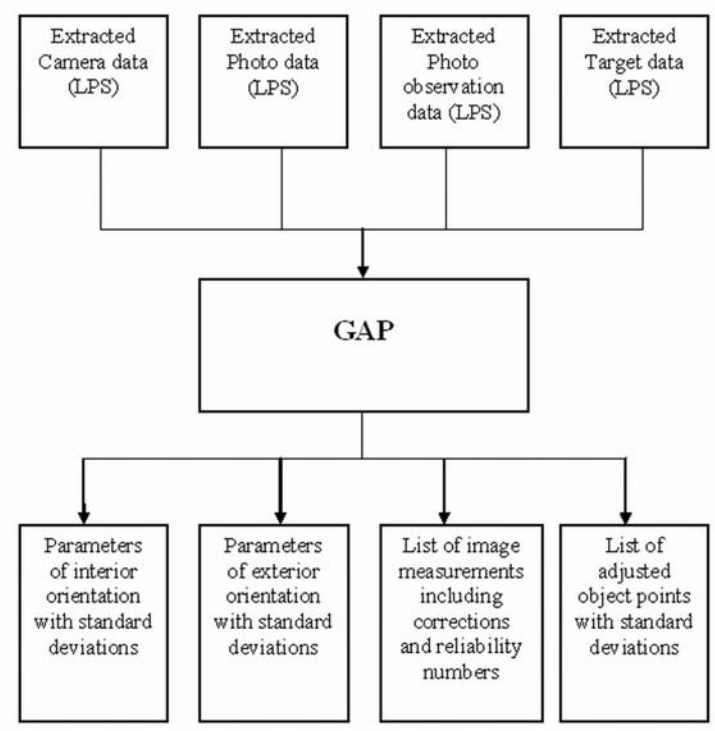

Figure 3.3: Data flow for GAP

Chandler *et al.* (2005) demonstrated that the external self-calibrating bundle adjustment GAP can be used to derive appropriate interior and exterior orientation parameters for a non-metric sensor, which was another convincing argument to adopt this software in this study.

Figure 3.3 represents schematically the file input required for GAP and its outputs. These inputs are provided in the triangulation report of LPS and a software routine provided by Chandler was used to reformat these data and create the input files. These input data are divided into four files: camera data, photo data, photo observation data and target data. Camera data represent the interior orientation of the camera to be calibrated. These parameters are fully selective and their significance can be established by comparing the estimated values with their statistical properties. Insignificant parameters were excluded from the bun-

dle adjustment to avoid over-parameterisation and the bundle adjustment was re-estimated. Photo data describe the exterior orientation parameters, which were treated as fully unknown parameters. Image point measurements are represented by photo observation data. The typical precision of automatic image matching is around 0.1 pixels (Dowman, 2001; Pyle *et al.*, 1997) and so the photo observation data were constrained by setting their standard deviation to 1/10 of a pixel, which was assumed to be representative of their precision. Target data describe measurements of photogrammetric target points. The standard deviations of these were set to 0.5mm, which corresponded with the precision of the Leica TC1010 total station. The output data of GAP are summarised in Section 2.5.4.

After successful recovery of the inner camera parameters, these were re-established into LPS. Transferring the calibrated values for the focal length and principal point offset was straightforward since they could be entered directly into a dialog box. Unfortunately, the parameters to model radial lens distortion (K_1, K_2, K_3) could not be directly transferred to LPS. The only possibility to establish the radial distortion for a sensor in LPS is by computing distortion values for a range of radial distances. The polynomial function (Equation 2.11) was used to compute these distortion values, which could then be transferred into LPS. Consequently, the photogrammetric model was successfully recovered and image pairs could be processed and used for DEM extraction. The process of automatic DEM extraction is explained in Section 3.2.2.

3.1.2 Plumb-line Calibration

It is known that the IOP, estimated through self-calibration, are correlated amongst each other and also with parameters of the exterior orientation (Brown, 1972; Fraser, 1982; Granshaw, 1980). To avoid these correlations, the plumb-line method was identified as an alternative approach to self-calibration for estimating lens distortion parameters of a sensor. However, appropriate computer software was

required to perform plumb-line calibration and a suitable plumb-line test facility needed to be constructed.

Fortunately, computer code to determining the radial and tangential distortion parameters of a sensor using the plumb-line calibration technique was provided by John G. Fryer (Department of Civil, Surveying and Environmental Engineering, University of Newcastle, Australia) in the form of a hardcopy. This software code was written in 1991 using the FORTRAN programming language and used the theory and equations developed by Brown in 1971. The maximum dimensions that could be processed were 76 lines and 90 points per line. Two input files were required: 'PLUMB.DAT' and 'INPUT.DAT'. The 'PLUMB.DAT' contains measured photo coordinates of points on each line and is structured in the form of: ID, x and y. The input structure must be rows before columns and each row must have a different number. This specific input structure is crucial to ensure that the software computes accurate results. The 'INPUT.DAT' contains control information such as number of total lines, *a priori* error estimates of the photo coordinates and *a priori* error estimates of the parameters to be determined. This provided the opportunity to select which distortion parameters are to be determined. Parameters could be excluded from estimation by setting their *a priori* error estimates to almost zero (eg. 0.1E−20). The distortion parameters were consequently fully selective and a lens model could be determined, which includes a single distortion parameter (K_1) or up to 3 radial distortion parameters (K_1, K_2, K_3) and 2 tangential distortion parameters (P_1, P_2). After entering the software code and compiling using a FORTRAN 77 compiler, a series of tests were conducted to ensure that this software provided accurate results.

The program 'NIB', developed by Chandler and used in Fryer *et al.* (1994), provided the opportunity to compute suitable input data for the plumb-line program. 'NIB' uses the extended collinearity equations (Equation 2.10) to transform known object coordinates into corresponding photo coordinates, using a set of known interior and exterior orientation parameters. A set of X, Y, Z object coordinates was created that represents perfect straight and planar horizontal and

vertical lines. Using these object coordinates and a simple interior and exterior orientation, corresponding photo coordinates could be computed. In addition, photo coordinates could be distorted by introducing known distortion parameters in the interior orientation of 'NIB'. Various sets of distorted photo coordinates were computed and transferred into the plumb-line program. Distortion parameters, computed by the plumb-line program, were then compared with distortion parameters, introduced in the interior orientation of 'NIB'. These tests revealed that the plumb-line program recovered introduced distortion parameters by 'NIB' perfectly (Table 3.1).

Once the plumb-line software was verified, a test field was then needed to calibrate any camera using the plumb-line method. An indoor test field was created composed of 198 retro-reflective target points, which could be used to generate a grid of straight horizontal (11) and straight vertical lines (18) (Figure 3.4). These target points were attached to a flat wall, situated in the Civil Engineering laboratory. The physical size of the array allowed lens distortion parameters for a camera to be estimated at a camera-object distance of between 1.0m and 3.0m at focal lengths of 24mm. The maximum camera-object distance was limited by the dimensions of this test field, which in turn was restricted by the dimensions of the wall.

Table 3.1: Verification of the plumb-line program

Software	K_1 $[m^{-2}]$	K_2 $[m^{-4}]$	K_3 $[m^{-6}]$	P_1 $[m^{-2}]$	P_2 $[m^{-2}]$
NIB	-50.00	-	-	-	-
Plumb-line	-50.00	-	-	-	-
NIB	-50.00	20000.0	-	-	-
Plumb-line	-50.00	20000.0	-	-	-
NIB	-50.00	20000.0	-40000000.0	-	-
Plumb-line	-50.00	20000.0	-40000000.0	-	-
NIB	-50.00	20000.0	-40000000.0	-5.0	-
Plumb-line	-50.00	20000.0	-40000000.0	-5.0	-
NIB	-50.00	20000.0	-40000000.0	-5.0	1.0
Plumb-line	-50.00	20000.0	-40000000.0	-5.0	1.0

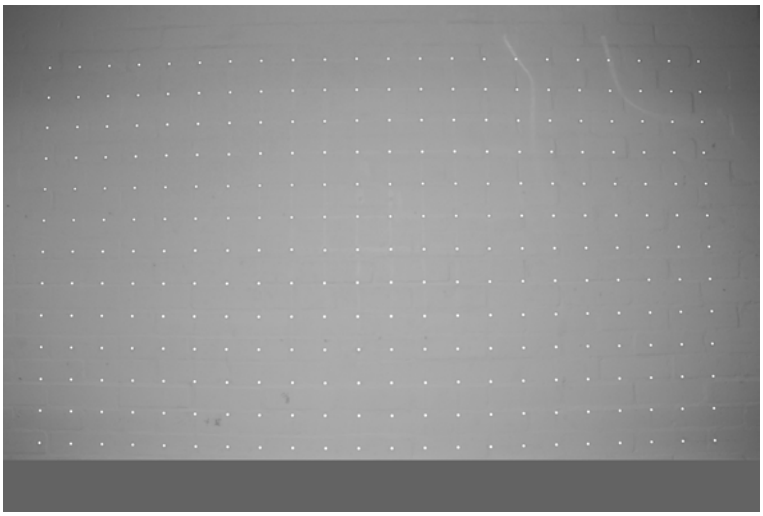

Figure 3.4: Indoor plumb-line test field

When considering potential case studies, the issue of determining a lens model at a medium range camera-object distance (approximately 8m) was identified. Consumer grade digital cameras are distinguished by a small image format and therefore require a short focal length in order to produce a wide angle of view (Luhmann *et al.*, 2006). But this wide angle of view was identified to be an issue when attempting to estimate a lens model of a consumer-grade digital camera through plumb-line calibration at a camera-object distance at medium range since the dimensions of the test field required exceeded the capacity of the laboratory. Consequently, the facade of a nearby building was identified, which provided appropriate dimensions and structures to be used for the plumb-line approach at a medium range camera to object distance (Figure 3.5). The horizontal and vertical lines created by mortar lines were identified to be apparently horizontal, which was then verified using a builders-level. These mortar lines could consequently be used for the plumb-line technique.

After test fields were created or respectively identified, a computer software was again required to automatically identify and measure points representing these straight lines. A closer investigation of the test fields revealed that both

Figure 3.5: Outdoor plumb-line test field

provide groups of pixels or 'blobs', represented by the retro-reflective target points and the crosses of the horizontal and vertical lines of mortar. Therefore, a Matlab script (Appendix A) was developed to identify and measure automatically the centre of blobs in an image, create input files and then execute the plumb-line program. The process of identifying and measuring the centre of the blobs of an image is represented in Figure 3.6. The pixel size and resolution in x and y of the sensor and the parameters in the 'INPUT.DAT' have also to be specified in the plumb-line program.

Unfortunately, not only the retro-reflective targets or the crosses of the horizontal and vertical lines of mortar, but also dirt particles on the wall were identified as potential 'blobs' (Figure 3.6b and c). These incorrectly identified objects had to be removed and filtered out. Therefore, threshold variables were specified to eliminate incorrectly identified objects. Three criteria were used for elimination: size, eccentricity and deviations from lines. Figure 3.7 depicts the revised image derived using these thresholds. These threshold variables have to be adjusted for different camera to object distances, because the size of the 'blobs' changes with varying distance.

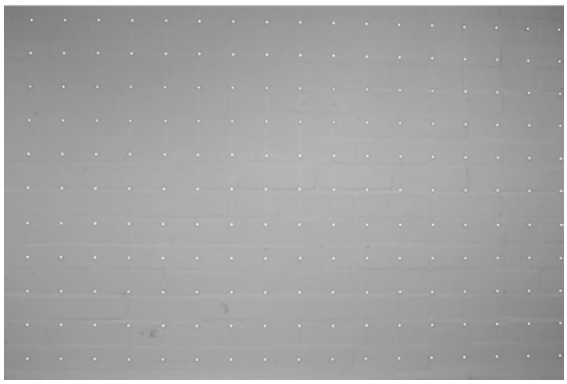

(a) Read in original image

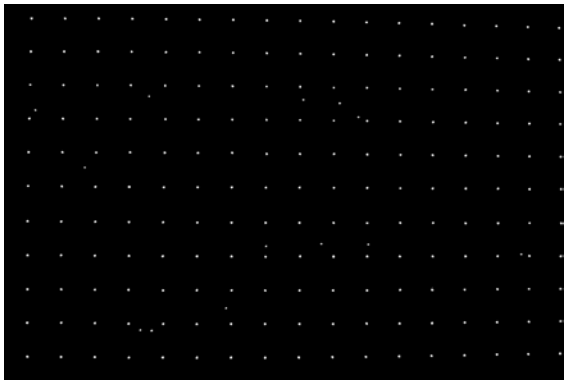

(b) Remove background and detect objects

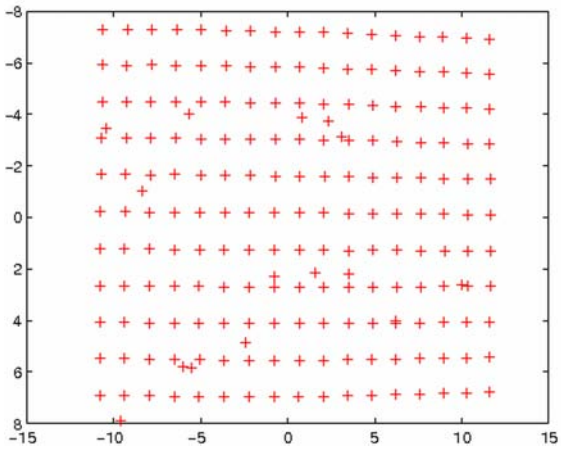

(c) Measure centre of detected objects

Figure 3.6: Matlab image processing for plumb-line technique (Indoor Test field)

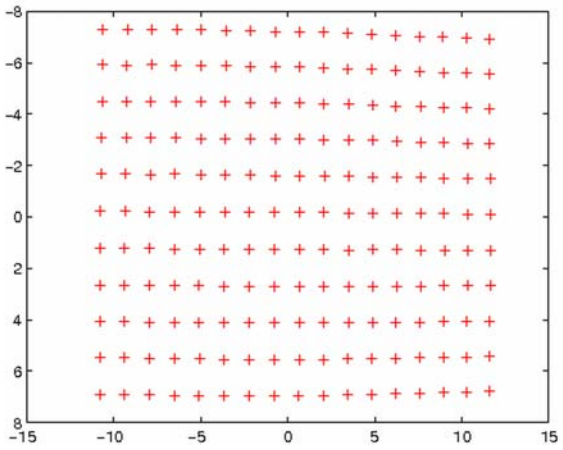

Figure 3.7: Revised image using threshold variables

After executing this Matlab script, an output file is created, which includes parameters for radial and tangential distortion with their statistical properties as well as computed distortion values for a range of radial distances.

Initial practical tests were conducted using a single image representing the plumb-line test field. Derived statistics regarding the distortion parameters revealed that these were determined with inappropriate reliability (e.g. a standard deviation of k_1 only 7× smaller than the actual distortion value). This issue was solved by modifying the plumb-line program and the Matlab script so that multiple images could be processed automatically. The use of multiple images increased the number of measurements that were available to determine the distortion parameters, which could then be estimated with appropriate reliability, i.e. a standard deviation of k_1 approx. 60× smaller than the actual distortion value. Figure 3.8 represents radial distortion curves with their statistical boundaries estimated using a single frame and 10 frames. The red line depicts the radial distortion with respect to radial distance. Blue lines indicate statistical boundaries (±1 standard deviation) for the computed radial distortion values. The data flow of the plumb-line calibration procedure is illustrated schematically in Figure 3.9.

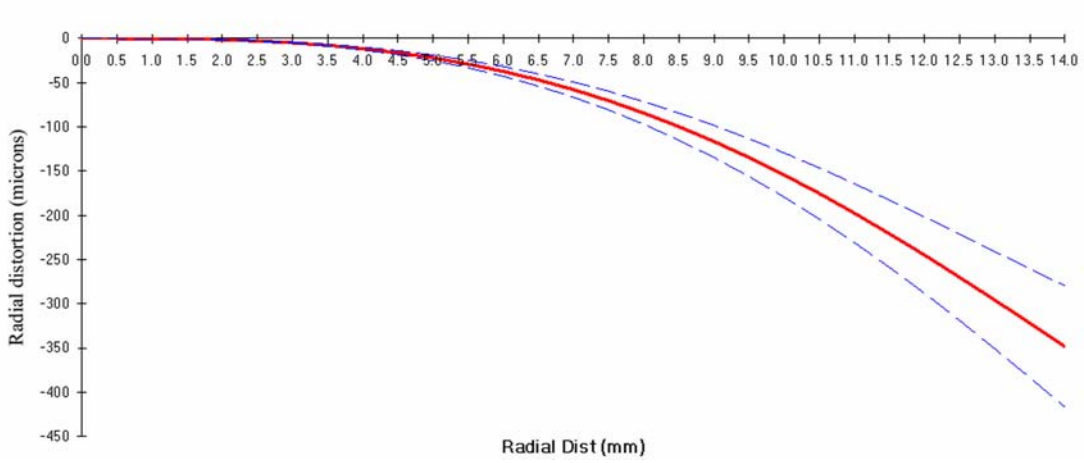

(a) Distortion curve and statistics using 1 image

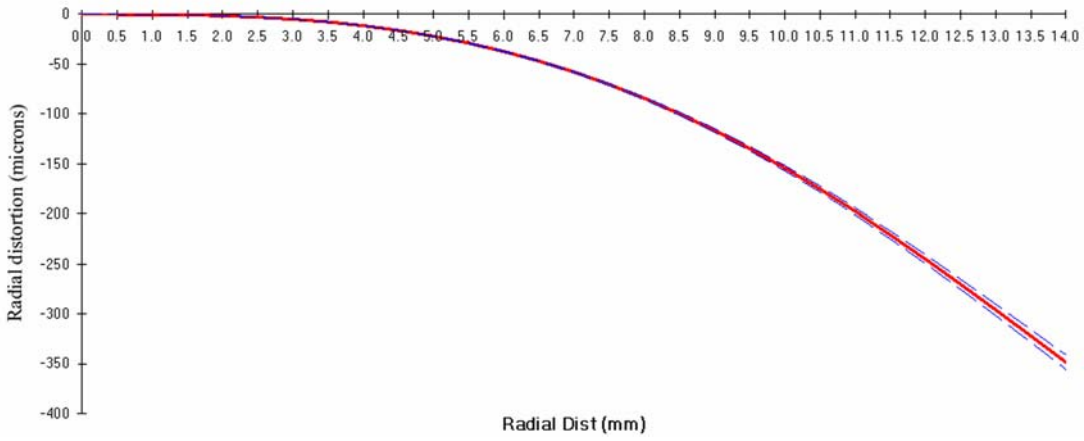

(b) Distortion curve and statistics using 10 images

Figure 3.8: Plumb-line distortion curves and statistics using 1 and 10 images

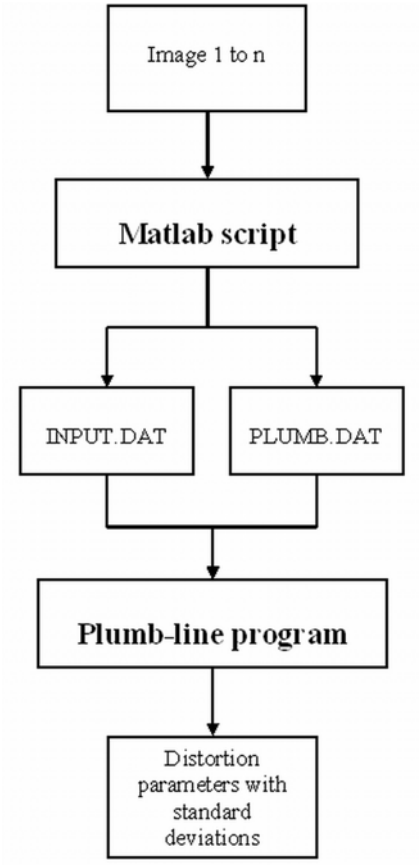

Figure 3.9: Data flow for plumb-line calibration

The development of the Matlab software combined with the Fortran plumb-line program provided the opportunity to derive an uncorrelated lens model for a sensor, independent of both GAP and LPS. Lens models derived using the plumb-line technique could also be transferred into LPS and could be used for image processing and subsequent DEM extraction. Comparing lens models estimated using self-calibration with lens models determined using plumb-line calibration, DEMs for both were extracted. Examining the accuracies of these DEMs, the impacts of the lens models in the object space were assessed. This is expanded upon in detail in the subsequent sections.

3.2 Quality Assessment

The quality of photogrammetric processing can be accessed in different ways and the self-calibrating bundle adjustment provides a diversity of criteria. The residuals of the control points can be used as an indication of the quality of the restitution. Very large residual values for control points indicate the presence of gross errors in the photogrammetric network, which can be attributed to poor quality control points or poorly measured photo coordinates. The quality of the control point coordinates was not an issue focussed upon in this study. Control points were carefully coordinated to sub-millimetre accuracy using a Leica TC1010 total station.

The quality of images used was always excellent so that the control points could be measured precisely and large residual values of photo observations were not detected. The residuals on photo observations reflect the difference between the measured and estimated photo coordinates of the automatically generated tie points. Large residual values indicate errors in the photogrammetric network, which are often caused by inaccurately identified tie points. For example, the tie point generation tool of LPS identifies similar features in two or more images. In case of a large residual value of a specific tie point, the software measures the photo coordinates for this tie point not on the identical position in each image. These erroneous tie points are then removed until an optimum solution can be achieved.

The standard deviations of the estimated interior orientation parameters reflect the significance of the parameters. These have to be carefully examined to evaluate whether or not a parameter is significant. Interior orientation parameters were evaluated as significant if their standard deviations were several times smaller than their estimated values. Such insignificant parameters were removed to avoid over-parameterisation, which can weaken the photogrammetric solution.

These criteria are not independent measures of the accuracy of a photogrammetric network. Only mean errors and standard deviations of 'check points',

which were not used to compute the solution for the network, provide truly independent measures. However, only a comparatively limited number of check points can generally be provided, which creates difficulties in evaluating reliable accuracy statistics. The technique described in Section 3.1.1 and used in Chandler *et al.* (2005), provides thousands of check points that can be used to evaluate the accuracy in the object space and was adopted for these studies. This is believed to be a suitable methodology to assess the quality of photogrammetric data and it is suggested that object accuracy is of more significance to most users.

3.2.1 Truth DEM

The 3D flat and planar test field (Figure 3.1a) with added square blocks was introduced in Section 3.1.1. As described before, 28 photogrammetric target points were distributed over the MDF board, including the four corners of the MDF board and at least two opposite upper corners of each wooden block. The missing coordinates of upper corners of square blocks could be computed using their known dimensions. This set of coordinates was then transferred into the surface generation tool of LPS, which provides the ability to create a surface using 3D scatter data. A DEM at 1mm resolution was created that provides thousands of check points in the object space, known as the 'Truth DEM'. A rendered block model of the 'Truth DEM' is presented in Figure 3.10. The 'Truth DEM' represents the real geometry and shape of the 3D laboratory test field and

Figure 3.10: Rendered block model of 'Truth DEM'; (vertical exaggeration 3×)

can be compared with derived photogrammetric representations. This process of comparison is detailed in Section 3.2.3. It was expected that the geometry of the wooden blocks causes significant areas of inaccurate data owing to dead ground or occlusion effects. However, only the flat part of the test field was important for the work in this thesis and the wooden blocks were excluded from statistics computed to evaluate accuracies achieved in the object space using consumer-grade digital cameras.

3.2.2 Automatically Extracted DEMs Using LPS

A digital elevation model can be described as a discrete 3D digital representation of a surface. After an appropriate restitution for the photogrammetric network was found, a 3D representation could be extracted using the automatic DEM generation tool of LPS. Three steps, image matching, ground point coordinate determination and interpolation, are required for DEM generation and the methods used by LPS to execute these processes were explained in Section 2.7. The success of these processes and consequently the quality of the generated DEM is influenced by a number of strategic parameters: search window size, correlation window size and correlation coefficient limit. These were also described in Section 2.7.

A search window size of 1 to 3 pixels in the y direction and 7 pixels in the x direction is sufficient when using a photogrammetric network with accurate restitution (Erdas Inc., 2003). A search window size of 7×3 pixels is the default setting in LPS and was adopted for DEM generation in this study.

The laboratory test field (Figure 3.1) was painted white and splattered with red and blue paint and therefore provided reasonable colour or grey level intensity variations for DEM extraction. The default correlation window size of 7×7 pixels was identified to be appropriate for DEM extraction using LPS.

Erdas Inc. (2003) recommends using a correlation coefficient limit larger than 0.7 and for image pairs with good radiometric quality and moderate terrain relief,

Table 3.2: Strategy parameters for automatic DEM extraction

DTM cell size	0.003 m × 0.003 m
Search window size	7 × 3
Correlation window size	7 × 7
Coefficient coefficient limit	0.80
Topographic surface type	Flat terrain
Object type	Open area
DTM filtering	High

a coefficient limit of 0.8. The default correlation coefficient limit is 0.8 and remained unchanged in this research.

The LPS software also provides the option of changing parameters to 'adaptive', which allows the software to automatically adjust the search window size, correlation window size and correlation coefficient limit. This option was deactivated in the DEM extraction process for simplicity. Tests revealed that DEMs representing the laboratory test field with optimum accuracy were produced using the strategy parameters summarised in Table 3.2.

An area of interest (AOI) was specified using the four photogrammetric target points located at the corners of the test field and raster DEMs for this area were extracted automatically at 3mm resolution using the LPS software. The derived raster DEMs, representing the whole test field, could then be compared with the 'Truth DEM'. This provided the opportunity to evaluate the quality of the photogrammetric data. The process of comparing raster DEMs with the 'Truth DEM' is described in the subsequent section.

3.2.3 DEM of Difference

The methodology adopted in this study, was to evaluate the quality of photogrammetric data by accessing accuracies in the object space, which is believed to be ultimately of more significance to most users. DEMs of difference were created by subtracting an automatically extracted raster DEM (Section 3.2.2) from the 'Truth DEM' (Section 3.2.1). Such DEMs of difference could be generated using

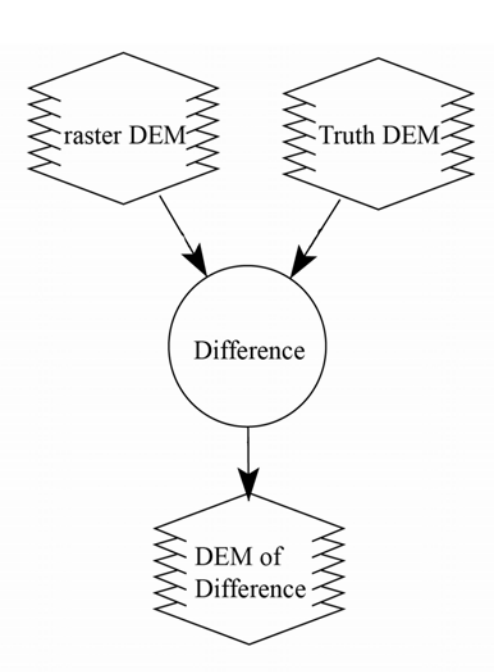

(a) Graphical Model for DEM of Difference

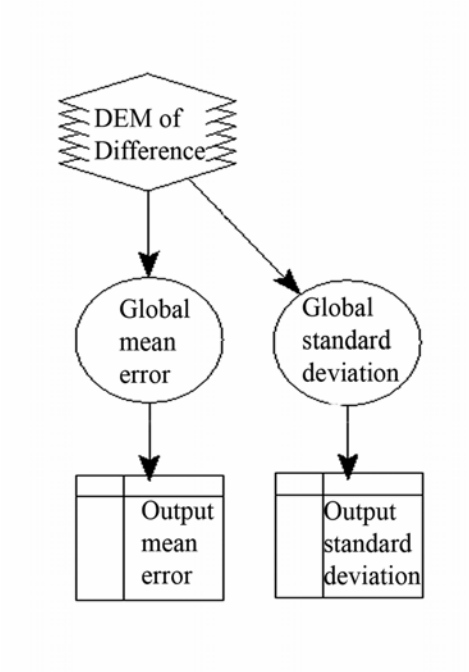

(b) Graphical Model for mean error and standard deviation

Figure 3.11: ERDAS IMAGINE graphical models

a simple graphical model, developed in ERDAS IMAGINE (Figure 3.11a), which represent vertical differences within the test field surface. The mean error and standard deviation of DEMs of difference were derived using another ERDAS Graphical Model (Figure 3.11b), with or without an area of interest. According to Li (1988), these statistics are an appropriate measure of DEM accuracy whereby the mean error is a measure of remaining systematic errors whilst the standard deviation quantifies random errors. Using these summative statistics, DEMs of difference could be compared to each other.

Additionally, the standard image viewer of LPS provides the opportunity to allocate a specific colour to a specific range of elevations. A coloured representation of a DEM of difference is represented in Figure 3.12. This visualisation method was particularly useful to identify areas distorted by gross errors. Initial tests demonstrated that significant areas of inaccurate DEM are especially

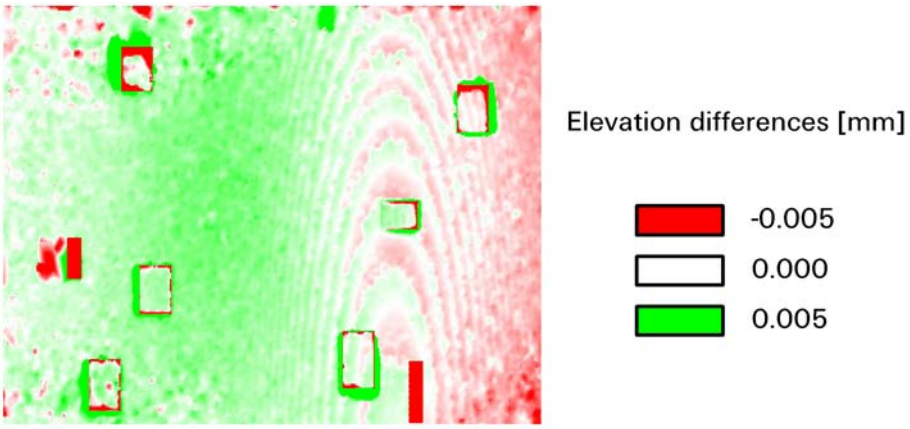

Figure 3.12: DEM of difference

situated adjacent to the wooden blocks. This clearly illustrates the shadowing effect of them and was expected. These gross errors obviously distorted the accuracy statistics that were derived for the DEMs of difference. In order to avoid the disturbing effect, statistics were also computed for an area of interest, which represents the central flat part of the test field and did not include the wooden blocks. A more realistic and representative accuracy assessment could consequently be quantified for each DEM of difference. By comparing the statistical values, the accuracy in the object space achieved and hence the quality of the photogrammetric data could be evaluated. Systematic error surfaces or domes were identified during quality analysis of photogrammetric data (Figure 3.12), which are further discussed in Section 3.4.

The techniques introduced in this section were adopted to fulfill the aim of assessing the geometric stability of consumer-grade digital cameras.

3.3 Assessment of Camera Stability

The main advantage of consumer-grade digital cameras are their convenience, portability and low cost. These cameras have not been traditionally designed

Figure 3.13: Nikon Coolpix 5400

for photogrammetric measurement, due to their uncertain geometry. The uncertainties can be partially resolved by calibration but their temporal stability and manufacturing consistency remain unknown. Therefore, the validity of the calibration data over a period of time should be carefully assessed before subsequent photogrammetric measurement.

The aim of stability analysis is to determine whether or not the interior orientation of a camera changes over time. The methodology adopted in this research was to evaluate the degree of similarity between two sets of IOP by assessing the impact of varying IOP on the accuracy in the object space.

Seven Nikon Coolpix 5400 digital cameras (Figure 3.13) were purchased by the Northumberland and Durham Rock Art Project in February 2005 (Barnett, 2006). These have been used regularly by teams of volunteers to systematically record 1500 rock art motifs located in the north of England (Chandler *et al.*, 2007). The need to calibrate these seven cameras provided the opportunity to evaluate

Table 3.3: Characteristics of the Nikon Coolpix 5400 camera

Feature	*Nikon Coolpix 5400*
Camera body	Compact
Resolution [pixel]	5 million
Image size [pixel]	2592 × 1944
Size of sensor [mm]	7.18 × 5.32
Size of pixel [μm]	2.77 × 2.77
Auto focus	Yes
Manual focus	Yes
Dimension [mm]	108 × 73 × 69
Weight [kg]	0.4
Cost [£]	240 (January 2005)

the stability and consistency of these sensors during normal operation in field conditions. It was judged that there was no further need to simulate disturbing impacts of the camera geometry, such as variations in temperature and moisture, external forces on the camera body or the use of the auto-focus device. A benefit of the presence of seven identical cameras was that manufacturing consistency could also be assessed. A detailed overview of the characteristics of the Nikon Coolpix 5400 digital camera is provided in Table 3.3.

3.3.1 Temporal Stability

The temporal stability of a camera can be assessed by comparing the degree of similarity between sets of IOP established for the same camera at various dates. The Nikon coolpix 5400 cameras were calibrated on the 4th of July 2005 using the calibration procedure described in Section 3.1.1. This was repeated after 4 days (8th of July 2005) and after a period of approximately 1 year (May, June, August 2006).

Comparing the values for focal length, principal point offset and radial distortion or using statistical testing to evaluate the degree of similarity between two sets of IOP, derived in various calibration sessions, is not a reliable measure to evaluate camera stability (Habib and Morgan, 2005). Consequently, another

measure to evaluate the similarity of sets of IOP had to be identified.

The accuracy of the calibration procedure in terms of accuracy of fit to the control points (restitution accuracy) can be used as a first indication of the suitability of sets of IOP. Each set of calibration images (4th & 8th July 2005, June/July 2006), captured with the same camera, was processed in LPS using IOP derived in the three calibration sessions. The RMS error in XYZ in the object space and the RMS residuals in xy in the image space were provided by the triangulation report of LPS. The restitution accuracy for each imagery/IOP combination could be assessed using these RMS errors. The maximal variation of the object and image RMS errors can indicate if sets of IOP are suitable for use in image processing but are not a reliable measure to evaluate the degree of similarity between them.

However, analysing accuracies in the object space derived from various imagery/IOP combinations for one camera, was identified to be a more reliable measure to evaluate the similarity of sets of IOP. This approach is also of more interest to most users. DEMs of difference were generated for each combination of sets of imagery and IOP, and mean error and standard deviation were computed for the two areas of the test object (Section 3.2.3). These statistical values provide an appropriate and independent measure to evaluate the accuracy of a sensor in the object space. A camera can be considered as temporally consistent, when it achieves similar accuracies in the object space using different combinations of sets of imagery and IOP. The seven Nikon Coolpix 5400 digital cameras were tested for temporal stability using this approach and results are presented in Chapter 4.

3.3.2 Consistency of Manufacture

The presence of seven identical Nikon Coolpix 5400 digital cameras provided the opportunity to assess the consistency of the manufacturing process. Three sets of IOP, originally derived with each of the seven cameras in calibration sessions on

various dates, were used in conjunction with sets of calibration frames captured with each camera on the 4th of July 2005. The restitution accuracies achieved for these cameras were analysed to derive an initial measure for the degree of similarity between sets of IOP.

The accuracies in the object space, achieved by generating DEMs of difference using the configurations presented above, were estimated. When a camera achieves similar accuracies in the object space using IOP from different cameras, this suggests some degree of conformance achieved during manufacture. Consequently, DEM accuracy statistics were analysed and the degree of manufacturing consistency for this type of camera could be evaluated.

Curiously, the presence of residual systematic error surfaces, discernable in DEMs of difference, were identified in this procedure. Minimising these error surfaces or domes became a key focus of this PhD programme.

3.4 Residual Systematic Error Surfaces

Chandler *et al.* (2005) investigated metric capabilities of low-cost digital sensors and identified residual systematic error surfaces or domes discernable in DEMs of difference. Errors such as these were also identified in this study, in which the geometric stability of the Nikon Coolpix 5400 cameras were investigated. Fryer and Mitchell (1987) attributed these residual systematic errors to an inaccurately estimated lens model.

Initial work focused on confirming these findings. However, it was recognised that a variety of parameters needed to be controlled to improve understanding, but the variability and uncertainties caused by conducting practical work frequently prevented this. The use of simulated data was considered to be an alternative and potentially a more productive approach.

3.4.1 The Simulation Process

A virtual test field ($1.4 \times 1.3m$) was conceived, composed of evenly distributed XYZ coordinates of hundreds of points. These coordinates were used to create a DEM at 1mm resolution known as the 'Virtual Truth DEM'. A simulation approach (Fryer *et al.*, 1994) was used to compute perfect photo coordinates from the XYZ coordinates of each point of the virtual test field, using predefined interior and exterior orientation parameters. Interior orientation parameters representing a Kodak DCS 460 digital camera were used to provide representative camera information including: principal distance, principal point offset and one parameter (K_1) to model the radial distortion. A vertical stereo image pair was selected, in which each image covered the whole of the test field at a camera to object distance set to 2.5m and a base-to-distance ratio of 1:7. The geometry of this pair was described by two sets of exterior orientation parameters. The derived photo coordinates and the interior and exterior orientation parameters were then re-established using the external bundle adjustment GAP (Chandler and Clark, 1992) to compute object coordinates for each point (Section 3.1.1). This provided the opportunity to control each parameter set, representing the interior and exterior orientation independently. The impact of changing one of these parameters was therefore reflected by the computed object coordinates, which are normally of paramount importance to users. The 3D surfacing tool of the ERDAS IMAGINE 8.7 software was employed to create a DEM through interpolation at 3mm resolution, which could be compared with the original 'Virtual Truth DEM'. Deviations in the planar surface within the derived DEM of difference could be then related directly to the parameter, which had been modified.

3.4.2 Radial Domes and the Lens Model

To confirm the findings of Fryer and Mitchell (1987), a stereo-pair configuration was simulated, which represents the photogrammetric normal case. This configuration remains important for routine data extraction in photogrammetry, recom-

mended and employed by automated DEM extraction software. The camera base is parallel to the object plane and the optical axes of the cameras intersect the object plane orthogonally. The simulation was employed to calculate photo coordinates for each point of the virtual test field using a known interior orientation and the exterior orientation described previously. The parameter K_1, modelling radial lens distortion, was changed by $\pm 20\%$ before using the GAP software to calculate object coordinates from the computed photo coordinates. The significant alteration of $\pm 20\%$ for K_1 was chosen in order to illustrate the effect of a significantly inaccurate lens model in the object space. The focal length and the parameters for the principal point offset remained unmodified. The computed object coordinates were imported into the ERDAS IMAGINE 8.7 software and a DEM created at 3mm resolution. These DEMs were compared with the virtual 'Truth DEM' by interpolation and subtraction. The deviations in difference DEMs could be related directly to changes in the lens model. These results are summarised in Chapter 4.

3.4.3 Mildly Convergent Configuration

It was hypothesised that a mildly convergent image configuration could minimise the systematic error surfaces. The exterior orientation of two photos were derived, where the optical camera axes intersect the object plane at the same point with an angle between these axes of approximately 10 degrees. The parameter K_1 was again changed by $+20\%$, which was also used in the normal case configuration. The simulation process was repeated and a DEM of difference created. Mean error and standard deviation were computed and compared with values derived using the normal configuration. The results summarised in Chapter 4 clearly indicate that a mildly convergent image configuration can indeed minimise the systematic error surfaces in DEMs caused by an inaccurate estimated lens model. This result is significant as it demonstrates that this approach can effectively improve the accuracy achievable with non-metric digital sensors.

3.4.4 Practical Test Using a Nikon D80 Camera

Two Nikon D80 digital cameras (Figure 3.14) were purchased for a research project, conducted at Loughborough University to measure flood flows via surface videography and photogrammetry. The need to calibrate these cameras provided the opportunity to validate the findings from the simulation process using real data. A detailed overview of the characteristics of the Nikon D80 camera is given in Table 3.4.

Table 3.4: Characteristics of the Nikon D80 camera

Feature	*Nikon D80*
Resolution [pixel]	10 million
Image size [pixel]	3872 × 2592
Size of sensor [mm]	23.6 × 15.8
Size of pixel [μm]	6.095 × 6.095
Auto focus	Yes
Manual focus	Yes
Dimension [mm]	132 × 103 × 77
Weight [kg]	0.7
Cost [£]	ca. 700 (September 2006)

Figure 3.14: Nikon D80

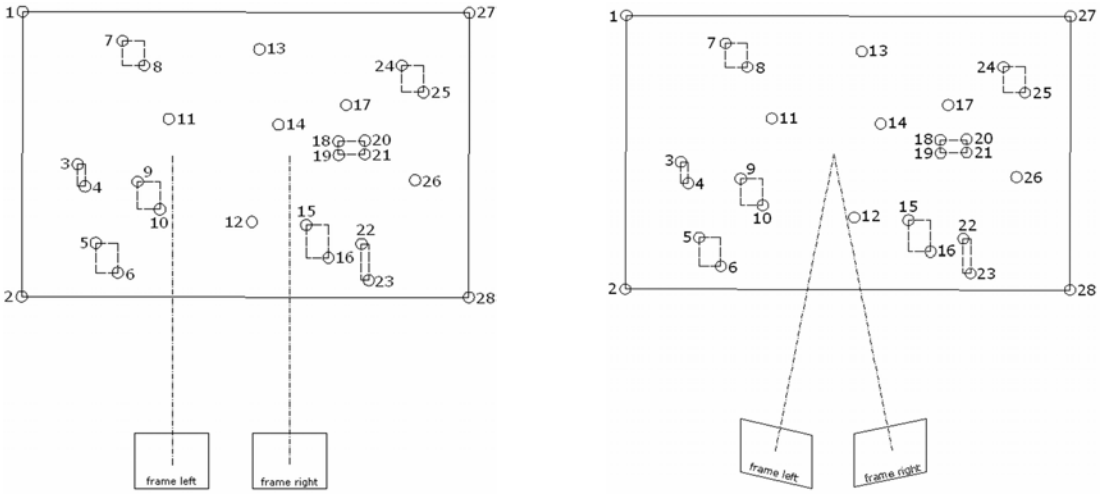

(a) Normal image configuration (b) Mildly convergent image configuration

Figure 3.15: Image configurations used for DEM extraction

For the calibration process a combined 3D and planar test field (Figure 3.1) was used, as introduced in Section 3.1.1. The interior orientation of the camera was determined using the self-calibrating bundle adjustment GAP. DEMs were extracted, employing the DEM generation tool of the LPS software. A vertical image pair, representing the normal case (Figure 3.15a), was used for DEM extraction. Two additional images were captured using a mildly convergent configuration with an angle of approximately 8 degrees between the optical camera axes (Figure 3.15b). DEMs were extracted for both configurations. The automatically generated DEMs were compared with the 'Truth DEM'. The interior orientation remained unmodified for the DEM extraction process and thus changes in elevation in DEMs of difference must be related to the change in image configuration. The results of this practical test verify the findings of the simulation process and demonstrate the potential of mildly convergent imaging for minimising errors arising from an erroneous lens model.

3.5 Summary

The methodologies that were used to achieve the aims and objectives (Section 1.1) of this study were explained in this chapter. The first section described the processes used for camera calibration and image restitution. This included the identification and development of appropriate test fields and computer software.

Secondly, the methods used in this study to assess the quality of photogrammetric data were introduced and their significance and reliability were discussed. In addition, the procedure of automatic DEM extraction using LPS was fully explained. Furthermore, the key points relating to the generation of DEMs of difference were introduced.

The techniques used in this research project to assess the geometric stability/consistency of consumer grade digital cameras were also described. Analysing accuracies in the object space derived from various imagery/IOP combinations for non-metric digital cameras was identified to be a suitable method by which to assess their geometric stability and manufacturing consistency over time.

An important issue was identified regarding residual systematic error surfaces or domes, discernable in DEMs of difference, caused by slightly inaccurately estimated lens distortion parameters. It was considered of great importance to investigate the effects of these domes on the resulting data quality and to develop a methodology to minimise these error surfaces.

The final stage of this research project comprised a methodology developed to minimise the residual systematic error surfaces using a mildly convergent image configuration for DEM extraction. A simulation process was introduced to clarify the correlation between estimated lens models and the domes and also to demonstrate that a mildly convergent image configuration can eradicate them. In addition, a practical test using a Nikon D80 digital camera was described, which verified the results of the simulation. The findings from these analyses are represented in chapter 4 and are discussed in Chapter 6.

CHAPTER 4

Results

The aim of stability analysis is to determine whether or not the IOP of a camera changes over time, which can be evaluated by estimating the degree of similarity between two sets of IOP (Habib *et al.*, 2006). The methodology used in this research is to establish camera stability by estimating accuracy and precision in the object space using various sets of IOP (Section 3.3).

This chapter represents the results of stability analysis using seven identical Nikon Coolpix 5400 cameras (Section 3.3). In addition, the criticality of interior orientation parameters were investigated and results are presented. However, during this investigation of the Nikon cameras, remaining residual systematic error surfaces or domes were identified, which were discernible in DEMs of difference. The methodology developed to minimise such systematic error surfaces was introduced in Section 3.4. This chapter also accounts for the findings of the developed methodology, which eradicates residual systematic errors in DEMs and the chapter concludes with a brief summary.

4.1 Geometric Stability of the Nikon Coolpix 5400 Camera

Initial work focused on the stability and consistency of seven identical Nikon coolpix 5400 digital cameras. These cameras were calibrated initially on the 4th of July 2005. This was repeated after 4 days and again in July 2006. The auto focus of the cameras was switch off and the variable zoom was not used. Table 4.1 summarises the derived calibration parameters for the cameras in three calibration sessions.

Table 4.1: Interior orientation parameters of the Nikon Coolpix 5400 cameras

Camera/Calibration date	*Focal length [mm]*	*x shift [mm]*	*y shift [mm]*	k_1 $[m^{-2}]$	k_2 $[m^{-4}]$
Camera 1					
4*th* July 2005	6.0532	0.1126	0.0160	−4252.54	91823116.4
8*th* July 2005	5.7569	0.0645	0.0045	−4860.19	98750238.6
30*th* June 2006	5.9569	0.0835	0.0018	−3930.01	89478251.4
Camera 2					
4*th* July 2005	6.1221	0.0686	−0.0227	−4138.45	79956008.6
8*th* July 2005	5.9325	0.0489	−0.0245	−4178.88	77394757.3
7*th* August 2006	5.9534	0.0485	−0.0180	−4107.89	91945105.5
Camera 3					
4*th* July 2005	6.0142	−0.0341	0.0031	−3737.62	79780726.0
8*th* July 2005	5.9863	−0.0403	−0.0005	−3493.28	81347775.3
22*th* August 2006	6.0546	0.0103	0.0311	−3683.03	78842334.3
Camera 4					
4*th* July 2005	5.8228	0.0373	0.0567	−3831.69	72908302.0
8*th* July 2005	6.0004	0.0452	0.0603	−4108.10	62118219.6
7*th* July 2006	5.9091	0.0559	0.0228	−4032.10	91698088.2
Camera 5					
4*th* July 2005	6.0521	0.0455	0.0085	−4192.29	94479257.6
8*th* July 2005	5.9522	0.0368	0.0194	−3983.49	87981900.1
12*th* July 2006	5.7736	0.0549	0.0011	−3712.29	80778794.6
Camera 6					
4*th* July 2005	5.9301	0.0636	0.0373	−4077.88	80376727.0
8*th* July 2005	5.8694	0.0546	0.0343	−4347.73	86863826.2
12*th* July 2006	5.9097	0.0533	0.0198	−4292.67	79863827.6
Camera 7					
4*th* July 2005	5.9504	0.0790	0.0380	−3989.83	95586407.7
19*th* June 2006	5.9714	0.0491	0.0893	−3995.43	91708770.8

Comparing these values, it is obvious that the focal length, parameters for the principal point offset and distortion parameter differ slightly for each of the cameras (e.g. maximum differences for camera 2: Δf=0.189mm, Δx=0.020mm, Δy=0.006mm, Δk_1=70.99m^{-2}, Δk_2=14550348.2m^{-4}). It was decided that the source, criticality and impact of these variations had to be further investigated (Section 4.1.1).

Table 4.2: MDF stability (Residuals of control points)

Point number	*X [mm]*	*Y [mm]*	*Z [mm]*
1	0.01	0.47	0.02
2	0.11	0.39	0.02
3	−0.29	0.14	0.01
4	−0.03	0.12	0.01
5	0.05	−0.11	0.05
6	0.03	−0.24	0.08
7	0.03	−0.45	0.05
8	−0.03	−0.51	0.09
9	0.05	−0.09	0.05
10	0.24	0.13	−0.12
11	−0.04	0.07	−0.01
12	0.04	0.00	−0.03
13	−0.02	0.00	−0.02
14	0.04	0.11	−0.01
15	−0.06	−0.46	0.04
16	−0.02	−0.32	−0.04
17	−0.01	0.12	−0.04
18	−0.08	−0.04	0.06
19	−0.03	−0.05	−0.05
20	0.11	0.09	−0.05
21	0.16	0.19	−0.16
22	−0.01	0.12	−0.01
23	0.10	0.09	−0.03
24	−0.04	−0.23	0.06
25	−0.04	−0.33	−0.02
26	−0.13	0.05	0.03
27	−0.13	0.52	0.01
28	−0.02	0.23	0.01
Mean error	0.0E+00	-3.6E-05	-3.6E-05
Standard deviation	±0.10	±0.26	±0.06

One issue, which could explain these differences, was the geometric stability of the MDF board. Variation of the geometry of the test field material between the initial and repeated calibration session would cause discrepancies of IOP. Therefore, the geometric stability of the MDF board had to be investigated.

The photogrammetric target points of the test field were coordinated in June 2005 and again in May 2006 (Section 3.1.1). A datum for both sets of coordinates was provided by the known XYZ coordinates of two reference points situated in the laboratory. Both sets of coordinates were compared using a 3D similarity transformation. The residuals (maximum 0.5mm) are summarised in Table 4.2 and demonstrate the geometric stability of the test field over time. Thus, any deviations between similarly derived IOP cannot be attributed to distortion of the MDF base material. Moreover, tests were conducted to clarify the criticality of varying IOP in the object space, which will be represented in the subsequent section.

4.1.1 Criticality of Interior Orientation Parameters

The variations of IOP identified in the previous section (Table 4.1) led to the conclusion that their criticality has to be examined to identify the impact of varying each interior orientation parameter on the accuracy in the object space.

In reviewing the magnitude of the occurring differences of IOP of each camera (Table 4.1) variations of parameters of approximately 8% were identified. It was judged that varying the parameters by ±8.5% is appropriate to investigate their criticality. Changing the parameters by ±17.0% intensifies the results. This could help to identify specific trends, caused by variation of the parameters. Each of the estimated camera parameters were changed independently by ±8.5% to ±17.0% using the IOP set of camera 4 derived on the 4th July 2005 exemplar for all cameras. DEMs of difference (Section 3.2.3) were extracted and accuracy statistics were estimated, which demonstrate the effect of varying IOP in the object space using real data.

Varying the Focal Length Table 4.3 summarises DEM accuracy achieved by varying the focal length. DEM accuracies estimated for the full test area are

Table 4.3: DEM accuracy by varying focal length

Camera/Parameter changed	*Full area (mean error ± standard deviation) [mm]*	*Central area (mean error ± standard deviation) [mm]*
Camera 4		
Calibration 4*th* July 2005	1.7 ± 6.3	1.4 ± 1.2
Focal length changed by −8.5%	1.9 ± 6.2	0.9 ± 1.1
Focal length changed by −17.0%	2.2 ± 6.5	0.6 ± 1.4
Focal length changed by +8.5%	1.6 ± 6.5	2.0 ± 1.2
Focal length changed by +17.0%	1.5 ± 7.5	2.9 ± 1.4

not conclusive since these statistics were distorted by the small number of gross failures for points adjacent to the wooden blocks (Section 3.2.3). In order to exclude these disturbing effects, accuracy statistics for DEM generation were also computed for an area of interest that represents the flat central part of the test object and did not include the wooden blocks. When the focal length was changed by ±8.5% and the exterior orientation was re-estimated, the mean error for the central test area of interest varied from 0.9 to 2.0mm. When it was changed by ±17%, the variation was 0.6 to 2.9mm. Somewhat surprisingly, optimum DEM accuracy for the central test area was not achieved using the IOP set derived by self-calibration. These results are not clear but indicate that estimates for the focal length achieved using GAP may be either slightly inaccurate or the object space is effected by other errors. It should be recognised that the focal length is highly correlated with parameters of the radial distortion and parameters of the exterior orientation. At this stage of the research, it was not possible to fully understand and interpret these findings. Therefore, these results will be further discussed in Section 4.2 and also in Chapter 6.

Varying the Principal Point Offset The next step was to investigate the criticality of the parameters of the principal point offset. These were also changed by ±8.5% and ±17.0% in the x and y directions. The results achieved for accuracies in the object space are represented in Table 4.4.

Table 4.4: DEM accuracy by varying parameter of the principal point offset

Camera/Parameter changed	*Full area (mean error ± standard deviation) [mm]*	*Central area (mean error ± standard deviation) [mm]*
Camera 4		
Calibration 4*th* July 2005	1.7 ± 6.3	1.4 ± 1.2
x changed by −8.5%	1.6 ± 6.3	1.3 ± 1.2
x changed by −17.0%	1.6 ± 6.2	1.3 ± 1.2
x changed by +8.5%	1.7 ± 6.2	1.4 ± 1.1
x changed by +17.0%	1.7 ± 6.2	1.4 ± 1.1
y changed by −8.5%	1.7 ± 6.3	1.4 ± 1.2
y changed by −17.0%	1.7 ± 6.3	1.4 ± 1.2
y changed by +8.5%	1.7 ± 6.2	1.4 ± 1.2
y changed by +17.0%	1.7 ± 6.3	1.4 ± 1.2
x and y not regarded in calibration	1.5 ± 6.2	1.0 ± 1.4

These estimates for DEM accuracy demonstrate that variations of the parameters describing the principal point offset have no significant effect on the accuracy in the object space using this image configuration. To further investigate the significance of the parameters of the principle point offset, only the focal length and the radial distortion parameters were determined using GAP. Using this parameter set, the accuracy achieved in the object space did not change significantly. This could suggest that the parameters of the principal point offset are insignificant in describing the interior orientation of the camera. However, the restitution accuracy was slightly degraded when these parameters were excluded from the solution. In addition, comparing the estimated values for the principal point offset to their standard deviation in the output of GAP, demonstrated that

these parameters are necessary (Section 3.1.1).

Considering these results, it was concluded that the parameters of the principal point offset are necessary to describe the interior orientation of the Nikon Coolpix 5400 cameras and should be estimated in the calibration process. However, the findings suggest that whilst variation of the principal point offset is not significant in terms of accuracy in the object space using this simple image configuration, it does affect the restitution accuracy. Again, these results will be further interpreted in Section 4.2 and Chapter 6.

Varying the Radial Distortion The results achieved by perturbing the radial distortion parameters are summarised in Table 4.5. The mean error deter-

Table 4.5: DEM accuracy by varying radial distortion parameter

Camera/Parameter changed	*Full area (mean error ± standard deviation) [mm]*	*Central area (mean error ± standard deviation) [mm]*
Camera 4		
Calibration 4*th* July 2005	1.7 ± 6.3	1.4 ± 1.2
k_1 changed by −8.5%	1.2 ± 6.7	0.4 ± 1.3
k_1 changed by −17.0%	0.7 ± 6.6	-0.6 ± 1.4
k_1 changed by +8.5%	2.0 ± 6.4	2.2 ± 1.4
k_1 changed by +17.0%	2.5 ± 6.4	3.2 ± 1.2
k_2 changed by −8.5%	1.5 ± 6.3	1.1 ± 1.2
k_2 changed by −17.0%	1.3 ± 6.8	0.8 ± 1.2
k_2 changed by +8.5%	1.9 ± 6.2	1.7 ± 1.1
k_2 changed by +17.0%	2.0 ± 6.4	1.9 ± 1.1
No lens model	4.3 ± 7.1	8.1 ± 1.6

mined for the central area of the test object differs from -0.6 to 3.2mm by altering the parameter k_1 by ±17.0%, which demonstrates a significant impact on the accuracy in the object space. It is also noticeable that the parameter k_2 has a less significant effect on DEM accuracy. Furthermore, excluding the radial distortion

from the self-calibration and determining DEM accuracies confirms the significance of these parameters for description of the inner camera geometry. However, in reviewing these results it is obvious that variations in parameters of radial distortion are highly critical in optimising accuracy in the object space, as suggested by Gruen and Beyer (2001b). These findings will be further discussed in Section 4.2 and in Chapter 6.

4.1.2 Temporal Stability

The seven Nikon Coolpix 5400 digital cameras were tested for temporal stability using the methodology of evaluating the degree of similarity between two sets of IOP by assessing the impact of varying IOP on the accuracy in the object space (Section 3.3). These cameras were calibrated on three dates: 4th of July 2005, 8th July 2005 and 12th July 2006. This provided the opportunity to assess their temporal stability over a period of approximately 1 year. This was achieved by simply comparing the degree of similarity between sets of IOP established at various dates. Table 4.6 summarises the accuracy of the calibration procedure in terms of accuracy of fit to the control points (restitution accuracy) of camera 5, which will be used as an exemplar. Similar results were achieved with the other cameras. The first column represents the dates on which the images of the test field were captured, whilst the second column tabulates the dates of IOP used for restitution. The rms error (mm) in the object space is summarised in columns three to five and the final two columns represent the rms residuals (μm) in the image space.

Sub-millimetre accuracy (average rms error of 0.3mm) in terms of fit to the control points was achieved by the camera, whichever combination of image sets and IOP was used. No significant variations are indicated by the accuracy statistics. Accuracy in the image space within each set of calibration images varied within the range of approximately 0.1 μm. However, variations in accuracy at a maximum of 0.4 μm are noticeable when statistics of different sets of images

Table 4.6: Restitution accuracy by using IOP from different dates

Camera/ Imagery date	*IOP date*	*Object rms error [mm]*			*Image rms error [μm]*	
		X	*Y*	*Z*	*x*	*y*
Camera 5						
4*th* July 2005	4*th* July 2005	0.3	0.2	0.4	0.63	0.55
4*th* July 2005	8*th* July 2005	0.2	0.2	0.2	0.63	0.57
4*th* July 2005	12*th* July 2006	0.5	0.4	0.4	0.68	0.69
8*th* July 2005	8*th* July 2005	0.4	0.2	0.3	0.80	0.82
8*th* July 2005	4*th* July 2005	0.2	0.2	0.3	0.79	0.85
8*th* July 2005	12*th* July 2006	0.4	0.3	0.4	0.90	0.87
12*th* July 2006	12*th* July 2006	0.4	0.3	0.4	0.96	0.82
12*th* July 2006	4*th* July 2005	0.3	0.2	0.4	0.94	0.83
12*th* July 2006	8*th* July 2005	0.3	0.2	0.4	0.97	0.85

are compared. This seems to be significant but it must be acknowledged that the automatic tie-point generation tool of LPS was used, which independently creates tie points in each image set. This explains the discrepancies in accuracy, which are caused by using slightly different sets of tie points in each image set and not by the IOP. These data demonstrate a high degree of consistency between all sets of IOP for the camera 5 exemplar. The other six cameras produced similar results and are not reproduced here for brevity.

Accuracies of DEM generation, estimated for camera 5 within the two areas of the test object, are represented in Table 4.7. These statistics were derived using different combinations of sets of imagery/IOP at various dates. The dates on which the images of the test field were captured are tabulated in column one, dates of IOP used for restitution in column two, whilst the last two columns represent mean error (mm) and standard deviation of error (mm) of the tested areas. The cameras achieved poor accuracies for the full test area, which was expected (Section 3.2.3). A small number of gross failures for points adjacent to the wooden blocks significantly distorted the accuracy statistics. It was assumed that the central area of the test object would be free of such errors. However,

Table 4.7: DEM accuracy by using IOP from different dates

Camera/ Imagery date	*IOP date*	*Full area (mean error ± standard deviation) [mm]*	*Central area (mean error ± standard deviation) [mm]*
Camera 5			
4*th* July 2005	4*th* July 2005	0.5 ± 7.2	1.8 ± 0.9
4*th* July 2005	8*th* July 2005	0.4 ± 5.8	1.1 ± 0.7
4*th* July 2005	12*th* July 2006	0.9 ± 7.1	2.5 ± 0.7
8*th* July 2005	8*th* July 2005	0.9 ± 6.1	1.4 ± 0.8
8*th* July 2005	4*th* July 2005	0.6 ± 6.9	1.3 ± 1.0
8*th* July 2005	12*th* July 2006	1.2 ± 5.8	1.9 ± 0.8
12*th* July 2006	12*th* July 2006	0.3 ± 6.0	1.6 ± 0.7
12*th* July 2006	4*th* July 2005	-0.1 ± 6.6	0.5 ± 0.9
12*th* July 2006	8*th* July 2005	-0.2 ± 5.6	0.7 ± 0.7

mean errors estimated for this area varied from 0.5 to 2.5mm and did not follow expectations. Even more surprisingly, the optimum accuracy in the object space was not achieved by generating DEMs using frames and IOP from the same date. It was concluded that the central area of interest was perhaps being affected by the same systematic error source (Wackrow *et al.*, 2007). This systematic error source subsequently became a key focus for this thesis and will be further discussed later in this chapter. The radial distortion curves established for the cameras in different calibration sessions are represented in Figure 4.1-4.6. The distortion curves are virtually indistinguishable up to a radial distance of 3mm. The absolute maximum radial distance of this particular sensor is just 4.5mm but as it is located in the corners of the format, is rarely used for measurement. Even so, the variation between any two curves at the maximum radial distance never exceeds 26 μm. These variations are not significant taking into account that these cameras are equipped as standard with a zoom lens (28 - 116mm) and are perhaps useful for measurement at medium accuracy level. However, the effect of variations of distortion parameter for measurement at a high accuracy level will be discussed in Section 4.2.2 and Chapter 6.

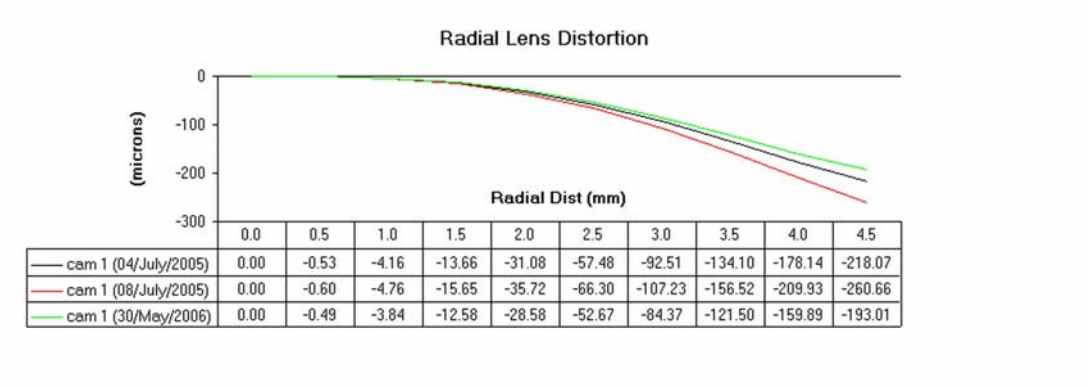

	0.0	0.5	1.0	1.5	2.0	2.5	3.0	3.5	4.0	4.5
cam 1 (04/July/2005)	0.00	-0.53	-4.16	-13.66	-31.08	-57.48	-92.51	-134.10	-178.14	-218.07
cam 1 (08/July/2005)	0.00	-0.60	-4.76	-15.65	-35.72	-66.30	-107.23	-156.52	-209.93	-260.66
cam 1 (30/May/2006)	0.00	-0.49	-3.84	-12.58	-28.58	-52.67	-84.37	-121.50	-159.89	-193.01

Figure 4.1: Radial lens distortion curves for camera 1

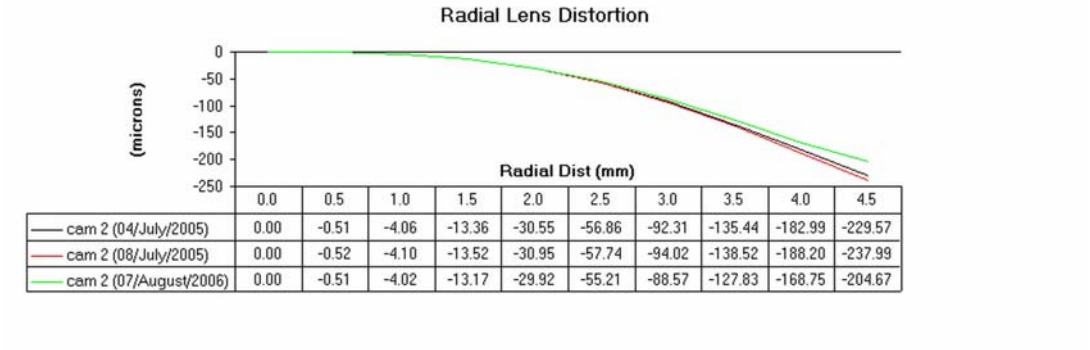

	0.0	0.5	1.0	1.5	2.0	2.5	3.0	3.5	4.0	4.5
cam 2 (04/July/2005)	0.00	-0.51	-4.06	-13.36	-30.55	-56.86	-92.31	-135.44	-182.99	-229.57
cam 2 (08/July/2005)	0.00	-0.52	-4.10	-13.52	-30.95	-57.74	-94.02	-138.52	-188.20	-237.99
cam 2 (07/August/2006)	0.00	-0.51	-4.02	-13.17	-29.92	-55.21	-88.57	-127.83	-168.75	-204.67

Figure 4.2: Radial lens distortion curves for camera 2

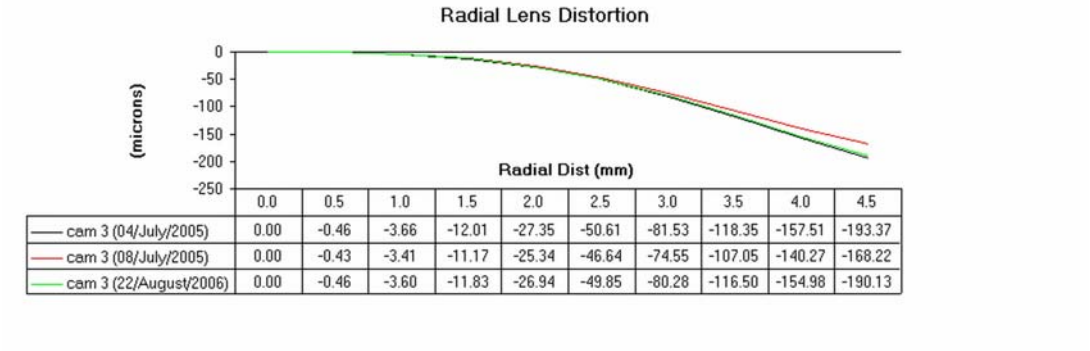

	0.0	0.5	1.0	1.5	2.0	2.5	3.0	3.5	4.0	4.5
cam 3 (04/July/2005)	0.00	-0.46	-3.66	-12.01	-27.35	-50.61	-81.53	-118.35	-157.51	-193.37
cam 3 (08/July/2005)	0.00	-0.43	-3.41	-11.17	-25.34	-46.64	-74.55	-107.05	-140.27	-168.22
cam 3 (22/August/2006)	0.00	-0.46	-3.60	-11.83	-26.94	-49.85	-80.28	-116.50	-154.98	-190.13

Figure 4.3: Radial lens distortion curves for camera 3

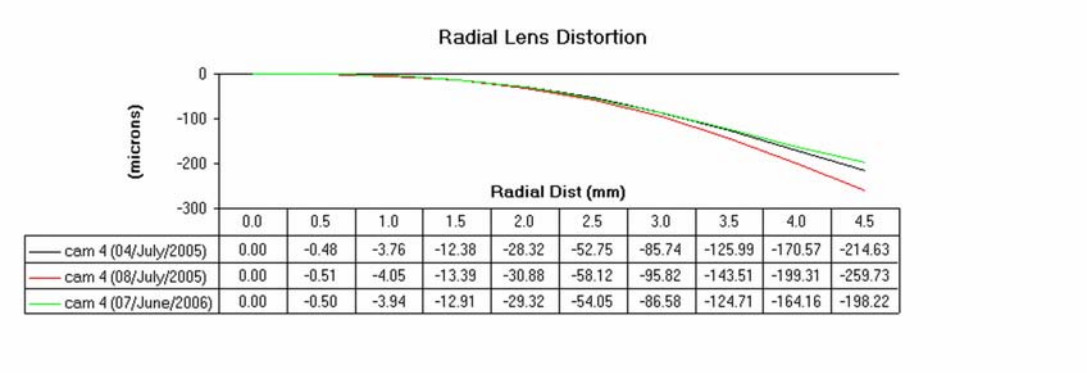

	0.0	0.5	1.0	1.5	2.0	2.5	3.0	3.5	4.0	4.5
cam 4 (04/July/2005)	0.00	-0.48	-3.76	-12.38	-28.32	-52.75	-85.74	-125.99	-170.57	-214.63
cam 4 (08/July/2005)	0.00	-0.51	-4.05	-13.39	-30.88	-58.12	-95.82	-143.51	-199.31	-259.73
cam 4 (07/June/2006)	0.00	-0.50	-3.94	-12.91	-29.32	-54.05	-86.58	-124.71	-164.16	-198.22

Figure 4.4: Radial lens distortion curves for camera 4

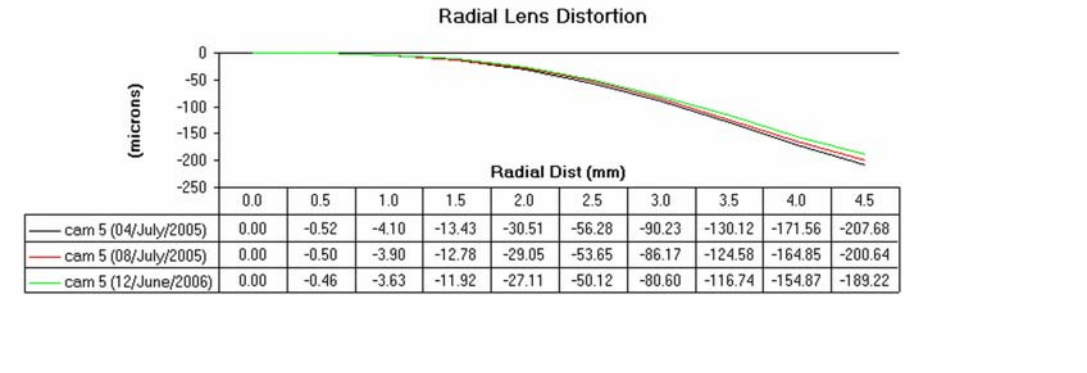

	0.0	0.5	1.0	1.5	2.0	2.5	3.0	3.5	4.0	4.5
cam 5 (04/July/2005)	0.00	-0.52	-4.10	-13.43	-30.51	-56.28	-90.23	-130.12	-171.56	-207.68
cam 5 (08/July/2005)	0.00	-0.50	-3.90	-12.78	-29.05	-53.65	-86.17	-124.58	-164.85	-200.64
cam 5 (12/June/2006)	0.00	-0.46	-3.63	-11.92	-27.11	-50.12	-80.60	-116.74	-154.87	-189.22

Figure 4.5: Radial lens distortion curves for camera 5

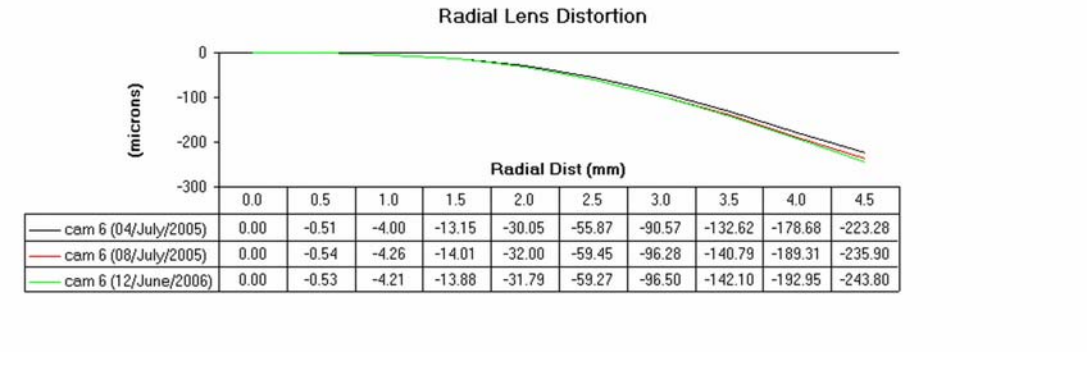

	0.0	0.5	1.0	1.5	2.0	2.5	3.0	3.5	4.0	4.5
cam 6 (04/July/2005)	0.00	-0.51	-4.00	-13.15	-30.05	-55.87	-90.57	-132.62	-178.68	-223.28
cam 6 (08/July/2005)	0.00	-0.54	-4.26	-14.01	-32.00	-59.45	-96.28	-140.79	-189.31	-235.90
cam 6 (12/June/2006)	0.00	-0.53	-4.21	-13.88	-31.79	-59.27	-96.50	-142.10	-192.95	-243.80

Figure 4.6: Radial lens distortion curves for camera 6

4.1.3 Manufacturing Consistency

The opportunity to assess the consistency of manufacture was provided by the availability of seven identical Nikon Coolpix 5400 digital cameras. Camera 4 and camera 5 are used in this thesis to provide a representative sample for the results obtained from all cameras. Three sets of IOP, originally derived with camera 4 in the calibration sessions on 4th, 8th July 2005 and 7th June 2006, were used in conjunction with the six calibration images captured with camera 5 on 4th July 2005 and exterior orientations were re-estimated. The restitution accuracies achieved for these two cameras are summarised in Table 4.8. Comparing these

Table 4.8: Restitution accuracy by using IOP from different cameras/dates

Camera/ Imagery date	*Camera/IOP date*	*Object rms error [mm]*			*Image rms error [μm]*	
		X	*Y*	*Z*	*x*	*y*
Camera 5	Camera 5					
4*th* July 2005	4*th* July 2005	0.3	0.2	0.4	0.63	0.55
Camera 5	Camera 4					
4*th* July 2005	4*th* July 2005	0.4	0.2	0.2	0.68	0.75
4*th* July 2005	8*th* July 2005	0.4	0.2	0.4	0.78	0.77
4*th* July 2005	7*th* June 2006	0.4	0.3	0.4	0.62	0.57

configurations, no significant discrepancies were observed (average object rms error of 0.3mm; variation of image rms error of 0.22μm). These statistics indicate that the sets of IOP are suitable for image restitution.

As described in Section 2.8.3, the method of establishing the similarity of sets of IOP by analysing the accuracies achieved in the object space (DEMs) is more significant than examining the restitution rms errors, particularly for practical applications. The DEM accuracies achieved using the configurations presented above are summarised in Table 4.9. As expected, poor accuracies in the object space were achieved for the whole test object. The mean errors estimated for the central test area varied between 0.6 to 2.1mm. By comparing the DEM accuracy statistics represented in Table 4.7 and 4.9, it is striking that camera 5 achieved a

Table 4.9: DEM accuracy by using IOP from different cameras/dates

Camera/ Imagery date	*Camera/IOP date*	*Full area (mean error ± standard deviation) [mm]*	*Central area (mean error ± standard deviation) [mm]*
Camera 5	Camera 5		
4*th* July 2005	4*th* July 2005	0.5 ± 7.2	1.8 ± 0.9
Camera 5	Camera 4		
4*th* July 2005	4*th* July 2005	0.5 ± 6.6	1.6 ± 0.6
4*th* July 2005	8*th* July 2005	-0.3 ± 6.8	0.6 ± 0.6
4*th* July 2005	7*th* June 2006	0.7 ± 7.1	2.1 ± 0.9

similar accuracy level, even though different IOP sets were used, derived using a different camera.

The radial distortion curves for the seven cameras achieved by self-calibration at various dates are represented in Figure 4.7. Conformity of curves of the seven cameras is especially demonstrated in Figure 4.7a, which represents results obtained in the calibration session dated the 4th July 2005. The radial distortion curves estimated for camera 3 at the 8th of July 2005 and camera 6 in June 2006 do not follow the general tendency. Such unexpected variations in radial lens distortion of a camera can cause systematic error surfaces or domes in DEMs (Chandler *et al.*, 2005; Fryer and Mitchell, 1987; Wackrow *et al.*, 2007) and effectively degrade the accuracy of DEMs derived (Section 3.4 and 4.1.1), (Wackrow and Chandler, 2008a). This result is significant since it indicates the need for a methodology to minimise systematic effects, caused by slightly inaccurately estimated lens distortion parameters. Minimising these effects can significantly increase the accuracy achievable with non-metric digital cameras (Section 4.2.2), (Wackrow and Chandler, 2008a). Further results that clarify the impact of variations in radial lens distortion as well as an approach, which minimises these effects will be presented in the subsequent sections.

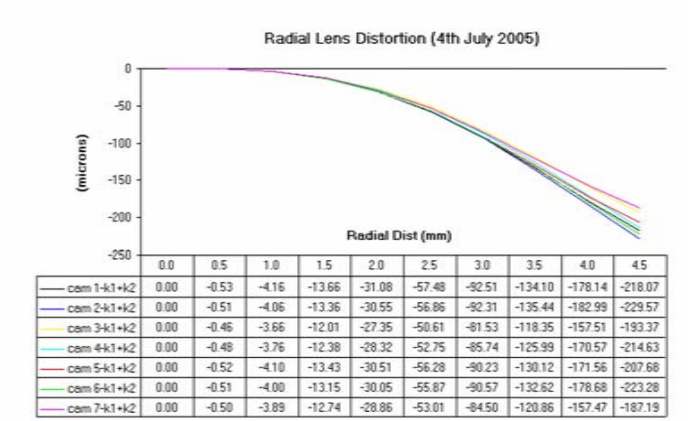

	0.0	0.5	1.0	1.5	2.0	2.5	3.0	3.5	4.0	4.5
cam 1-k1+k2	0.00	-0.53	-4.16	-13.66	-31.08	-57.48	-92.51	-134.10	-178.14	-218.07
cam 2-k1+k2	0.00	-0.51	-4.06	-13.36	-30.55	-56.86	-92.31	-135.44	-182.99	-229.57
cam 3-k1+k2	0.00	-0.46	-3.66	-12.01	-27.35	-50.61	-81.53	-118.35	-157.51	-193.37
cam 4-k1+k2	0.00	-0.48	-3.76	-12.38	-28.32	-52.75	-85.74	-125.99	-170.57	-214.63
cam 5-k1+k2	0.00	-0.52	-4.10	-13.43	-30.51	-56.28	-90.23	-130.12	-171.56	-207.68
cam 6-k1+k2	0.00	-0.51	-4.00	-13.15	-30.05	-55.87	-90.57	-132.62	-178.68	-223.28
cam 7-k1+k2	0.00	-0.50	-3.89	-12.74	-28.86	-53.01	-84.50	-120.86	-157.47	-187.19

(a) cameras 1-7

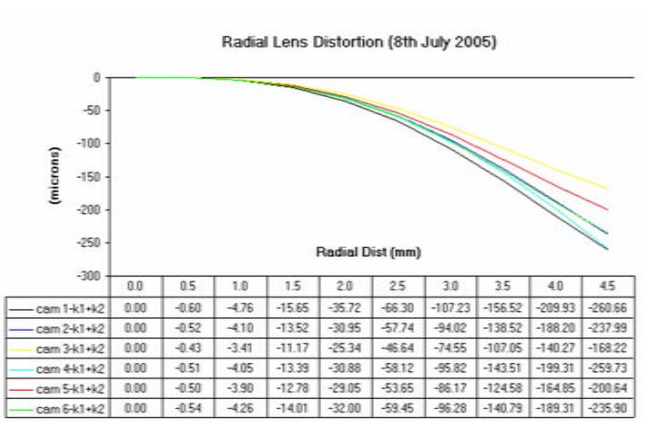

	0.0	0.5	1.0	1.5	2.0	2.5	3.0	3.5	4.0	4.5
cam 1-k1+k2	0.00	-0.60	-4.76	-15.65	-35.72	-66.30	-107.23	-156.52	-209.93	-260.66
cam 2-k1+k2	0.00	-0.52	-4.10	-13.52	-30.95	-57.74	-94.02	-138.52	-188.20	-237.99
cam 3-k1+k2	0.00	-0.43	-3.41	-11.17	-25.34	-46.64	-74.55	-107.05	-140.27	-168.22
cam 4-k1+k2	0.00	-0.51	-4.05	-13.39	-30.88	-58.12	-95.82	-143.51	-199.31	-259.73
cam 5-k1+k2	0.00	-0.50	-3.90	-12.78	-29.05	-53.65	-86.17	-124.58	-164.85	-200.64
cam 6-k1+k2	0.00	-0.54	-4.26	-14.01	-32.00	-59.45	-96.28	-140.79	-189.31	-235.90

(b) cameras 1-6

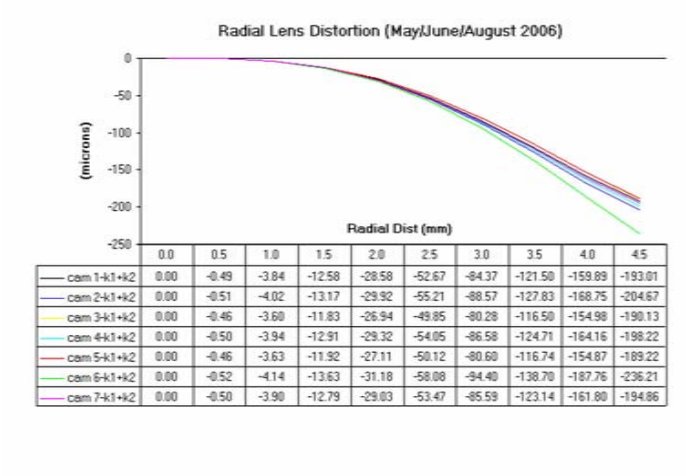

	0.0	0.5	1.0	1.5	2.0	2.5	3.0	3.5	4.0	4.5
cam 1-k1+k2	0.00	-0.49	-3.84	-12.58	-28.58	-52.67	-84.37	-121.50	-159.89	-193.01
cam 2-k1+k2	0.00	-0.51	-4.02	-13.17	-29.92	-55.21	-88.57	-127.83	-168.75	-204.67
cam 3-k1+k2	0.00	-0.46	-3.60	-11.83	-26.94	-49.85	-80.28	-116.50	-154.98	-190.13
cam 4-k1+k2	0.00	-0.50	-3.94	-12.91	-29.32	-54.05	-86.58	-124.71	-164.16	-198.22
cam 5-k1+k2	0.00	-0.46	-3.63	-11.92	-27.11	-50.12	-80.60	-116.74	-154.87	-189.22
cam 6-k1+k2	0.00	-0.52	-4.14	-13.63	-31.18	-58.08	-94.40	-138.70	-187.76	-236.21
cam 7-k1+k2	0.00	-0.50	-3.90	-12.79	-29.03	-53.47	-85.59	-123.14	-161.80	-194.86

(c) cameras 1-7

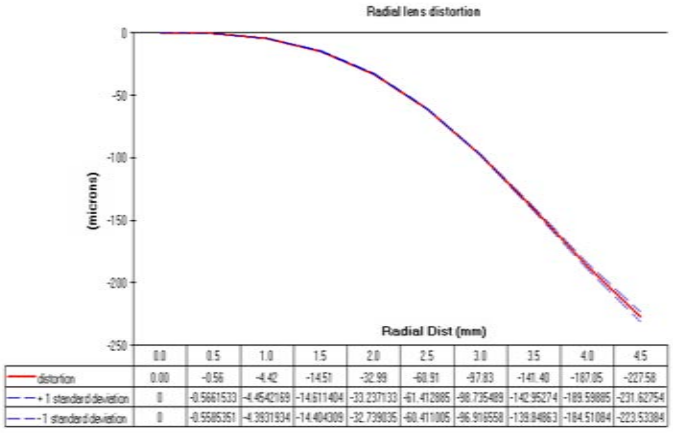

	0.0	0.5	1.0	1.5	2.0	2.5	3.0	3.5	4.0	4.5
distortion	0.00	-0.56	-4.42	-14.51	-32.99	-60.91	-97.83	-141.40	-187.05	-227.58
+1 standard deviation	0	-0.5661533	-4.4542169	-14.611404	-33.237133	-61.412985	-98.735489	-142.95274	-189.59885	-231.62754
-1 standard deviation	0	-0.5585351	-4.3831934	-14.404309	-32.739035	-60.411005	-96.916558	-139.84863	-184.51084	-223.53384

(d) curve with standard deviation

Figure 4.7: Comparing radial lens distortion curves of the Nikon Coolpix 5400 cameras

4.2 Minimising Systematic Error Surfaces

The potential of the Nikon Coolpix 5400 digital camera to maintain their temporal stability and manufacturing consistency was demonstrated in Section 4.1 and findings were published in Wackrow *et al.* (2007). However, this work also identified residual systematic error surfaces or domes discernible in digital elevation models. Similar error surfaces were also identified in Chandler *et al.* (2005). Fryer and Mitchell (1987) attributed these domes to an inaccurately estimated lens model (Section 3.4).

This section focuses on confirming the findings using simulated data and also demonstrating that a mildly convergent image configuration can minimise such systematic effects. In addition, a practical test using a Nikon D80 digital camera was conducted to confirm these findings. Results of the simulation and the practical test will both be presented in this section.

4.2.1 The Simulation

A variety of parameters have to be determined when using a digital camera for accurate photogrammetric measurement. The results presented in Section 4.1.1 indicate that these parameters need to be controlled fully in order to improve understanding, but the variability and uncertainties caused by conducting practical work frequently prevents this. An alternative and potentially a more productive approach is through the use of simulated data.

The simulation process described in Section 3.4.1 was employed to further investigate the results represented in Section 4.1.1, which were derived using a practical approach. A flat test object and a stereo pair configuration were simulated. The image configuration used describes the aerial photogrammetric normal case. The focal length was changed by $\pm 20\%$ and the exterior orientation was recomputed in LPS prior to creating DEMs of difference. The parameters of interior orientation describing the principal point offset and radial distortion remained unmodified. The derived difference images demonstrated no effects

in the object space by changing the focal length. The parameters of exterior orientation fully compensated for this effect by shifting the camera position in the direction of the camera axis. Similar results were obtained by changing the parameters of the principal point offset. Again, the exterior orientation fully compensated for these effects by shifting the camera position in the respective direction. This is significant as the results demonstrate that the systematic effects in the object space were not caused by variation of the focal length or principal point offset, at least not in the case of using vertical imagery and a flat test object.

Results established by changing the radial distortion parameter K_1 by $\pm 20\%$ (± 7 pixel at a radial distance of 3mm) are represented in Figure 4.8 and 4.9. Areas in the DEMs with less than -5mm are illustrated by solid red, whilst solid green regions indicate height differences greater than $+5$mm. White areas represent regions of no elevation differences. These figures visualise elevation differences of the computed object coordinates from their theoretical values, exhibiting clear evidence of a dome or 'bowl', depending upon the sign of the change to K_1. These results clearly demonstrate

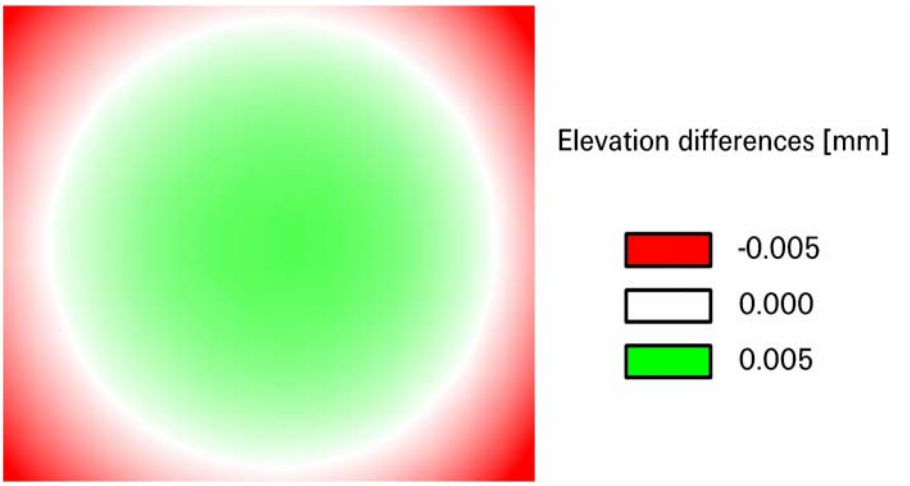

Figure 4.8: Elevation differences, K_1 changed by $+20\%$ (normal case)

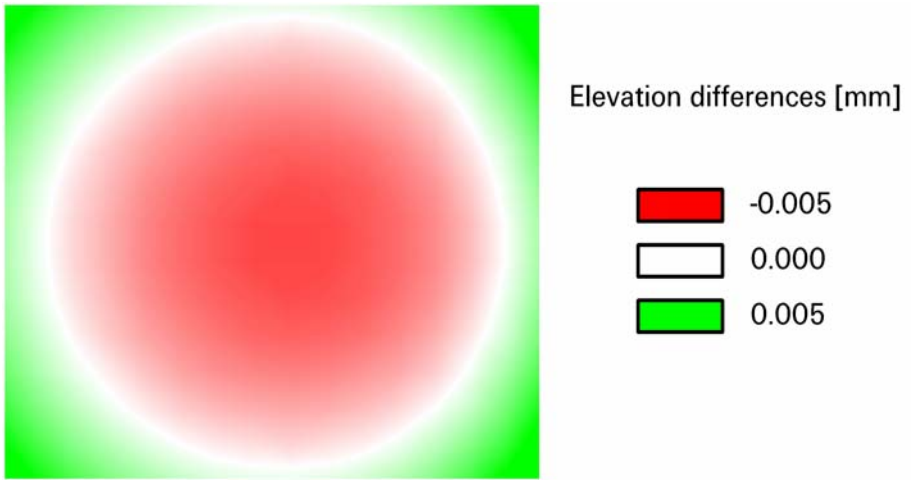

Figure 4.9: Elevation differences, K_1 changed by -20% (normal case)

that the remaining systematic error surfaces are solely caused by inaccurate lens distortion parameters, confirming the findings of Fryer and Mitchell (1987). The centre of both the dome and bowl, represented in Figure 4.8 and 4.9, coincide with the centre of the image and are symmetrically shaped. It was hypothesised that the shape and position of the centre may vary with a change in the image configuration. This had to be investigated further to improve understanding of these systematic effects. Therefore, the simulation was repeated to systematically test various image configurations. Amongst others, convergent image configurations were simulated and a coherence between domes and the convergence of the image configuration could be identified. Finally, a configuration was tested using simulated data in which the optical axes of the two images intersect the object plane at the same point (Figure 3.15), which was described by the exterior orientation. The parameter K_1 was again changed to $+20\%$. The derived DEM of difference is illustrated in Figure 4.10. It is observable that the dome was almost totally eradicated, an observation which is even more remarkable when taking into account that the DEM representation (Figure 4.10) was rescaled to just $\pm$1mm!

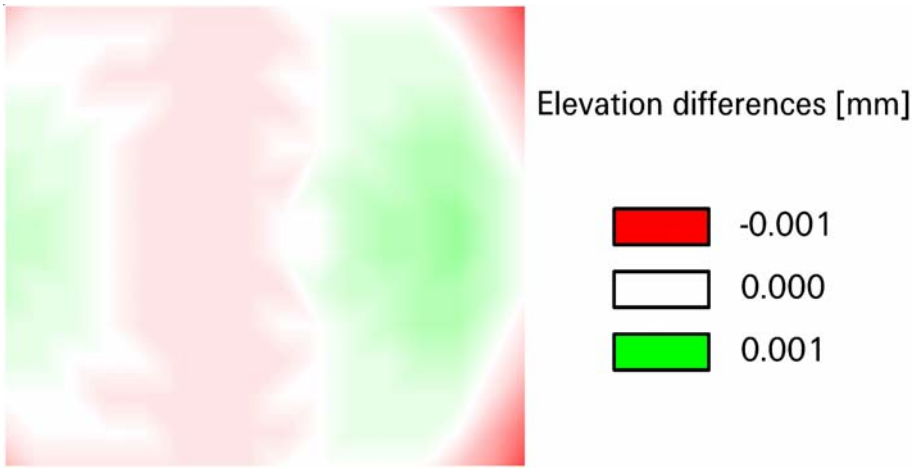

Figure 4.10: Elevation differences, K_1 changed by +20% (convergent case)

Although these simulations provide a convincing qualitative argument that residual systematic error surfaces can be minimised using a mildly convergent image configuration, it remains necessary to prove the results using quantitative data. A reliable measure of the accuracy in the object space is the mean error and standard deviation of error derived from DEMs of difference (Li, 1988), (Section 2.8.3). The mean error represents systematic effects, whilst the standard deviation quantifies random effects (Chandler *et al.*, 2005). DEM accuracies for the three simulations described using the two configurations are summarised in Table 4.10. The first column represents the image configuration used, whilst the second

Table 4.10: DEM accuracy for the simulation process

Configuration/test	*Changes in lens model*	*Mean error ± standard deviation [mm]*
Normal case	+20%	-0.56 ± 2.1
Normal case	−20%	0.49 ± 1.9
Convergent case	+20%	0.02 ± 0.1

column tabulates the changes applied to the lens model. The final column summarises the mean error and standard deviation of error for the difference images.

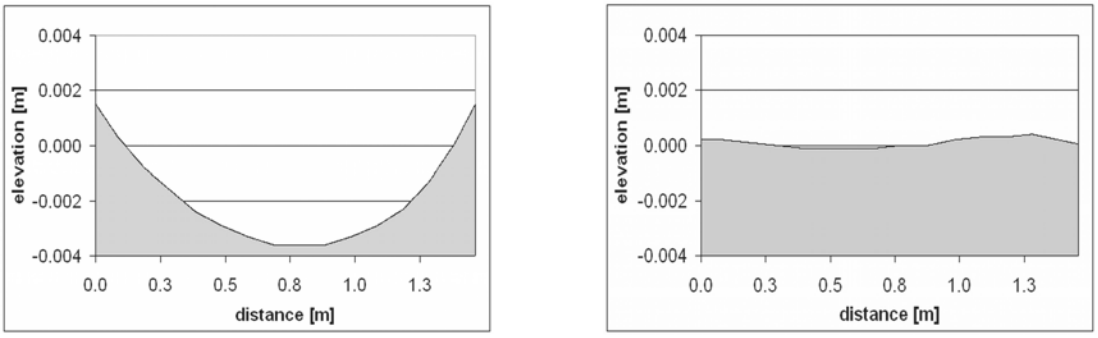

(a) Normal case (lens model +20%) (b) Convergent case (lens model +20%)

Figure 4.11: Cross sections through DEMs of difference using simulated data

As expected, using the normal image configuration and applying changes to the lens model of ±20%, the mean error changed by 1.05mm and the algebraic sign switched. The standard deviation however remained stable. This symmetrical variation is not of concern because the mean error and standard deviation of error followed the theoretical expectations exactly.

Using the mildly convergent image configuration and with the lens model changed by +20%, a mean error of only 0.02mm and a standard deviation of error of just 0.01mm for accuracy of DEM generation was achieved. These results are also visualised in Figures 4.11a and b, representing cross sections through the DEMs of difference (Figures 4.9 and 4.10) using the normal and convergent case, respectively. The accuracy in the object space using the convergent case improved by a factor of 28 in respect to the accuracy achieved using the normal case. This simulation is highly significant as it demonstrates that a mildly convergent image configuration can eradicate the residual systematic error surfaces in DEMs extracted with an inaccurate lens model. Similar results were achieved by conducting these tests using a non flat virtual test field (height elevations between 20 to 30 cm), (Figure 4.12). The simulations (K_1 changed by ±20%) were repeated using the normal and convergent image configuration and the non flat virtual test field. Results of these simulations are represented in Figure 4.13, 4.14

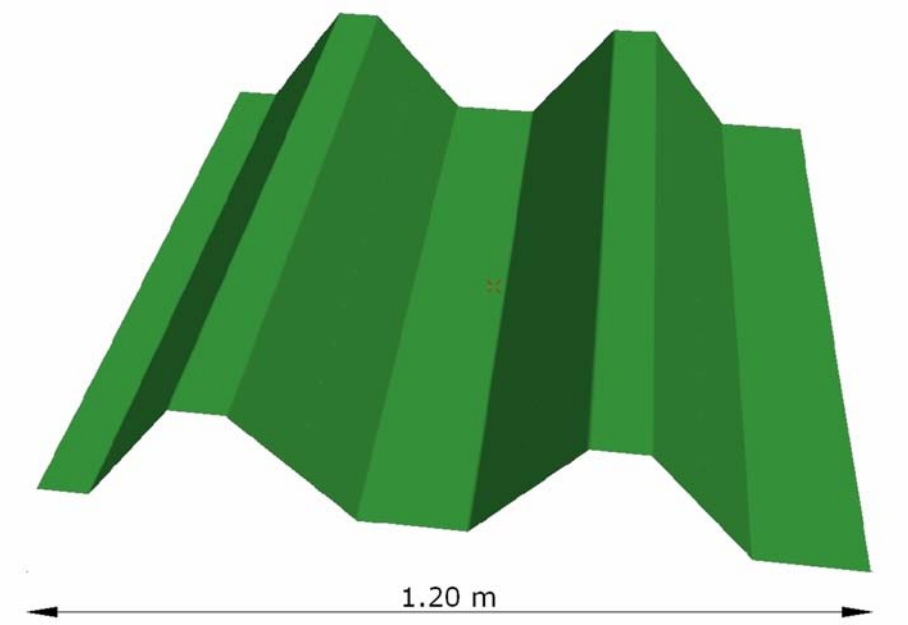

Figure 4.12: Non flat virtual test field

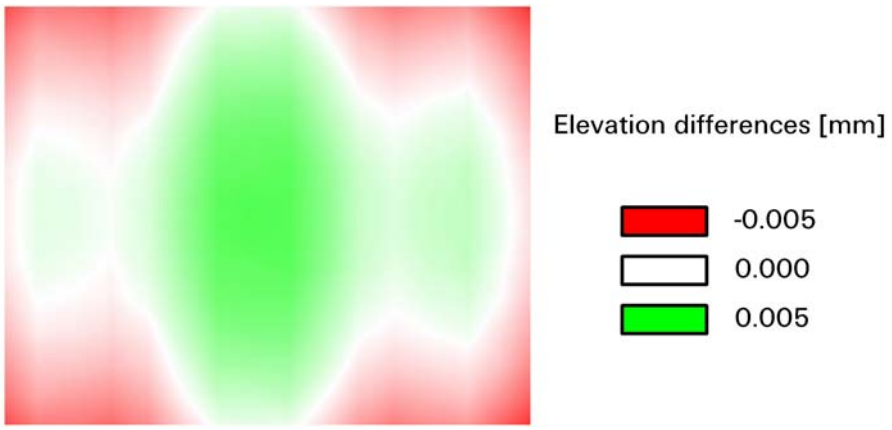

Figure 4.13: Elevation differences, K_1 changed by +20% (normal case)

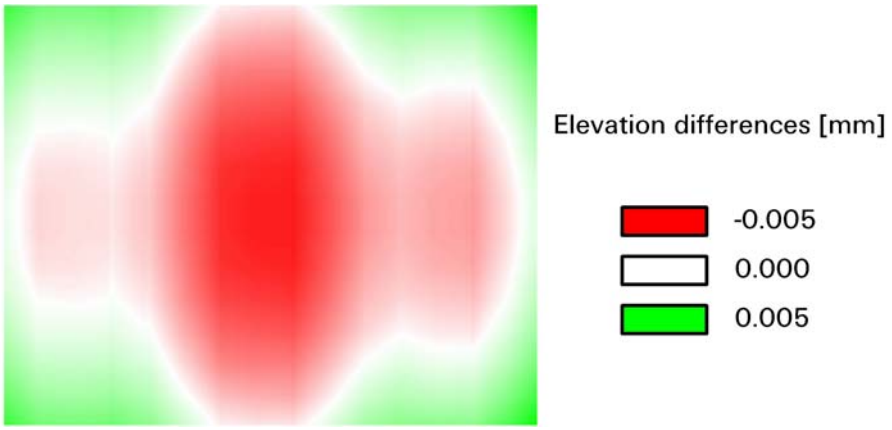

Figure 4.14: Elevation differences, K_1 changed by -20% (normal case)

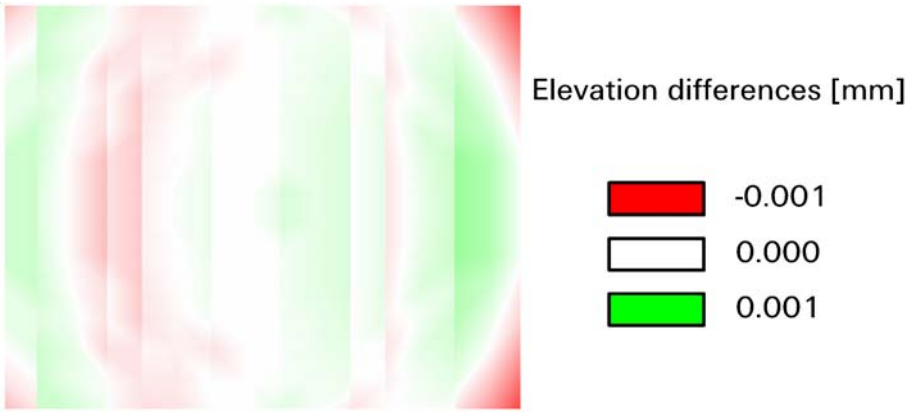

Figure 4.15: Elevation differences, K_1 changed by $+20\%$ (convergent case)

and 4.15. The simulations conducted using the non flat virtual test object demonstrate that a mildly convergent image configuration can minimise remaining systematic error surfaces in DEMs, caused by an inaccurate lens model using vertical imagery. This was judged to be a significant finding and resulted in a second published paper (Wackrow and Chandler, 2007). The finding is significant also, since it demonstrates that the suitability of the methodology described is not restricted by a flat and planar object. This approach is also applicable if non flat objects are measured using photogrammetry.

A practical test will be presented in the subsequent section, which confirms the findings of the simulation.

4.2.2 Practical Test Using a Nikon D80 Camera

The findings represented in Section 4.2 using simulated data needed to be confirmed by a test conducted using real data. The need to calibrate two Nikon D80 digital cameras provided the opportunity to validate the findings of the simulation. The methodology used for this practical test is described in detail in Section 3.4.4. A test object was again provided by the test field, which was also used for stability analysis of the Nikon Coolpix 5400 digital cameras (Figures 3.1a and b). Vertical image pairs of the test field, representing the normal configuration and the convergent case (angle of approximately 8 degrees between the camera axes) were used for DEM generation. The automatically generated DEMs for both configurations were compared with the 'Truth DEM', representing the real shape and geometry of the test object (Section 3.2.3). Figures 4.16 and 4.17 illustrate the DEMs of difference for the normal and convergent case using the Nikon D80 camera in which the elevation differences were both scaled to ±3mm. The radial dome which is clearly apparent in Figure 4.16 was virtually eliminated through using the mildly convergent image configuration (Figure 4.17). Similar results were achieved using other test images but are not reproduced here for brevity.

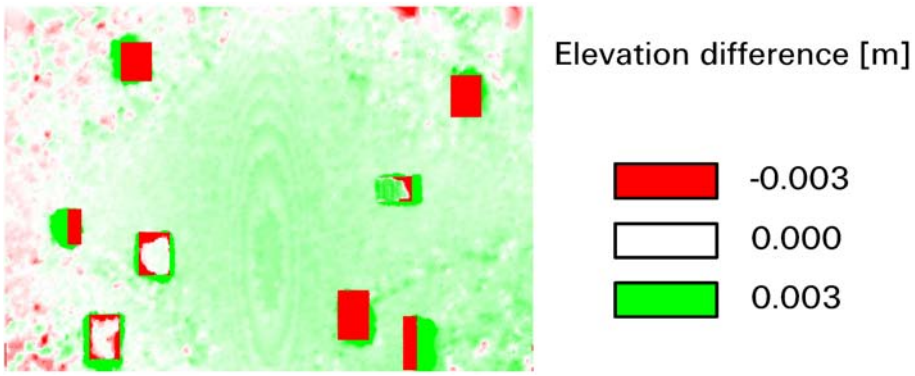

Figure 4.16: Elevation differences Nikon D80: normal case

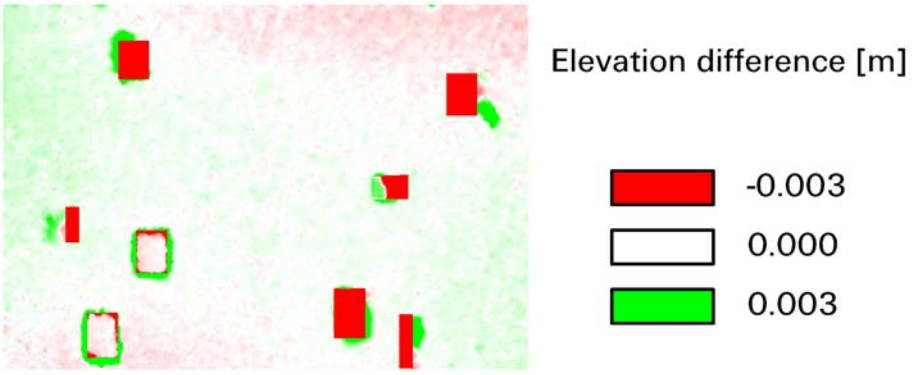

Figure 4.17: Elevation differences Nikon D80: convergent case

Table 4.11: DEM accuracy for the Nikon D80 camera

Configuration/ test	*Full area including wooden blocks (mean error ± standard deviation) [mm]*	*Central area (mean error ± standard deviation) [mm]*	*Full area excluding wooden blocks/shadow (mean error ± standard deviation) [mm]*
Normal case	-0.9 ± 9.9	0.9 ± 0.1	0.4 ± 0.4
Convergent case	-1.5 ± 10.0	0.3 ± 0.1	0.1 ± 0.2

Mean error and standard deviation of error are represented in Table 4.11. The first column tabulates the image configuration used, whilst the second column represents mean error and standard deviation of error for the whole physical structure of the test object. It was predicted that the camera achieved poor accuracy for the full test field area using both image configurations. Significant areas of inaccurate data in the vicinity of the wooden blocks owing to dead ground or occlusion effects can be clearly identified in Figures 4.16 and 4.17, which distorted the overall accuracy derived (Section 3.2.3). In order to exclude these gross errors from the statistics, mean error and standard deviation of error were also computed for an area of interest situated in the centre of the test object. This represented the flat part of the test field and did not include the wooden blocks. Results for both configurations are listed in column three of Table 4.11. However, this specific area is distorted by a dome, which can be clearly identified in Figure 4.16 and is also represented by a mean error (0.9mm) estimated using the normal case. The accuracy for the central area of the test object increased by a factor of three (mean error of 0.3mm) when determined using the convergent image configuration. Column four of Table 4.11 summarises accuracy estimated for the whole imaging area for both configurations but data in the vicinity of the wooden blocks were excluded from computation of the statistic. Comparing the mean error of the normal configuration (0.4mm) with the mean error of the convergent configuration (0.1mm), demonstrates a notable increase in accuracy by a factor of four. This result is also visualised in Figure 4.18a and b, which

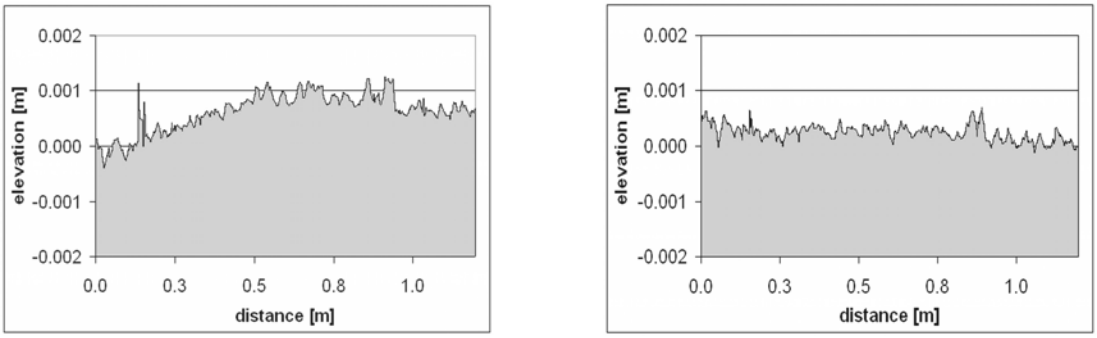

(a) Normal configuration

(b) Convergent configuration

Figure 4.18: Cross sections through DEMs of difference using a Nikon D80 camera

represent cross sections through the DEMs of difference generated using both configurations.

The fact that a mildly convergent image configuration used for DEM generation can eradicate disturbing effects caused by an inaccurate lens model, demonstrates the significance of this result. This finding was also verified through the use of simulated data (Section 4.2.1). Results presented in this chapter will be discussed further in Chapter 6.

4.3 Summary

The results of the stability analysis of the Nikon Coolpix 5400 digital camera over a 1-year period were presented in this chapter. This type of camera is capable of generating DEMs to an accuracy of 1.4mm, from a distance of approximately 1.5 m using IOP derived by self-calibration and imagery obtained by any of these cameras. In addition, the criticality of the interior orientation parameters were analysed. Results revealed that the parameters to model the radial lens distortion are most critical in terms of the accuracy achievable in the object space.

Presented results of stability analysis also identified residual systematic error surfaces in difference images, which are caused by slightly inaccurate lens distor-

tion parameters. These effectively constrain the accuracy achievable. Simulated data were used to demonstrate that inaccurately estimated radial lens distortion parameters are the source of the radial domes discernible in DEMs of difference. The simulation also demonstrated successfully that using a mildly convergent image configuration for DEM generation minimises the systematic error surfaces (Figure 4.11). Finally, a practical test, conducted using a Nikon D80 digital camera has confirmed the findings of the simulation. These results will be further verified and developed further by conducting two contrasting case studies, which will be presented in the subsequent chapter.

CHAPTER 5

Case Studies

Results presented in Chapter 4 demonstrated successfully the stability of the Nikon Coolpix 5400 digital cameras but also identified residual systematic error surfaces caused by slightly inaccurately estimated lens distortion parameters. In addition, the potential of a mildly convergent image configuration, which minimises these error surfaces, was introduced using simulated data. This was verified by a series of simple practical tests.

This chapter represents two case studies conducted to further verify the potential of the convergent image configuration to minimise residual systematic error surfaces in DEMs. In the first, accurate measurement of a flume bed surface, using digital photogrammetry and a consumer grade digital camera (Canon EOS 10D), provided the opportunity to conduct a case study in a semi-controlled environment. A series of images describing the aerial normal and convergent image configurations of the flume bed surface were acquired. Mosaic DEMs were extracted and the experimental setup and results will be presented in Section 5.1.

In the second case study, a photogrammetric method will be described to measure a dynamic water surface on a small river in Loughborough using a pair of synchronised Nikon D80 digital cameras. In contrast to the first case study and the practical test described in Chapter 4, oblique imagery representing both the normal and convergent configurations were used to measure this water sur-

face. Prior to conducting this case study, simulated data were used to investigate whether an oblique convergent image configuration also has the potential to minimise residual systematic error surfaces caused by an inaccurate lens model. The findings of the simulation and the case studies will be presented in Section 5.2.

5.1 Measuring a Flume Bed Surface

A flume river bed, situated in a laboratory and simulating the fluvial process operating within a braided river system, is depicted in Figure 5.1. Previous work conducted on a similar flume by Stojic *et al.* (1998) and Chandler *et al.* (2001) demonstrated the potential of digital photogrammetry for measuring the bed forms and their development. The dimensions of the flume (18.6 × 3.0 m) and the position of the photogrammetric target points (88) are illustrated in Figure 5.2. These were fixed alongside both walls as well as in two almost straight rows along the flume bed and coordinated using the theodolite intersection method.

Figure 5.1: Overview of the laboratory flume

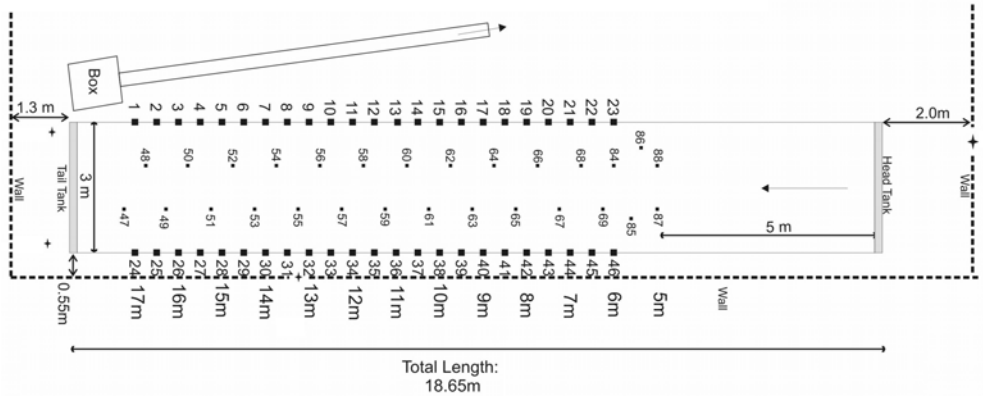

Figure 5.2: Dimensions of the laboratory flume

The target points along the flume walls provided sufficient control for photogrammetric restitution, whilst check point data to assess the accuracy in the object space were derived using target points situated within the flume bed.

For image acquisition, a 6 mega-pixel Canon EOS 10D digital camera, equipped with a Canon 20 mm fixed lens, was pre-calibrated at Loughborough University. The methodology used for calibrating this camera was described in Section 3.1.1, and was also employed for camera calibration in Chandler *et al.* (2005); Wackrow *et al.* (2007) and Wackrow and Chandler (2008a). Eight calibration frames of the test field were processed using LPS. The focal length, parameters for the principal point offset and two parameters to model radial distortion were sufficient to describe the interior orientation of this camera lens system (Section 3.1.1) and were estimated using the self-calibrating bundle adjustment GAP. These parameters were then imported into LPS and used for subsequent surface measurement of the flume bed using the ATE (Automatic Terrain Extraction) module of LPS.

The opportunity to position the camera above the flume bed was provided by an overhead gantry running lengthwise along the flume, mounted approximately 2.9 m above the flume. An image strip of the flume was acquired initially using the aerial photogrammetric normal configuration, in which the camera base was parallel to the object and the camera axes intersected the mean object plane

orthogonally. This configuration was also used for the practical test using the Nikon D80 digital camera, described in Section 4.2.2. The overlapping area of the adjacent images was approximately 60%, a figure commonly used in aerial photogrammetry (Kraus, 1994; Lillesand and Kiefer, 1994). This flight strip was processed using LPS. It was essential to measure the control points manually before 100 tie points for each image pair were measured using fully automated methods. A DEM was extracted for each image pair of the flight strip using the method described in Section 3.2.2. Single DEMs derived from each image pair were then merged using the mosaic tool of Erdas Imagine. This tool provides a fully automated process to create mosaic DEMs or mosaic ortho photographs. This mosaic DEM represents the entire surface of the flume bed. Since the dimensions of the mosaic DEM are so large, only a randomly selected part of it is illustrated in Figure 5.3, which was derived using the normal image configuration.

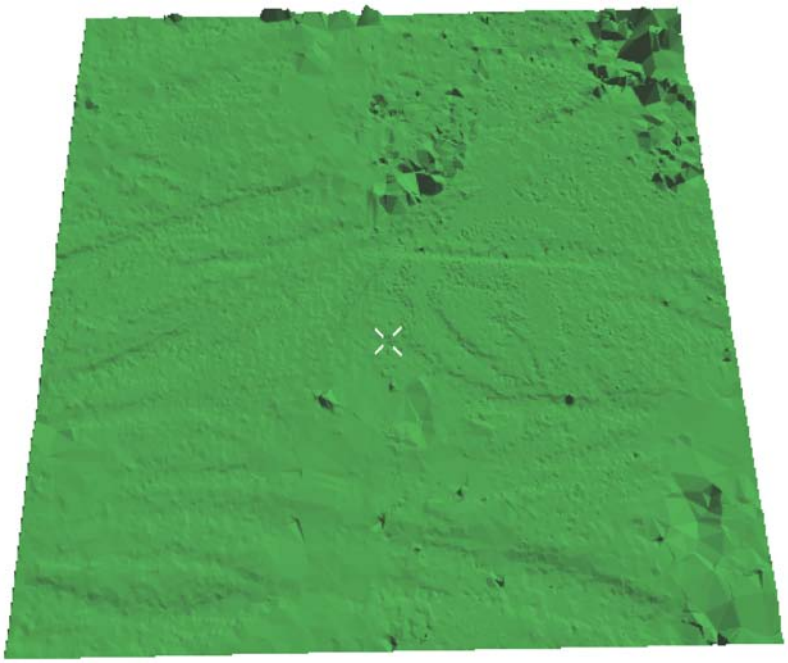

Figure 5.3: Mosaic DEM using normal case

Two additional image strips were subsequently captured, representing a convergent image configuration. Based upon the work presented earlier (Section 3.4.3, 3.4.4 and 4.2) the camera axes of the image pairs should intersect the object plane exactly at the same point. It was recognised that this requirement would cause practical difficulties to implement. This was identified to be an issue in this practical setup. The overhead gantry was mounted very close to the ceiling (Figure 5.1). Therefore, it was very difficult to visually use the view finder of the camera to ensure an accurate camera orientation and position in which the camera axes intersect the object plane at the same point. The first image strip was acquired with the camera tilted in the "flight" direction. The starting position of the camera was marked at the overhead gantry and the camera was moved forward always exactly the same distance. The overlap area of adjacent images was again approximately 60%. Images of the second flight strip were captured with the camera tilted contrary to the flight direction. Because of the difficulty described above, the view finder of the camera could only approximately position the camera to capture the first image of the second flight strip and ensure that the camera axes intersected the object plane at the same point for this first convergent image pair. The distance between the starting points of the camera for each flight strip was then measured and the camera was then moved exactly the same distance to acquire all images along the second flight path. It was assumed therefore that the camera axes of each convergent image pair intersected the object plane at the same point, with the camera axes describing an angle of approximately 18 degrees between them. The same set of control points was used for photogrammetric processing as for the normal case. A mosaic DEM of the flume was again generated, but using the mildly convergent image configuration. An area of this, identical to that represented in Figure 5.3, is depicted in Figure 5.4. It is clear that the texture of the left half of the mosaic DEM (Figure 5.3) derived using the normal configuration is smooth, whilst the right part is slightly rough. The data extracted using different image pairs do not fit perfectly with each other, an effect also noticed in Stojic *et al.* (1998). It is visually apparent

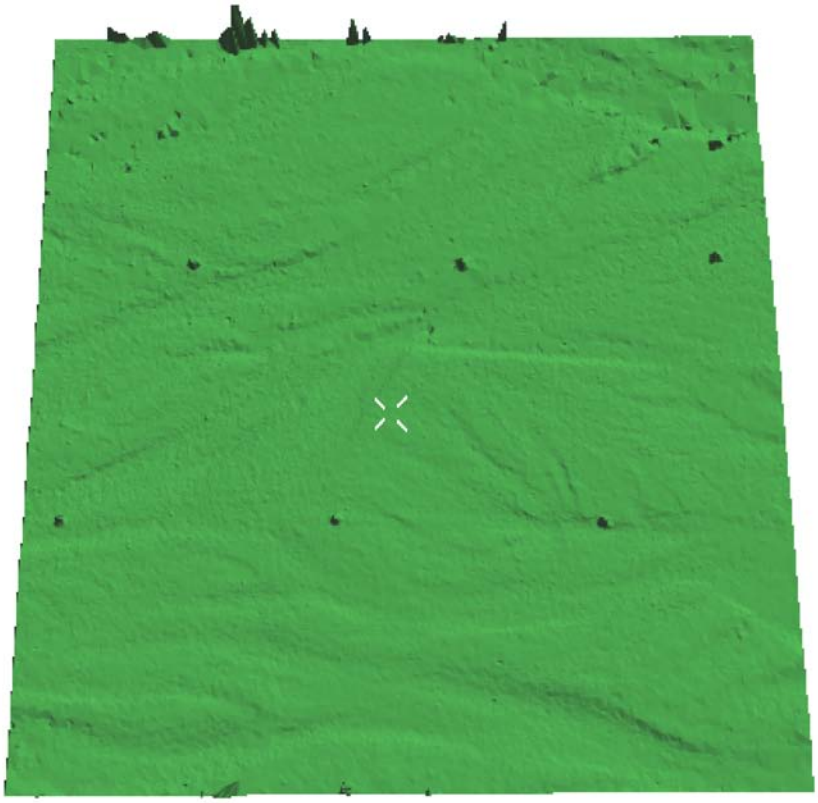

Figure 5.4: Mosaic DEM using convergent case

that the texture (Figure 5.4) derived using the convergent configuration is similar throughout the entire mosaic DEM. In addition, the areas exhibiting gross errors have reduced significantly, which has had the additional effect of emphasising the centrally located control targets.

5.1.1 Data Accuracy of the Laboratory Flume

The self-calibration bundle adjustment provides a diversity of criteria to assess the quality of photogrammetric data. The residuals of control points reflect differences between measured and computed coordinate values, which can be used as a first indication of the quality of the restitution of the photogrammetric network. Unfortunately, these criteria do not provide truly independent measures of the

accuracy of the network. However, rms errors derived from true check points, not used to compute the restitution, can provide independent measures of accuracies achieved, in the object space (Section 3.2).

Table 5.1 summarises the accuracies achieved in the object using a set of check

Table 5.1: Check point rms error (best possible lens model)

Image Configuration	*Check point rms error [mm]*		
	X	*Y*	*Z*
Normal	0.2	0.4	1.7
Convergent	0.2	0.3	0.2

points for both the normal and convergent image configurations. These statistics were derived using the best possible lens model achievable for the camera through self-calibration. Using the convergent configuration, a significant improvement in accuracy, particularly in the direction of the camera axes is discernable (reduction in rms error from 1.7mm to 0.2mm). This result is not surprising since it can be assumed that extracted data using the normal case are disturbed by remaining residual systematic error surfaces, caused by slightly inaccurately estimated lens distortion parameters. In the convergent configuration, these disturbing effects have been minimised (Wackrow and Chandler, 2008a)(Appendix B).

However, to emphasise the benefits of adopting a convergent configuration, the lens model used for the Canon camera was deliberately degraded and determined check point rms errors are tabulated in Table 5.2. As expected, a significant change in accuracy in the direction of the camera axis for the normal configuration could be observed (rms error 6.6mm). The accuracy achieved using the

Table 5.2: Check point rms error (inaccurate lens model)

Image Configuration	*Check point rms error [mm]*		
	X	*Y*	*Z*
Normal	0.4	0.6	6.6
Convergent	0.2	0.6	2.0

mildly convergent configuration was also significantly affected, which was more unexpected. Investigating the convergent image configuration setup further, it was established that the camera axes did not intersect the object plane at exactly the same point, but at a point slightly (8-22cm) below the flume bed. The actual computed camera axes related to the flume bed surface, are represented in Figure 5.5. Thus, the effect on accuracy derived using the convergent image configuration perhaps exceeded expectations. Overall, accuracy statistics established for check point data using both configurations, certainly demonstrate the potential of the mildly convergent image configuration to minimise residual systematic errors, even though a significantly inaccurate lens model was used.

Although Table 5.1 and 5.2 provided a convincing quantitative argument, it was judged necessary to visualise the effect of the convergent image configuration. The automatically extracted mosaic DEMs (Figure 5.3 and 5.4) were compared by interpolation and subtraction. The derived DEM of difference is represented in Figure 5.6. Areas with elevations less then -5mm are illustrated by solid red,

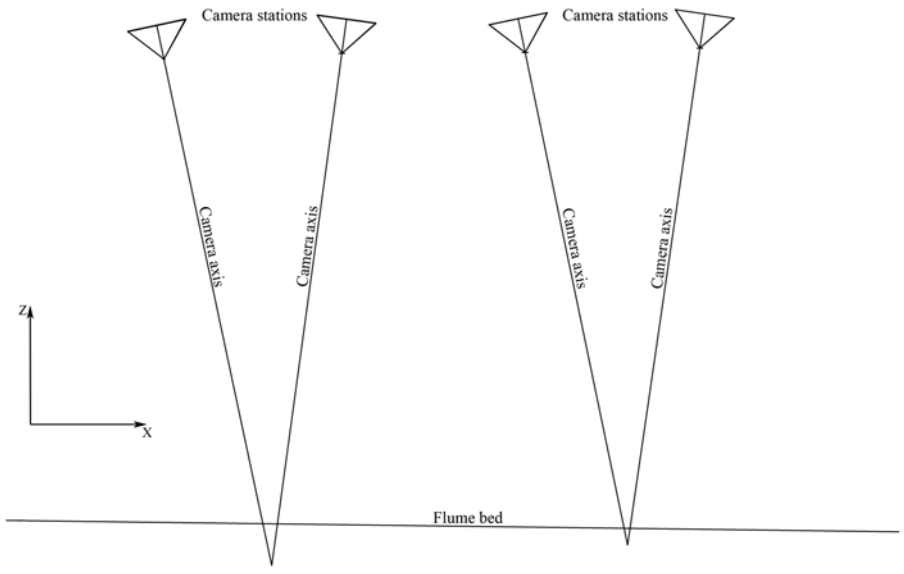

Figure 5.5: Camera configuration convergent case

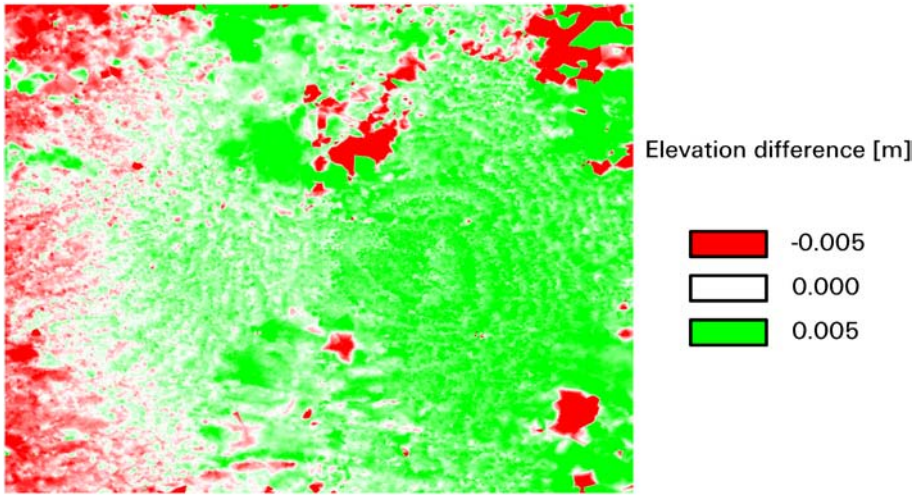

Figure 5.6: DEM of difference of the flume

while solid green regions indicate height differences greater then +5mm. White areas represent regions of no height differences. A dome can be clearly identified, slightly shifted to the right of the centre of the difference image.

These results demonstrate that residual systematic effects arising by slightly inaccurately estimated lens distortion parameters certainly degrade achieved accuracies with consumer-grade digital sensors, using the normal image configuration but can be minimised using a mildly convergent image configuration. This was reported in Wackrow and Chandler (2008a)(Appendix B).

5.2 Measurement of a Dynamic Water Surface

A small river, situated in Loughborough, was selected as a study site to support the development of a technique to measure the topographic surface of a flooding river in Farnham, Surrey (Chandler *et al.*, 2008; Wackrow and Chandler, 2008b) and also provided a useful case study for this thesis.

In the preceding chapters describing this PhD programme, only vertical imagery and comparatively flat test objects had been used for simulations and

practical tests to investigate the potential of a convergent image configuration to minimise domes in DEMs. Visiting the study site at the river in Loughborough revealed that oblique image pairs would have to be used to measure the water surface. This provided the opportunity to investigate if a convergent image configuration can minimise domes arising from an inaccurate lens model, even if the geometrically more complex oblique perspective is used.

5.2.1 Simulating Oblique Image Configurations

The systematic error surfaces created by an inaccurate lens model were investigated in Section 4.2 using simulated data. It was decided to again use simulated data using normal and convergent image configurations in an oblique perspective. This simulation process and the flat, planar virtual test field were described fully in Section 3.4.1.

In the proceeding chapters of this thesis, representations of DEMs of difference, derived using the aerial normal and convergent configurations, were only focused on the visualisation of differences in height (Z axis) between the "Virtual Truth DEM" and automatically generated DEMs. It was judged that a more meaningful visualisation of DEMs of difference, which demonstrate the direction (X, Y, Z) of the distortion of the surface, is needed to improve understanding. A Matlab routine was developed, which generates not only a surface representation for a DEM of difference but also computes distortion vectors for each point of the test object. The surfaces and individual distortion vectors computed by the MATLAB routine demonstrate the directions of distortion of a surface at each point of the virtual test object. The results presented in Section 4.2.1 (Figure 4.8 and 4.10) using simulated data and the aerial normal and convergent configurations are again depicted in Figure 5.7 and 5.8 using this MATLAB routine. This will help to compare results derived using aerial configurations with results derived using oblique configurations. Figure 5.7a depicts the distorted surface

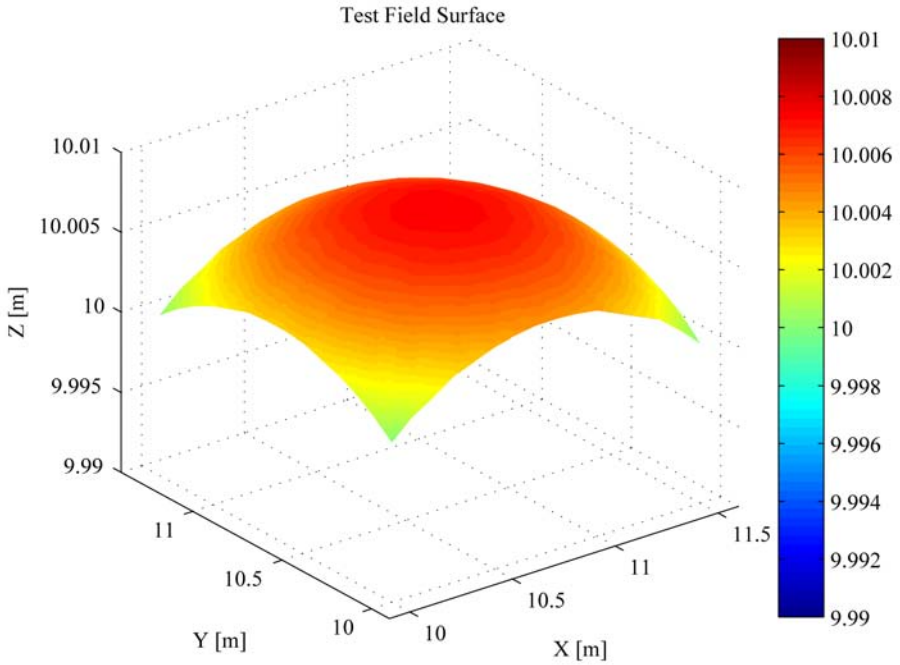

(a) Test field surface normal case

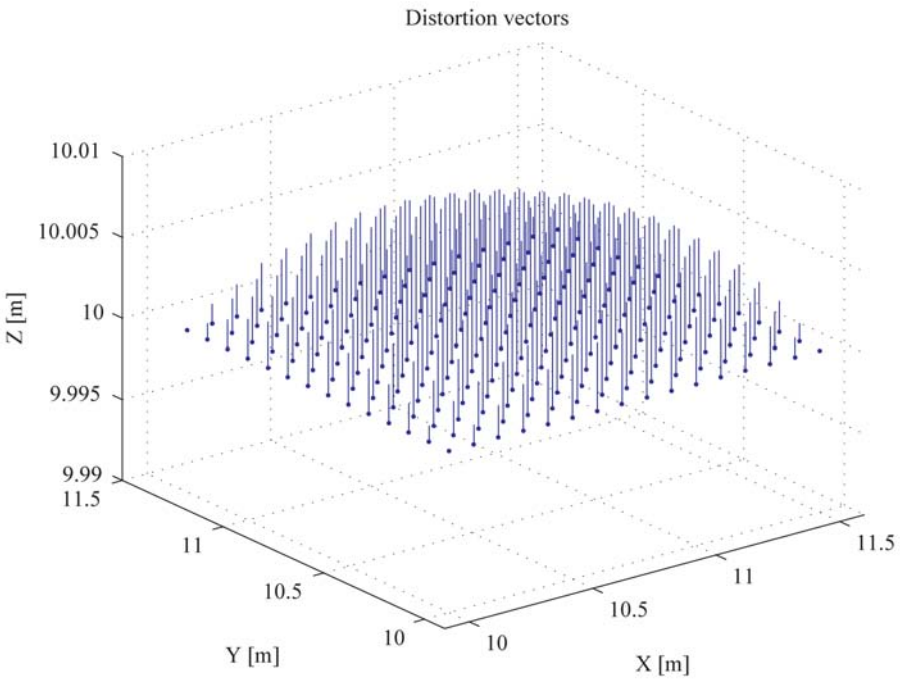

(b) Distortion vectors normal case

Figure 5.7: Aerial normal configuration

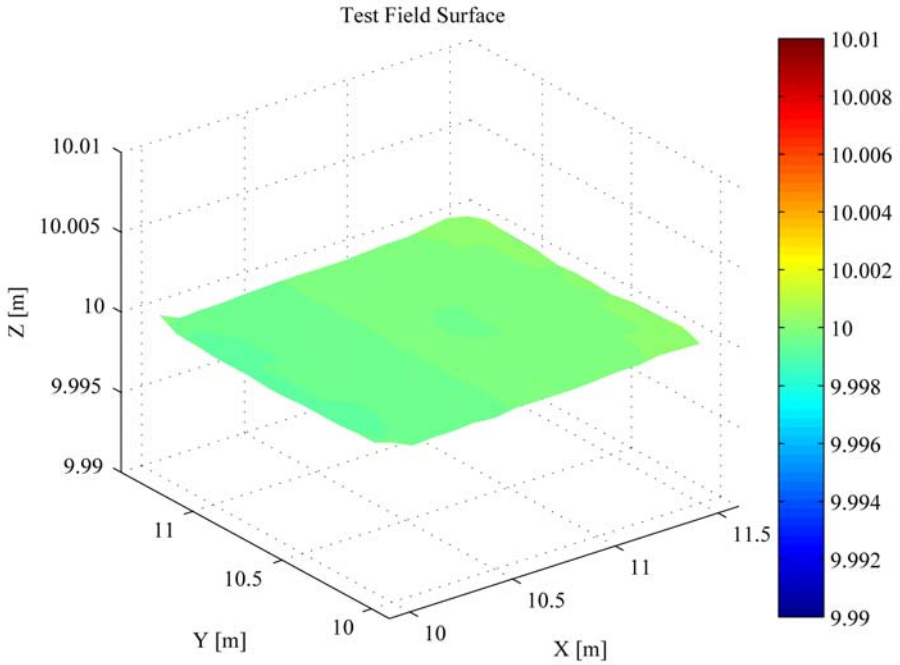

(a) Test field surface convergent case

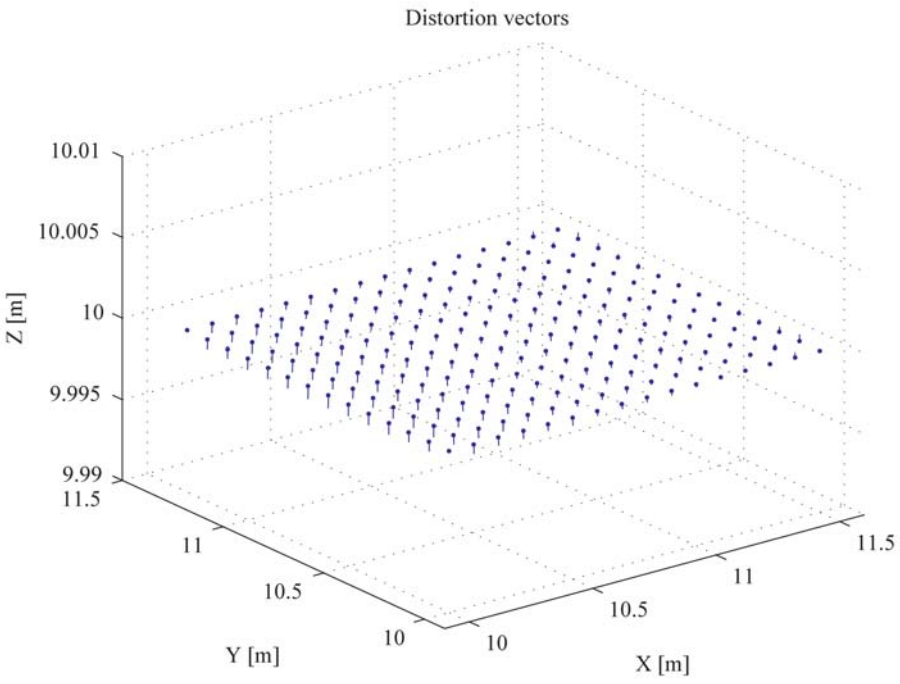

(b) Distortion vectors convergent case

Figure 5.8: Aerial convergent configuration

using the normal configuration (Figure 4.8), whilst distortion vectors, computed for each point of the virtual test field, are represented in Figure 5.7b. It demonstrates that the main effect on a flat surface arises from an inaccurate lens model using the aerial normal image configuration, can be identified in the direction of the camera axis. As demonstrated in Section 3.4.1 (Figure 4.10) the dome was almost eradicated using an aerial convergent configuration, which is again presented in Figure 5.8a and b. Having been reminded of the results represented in Chapter 4, the simulation was used to investigate the effect in the object space caused by an inaccurate lens model using image pairs describing an oblique normal and oblique convergent configuration.

Two sets of exterior orientation parameters describing an image pair, which represent the normal case with an imaging angle of 45 degrees (Figure 5.9) were used in the simulation. The imaging angle of 45 degrees creates a significant depth in the object, contrary to the aerial configurations tested. The simulation was used to compute perfect photo coordinates for the X, Y, Z coordinates of the virtual test field, using predefined interior and exterior orientations. The parameter K_1 describing the radial lens distortion was changed by 20%, prior to deriving object coordinates using the external bundle adjustment GAP.

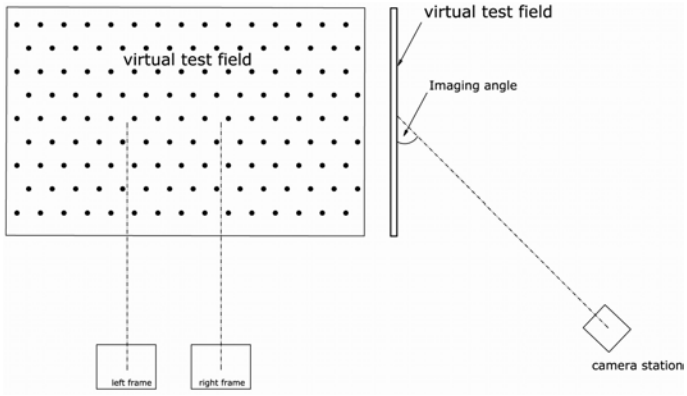

Figure 5.9: Camera configuration - oblique normal case

The MATLAB routine was employed to create a 3D surface and evaluate the distortion vectors using the computed object coordinates. The derived surface representation is illustrated in Figure 5.10a, whilst the individual distortion vectors for the test object are depicted in Figure 5.10b. These figures clearly indicate the presence of a dome, caused by the inaccurate lens model. It can also be identified that the distortion of the surface increases with the depth of the object.

Tests represented in Chapter 4 demonstrated that a mildly convergent image configuration minimises domes arising from an inaccurate lens model in the aerial case. Similar results were expected using a mildly convergent configuration in the oblique case. The two sets of exterior orientation were changed to describe a convergent image configuration, with the imaging angle set to 45 degrees. The lens model was again changed by 20% and the simulation was repeated. The derived surface and distortion vectors are illustrated in Figure 5.11a and b. As expected, the mildly convergent image configuration almost eradicated the dome, even though an oblique convergent image pair was used, characterised by significant depth in the object.

Various tests were conducted using a diversity of imaging angles and similar results, such as represented above, were obtained, but are not presented for brevity. However, for the case study to measure the floating water surface at the river in Loughborough, an approximately 30 degree imaging angle was used. Luhmann *et al.* (2006) states that the imaging angle should not be less than 20 degrees. It was considered necessary to test an image configuration with an imaging angle between 20 and 30 degrees using simulated data, prior to conducting the actual case study at the river. Results should prove some insight into the potential of a highly oblique and mildly convergent image configuration for the river study.

Two sets of exterior orientation parameters describing a normal and mildly convergent configuration respectively using an imaging angle of 24 degrees and again an inaccurate lens model of 20% were used in the simulation. Results of these simulations are represented in Figures 5.12 and 5.13.

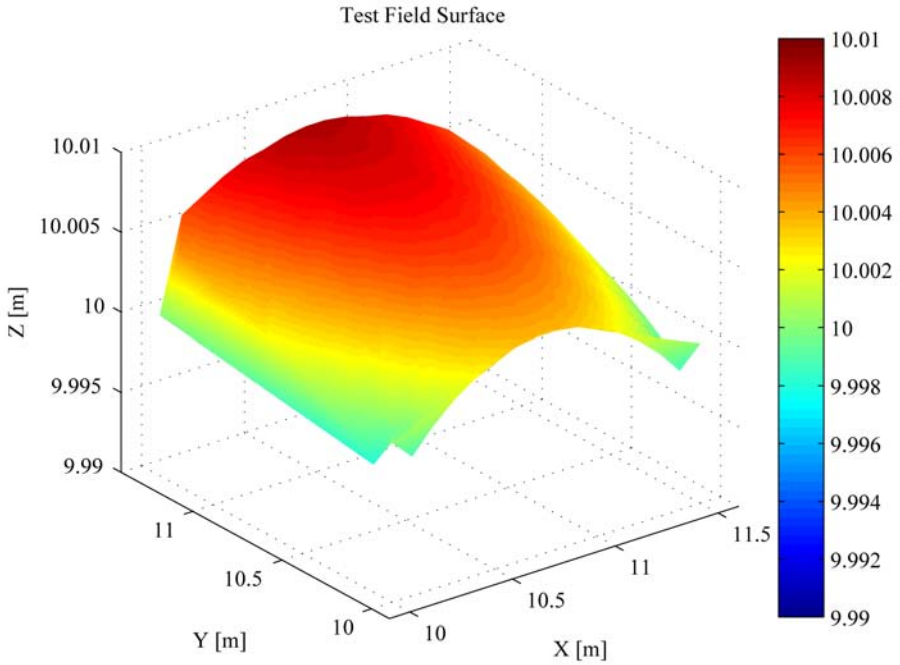

(a) Test field surface normal case

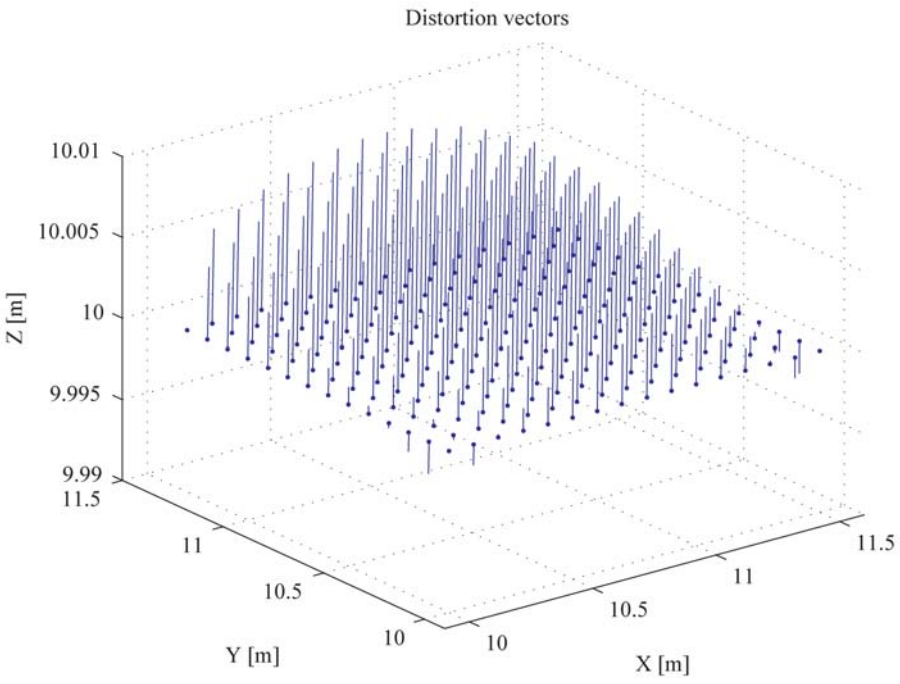

(b) Distortion vectors normal case

Figure 5.10: Oblique (45 degrees) normal image configuration

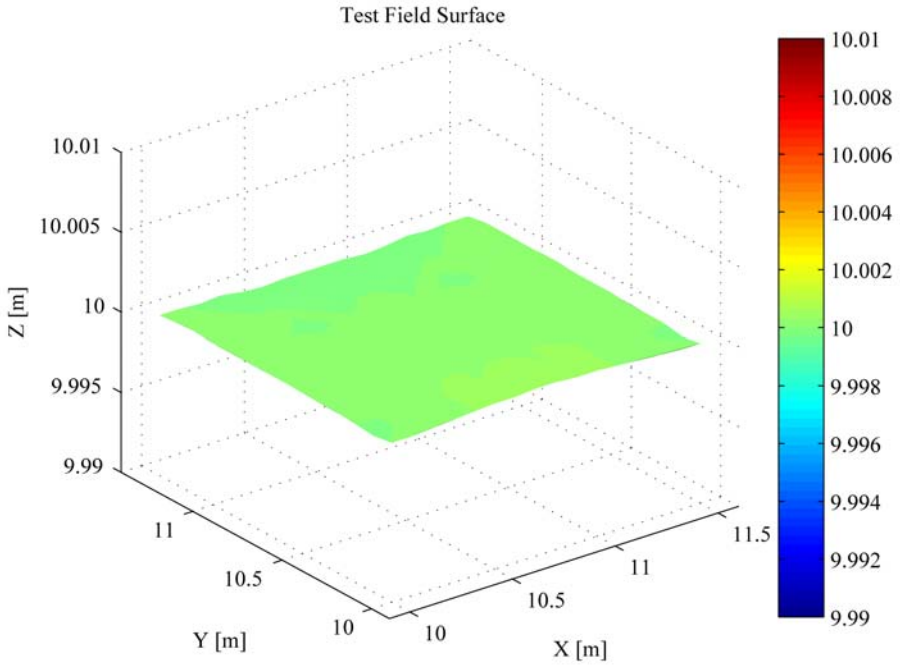

(a) Test field surface convergent case

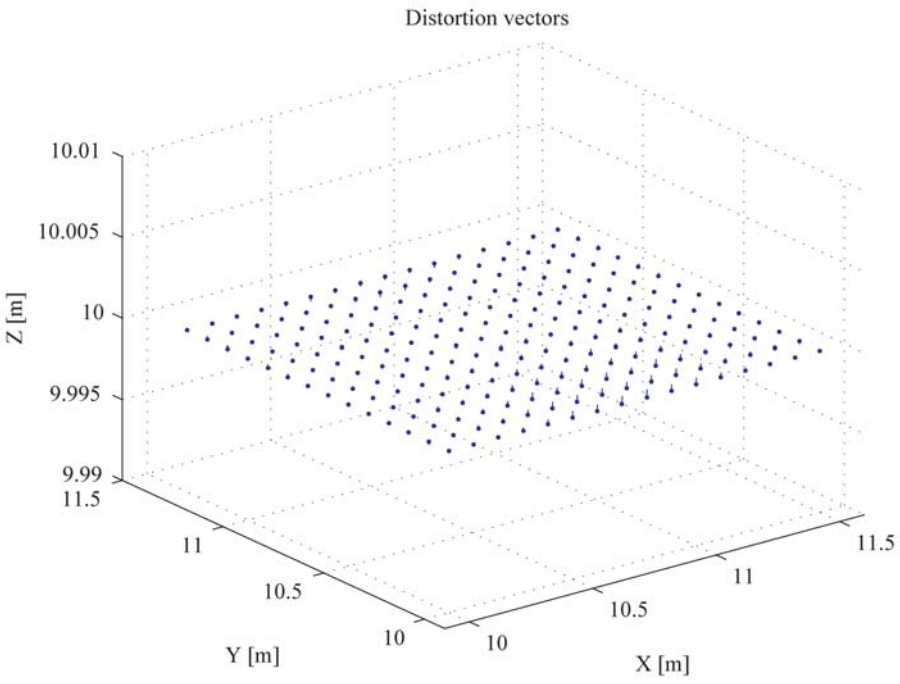

(b) Distortion vectors convergent case

Figure 5.11: Oblique (45 degrees) convergent image configuration

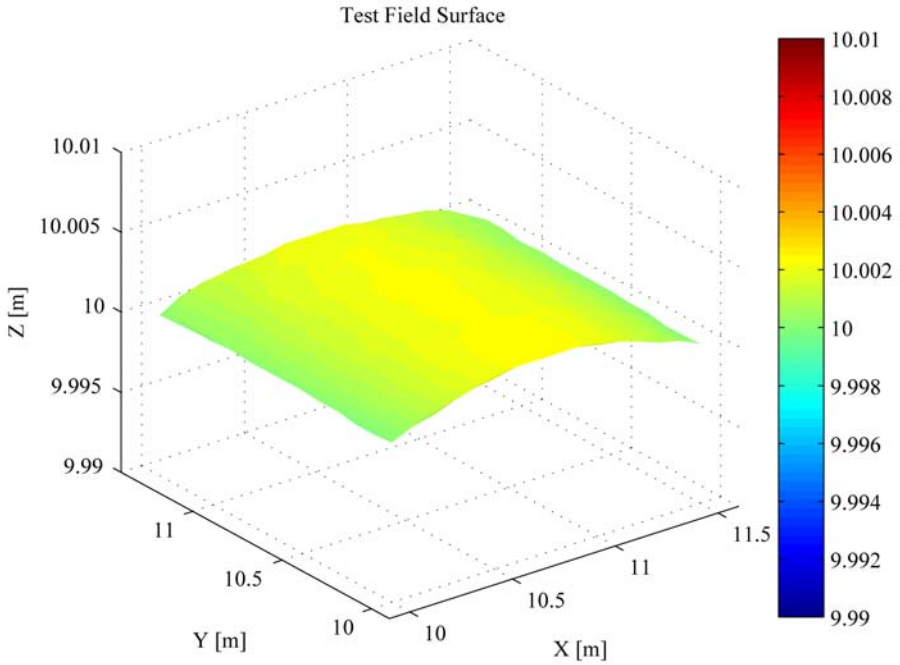

(a) Test field surface normal case

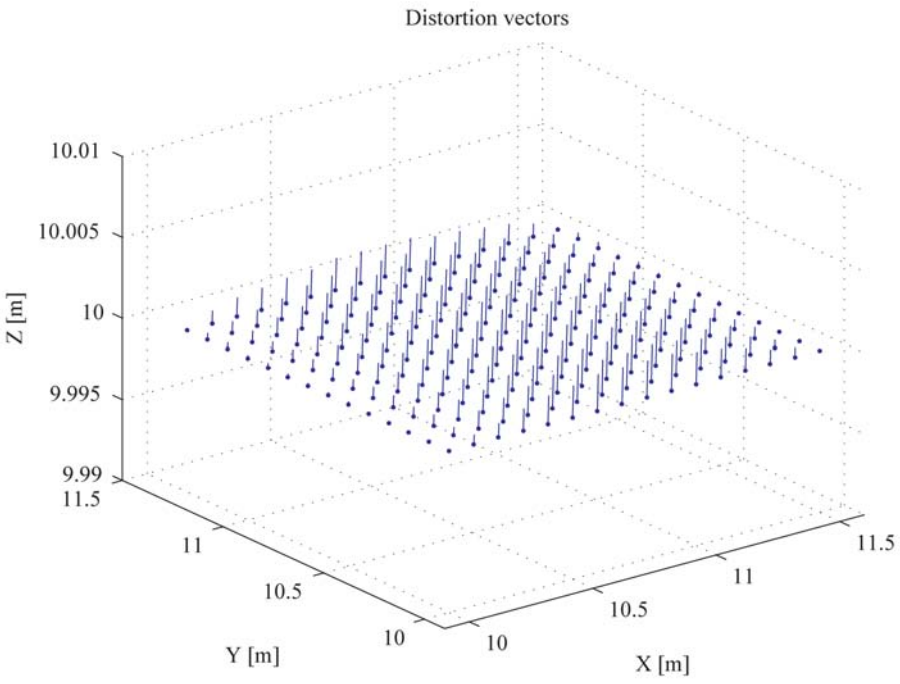

(b) Distortion vectors normal case

Figure 5.12: Oblique (24 degrees) normal image configuration

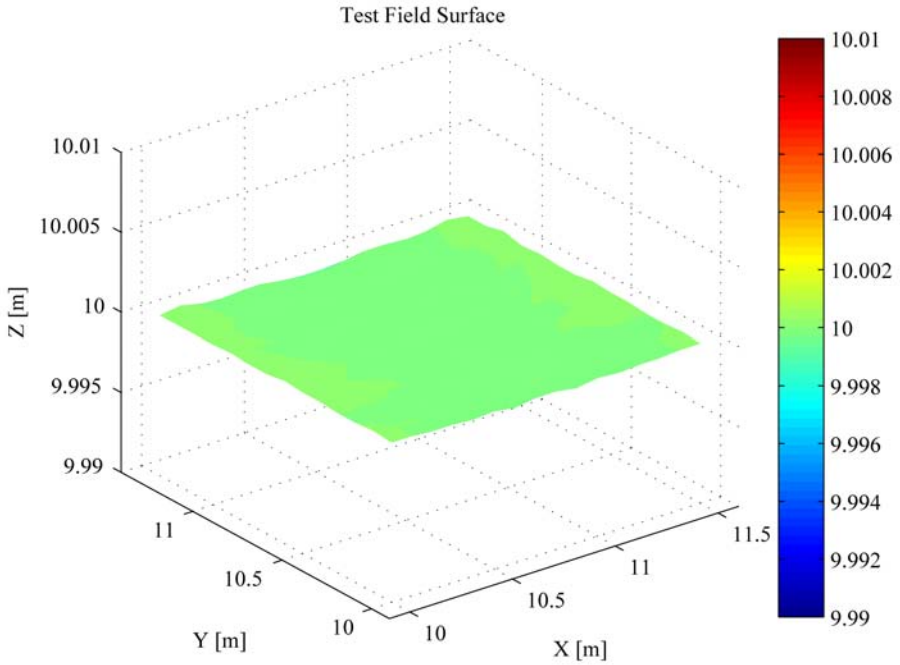

(a) Test field surface convergent case

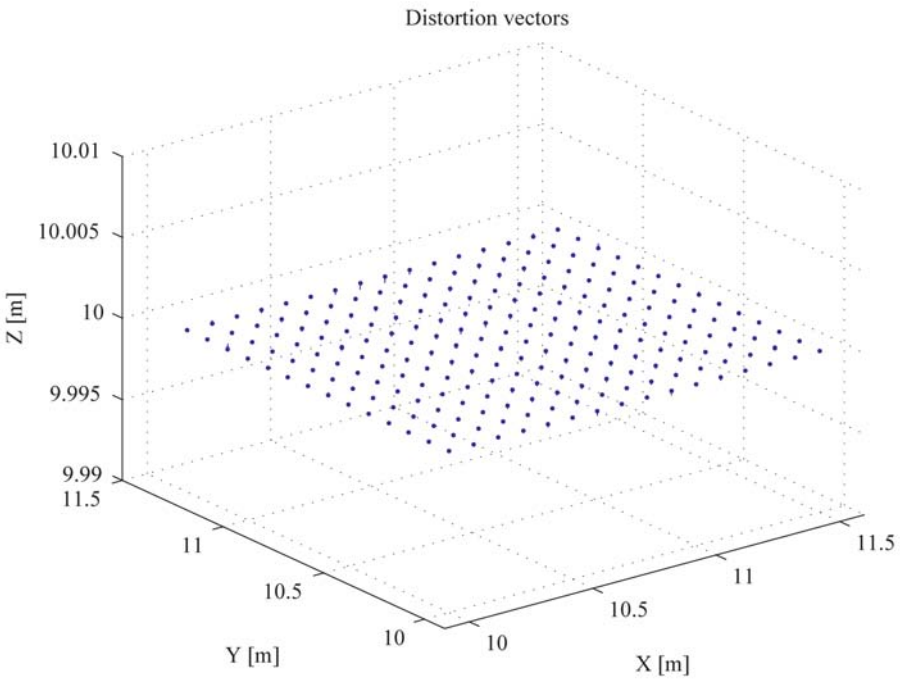

(b) Distortion vectors convergent case

Figure 5.13: Oblique (24 degrees) convergent image configuration

A dome is identifiable in Figures 5.12a and b, in which the oblique normal configuration with an imaging angle of 24 degrees was used, but this is not as distinctive as the domes illustrated in Figures 5.7a and b and Figures 5.10a and b.

Comparing these results demonstrates that the impact of an inaccurate lens model on the accuracy in the object space is less significant, when using a highly oblique image configuration. This finding will be further discussed in the following section, which presents a methodology to measure a dynamic water surface using real data. However, these results (Figures 5.13a and b) do demonstrate that using a highly oblique convergent image configuration minimises the systematic error surface arising from inaccurate lens distortion parameters. This is significant since it increases the flexibility of the developed methodology, for use on not only vertical convergent image configurations but also oblique convergent configurations.

5.2.2 Practical Test Measuring a Dynamic Water Surface

Tests conducted (Section 5.2.1) using simulated data have successfully demonstrated that a highly oblique convergent image configuration minimises residual systematic errors caused by slightly inaccurately estimated lens distortion parameters. The need to develop a system to measure the topographic surface of a flooding river in Farnham, Surrey (Chandler *et al.*, 2008) provided the opportunity to verify the findings of the simulation using real data.

A small river situated in Loughborough was identified to conduct a case study to measure a dynamic water surface. The river was approximately 4m wide and 0.3 to 0.4m in depth under normal fluvial conditions. Temporary photogrammetric target points were distributed along the river banks to provide conventional photogrammetric control. These were coordinated using a reflectorless Total Station (Figure 5.14).

Evaluating the accuracy in the object space consisting of a dynamic water surface was identified as a main difficulty in this study. Analysis of the residuals

Figure 5.14: Experimental setup on the river at Loughborough

of the control points can be used as a first indication of the accuracy of the network restitution, but is not independent (Section 3.2). The dynamic nature of the water surface prevented the use of a DEM of differences, which was repeatedly and successfully employed in this research to assess accuracies in the object space (Sections 3.2.3, 4.1.2, 4.1.3 and 4.2.2). However, using independent check point data (Section 3.2) was considered to be an appropriate approach. Unfortunately, it was difficult to distribute a suitable number of check points close to the water surface of the running river. The solution involved placing a survey staff close to the water surface and using its graduations to provide appropriate check point data (Figure 5.15). The staff graduations were coordinated using the reflectorless Total Station (Figure 5.14) and could be compared with estimates established by photogrammetry using both the normal and convergent image configurations. Differences between these data sets would allow the achieved accuracies in the

Figure 5.15: Survey staff positioned close to the water surface

object space to be quantified.

A bridge across the river provided an ideal platform to position a pair of Nikon D80 digital cameras (10 Mega-pixel), both equipped as standard with a variable zoom lens (18-70mm). The cameras were mounted on photographic tripods (Figure 5.16). The cameras were pre-calibrated for the practical test presented in Section 4.2.2 using the methodology described in Section 3.4.4 with the zoom lens of each camera fixed to 24mm using electrical tape. At the time of this case study, the derived calibration data were out of date since these cameras had been used for a range of tasks, which involved changing the focal length of these cameras by removing the electrical tape. However, it was initially considered appropriate to simply fix the focal length of each camera again to 24mm and to use the interior orientation parameters derived by the earlier test field calibration to process the new data. This provided the additional opportunity to investigate whether the focal length of zoom lenses could be restored accurately. The camera to object distance was approximately 8m and the cameras

Figure 5.16: Camera setup on the river at Loughborough

were synchronised using two cables connected via a single operation switch. An oblique image pair of the river surface was captured using the normal image configuration, whilst a second image pair was derived using a mildly convergent configuration. The convergent angle between the camera axes was approximately 10 degrees and intersected the object plane at the same point. The imaging angle added up to approximately 30 degrees for both image pairs captured. The image pairs describing the normal and convergent image configurations were processed using the LPS software. Photogrammetric control was provided by the target points along the river banks and interior orientation parameters were supplied by pre-calibration. Restitution accuracies achieved using the normal and convergent configurations are summarised in Tables 5.3 and 5.4. The output of the bundle adjustment of LPS revealed that the cameras achieved poor restitution accuracy using both configurations in conjunction with the calibration data derived by the

Table 5.3: Restitution accuracy achieved for the normal image configuration

Interior orientation used	*Object rms error [mm]*			*Image rms error [μm]*	
	X	*Y*	*Z*	*x*	*y*
Test field calibration	0.86	0.41	0.34	37.49	17.73
Re-estimated focal length	0.05	0.03	0.05	3.58	2.96

Table 5.4: Restitution accuracy achieved for the convergent image configuration

Interior orientation used	*Object rms error [mm]*			*Image rms error [μm]*	
	X	*Y*	*Z*	*x*	*y*
Test field calibration	0.81	0.37	0.35	35.39	16.55
Re-estimated focal length	0.05	0.03	0.05	1.69	1.95

earlier test field calibration, clearly identified by analysing the image rms errors. The major concern was the fact that the focal length of the zoom lenses were re-fixed to 24mm using electrical tape. It was assumed that the focal length of each lens had not changed significantly, which appears to have been an erroneous assumption. These changes, when uncompensated for, can degrade the accuracy achievable, particularly when objects are recorded that are characterised by significant camera object distance variation, or depth (Section 4.1.1 and 6.2). Instead of re-calibrating the cameras using the test field approach, it was considered that the simple stereo pair configurations (either normal or convergent) were sufficient to re-estimate the focal length for each camera lens using the self-calibrating bundle adjustment GAP. The results are represented in Table 5.5. Analysing the

Table 5.5: Estimated focal lengths for the Nikon D80 cameras

Calibration method used	*Image configuration*	*Focal length [mm]*	
		camera left	*camera right*
Test field calibration	8 calibration frames	24.51	24.51
River configuration	Normal case	23.60	22.46
River configuration	Convergent case	23.64	22.51

values determined for the focal length of each lens demonstrates that these have significantly changed between conducting the test field calibration and the use of the cameras in this case study. This clearly identifies that the approach of restoring the focal length of the zoom lenses to 24mm visually and then fixing using electrical tape was not successful. However, these results also demonstrate that each camera was capable of maintaining their focal length during the time necessary to capture imagery in the case study. The values estimated for the focal length of each camera did not vary significantly when changing the camera configuration from the normal case to the convergent case (discrepancy 0.004mm left camera and 0.005mm right camera). Therefore, both the focal lengths estimated for each camera using the normal and convergent cases are applicable for all images captured during this application.

The image pairs representing the normal and convergent configurations were processed again using re-estimated values for the focal lengths, whilst parameters of the principal point offset and radial distortion were determined by test field calibration. Restitution accuracies achieved are summarised in Tables 5.3 and 5.4. Results indicate that the restitution accuracy has improved significantly (object and image rms errors) by use of the re-established values for the focal length for each camera. It demonstrates that an inaccurately determined focal length substantially degrades the accuracy achievable, particularly when recorded objects are characterised by significant depth (Section 6.2). However, these tests also identified that a simple stereo pair configuration with sufficient 3D control within the same depth volume is capable of recovering the focal length of a lens camera system accurately through self-calibration.

An adequate number of check points, not including those used to compute the restitution of the image pairs, can provide independent data to assess the accuracy in the object space. These check point data were provided by the position of the major staff graduations of the surveying staff (Figure 5.15), coordinated using a reflectorless Total Station. These check points were also measured manually in each image using the point measurement tool of LPS. The bundle adjustment of

LPS was then employed to derive X, Y, Z estimates for these check points. Estimates derived using both methods could be compared, indicating the accuracy achieved using the normal and convergent image configurations. Figure 5.17 represents residuals for the staff graduations in the X and Z plane, established using the normal configuration. A systematic pattern or dome can be clearly identified. This systematic effect is also indicated by a mean error of 2.2mm, whilst random errors are represented by the standard deviation of ±3.9mm. Simulations (Section 4.2.1 and 5.2.1) and practical tests (Section 4.2.2 and 5.1) conducted in this PhD study have demonstrated that such residual systematic effects are caused by inaccurately estimated lens distortion parameters. Additionally, the lens model

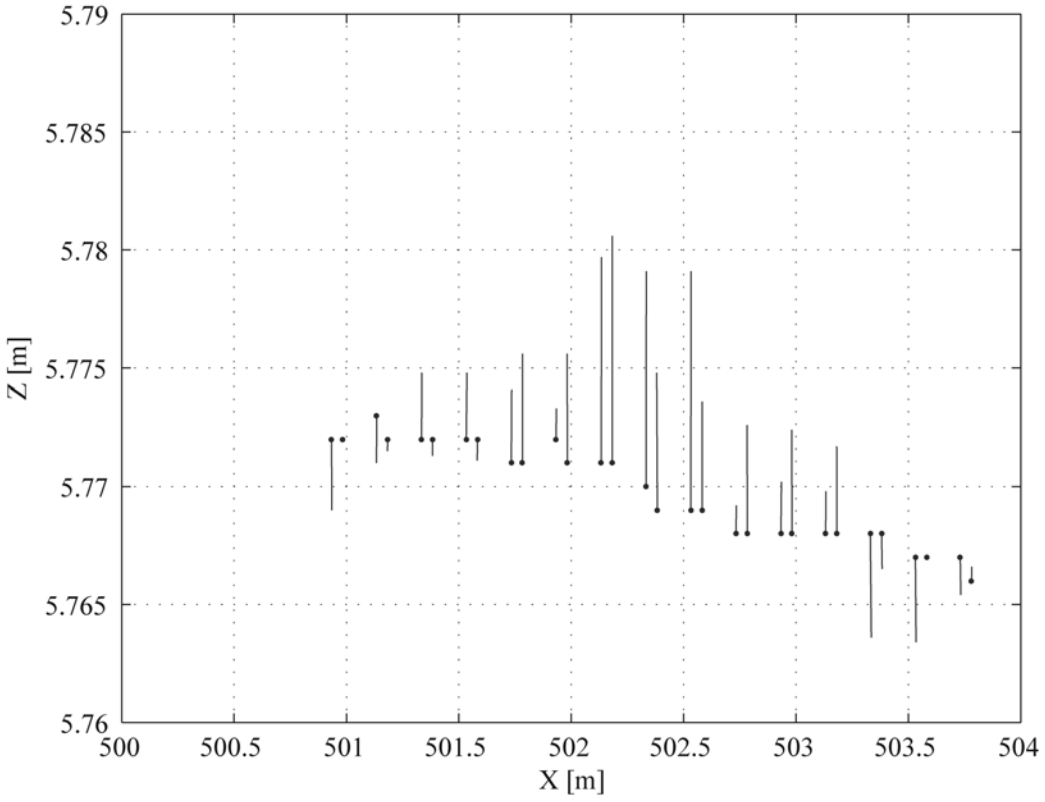

Figure 5.17: Distortion vectors of the survey staff graduations (normal case)

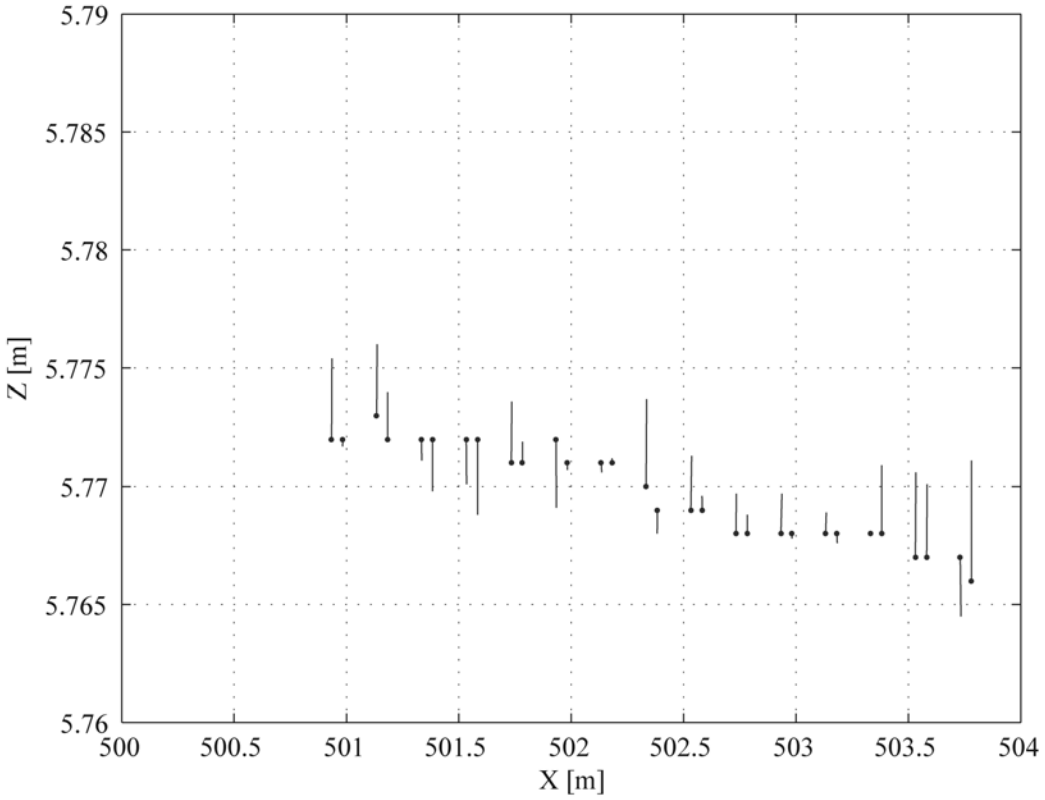

Figure 5.18: Distortion vectors of the survey staff graduations (convergent case)

used in this case study has proven to be slightly inaccurate in the practical test presented in Section 4.2.2, so that the residual systematic errors identified can be attributed to this. The procedure described was repeated using the oblique convergent image configuration and residuals established for the staff graduations are represented in Figure 5.18. Comparison with Figure 5.17 clearly demonstrates that the systematic errors were almost eradicated using the convergent configuration, which is also summarised by a mean error of 0.7mm (2.2mm normal case). The random errors were also minimised, which is identified by a standard deviation of ±2.1mm (±3.9mm normal case). This result is significant as it again implies that a mildly convergent image configuration can eradicate residual sys-

tematic errors caused by an inaccurate lens model even for oblique imagery and verifies the findings of the simulation (Section 5.2.1).

After an appropriate solution for restitution of the oblique convergent stereo pair was found, a DEM of the water surface could be extracted using the DEM generation capability of LPS (Section 3.2.2) but it was essential to provide a sufficient number of evenly distributed tie points representing the water surface of the river. Suitable seeding material had to be identified, which provided appropriate texture for the image-matching algorithm of the LPS software and truly represents the water surface. Since this research was conducted on a real river, only biodegradable material was suitable for environmental reasons. Initial tests were conducted using saw dust and fallen leaves for seeding. Unfortunately, the grain size of saw dust proved to be inadequate. The leaves could not provide suitable contrast in the image so that the automatic tie point generation routine of LPS could not be used to sufficiently establish accurate object measurements. Using larger wood chippings generated by a saw solved the issue of grain size, but it was identified that poor lighting conditions at the study site could cause difficulties in identifying tie points using LPS due to a lack in contrast. White polyester packing chips, which are regular in size and shape, would be the obvious seeding material but are not acceptable from an environmental perspective. Fortunately, white biodegradable foam packing chips are available, which disintegrate when in contact with water. These were used in this case study to provide appropriate texture for the tie point generation tool of LPS. The issue of seeding materials and the development of a simple seeding distribution system is also a subject in Chandler *et al.* (2008). A appropriate number of tie points could be generated and a DEM with a resolution of 5mm was created using LPS. These data were then transferred into a MATLAB routine to create a visualisation of the water surface (Figure 5.19). The position of the surveying staff is clearly identifiable in this illustration. It is also notable that the physical structure of the dynamic water surface is well presented. It is believed that the findings of this case study

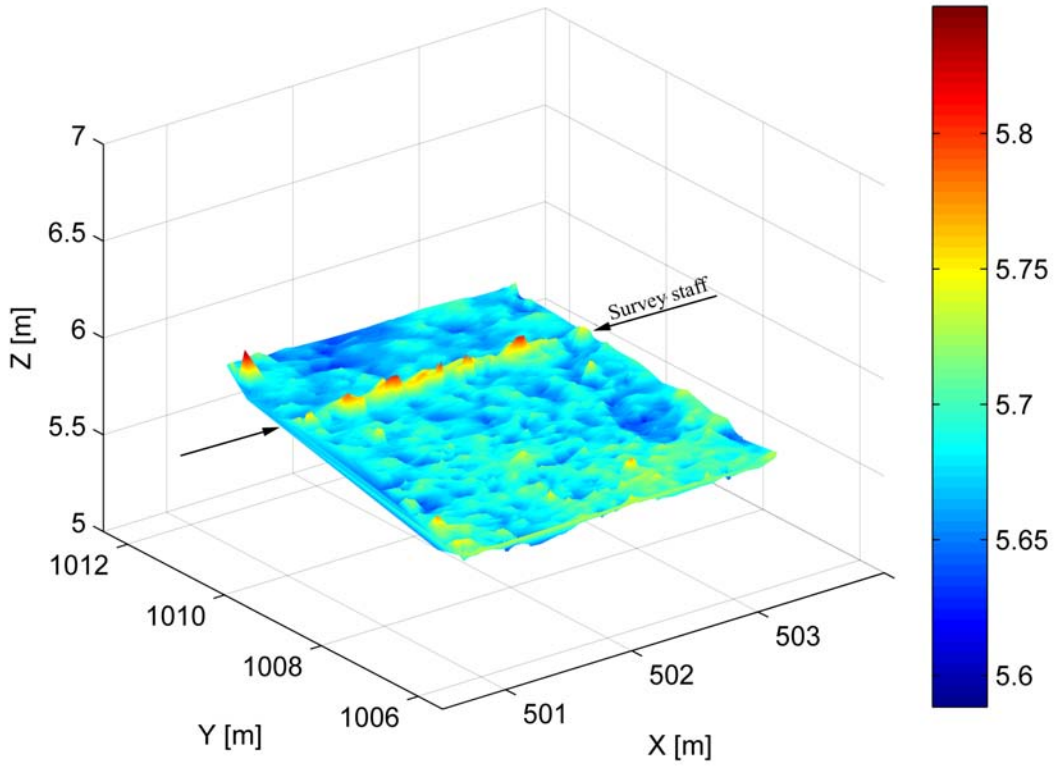

Figure 5.19: Loughborough river surface

will promote the development and further use of a simple and cheap system to measure the topographic surface of a flooding river.

5.3 Summary

The case study conducted to measure a flume bed surface in a semi-controlled environment has successfully demonstrated that residual systematic error surfaces caused by inaccurately estimated lens distortion parameters can be minimised using a mildly convergent image configuration, at least for near vertical imagery. This verifies the findings presented in Chapter 4. It also identified that the camera axes using the convergent configuration should intersect the object plane

as closely as possible at the same point.

Simulated data were used to demonstrate the potential of convergent image configurations to eradicate domes arising from an inaccurate lens model in the case of oblique image geometries. This is highly significant as it increases the flexibility of the developed methodology since oblique image configurations are often used in close range applications. These findings were confirmed by a test conducted to measure a dynamic water surface using real data, which will also support the development of a measuring system to model the topographic surfaces of a river. The findings of the case studies and the implications of this whole research project will be further discussed and evaluated in the following chapter.

CHAPTER 6

Discussion

The experimental work of this PhD study was presented in Chapter 4 and 5 and some additional questions were identified. This chapter discusses these issues and further tests will be presented, which were conducted to clarify these. Also some interesting results were obtained by conducting these additional tests, which culminate in recommendations for further research. Finally, an overview is provided that attempts to establish a relationship between achieved accuracies and costs of various non-metric digital cameras.

6.1 Disturbing Effects on Camera Stability

Several factors can have an impact on the geometric stability of a camera. These includes both the design of a sensor and the impact of external forces. The Nikon Coolpix 5400 digital camera used for stability analysis in this study is equipped with a built in zoom lens. When the camera is turned off, the lens moves automatically in the 'turned off mode', which means that the lens is retracted into the camera body. Every time the camera is switched on, the lens has to move automatically to the correct position, hopefully to accomplish identical internal geometry (focal length). To achieve this, the mechanical movement of the lens has to be highly accurate. Moreover, this feature is used by various manufactures

of consumer-grade digital cameras and there is concern in terms of geometric stability of these sensors. External forces caused by mishandling (shaking, slight knocks due to transport) the camera before or in between acquiring images for photogrammetric measurement tasks, could effect particularly the functionality of the mechanical components of a camera and can disturb their geometric stability. Tests to investigate such effects on the stability of a camera were conducted by (Bosch *et al.*, 2005) using a Olympus C-5050 consumer grade digital camera. However, the authors concluded that the factors described above do not have a significant impact on the geometric stability of this camera.

The seven Nikon Coolpix 5400 cameras used for stability analysis in this study were purchased by English Heritage for the Northumberland and Durham Rock Art Project in February 2005. These were calibrated initially on the 4th of July 2005, when the cameras were relatively new and in immaculate condition. The calibration process was repeated after 4 days. During the subsequent 12 months, these cameras were used regularly in the field by teams of volunteers to record 1500 rock art motifs located in the north of England (Chandler *et al.*, 2007). The seven cameras were then re-calibrated in July 2006 at Loughborough and clear physical marks (scratches on the camera body) could be observed on each of the seven cameras. The physical marks on each camera suggest that these had clearly been exposed to external forces during field work. Therefore, it was judged that there was no need to further simulate disturbing effects caused by external forces (Section 3.3). Despite these, cameras demonstrated remarkable geometric stability and manufacturing consistency (Chapter 4). This led to the conclusion that the disturbing effects discussed, have only minimum impact on the geometric stability of the Nikon Coolpix 5400 cameras.

However, it could well be that extreme temperature values (below zero or above 30 degrees) may have an impact on the validity of established IOPs for these cameras. Although, such conditions could be easily simulated in a laboratory environment, it could also harm the cameras. This would have compromised the success of the Northumberland and Durham Rock Art Project and was not

conducted. Investigating the impact of extreme temperature values on its stability may still be an interesting task for future research.

6.2 Role of Primary IO Parameters Using Oblique Imagery

The impact of varying the focal length and principal point offset on the accuracy in the object space were investigated in Section 4.2.1 using simulated data. Results demonstrated that the parameters of exterior orientation fully compensate the disturbing effects caused by inaccurate parameters for focal length and principal point offset, when a flat test object and the aerial photogrammetric normal case is used. These results were perhaps expected since this simple image configuration provides no depth in the object. However, an oblique image configuration will provide significant object depth and this case will also apply to vertical viewing of an object a similar amount of depth such as a valley. The case study (Section 5.2) conducted to measure the water surface of a river identified that variations of the focal length can degrade the accuracy achievable. Thus, the effects on accuracy in the object space by varying the parameters describing the focal length and principal point offset using oblique image configuration were further investigated using simulated data. Results of these simulations are presented in the following sections.

6.2.1 Impact of Varying the Focal Length Using Oblique Imagery

Initial results represented in Section 4.1.1 demonstrated that variations of the parameter describing the focal length has no significant impact on the accuracy in the object space if a flat test object and an aerial normal image configuration are used. The parameters of exterior orientation fully compensate for these disturbing effects. However, practical work conducted to measure a river surface

(Section 5.2.2) identified that an inaccurate focal length can degrade the accuracy achievable if an object is recorded characterised by a significant object depth. It was decided to use the simulation (Section 3.4.1) again to investigate the impact of an inaccurate focal length, with specific reference to oblique imagery.

The sets of exterior orientation employed in this simulation are similar to those used in Section 5.2.1 and described either the normal configuration or convergent configuration with specific reference to oblique imagery. Both image configurations used an imaging angle of 24 degrees (Figure 5.9), which provided a significant depth in the object. Variations of the focal length of approximately 2% were identified in various camera calibration test using the Nikon Coolpix 5400 digital cameras (Section 4.1). It was decided to use this realistic variation for the simulation, thus the focal length was changed by -2%. The case study conducted to measure the river surface (Section 5.2.2) proved that restoring the focal length of a camera can be difficult and can result in significant large variations of this parameter. A larger variation of the focal length of -20% was also introduced to demonstrate the impact on the accuracy more forcefully. The parameters representing the principal point offset and radial lens distortion remained unmodified. The results achieved, using the normal oblique configuration for two focal lengths, are represented in Figure 6.1 and 6.2. The distortion of the test surface through introducing these systematic errors is clearly identifiable. It is also observable that the distortion of the test surface increases within the depth of the object, which is particularly apparent in Figure 6.2.

Initial tests conducted to investigate the impact of varying the parameter of the focal length using a flat test object and the aerial normal image configuration (Section 4.1.1), revealed that the exterior orientation parameters fully compensated these effects through correlation between interior and exterior orientation parameters. Results achieved in this simulation demonstrate that the exterior orientation is not capable of compensating for the disturbing effects caused by an inaccurate focal length, using the normal oblique image configuration. This was

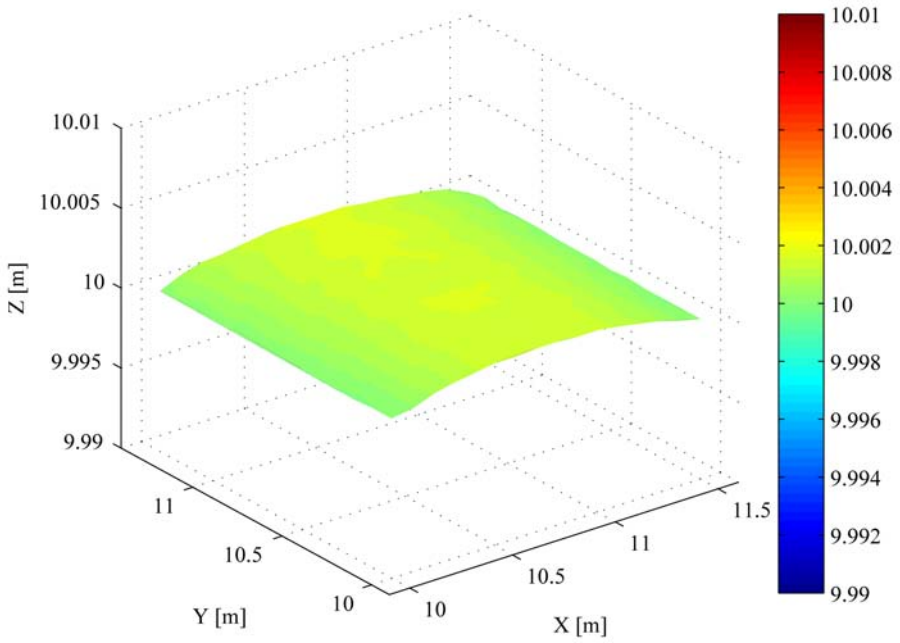

(a) Test field surface

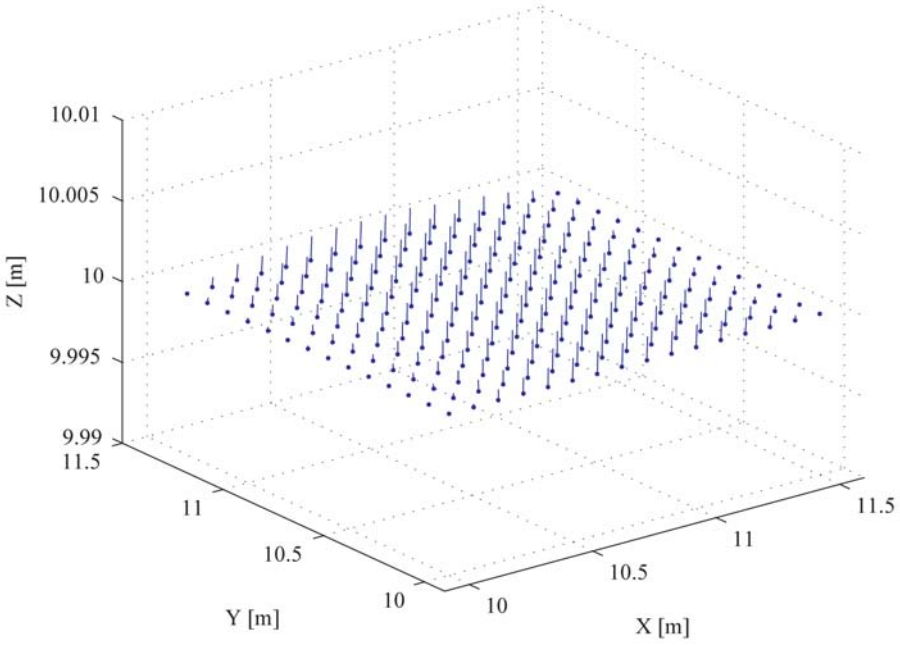

(b) Distortion vectors

Figure 6.1: Normal oblique configuration, f changed by -2%

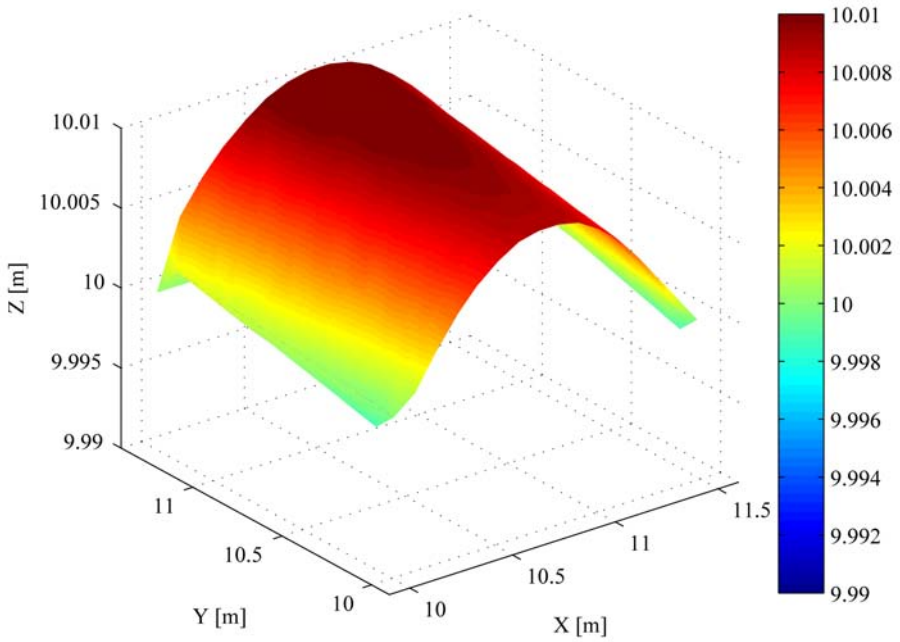

(a) Test field surface

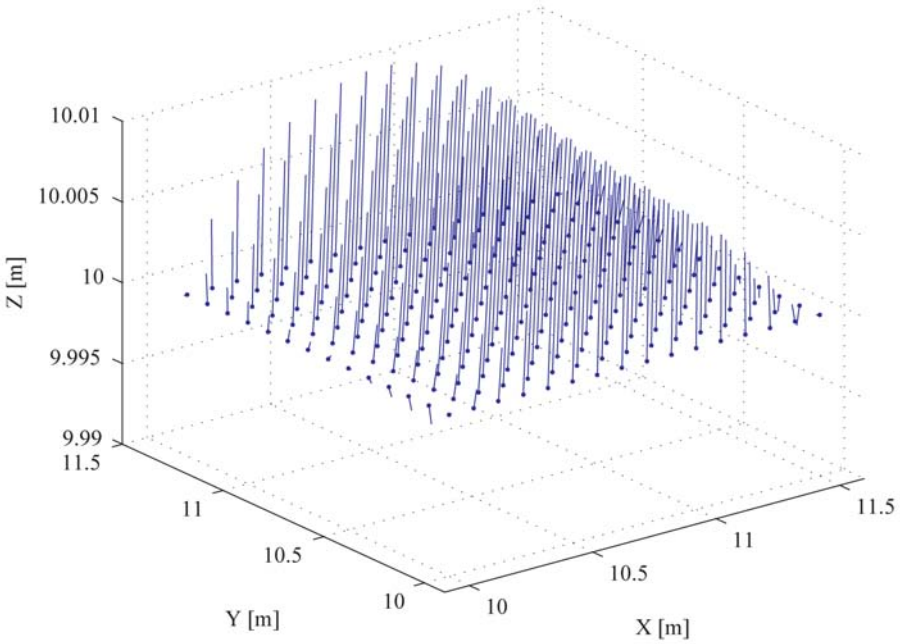

(b) Distortion vectors

Figure 6.2: Normal oblique configuration, f changed by -20%

expected since using oblique imagery introduces a significant depth in the object in contrast to aerial image configurations with reference to a flat test object. However, the results presented in Chapter 4 and 5 demonstrated that a mildly convergent image configuration (normal or oblique) minimises residual systematic error surfaces or domes caused by inaccurate radial lens distortion parameters. It seemed plausible that such an image configuration could maybe also minimise the systematic errors arising from an inaccurate focal length. The two sets of exterior orientation parameters were changed to represent an image pair, which described a mildly convergent oblique image configuration. The focal length was again changed by -2% and -20%, and the simulation was repeated. Derived surfaces of the test object and the corresponding individual distortion vectors are represented in Figure 6.3 and 6.4. The results demonstrate that the systematic errors caused by an inaccurate focal length are not minimised when using a convergent oblique image configuration. It also indicates a switch of the mathematical sign between deviations derived using the normal oblique and convergent oblique configuration (Figure 6.2 and 6.4). This was surprising and not expected but is perhaps caused by the function of systematic change in depth and relative orientation. These tests demonstrated that the parameters of exterior orientation cannot compensate for the disturbing effects caused by an inaccurate focal length when either using a normal oblique or convergent oblique configuration. These results correspond closely and clarify the findings achieved in the case study conducted to measure a dynamic water surfaces, represented in Section 5.2.2.

Reflecting the results achieved in this section, particularly the switch of the mathematical sign of the deviations (Figure 6.2 and 6.4), led to the implication that a half convergent oblique image configuration (Figure 6.5) may perhaps minimise the disturbing effects caused by an inaccurate focal length. It was decided to investigate the impact of varying the focal length using such an image configuration.

The two sets of exterior orientation parameters were changed to represent a half convergent oblique image configuration. Changes of -2% and -20% of the

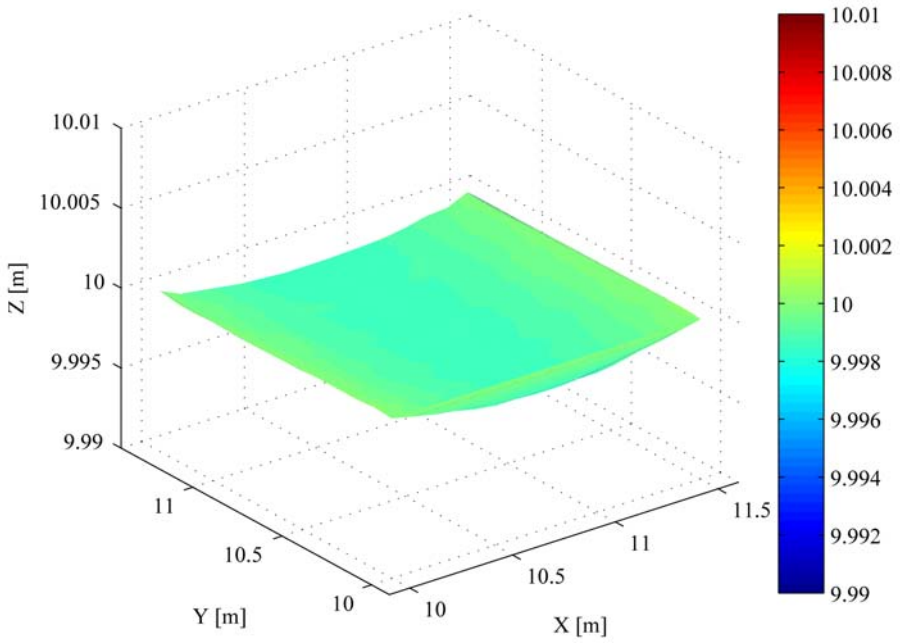

(a) Test field surface

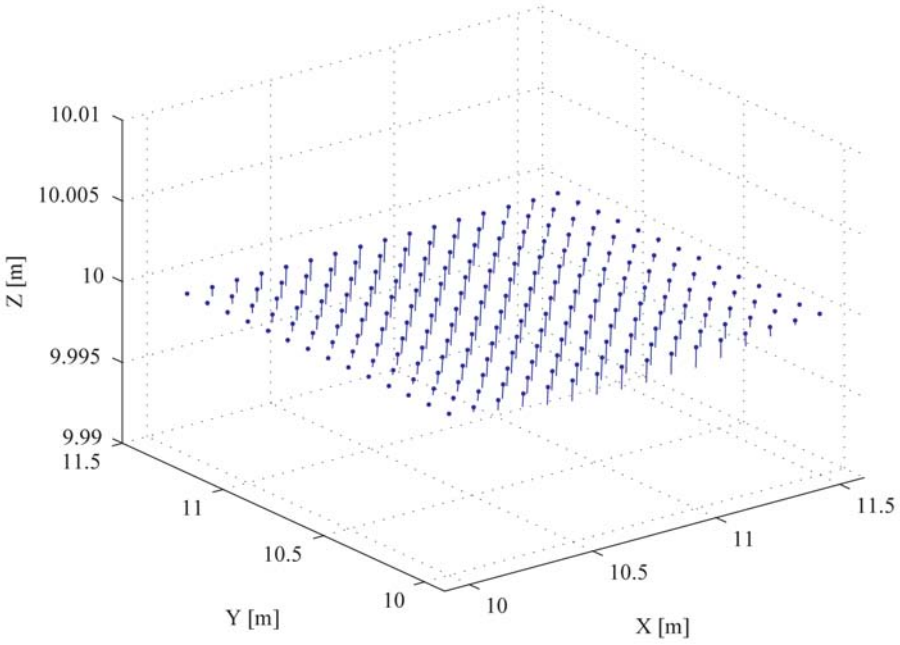

(b) Distortion vectors

Figure 6.3: Convergent oblique configuration, f changed by -2%

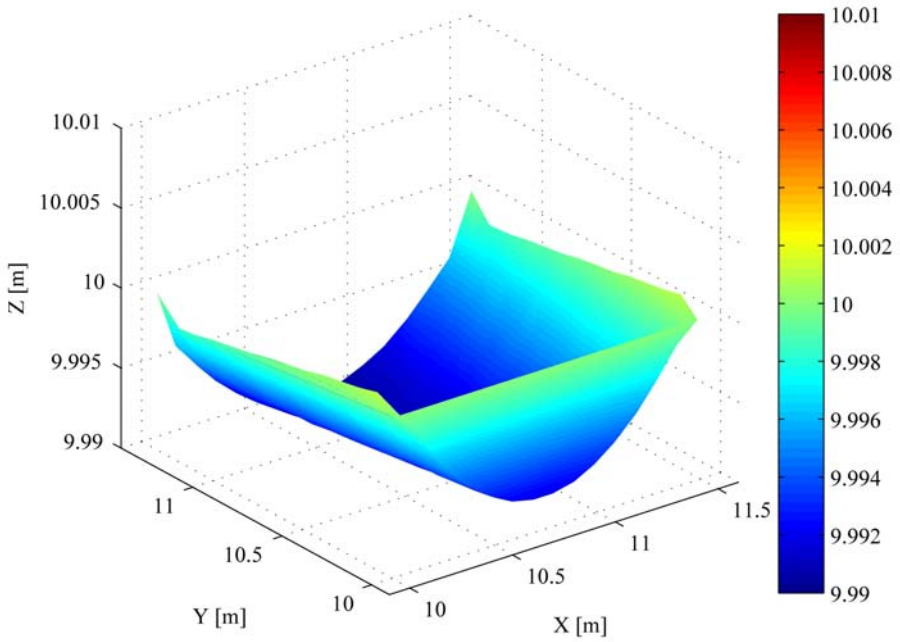

(a) Test field surface

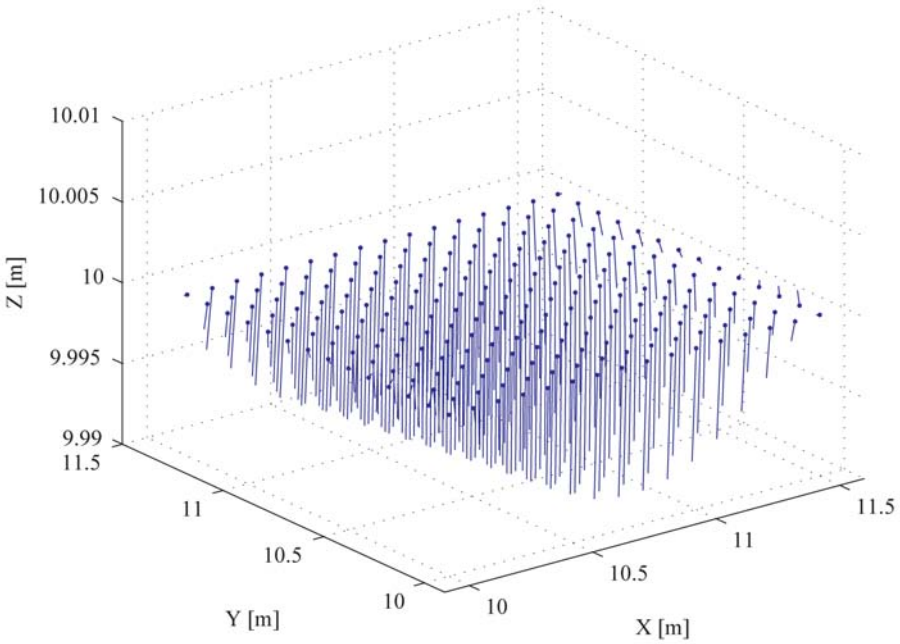

(b) Distortion vectors

Figure 6.4: Convergent oblique configuration, f changed by -20%

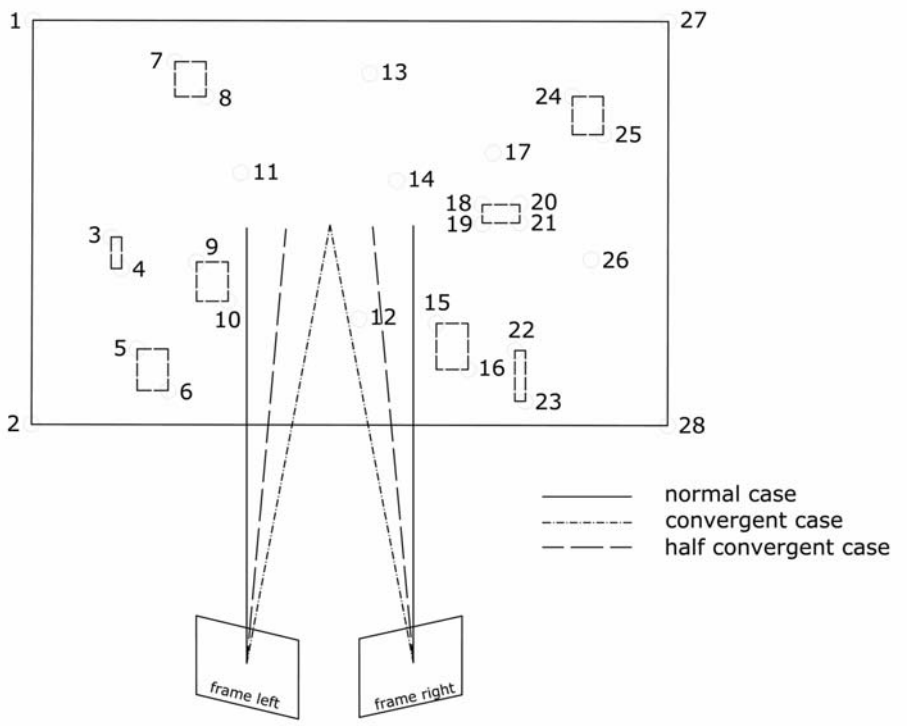

Figure 6.5: Half convergent configuration

focal length were introduced and the simulation was repeated. Results of this simulation, presented in Figure 6.6 and 6.7, demonstrate that a half convergent oblique image configuration minimises systematic errors caused by an inaccurate focal length. But it occurs that implementing such an image configuration in a practical task for close range photogrammetry would be difficult. However, the application described in Section 5.2 to measure a water surface of a river provides a possibility to achieve a half convergent image configuration. The camera axes can be aligned to a point beyond the survey staff. The intersection of the staff graduation with both camera axes provide an appropriate indication where each camera has to be pointed to implement a half convergent image configuration.

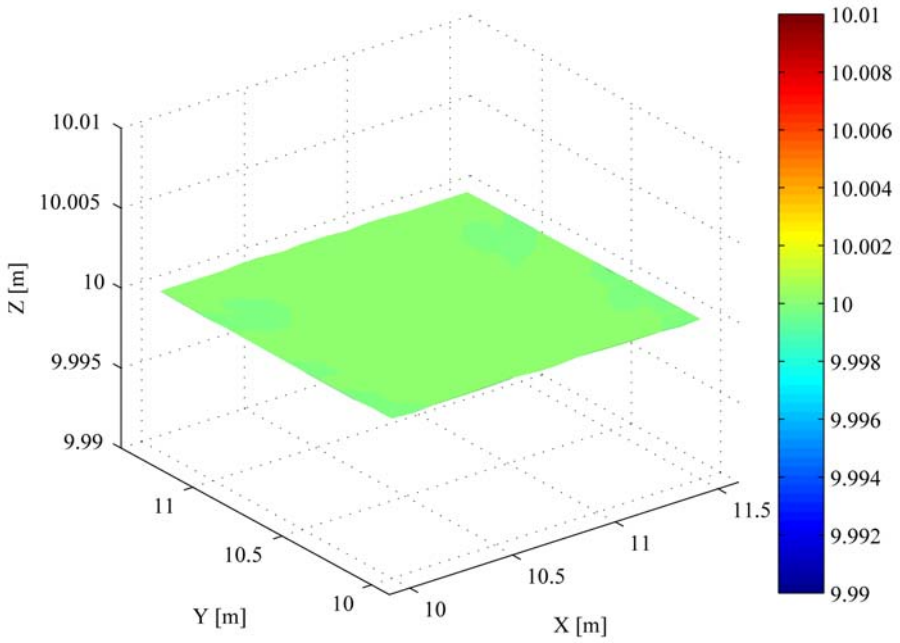

(a) Test field surface

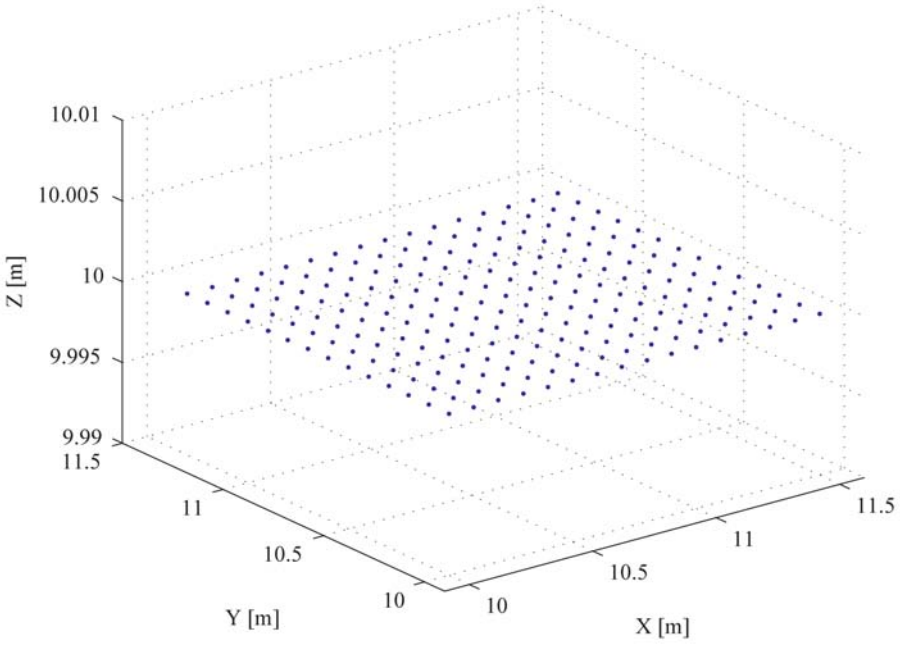

(b) Distortion vectors

Figure 6.6: Half convergent oblique configuration, f changed by -2%

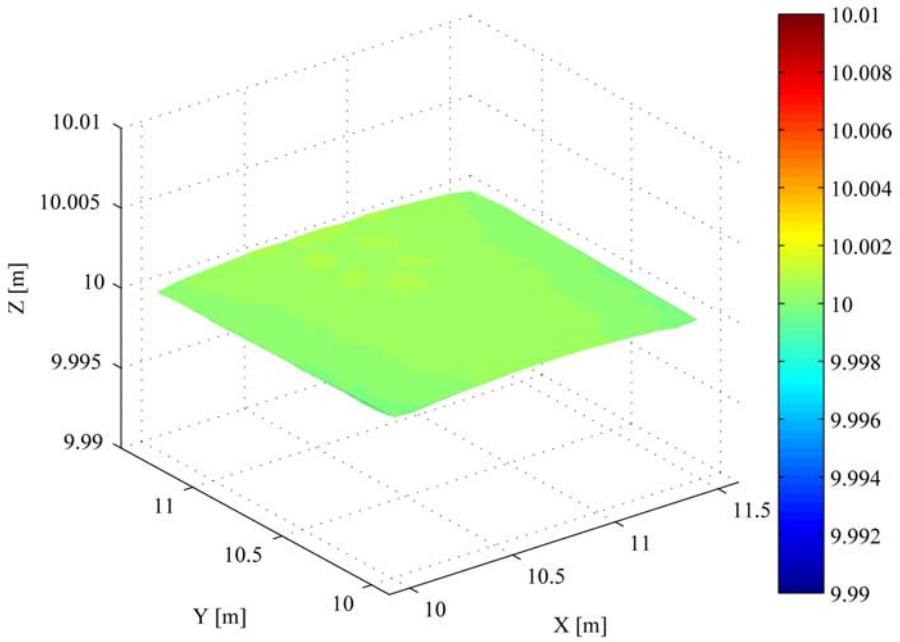

(a) Test field surface

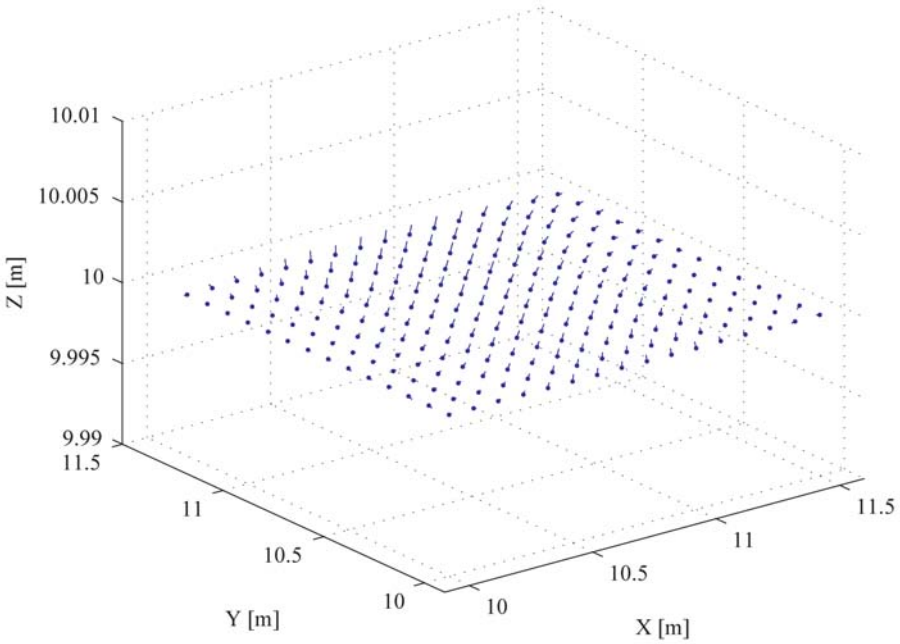

(b) Distortion vectors

Figure 6.7: Half convergent oblique configuration, f changed by -20%

Test conducted using simulated data demonstrate that an inaccurate focal length can degrade the achievable accuracy in the object space using highly oblique imagery. Somewhat surprisingly, the simulations also identify that a half convergent oblique image configuration can minimise these systematic errors arising by an inaccurate focal length. Investigating the relationship between variations of the focal length and image configuration may also be an interesting task for future research.

6.2.2 Impact of Varying the Principal Point Offset Using Oblique Imagery

The initial results presented in Section 4.1.1 demonstrated that if an aerial normal image configuration and a flat test object are used, variations of the parameters describing the principal point offset have no significant effect on the accuracy in the object space. The parameters of the exterior orientation fully compensate for these disturbing effects. However, it was expected that when the object is characterised by significant depth, systematic errors in the object space would arise from any inaccuracy in the estimation of the principal point offset parameters. The proven method of using simulated data (Section 3.4.1) was again employed to investigate the effect of inaccurate principal point offset parameters, with specific reference to oblique image configurations. The sets of exterior orientation used in these simulations described either the normal oblique or convergent oblique image configuration and are similar to those used in the previous section 6.2.1. Deviations of the principal point offset of 0.015mm in the x direction and -0.020mm in the y direction were introduced by modifying the interior orientation. The values were utilised as estimates of the same order of magnitude for the principal point offset were determined in various camera calibration tests. These simulations highlight the impact on accuracy of typical principal point offset values using oblique image configurations. Results achieved for both the normal and convergent oblique image configuration are depicted in Figure 6.8 and 6.9 respectively.

The perturbation of the test object through systematic errors, arising from inaccurate principal point offset parameters, are clearly identifiable in Figure 6.8a and 6.9a. The individual distortion vectors derived for the test surface (Figure 6.8b and 6.9b) also distinguish these effects.

Initial results, presented in Section 4.1.1, demonstrated that the exterior orientation parameters can compensate for these systematic effects through correlation between interior and exterior orientation. However, a flat test object and the aerial normal image configuration was used in this instance. This configuration was obviously lacking in object depth. The findings of these simulations demonstrate that inaccuracies of the estimation of the parameters of the principal point offset of a camera, cause systematic errors in the object space, when the recorded object is featured with significant depth. The exterior orientation parameters are unable to compensate for the systematic errors using either the normal oblique or convergent oblique image configuration. A switch of the mathematical sign of the deviations derived using both configurations was also not clearly observable. This was a feature identified in the simulations conducted to investigate the effect of varying the focal length on oblique imagery (Section 6.2.1), with the result that a half convergent oblique image configuration minimised such systematic errors.

The two sets of exterior orientation parameters, which describe the half convergent oblique configuration, were established in the simulation process to investigate if this configuration minimises the effect caused by inaccurate principal point offset parameters. The simulation was repeated and results are depicted in Figure 6.10. It is notable that the surface representation has not improved using this image configuration.

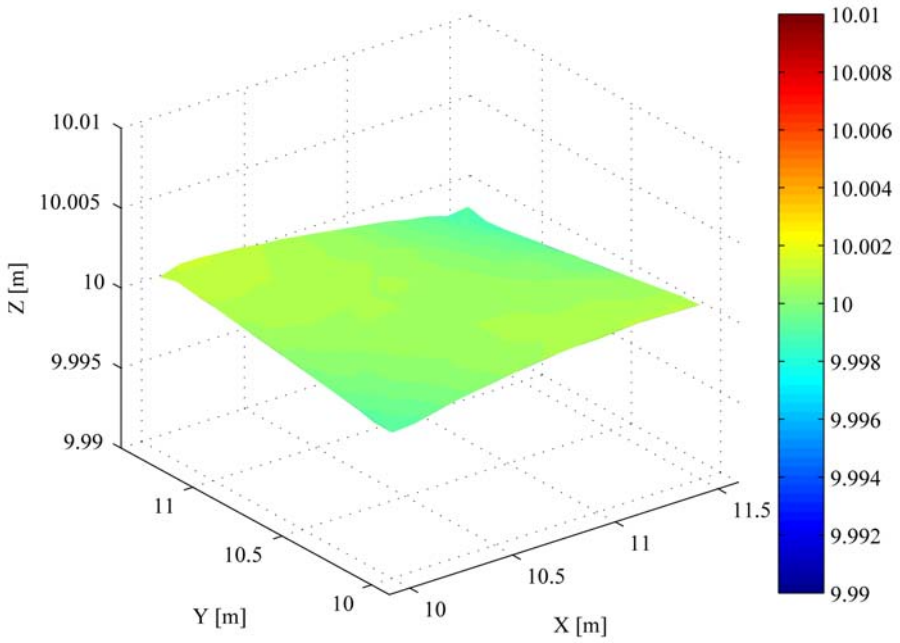

(a) Test field surface

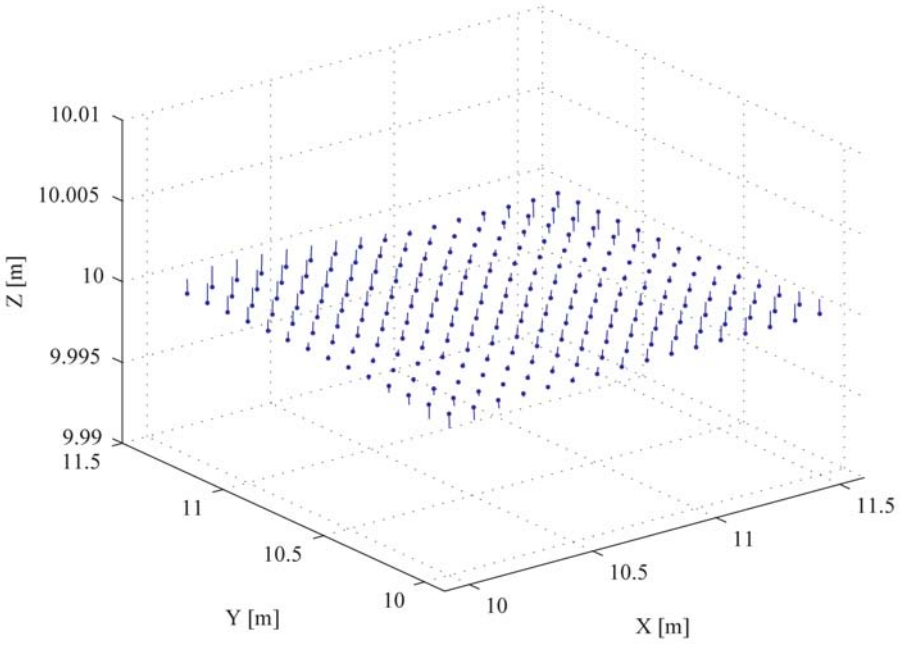

(b) Distortion vectors

Figure 6.8: Normal oblique configuration, principal point effect

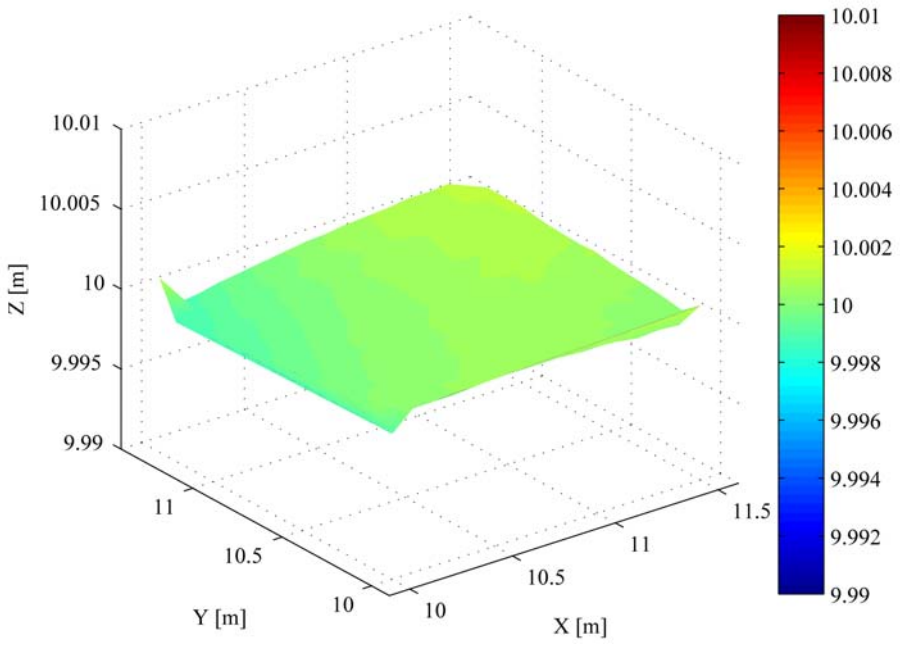

(a) Test field surface

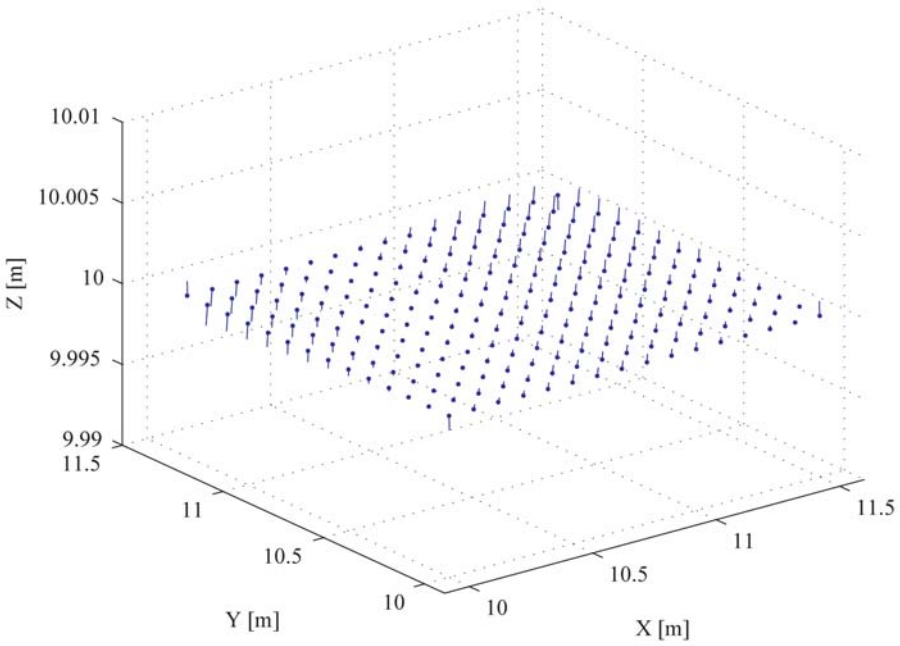

(b) Distortion vectors

Figure 6.9: Convergent oblique configuration, principal point effect

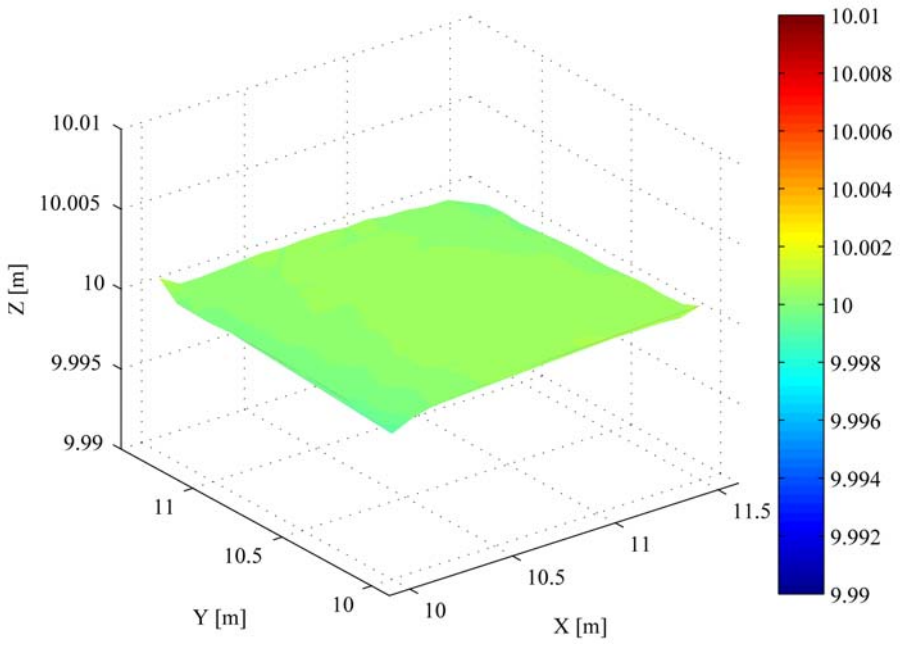

(a) Test field surface

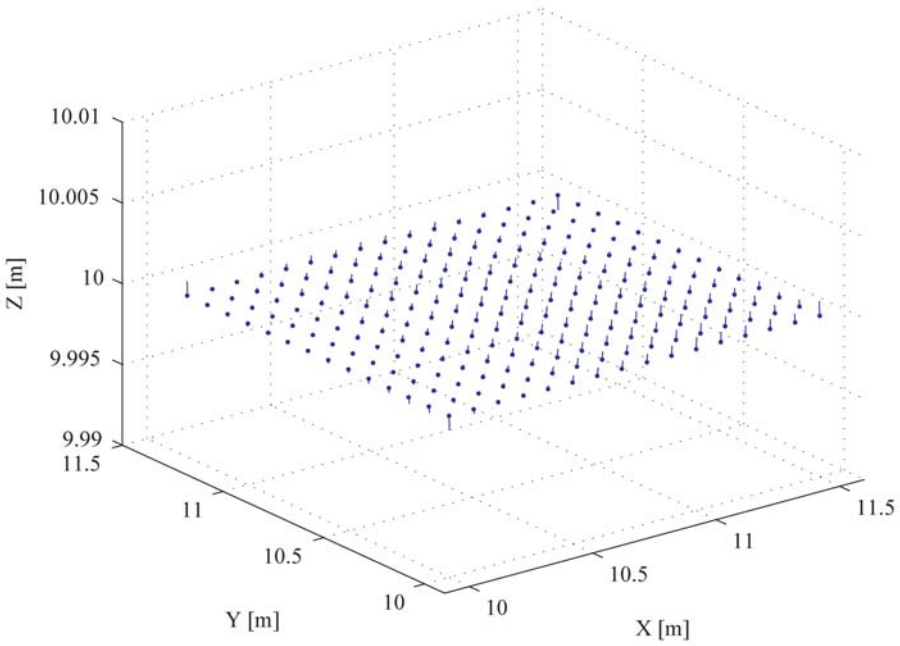

(b) Distortion vectors

Figure 6.10: Half convergent oblique configuration, principal point effect

Tests conducted using simulated data demonstrate that inaccurate principal point offset parameters disturb the achievable accuracy in the object space using highly oblique image configurations, which provide a significant depth in the object. None of these subset image configurations was capable of minimising the disturbing effects, caused by inaccurate principle point offset parameters. Further tests have to be conducted to ascertain whether an association between the parameters of the principal point offset and other image configurations, not tested in these simulations, exist and perhaps can improve the accuracy of data extracted.

6.3 Determinability of Camera Parameters

Practical tests using the Nikon Coolpix 5400 cameras and Nikon D80 cameras demonstrated the difficulty of deriving perfect lens distortion parameters through self-calibration (Chapter 3 and 4) using the calibration method described in Section 3.1.1 and Wackrow *et al.* (2007). Additional tests were conducted using simulated data to further investigate and clarify this issue.

A set of interior orientation parameters including focal length, principal point offset and k_1 to model for radial lens distortion, was introduced into the simulation (Section 3.4.1). Photo-coordinates for the X, Y, Z coordinates of the test field were determined using three sets of exterior orientation. These perfectly estimated photo-coordinates were then re-established into the external self-calibration bundle adjustment GAP (Section 2.5.4) to determine the interior and exterior orientation parameters, which were treated as unknown. The parameters introduced in the simulation could be compared with parameters estimated through self-calibration to indicate their determinability. Results of these tests are represented in Table 6.1.

The first configuration (6 calibration frames, convergent, two frames rotated) was used for basic camera calibration in Chandler *et al.* (2005), Wackrow *et al.* (2007) and Wackrow and Chandler (2008a). Discrepancies for the parameters describing the focal length and principal point offset were not a major concern.

Table 6.1: Recovered interior orientation parameters

Image Configuration	*Focal length [mm]*	*x shift [mm]*	*y shift [mm]*	k_1 $[m^{-2}]$
Introduced parameters	24.5000	0.4000	−0.3000	−107.20
Estimated using 6 frames	24.3239	0.3541	−0.1669	−102.11
Estimated using 17 frames	24.5008	0.3070	−0.1456	−103.93
Estimated using 'perfect configuration'	24.5000	0.4000	−0.3000	−107.20

When objects are recorded, which are devoid of any significant depth, these discrepancies would be compensated by modified exterior orientation parameters (Section 4.1.1) because of correlation between interior and exterior orientation, which is well established (Fraser, 1997; Granshaw, 1980; Maas, 1999). In case that an object is recorded, which is characterised by significant depth, the parameters of focal length and principal point offset could be re-estimated through on-the-job calibration to compensate for these discrepancies (Section 6.2.1 and 6.2.2). However, the discrepancy (approximately 4%) of the estimated lens distortion parameter relative to its known value remained and consequently degraded the accuracy achievable.

To examine the possibility of improving the determinability of the camera parameters, eleven additional frames were introduced, to extend the configuration (convergent, two frames rotated, large horizontal and vertical base, two object planes). Only a minor improvement was achieved in determining the camera parameters (discrepancy of the lens model approximately 3%). Such an approach is only practicable when fully automated measurement methods are available.

The 'perfect configuration', a true multi-station camera configuration (Figure 6.11) in which the camera stations were located all around a wholly transparent test field and each control point was visible from each camera station, was finally tested. As expected, the estimated interior orientation parameters were perfectly determined. However, it has to be recognised that such a configuration is clearly impracticable due to difficulties arising from target occlusion.

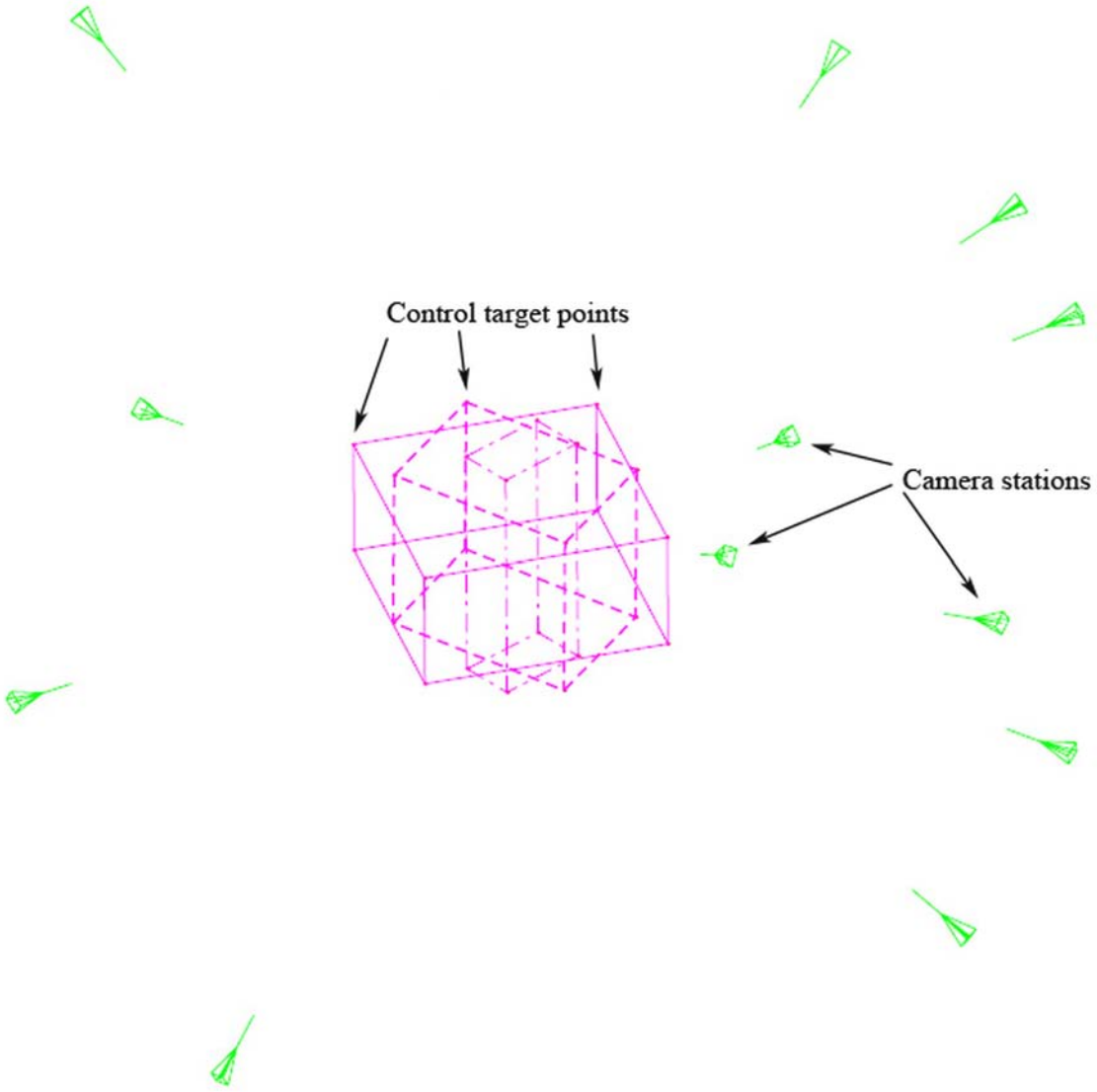

Figure 6.11: True multi-station camera configuration

These test demonstrated that only the perfect camera configuration was capable of recovering the interior orientation parameters completely. Using the practicable camera configuration, the radial lens distortion parameter was recovered to an accuracy of 96% (6 calibration frames) from its known theoretical value and has only slightly improved using the 17 frame configuration. This character-

istic is a feature of self-calibration that has been reported in Honkavaara *et al.* (2006) and Wackrow and Chandler (2008a). However, the parameters recovered using practicable configurations are certainly acceptable for measurement tasks, which require medium accuracy (Fraser, 1997). The apparent difficulty of achieving a perfect lens model through self-calibration justifies seeking an alternative approach, which was achieved in this study. By adopting a mildly convergent image configuration for DEM extraction, systematic errors arising from slightly inaccurately estimated lens model can be minimised and this improves the accuracy achievable with consumer grade digital cameras. This alternative approach represents a radical new method, which removes the need for a high accuracy lens model. For recording many objects a simple convergent camera configuration is all that is required (Section 4.2, 5.1 and 5.2).

6.4 Guidelines for accurate spatial measurement using consumer-grade digital cameras

Research conducted in this thesis has developed the potential of using consumer-grade digital cameras for more accurate spatial measurement. It has been reported that the collaboration with the English Heritage to record rock art motifs in Durham and Northumberland successfully demonstrated that with professional guidance, non photogrammetrists are capable of conducting measurement tasks using consumer-grade digital cameras (Bryan, 2007). A previously published 'guidance document' known simply as the "3 × 3 Minimum Rules for Photogrammetry" was defined by Brunner (Herbig and Waldhäusl, 1997), which helps everyone to use a camera for photogrammetry. The guidance of Brunner includes 3 main rules, which can be divided in: geometrical rules, photographical rules and organisational rules. It was judged that particularly the geometrical and photographical rules should perhaps be extended using the results of this research project.

The first step of using a consumer-grade digital camera should be focussed on deriving appropriate interior orientation parameters, particularly the lens model, because these parameters are rarely available for such type of sensors. The research presented in Section 4.1.1, 4.2.1, 4.2.2, 5.1.1, 5.2.1, 5.2.2 and 6.2 identified that the main source of systematic errors in the object space are caused by inaccurately estimated lens distortion parameters. Although the findings presented in Section 6.3 demonstrated difficulties in achieving the perfect lens model through self-calibration it should be noticed that it is well worth the effort to establish the most accurate lens model possible for a camera. A modest lens model can reduce these systematic errors to a minimum. Therefore, prior to the use for spatial measurement, consumer-grade digital cameras should be calibrated using the test field calibration method to derive an approximately lens model.

Having derived an approximate lens model for the camera lens system, the 3 geometrical rules of Brunner can be followed with the exception of using the normal case for the geometry of stereo-photography. The methodology developed in this research project (Section 3.4, 4.2, 5.1.1, 5.2.1 and 5.2.2) demonstrated that the convergent image configuration (Figure 3.15b) minimises residual systematic error surfaces caused by slightly inaccurately lens distortion parameters. There are also other benefits. The convergent configuration provides 100% overlap of image pairs and hence efficient coverage of the object. Also complex sites can be captured using "pairs" rather then in "strips", which is the traditional coverage methodology used for aerial photography. The mildly convergent image configuration is strongly recommended to describe the geometry of stereo-photography instead of using the normal case as recommended in the geometrical rules by Brunner (Herbig and Waldhäusl, 1997).

The photographical rules of Brunner explain that the interior orientation of the camera has to be constant. However, research conducted in this PhD study demonstrated that a simple stereo pair configuration is sufficient to estimate the focal length and principal point offset for a sensor through in-situ calibration (Section 2.4.2). This is particularly important if objects are to be recorded, which

are characterised by a significant depth in the object. The results presented in Section 6.2 demonstrated that extracting accurate spatial measurements from such objects, an accurate focal length and parameters describing the principal point offset are essential to extract accurate data. It is recommended to estimate the focal length and principal point offset for a camera using images captured to model the actual object through in-situ calibration.

Combining the "3 × 3 Minimum Rules for Photogrammetry" proposed by Brunner with the assumptions explained previously, guidance for accurate spatial measurement using consumer-grade digital cameras can be briefly written as follows:

1) Test field calibration to derive an appropriate lens model.

2) Provide sufficient control information for restitution (e.g. Section 5.1 and 5.2).

3) Object recording using convergent image pair configuration with an overlap of $90 - 95\%$ and if multiple image pairs are combined to mosaics (Section 5.1), an appropriate overlap between adjacent convergent image pairs can be $5 - 10\%$.

4) If depth in object, in-situ calibration to derive focal length and principal point offset.

5) Spatial measurement using digital photogrammetry, ATE.

These simple steps can provide the possibility for every lay person to use consumer-grade digital cameras for accurate spatial measurement.

6.5 Radial Distortion in Different Colour Channels

Results presented in Chapter 4 demonstrated the stability of consumer-grade digital cameras but also identified residual systematic error surfaces or domes, visible

in DEMs of difference. These are caused by slightly inaccurate estimated lens distortion parameters. The digital cameras used to conduct practical tests in this study recorded 'colour' imagery and the optical phenomenon known as chromatic aberration is an issue that arises with the use of RGB sensitive CCD sensors. Chromatic aberration causes smear effects on a photogrammetric target (white blob on black background) (Cronk *et al.*, 2006) and can cause misrepresentation of objects, detected using automated methods. Furthermore, chromatic aberration can impact on the recovery of lens distortion parameters because strictly, different radial distortion curves apply for the red, blue and green colour channels (Cronk *et al.*, 2006; Remondino and Fraser, 2006). It was therefore judged essential examine and investigate the impact of this effect further.

The effect of chromatic aberration was examined in this research using the Nikon D80 digital camera, with the focal length of the zoom lens fixed to 24mm, and the plumb-line calibration method (Section 3.1.2). Five RGB images of the laboratory test field (Figure 3.4) were captured. The red, blue and green colour channels of each image were extracted using the Photoshop software package. The radial distortion parameters (k_1, k_2) for red, blue and green channels, RGB images and greyscale images were determined. These estimated radial distortion parameters are uncorrelated to other parameters of interior and exterior orientation, an advantage of the plumb-line approach. Any discrepancies between the estimated radial distortion coefficients must therefore be attributed to chromatic aberration. The radial distortion curves achieved are represented in Figure 6.12, but differences between these distortion profiles are not identifiable using this form of representation. A more meaningful visualisation of discrepancies between these distortion curves are depicted in Figure 6.13. This figure shows variations in radial distortion for red, blue and green channels and RGB images relative to the distortion curve achieved for the greyscale images.

The profiles depicts in Figure 6.13 indicate that radial distortion in the red colour channel is largest and differs at the edge of the sensor by approximately

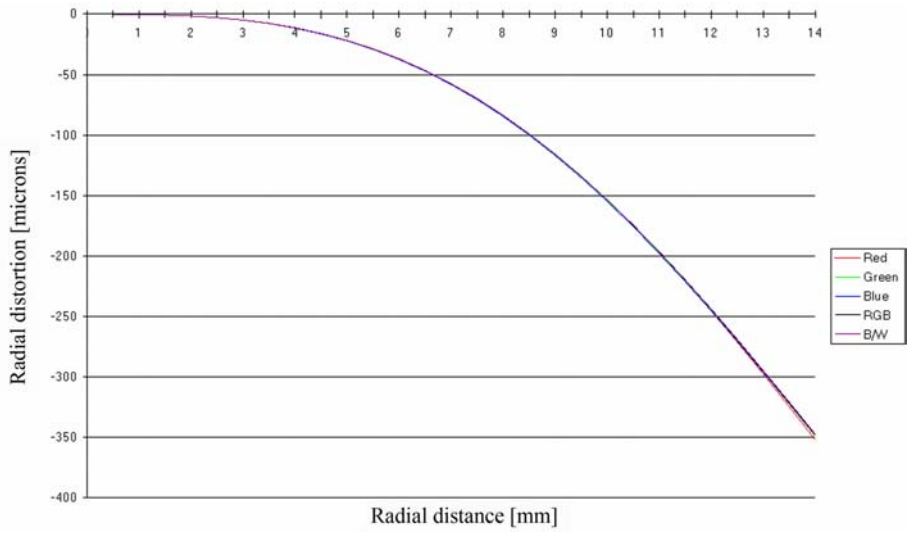

Figure 6.12: Radial distortion curves in different colour channels

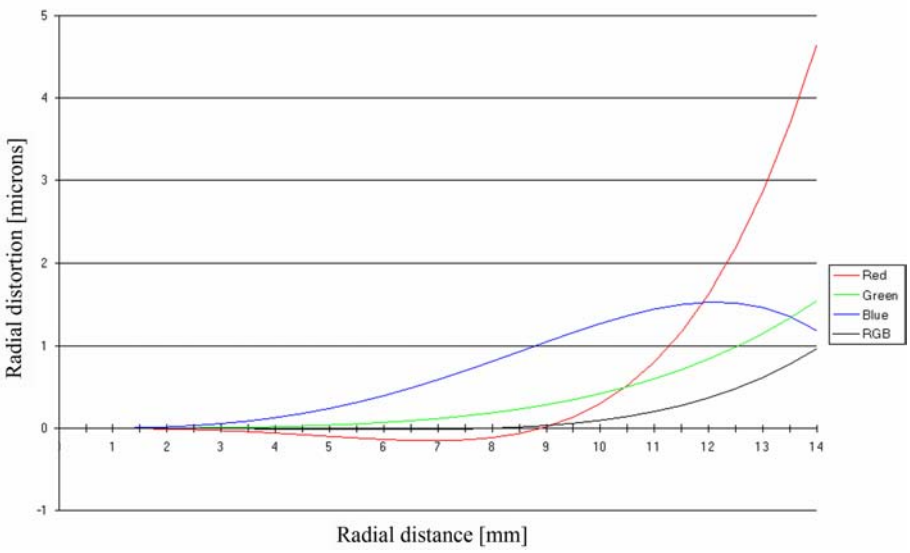

Figure 6.13: Radial distortion curves showing differences in colour channels with respect to a mean B/W curve

4.7μm (0.8 pixel) with respect to the distortion profile achieved for the greyscale images. Remondino and Fraser (2006) identified that the blue channel exhibit the largest radial distortion (10 pixel at the sensor edge) but this test was conducted using a Sony DSC F828 digital camera with a focal length of 10mm. However, these results demonstrated that different radial distortion coefficients apply for the red, blue and green channels, because of chromatic aberration. The effect is small and perhaps not significant for photogrammetric measurement applications for which medium accuracy, as defined by Fraser (1997), is required but are certainly essential for measurement tasks demanding high accuracy.

The results achieved through investigating radial lens distortion in different colour channels correspond closely with the findings in Cronk *et al.* (2006) and Remondino and Fraser (2006). If necessary, chromatic aberration can be accounted for by recording single coloured imagery through the use of an external filter (Remondino and Fraser, 2006) or by pre-processing the imagery to model this effect (Cronk *et al.*, 2006).

6.6 Quantification of Impact of Inaccuracy of the Lens Model

Research conducted in this PhD study demonstrated that slightly inaccurately estimated lens distortion parameters degrade the accuracy of data that can be extracted. The accuracy achievable can be significantly improved using a mildly convergent image configuration (Section 3.4.3, 4.2, 4.2.2, 5.1, 5.2). Quantifying the impact on accuracy in the object space, caused by the degree of imprecision of estimated radial lens distortion parameters, is difficult. However, it is worth trying to quantify even though other uncertainties are introduced.

The values of estimated distortion parameters vary for different camera-lens-systems. To describe a maximum radial distortion of, for example 500 μm for the Nikon Coolpix 5400 digital camera (wide angle zoom lens), the radial distortion

parameter k_1 would be $-2350\ m^{-2}$ whilst k_1 would only be $-107.2\ m^{-2}$ to introduce the same maximum radial distortion to the Kodak DCS460 camera (24mm fixed lens). To reduce the confusion, a percentage value was used in this study to quantify the degree of inaccuracy of radial distortion parameters for different sensors. However, this approach would describe only changes of the radial distortion parameters but it may be of more interest to quantify these discrepancies using a measure that indicates the impact of varying distortion parameters on the object with respect to the distortion profile of a lens.

The maximum radial distortion of a lens was judged to provide an appropriate measure to indicate the impact of varying radial distortion parameters on the accuracy in the object space. Simulated data (Section 3.4.1) was again generated using interior camera geometry of the Kodak DCS460 camera. The exterior orientation described both the normal and convergent image configuration, for both aerial and oblique cases. A radial distortion parameter (k_1) was identified that introduced a maximum radial distortion of 500 μm to the camera lens system. This parameter was modified so that the maximum radial distortion changed exactly in steps of $\pm 20\ \mu m$ and accuracies achieved in the object space were determined using repeated bundle adjustments. Results achieved using the normal and convergent image configuration for aerial imagery are summarised in Table 6.2 whilst Table 6.3 represents similar results achieved using the oblique case. The first column represents estimates for the radial distortion parameter k_1, the second column tabulates values of the maximum radial distortion, whilst changes of the maximum radial distortion are shown in the third column. Columns 4 to 5 represent achieved accuracies in the object space using normal and convergent image configuration.

Results correspond with the findings represented in Chapter 4 and 5. These demonstrate again that using a mildly convergent image configuration minimises the systematic error surfaces caused by inaccurate estimated lens distortion parameters for both aerial or oblique imagery. It also identifies that the impact of discrepancies of an inaccurate lens model in the object space is less significant

Table 6.2: Variation in object accuracies for differing lens models - aerial case

K_1	*Max. radial distortion*	*Variation of max. radial distortion*	*Accuracy normal case (mean error ± standard deviation)*	*Accuracy convergent case (mean error ± standard deviation)*
$[m^{-2}]$	$[\mu m]$	$[\mu m]$	*[mm]*	*[mm]*
-85.64	400	-100	3.4 ± 1.3	0.18 ± 0.05
-89.92	420	-80	2.7 ± 1.0	0.13 ± 0.04
-94.20	440	-60	2.1 ± 0.8	0.10 ± 0.03
-98.48	460	-40	1.4 ± 0.5	0.08 ± 0.03
-102.77	480	-20	0.7 ± 0.3	0.02 ± 0.03
-107.20	**500**	**0**	**0 ± 0**	**0 ± 0**
-111.33	520	20	-0.7 ± 0.3	-0.02 ± 0.03
-115.61	540	40	-1.4 ± 0.5	-0.09 ± 0.03
-119.89	560	60	-2.1 ± 0.8	-0.10 ± 0.04
-124.18	580	80	-2.8 ± 1.1	-0.14 ± 0.05
-128.64	600	100	-3.6 ± 1.3	-0.19 ± 0.05

Table 6.3: Variation in object accuracies for differing lens models - oblique case

K_1	*Max. radial distortion*	*Variation of max. radial distortion*	*Accuracy normal case (mean error ± standard deviation)*	*Accuracy convergent case (mean error ± standard deviation)*
$[m^{-2}]$	$[\mu m]$	$[\mu m]$	*[mm]*	*[mm]*
-85.64	400	-100	1.1 ± 0.5	0.02 ± 0.07
-89.92	420	-80	0.8 ± 0.4	0.02 ± 0.06
-94.20	440	-60	0.6 ± 0.3	0.02 ± 0.06
-98.48	460	-40	0.4 ± 0.2	0.01 ± 0.05
-102.77	480	-20	0.2 ± 0.1	0.01 ± 0.05
-107.20	**500**	**0**	**0 ± 0**	**0 ± 0**
-111.33	520	20	-0.1 ± 0.1	-0.04 ± 0.05
-115.61	540	40	-0.3 ± 0.2	-0.04 ± 0.05
-119.89	560	60	-0.5 ± 0.3	-0.05 ± 0.05
-124.18	580	80	-0.7 ± 0.4	-0.05 ± 0.05
-128.64	600	100	-1.0 ± 0.5	-0.05 ± 0.05

using oblique imagery compared to aerial imagery, also demonstrated in Section 5.2.1. The real value of these Tables (Table 6.2 and 6.3) is that they may be also used to assess the impact of an inaccurate lens model on accuracy in the object space for any sensor. The magnitude of change in maximum radial distortion

can be identified and then compared with correspondingly values of Table 6.2 or 6.3. Although, differing characteristics of sensors (different maximum distortion of the lens), image configurations (imaging angle for oblique imagery) and camera-to-object distances will slightly distort the accuracy statistics achieved with a different sensor, they are expected to be broadly similar in magnitude.

It is believed that the approaches described, using a percentage value of distortion parameters or the maximum radial distortion of a lens, are appropriate to quantify the degree of inaccuracy of a lens model.

6.7 Cost - Resolution - Accuracy

An active consumer market has meant that the sensor resolution of digital cameras has increased rapidly, with new ranges of 5-40 mega-pixel cameras becoming available at even lower prices. The question arises whether accuracies increase dramatically using high end sensors compared to sensors at the low end of the range, and whether the enormous price difference can be justified from a spatial measurement perspective.

Various non-metric digital cameras (Table 6.4), representing a range of sensor resolutions from 5 to 21 mega-pixel, were calibrated during this PhD study. The interior and exterior orientation parameters for each sensor were determined

Table 6.4: Calibrated non-metric digital cameras

Camera	*Resolution [Mega-pixel]*	*Lens*	*Cost [£]*
Nikon Coolpix 5400	5	built in zoom lens	240 (January 2005)
Kodak DCS460	6	24 mm fixed lens	approx. 500
Nikon Coolpix D80	10	zoom lens (18-70 mm)	700 (September 2006)
Canon EOS 1DS	21	28 mm fixed lens	5200 (February 2008)

through self-calibration, described in Section 3.1.1. Accuracy statistics for these were established using the DEM of difference methodology using the normal configuration (Section 3.2). It was thought useful to compare the accuracies achieved

against cost and so achieved accuracies in the object space for these cameras were plotted against their acquisition cost (Figure 6.14). The theoretical accuracy in the direction of the camera axis can be expressed by the standard mathematical equation (Luhmann *et al.*, 2006):

$$s_Z = \frac{h}{b} \times \frac{h}{c} s_{px'} \tag{6.1}$$

where s_Z is the accuracy in the camera direction, b is the length of the photo base, c is the focal length, h is the camera-to-object distance and $s_{px'}$ is the image precision. The theoretical accuracy for the four cameras were computed using a camera-to-object distance of 1.5 m, a photo base of 0.23 m, focal length as established in the calibration process. The typical precision of automatic image matching is around 0.1 pixel (Dowman, 2001; Pyle *et al.*, 1997). Therefore, $\frac{1}{10}$ of the pixel size for each camera was used to provide a conservative value for image precision. The theoretical accuracy of each camera was computed and is depicted in Figure 6.14. Examination revealed that none of the cameras achieved their theoretical accuracy. This was not surprising. Although accuracy statistics used in Figure 6.14 were achieved using the normal image configuration and camera parameters derived through self-calibration, these statistics were disturbed by remaining residual systematic errors caused by slightly inaccurate estimated lens distortion parameters. However, the test conducted using the Nikon D80 digital camera (Section 4.2.2) demonstrated that this camera **is** capable of achieving the theoretical accuracy when a mildly convergent image configuration is used to minimise these systematic effects (Wackrow and Chandler, 2008a). Time constraints meant that these data were not available for all sensors. Nevertheless, the experience gained in conducting this research project would suggest that they could certainly achieve their theoretical accuracy, when using a mildly convergent image configuration.

Both profiles represented in Figure 6.14 demonstrate a significant increase in accuracy for just a small rise in cost in the range from 5 to 10 mega-pixel. It also indicates that improvement in accuracy between the 10 mega-pixel camera and

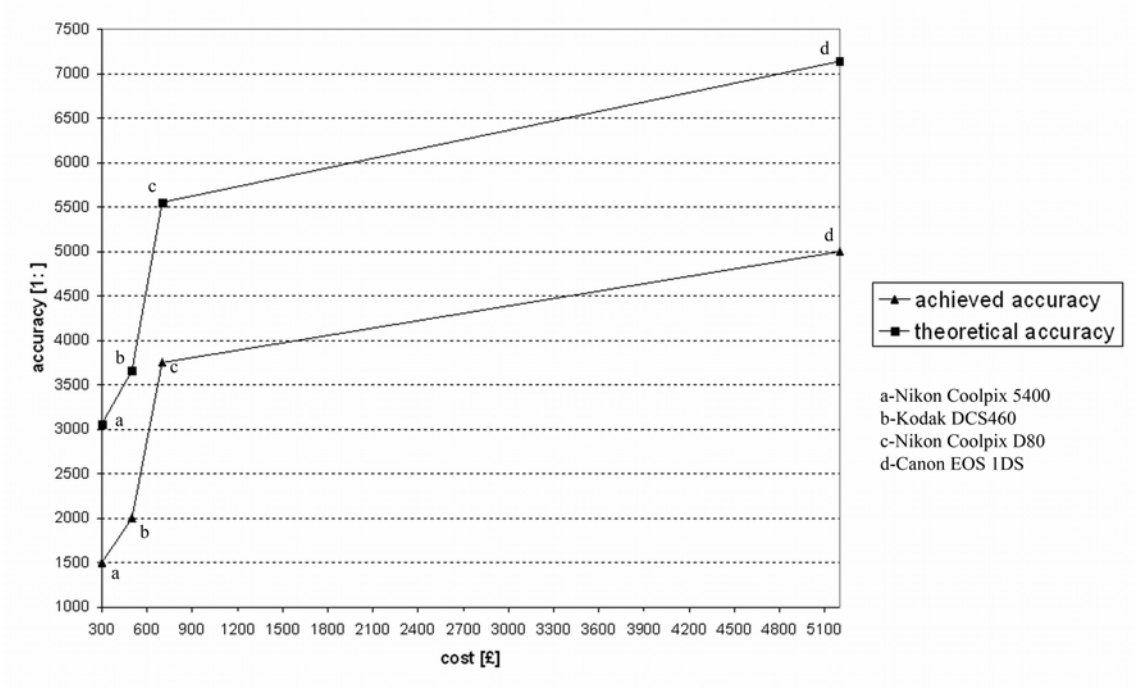

Figure 6.14: Overview of cost-accuracy-ratio of non-metric sensors

the 21 mega-pixel sensor is less significant, whilst the acquisition cost increase by a multiple. Taking an adventurous glimpse into the future, based on the sample of the four sensors tested, it is suggested that this trend may well continue. Sensor resolution will no doubt increase rapidly, but there will always be a premium price for the highest resolution at any instant of time (i.e. Hasselblad H3DII-39MS, (Hasselblad, 2008)).

The level of accuracy required for photogrammetric measurement applications should be always specified to avoid over specification and therefore unnecessary increase in costs. Using a digital sensor with a resolution of 10 mega-pixel for measurement tasks and equipping this with a lens of high chromatic and geometric quality (i.e. low chromatic aberration and minimal deviation from collinearity) could significantly improve the accuracy achievable. This could be an alternative to the attempt of improving accuracy by increasing sensor resolution and could

assist to reduce costs for photogrammetric measurement systems.

6.8 Medium versus High Accuracy - What is the Boundary?

In this study, it was difficult to evaluate the accuracy achieved in practical tests using consumer-grade digital cameras, because a clear boundary between medium and high accuracy for 3D optical measuring systems could not be identified in the literature. Existing standards to evaluate the accuracy of optical 3D measuring systems are reviewed and the difficulty of defining a boundary between medium and high accuracy is discussed.

A practical acceptance and reverification method for the evaluation of the accuracy of optical 3D measuring imaging systems based on area scanning are described in the VDI/VDE 2634 Part 2 standard. The test object and methodology used in this research project to assess the accuracy of consumer-grade digital cameras (Section 3.1.1) were developed in accordance with the VDI/VDE 2634 Part 2 standard. As recommended by Li (1988) the mean error derived for DEMs of difference (Section 2.8.3 and 3.2.3) was defined as an appropriate quality parameter in order to assess camera accuracy. However, the VDI/VDE 2634 Part 1 standard describes a practical acceptance and reverification method for the evaluation of the accuracy of optical 3D measuring image systems with point-by-point probing. The quality parameter used, is the length measurement error derived using various predefined distances on a test object. This method is also used to assess the accuracy achieved using digital sensors (Shortis *et al.*, 2006). However, this research project has identified systematic error surfaces in the object space caused by inaccurately lens distortion parameters. It was also demonstrated that these errors affect a significantly large area of the object (Section 4.2.1 and 4.2.2). The assumption can be made that the methods described in the VDI/VDE 2634 Part 1 and 2 standard may not be able to account for all systematic effects of

a measuring system, because only sample testing along measuring lines of the test volume is used to evaluate the accuracy. The methodology to evaluate the accuracy in the object space for digital sensors described in this study may be an alternative approach since it includes the analysis of the entire test object to fully detect and account for remaining systematic errors.

Although the phrases 'medium' and 'high accuracy level' are frequently used in the literature (Beyer, 1995; Fraser, 1997; Peipe, 1996), it was found to be difficult to relate the accuracies achieved for the digital sensors used in this study (Section 6.7) to these accuracy levels. The incorrect use of the phrases precision (Section 2.8.1) and accuracy (Section 2.8.3) in the literature causes confusion. For example, Fraser (1997) defines that a medium accuracy level for close range photogrammetry may be achieved when an object space triangulation **accuracy** of 1:100000 is attained, using close range digital camera self-calibration. Following Fraser (1997), an object space triangulation **accuracy** of 1:250000 would describe a 'high accuracy' level for close range photogrammetry. However, strictly speaking the phrase 'object space triangulation **precision**' should be used instead, which can provide an initial indication of the anticipated accuracy of triangulated object point coordinates (Fryer *et al.*, 2007). Precision and accuracy are only equivalent if the measuring system is free of systematic errors. This can be achieved if a fully calibrated metric camera with stable interior orientation is used for close range photogrammetric measurement (Fryer *et al.*, 2007). Using consumer-grade digital cameras for spatial measurement, a clear distinction between precision and accuracy is necessary. This would avoid confusion and then provide useful measures necessary to assess and compare accuracies in the object space achieved with non-metric digital sensors.

A clear boundary between medium and high accuracy for close range photogrammetric applications using consumer-grade digital cameras could not be identified in the literature. The limits for quality parameters used to assess the accuracy of a measuring system are likely to be specified by the manufacturer and the user, respectively (VDI/VDE 2634 Part 2). This can explain the difficulty

in defining a strict boundary between accuracy levels. The boundary separating medium and high accuracy with respect to recording rock-art motifs may be specified to 1:3,000 using simple stereo-pair image configurations. However, the required accuracy of a measuring system in the field of medical photogrammetry using a convergent, multi-station photogrammetric network may be far beyond 1:3,000 and the limit specified to separate medium from high accuracy varies respectively. This explains the difficulty of identifying a general boundary separating medium and high accuracy across various photogrammetric measurement applications. It also indicates the importance of carefully specifying the accuracy level required for individual measurement tasks. If specified, this would avoid confusion, over specification and unnecessary measurement costs.

6.9 Summary

This chapter took the opportunity to examine the external disturbing effects on camera stability, using the Nikon Coolpix 5400 digital cameras as an exemplar. It also identified that these external disturbing effects are not significant for the geometric stability of consumer grade digital cameras. The only caveat would be examining these cameras under extreme temperature, which could be an interesting task for further research.

The impact of inaccuracy of the focal length and principal point offset was investigated using simulated data. The simulation demonstrated that systematic errors caused by an inaccurate estimate for the focal length are significant if oblique imagery is used. Surprisingly, these can be minimised using a half convergent oblique image configuration but this is generally impracticable, because using the view finder of a camera to achieve such a configuration is difficult. A similar approach was used for investigating variations of the principal point offset but concluded that none of the image configurations tested can minimise the disturbing systematic effects. However, the focal length and principal point offset can readily be estimated through on-the-job calibration method.

This study demonstrated difficulties in recovering accurate lens distortion parameters through self-calibration, which caused residual systematic errors in data that can be extracted. This issue was further investigated (Section 6.3) using simulation. Results demonstrated that only the perfect configuration was capable of recovering the interior orientation of a sensor fully. The uncertainty in deriving an impeccable lens model justified seeking an alternative approach, which culminates in the simple methodology of adopting a mildly convergent image configuration for DEM extraction to minimise these error surfaces.

The optical phenomenon known as chromatic aberration was a concern since RGB sensitive CCD sensors were solely used during this research project. This effect was investigated using imagery acquired using the Nikon D80 digital camera and the plumb-line calibration approach. Radial distortion curves for red, blue and green channels and RGB images were compared with a distortion curve derived using greyscale images. Results demonstrated that although slightly different distortion profiles apply for different colour channels, these discrepancies are not significant. This is certainly the case for photogrammetric measurements requiring medium accuracy but should be considered if tasks demand the highest accuracy.

Quantifying the degree of imprecision of radial distortion parameters was identified to be difficult since estimates for these vary significantly for different class of sensors. The variation of radial distortion parameters was initially quantified using percentage values, which proved to be appropriate. However, quantifying discrepancies of these parameters by relating their variation to changes of the maximum radial distance provides a more useful alternative approach. Such statistics were computed for the Kodak DCS460 digital camera (Tables 6.2 and 6.3). These tables could be used to quantify the discrepancies arising from inaccurate lens distortion parameters, and to quantify achievable accuracies in the object space for any sensor.

Finally, the acquisition cost of four digital cameras, representing a range of sensor resolution from 5 to 21 mega-pixel, were compared against the accuracy

achieved during the practical tests and compared with their theoretical accuracy. This indicated that the ratio of improvement in accuracy to increase in cost does not behave in a linear way. Analysing the level of accuracy required for photogrammetric measurement tasks, prior to purchasing a digital sensor was identified to be crucial to avoid any unnecessary increase in expenditure.

CHAPTER 7

Conclusion

This study explored the value of consumer-grade digital cameras to conduct spatial measurements. The internal geometry of consumer-grade digital cameras should be considered unstable since these have not been designed for spatial measurement. The photogrammetric potential of consumer-grade digital cameras has been frequently reported in the literature, because their uncertain geometry can be partially resolved by calibration. However, their temporal stability and manufacturing consistency remain unknown and has been reported less frequently. The review of literature revealed an absence of a standard for quantitative analyses of camera stability, which justified seeking an appropriate method to assess the geometric stability of consumer-grade digital cameras. The initial project aim was identified: *'assess the temporal stability and manufacturing consistency of a typical consumer-grade digital camera'*. The need to calibrate seven identical Nikon Coolpix 5400 digital cameras provided the opportunity to determine the temporal stability and manufacturing consistency of a typical sensor, which culminated in accomplishing the initial aim of this study.

The work conducted to assess the geometric stability of consumer-grade digital cameras also identified remaining residual systematic error surfaces or domes, which are discernable in digital elevation models. An additional project aim was formulated as: *'investigate, clarify and minimise remaining residual systematic*

error surfaces in digital elevation models'. If accomplished, this would suggest that the accuracy obtainable with non-metric digital sensors can be effectively improved.

Various achievements were obtained in the course of carrying out research to satisfy the main aims of this project, which are summarised in the subsequent section.

7.1 Achievements of this Research Project

The achievements of this research project can be summarised as follows:

- Development of a Matlab routine for automatic object detection and measurement.

A developed Matlab routine (Appendix A) was successfully developed, which automatically identifies and measures the centre of object features located along straight lines using multiple images. This script also provides appropriate data suitable for direct input to an external Fortran code, which uses the plumb-line calibration approach to compute radial and tangential distortion parameters. An advantage of this algorithm is its inherent flexibility, to estimate lens models for digital sensors at various (close to medium range) camera to object distances using diverse types of test fields (Figure 3.4 and 3.5). The output includes parameters for radial and tangential distortion with their statistical properties as well as computed distortion values for a range of radial distances. This provides the opportunity to transfer derived distortion parameters for a camera into software packages used for image processing and digital photogrammetry.

- Development of a methodology to assess the temporal stability and manufacturing consistency of consumer-grade digital cameras.

The degree of similarity between sets of interior orientation parameters was evaluated by analysing accuracies in the object space achieved using consumer-grade

digital cameras. Automatically extracted DEMs derived using camera data representing a flat and planar test field were compared with the 'Truth DEM' by interpolation and substraction. The 'Truth DEM' represented the real geometry of the test field. The derived DEMs of difference represented elevation differences between the truth and automatically extracted surface representations. Mean error and standard deviation of DEMs of difference were derived using an Erdas Graphical Model and these statistics provide appropriate measures to assess the accuracy in the object space achieved with digital sensors. Digital cameras can be considered consistent from a temporal and manufacturing perspective if a similar accuracy level in the object space is achieved using sets of IOP derived in various calibration sessions. Comparing these accuracy levels then reveal their stability over time and assesses manufacturing consistency.

- Assessment of geometric stability and manufacturing consistency of consumer-grade digital cameras.

The temporal stability and manufacturing consistency of seven identical Nikon Coolpix 5400 digital cameras were assessed successfully over a 1-year period using the described methodology. Results demonstrate a high degree of temporal stability and remarkable manufacturing consistency for this type of digital camera. This finding is significant, as it implies that consumer-grade digital cameras are capable of maintaining their internal geometry over time, based on the sample of seven cameras of one type. This study identified that such digital cameras are suitable for many spatial measurement applications, requiring medium accuracy level. However, tests conducted to assess the stability of these cameras have also identified remaining residual systematic error surfaces (domes), discernable in DEMs.

- Using simulated data to verify the theory that attributes domes in DEMs to an inaccurately estimated lens model.

The literature demonstrated that these domes have been noted in past work and a theoretical proof explaining them was given by Fryer and Mitchell (1987). It appears that any uncorrected residual x parallaxes create a systematic offset in computed elevations, causing a flat object to appear curved. Tests were conducted using simulated data to confirm this finding and demonstrated that these domes are certainly caused by inaccurately estimated radial lens distortion parameters.

- Using simulated data to investigate the determinability of radial distortion parameters through self-calibration.

Practical tests, conducted in this study using consumer-grade digital cameras, demonstrated the difficulty of recovering **perfect** radial lens distortion parameters through a self-calibrating bundle adjustment. This issue was further investigated using simulated data and demonstrated that recovered radial distortion parameters differed slightly from their theoretical values. This characteristic is a feature of self-calibration, which is recognised and has been reported in the literature. Only the 'perfect configuration' (Figure 6.11) is capable of fully recovering parameters of interior orientation, but this configuration is generally impracticable (Section 6.3). The practical difficulty involved in deriving a completely accurate lens model for consumer-grade digital cameras justified searching for an alternative approach to minimising remaining systematic error surfaces. Another possibility to improve the estimation of lens distortion parameters can be achieved by applying the distortion correction iteratively. The corrected image position of each particular iteration is utilised as the starting point for the following correction value calculation. The iterative process is continued until the computed correction is insignificant (Luhmann *et al.*, 2006).

- Minimisation of residual systematic error surfaces in digital elevation models, caused by inaccurately estimated lens distortion parameters.

A stereopair configuration, in which the camera base is parallel to the object plane and where the optical axes of the cameras intersect the object plane orthogonally,

is known as the photogrammetric normal case. This configuration remains important when using automated DEM extraction software. It was hypothesised that modifying this image configuration could perhaps minimise the remaining domes in DEMs. Simulated data were used to investigate various image configurations systematically. Results of these simulations identified that a mildly convergent image configuration minimises residual systematic error surfaces, caused by inaccurately estimated lens distortion parameters.

- Confirming that a mildly convergent image configuration minimises residual systematic error surfaces in DEMs by conducting two case studies.

Two case studies were used to verify the methodology developed, which minimises remaining residual systematic error surfaces in DEMs. The first case study was conducted to measure a flume bed surfaces in a semi-controlled environment using aerial imagery. The second case study was conducted to measure a dynamic water surface, which also supported the development of a measuring system to model the topographic surface of a running river. The need to use oblique imagery in the second case provided the opportunity to demonstrate the flexibility of the developed methodology, since oblique image configurations are often used in close range photogrammetry. Results achieved in both case studies demonstrated that a mildly convergent image configuration minimises disturbing effects, caused by inaccurately estimated lens distortion parameters. This finding is significant for DEM generation using consumer-grade digital cameras, since this reduces the need for establishing an highly accurate lens model through conventional calibration methods.

- Developed guideline, which provide new opportunities for spatial measurements using consumer grade digital cameras.

A step by step guidance (Section 6.4) was developed, which includes 4 main rules: calibration of digital cameras, providing sufficient control information for

image restitution, object recording and spacial measurement using photogrammetry. Following these main rules allows non experts to use non-metric digital cameras for wider applications of spatial measurements, e.g. surface roughness, body/sports measurements or medical imaging.

7.2 Recommendations for Future Work

Additional work could extend the investigation on the stability of consumer-grade digital cameras by exposing such sensors to extreme temperature values. In addition, using non-metric digital cameras in a high altitude environment may also affect the validity of interior orientation parameters, determined near sea level. These tests would reveal if consumer-grade digital cameras are capable of maintaining their internal geometry under more challenging environmental conditions, possibly expanding the field of applications further.

Stability analyses were conducted in this research project using a single camera to object distance of approximately 1.5 m. An additional study is perhaps needed to analyse the stability of non-metric digital cameras using a more extensive range of camera to object distances. This would perhaps increase the flexibility of object recording using such cameras when interior orientation parameters estimated are valid for different camera to object distances.

This PhD project reported uncertainties in determining perfect radial lens distortion parameters for consumer-grade digital cameras through self-calibration. These discrepancies can degrade the accuracy achievable with non-metric cameras. Although a methodology was developed in this study that minimises such systematic effects, comparing the precision of radial distortion parameters of a digital camera established through self-calibration using different camera calibration software, such as Photomodeller, STARS, LPS, VMS and Eye Witness could assist in revealing the ultimate solution for camera self-calibration.

Finally, the potential of a mildly convergent image configuration to minimise residual systematic errors in DEMs was demonstrated in this research using a

stereopair for DEM generation. An additional study is needed to investigate a multi-station camera configuration for DEM extraction, in which the cameras are positioned around a flat object and the optical axes of the cameras intersect the object plane at the same point. Unfortunately, almost all of the available software package (LPS, PI-3000, PhotoModeler) provide only the possibility of using a stereo-pair for DEM generation. However, the ETH image matching package (SAT-PP) provides a surface generation tool using multiple convergent imagery (Remondino and Menna, 2008). Using imagery recorded with the multi-station camera configuration described previously combined with the ETH image matching package, the accuracy in the object space achievable with non-metric digital cameras could be further increased.

7.3 Final Comment

The finding, established in this research project, that a convergent image configuration minimises systematic errors in DEMs suggests that a new approach to increasing the accuracy of optical 3D measurement systems should be adopted. Instead of concentrating solely on camera calibration, the focus should be on image configuration. This also opens up new opportunities and the wider applications of spatial measurement using consumer-grade digital cameras.

References

Ackermann, F., Ebner, H. and Klein, H. (1970). Ein Rechenprogramm für die Streifentriangulation mit unabhängigen Modellen. *Bildmessung und Luftbildwesen*, Heft **4**/1970, 206–217.

Ahmad, A. and Chandler, J.H. (1999). Photogrammetric capabilities of the Kodak DC40, DCS420 and DCS460 digital cameras. *Photogrammetric Record*, **16**(94), 601–615.

Barnett, T. (2006). *Northumberland and Durham Rock Art Project*. http://pscm.northumberland.gov.uk/pls/portal92/docs/2091.pdf [Accessed: 9th November 2007].

Beyer, H.A. (1995). Quality control in industry with digital photogrammetry. *Optical 3-D Measurement Techniques III* (Ed. A. Grün and H. Kahmen), Wichmann, Heidelberg, 29-38.

Bosch, R., Külür, S. and Gülch, E. (2005). Non-metric camera calibration and documentation of historical buildings. *CIPA XX International Symposium*, 142–147.

Bouguet, J.Y. (2000). *Camera calibration toolbox for Matlab*. http://www.vision.caltech.edu/bouguetj/calib_doc/index.html [Accessed: 27th September 2007].

Brown, D.C. (1956). The simultaneous determination of the orientation and lens distortion of a photogrammetric camera. *RCA data Reduction Technical Report*, No:**33**.

Brown, D.C. (1971). Close-range camera calibration. *Photogrammetric Engineering*, **37**(8), 855–866.

Brown, D.C. (1972). Calibration of close range cameras. *Photogrammetric Engineering*, **19**(5), 26 pages.

Brown, D.C. (1976). The bundle adjustment - progress and prospects. *Photogrammetric Engineering*, **21**(3), 1–33.

Brown, D.C. (1982). Stars, a turnkey system for close range photogrammetry. *International Archives of Photogrammetry and Remote Sensing*, **24**(1), 68–87.

Brown, D.C. and Dold, J. (1995). V-STARS - A system for digital industrial photogrammetry. *Optical 3-D Measurement Techniques III* (Ed. A. Grün and H. Kahmen), Wichmann, Heidelberg, 12-21.

Bryan, P. (2007). Personal communication at the RSPSoc annual conference, 11th to 14th September 2007.

Burrough, P.A. and Goodchild, M.F. (1998). *Principles of Geographical Information Systems*, Oxford University Press, Oxford. 333 pages.

Chandler, J.H. (1989). *The acquisition of spatial data from archival photographs and their application to geomorphology*. Ph.D. thesis, Department of Civil Engineering, City University London. 300 pages.

Chandler, J.H. and Clark, J.S. (1992). The archival photogrammetric technique: further applications and development. *Photogrammetric Record*, **14**(80), 241–247.

Chandler, J.H. and Padfield, C.J. (1996). Automated digital photogrammetry on a shoestring. *Photogrammetric Record*, **15**(88), 545–559.

Chandler, J.H., Shiono, K., Rameshwaren, P. and Lane, S.N. (2001). Measuring flume surfaces for hydraulics research using a Kodak DCS460. *Photogrammetric Record*, **17**(97), 39–61.

Chandler, J.H., Buffin-Belanger, T., Rice, S., Reid, I. and Graham, D.J. (2003). The accuracy of river bed moulding/casting system and the effectiveness of a low-cost digital camera for recording river bed fabric. *Photogrammetric Record*, **18**(103), 209–223.

Chandler, J.H., Fryer, J.G. and Jack, A. (2005). Metric capabilities of low-cost digital cameras for close range surface measurement. *Photogrammetric Record*, **20**(109), 12–26.

Chandler, J.H., Bryan, P. and Fryer, J.G. (2007). The development and application of a simple methodology for recording rock art using consumer-grade digital cameras. *Photogrammetric Record*, **22**(117), 10–21.

Chandler, J.H., Wackrow, R., Sun, X., Shiono, K. and Rameshwaran, P. (2008). Measuring a dynamic and flooding river surface by close range digital photogrammetry. *XXI ISPRS Congress, Beijing 2008*.

Clarke, T.A. and Fryer, J.G. (1998). The development of camera calibration methodes and models. *Photogrammetric Record*, **16**(91), 51–66.

Clarke, T.A., Wang, X. and Fryer, J.G. (1998). The principal point and CCD cameras. *Photogrammetric Record*, **16**(92), 293–312.

Cooper, M.A.R. and Cross, P.A. (1988). Statistical concepts and their application in photogrammetry and surveying. *Photogrammetric Record*, **12**(71), 637–663.

Cooper, M.A.R. and Robson, S. (2001). Theory of close range photogrammetry. *Close range photogrammetry and machine vision* (Ed. K.B. Atkinson), Whittles, Caithness. 371 pages.

Cronk, S., Fraser, C. and Hanley, H. (2006). Automated metric calibration of colour digital cameras. *Photogrammetric Record*, **21**(116), 335–372.

Dold, J. and Peipe, J. (1995). High resolution data acquisition to observe moving objects. *International Archives of Photogrammetry and Remote Sensing*, **30**(5W1), 36–39.

Dowman, I.J. (2001). Fundamentals of digital photogrammetry. *Close range photogrammetry and machine vision* (Ed. K.B. Atkinson), Whittles, Caithness. 371 pages.

Erdas Inc. (2003). *Leica Photogrammetry Suite Orthobase & Orthobase Pro User's guide*, Leica Geosystems and GIS & Mapping, LLC, Atlanta. 516 pages.

Fraser, C.S. (1982). Film unflatness effects in analytical non-metric photogrammetry. *International Archives of Photogrammetry and Remote Sensing*, **24**(5), 156–166.

Fraser, C.S. (1997). Digital camera self-calibration. *ISPRS Journal of Photogrammetry & Remote Sensing*, **52**(1997), 149–159.

Fraser, C.S. and Brown, D.C. (1986). Industrial photogrammetry - new developments and recent applications. *Photogrammetric Record*, **12**(68), 197–217.

Fraser, C.S., Shortis, M.R. and Ganci, G. (1995). Multi-sensor system self-calibration. *Videometrics IV. SPIE*, vol. 2598, 2–18.

Fraser, C.S., Woods, A. and Brizzi, D. (2005). Hyper redundancy for accurate enhancement in automated close range photogrammetry. *Photogrammetric Record*, **20**(111), 205–217.

Fryer, J.G. (2001a). Camera calibration. *Close range photogrammetry and machine vision* (Ed. K.B. Atkinson), Whittles, Caithness. 371 pages.

Fryer, J.G. (2001b). Introduction. *Close range photogrammetry and machine vision* (Ed. K.B. Atkinson), Whittles, Caithness. 371 pages.

Fryer, J.G. and Brown, D.C. (1986). Lens distortion for close-range photogrammetry. *International Archives of Photogrammetry and Remote Sensing*, **52**(1), 51–58.

Fryer, J.G. and Fraser, C.S. (1986). On the calibration of underwater cameras. *Photogrammetric Record*, **12**(67), 73–85.

Fryer, J.G. and Mitchell, H.L. (1987). Radial distortion and close range stereophotogrammetry. *Australian Journal of Geodesy, Photogrammetry and Surveying*, **46/47**, 123–138.

Fryer, J.G., Chandler, J.H. and Cooper, M.A.R. (1994). On the accuracy of heighting from aerial photographs and maps: implications to process modellers. *Earth Surface Processes and Landforms*, **19**, 577–583.

Fryer, J.G., Mitchell, H. and Chandler, J.H. (2007). *Applications of 3D Measurement from images*, Whittles, Caithness. 384 pages.

Granshaw, S.I. (1980). Bundle adjustment methods in engineering photogrammetry. *Photogrammetric Record*, **10**(1), 181–207.

Gruen, A. (2001a). Development of digital mehtodology and systems. *Close range photogrammetry and machine vision* (Ed. K.B. Atkinson), Whittles, Caithness. 371 pages.

Gruen, A. and Beyer, A.H. (2001b). Calibration and orientation of cameras in computer vision. *System calibration through self-calibration,* Volume 34 (Eds. A. Gruen and T. S. Huang), Springer, Heidelberg, 34, 163-193.

Gugan, D.J. (1989). Future trends in photogrammetry. *Photogrammetric Record*, **13**(73), 79–84.

Habib, A. and Morgan, M. (2005). Stability analyses and geometric calibration of off-the-shelf digital cameras. *International Archives of Photogrammetry and Remote Sensing*, **71**(6), 733–741.

Habib, A., Pullivelli, A., Mitishita, E., Ghanma, M. and Kim, E.M. (2006). Stability analyses of low-cost digital cameras for aerial mapping using different georeferencing techniques. *Photogrammetric Record*, **21**(113), 29–43.

Hasselblad (2008). *Hasselblad H3DII-39MS*. http://www.hasselblad.co.uk/promotions/h3d-ii.aspx [Accessed: 12th June 2008].

Heikkilä, J. and Silvén, O. (1997). A four-step camera calibration procedure with implicit image correction. *Proceedings of the 1997 Conference on Computer Vision and Pattern Recognition (CVPR '97)*, 1106–1112.

Herbig, U. and Waldhäusl, P. (1997). APIS - Architectural photogrammetry information system. *International Archives of Photogrammetry and Remote Sensing*, **XXXII**(5C1B), 23–27.

Honkavaara, E., Ahokas, E., Hyyppä, J., Jaakkola, J., Kaartinen, H., Kuittinen, R., Markelin, L. and Nurminen, K. (2006). Geometric test field calibration of digital photogrammetric sensors. *ISPRS Journal of Photogrammetry and Remote Sensing*, **60**(6), 387–399.

Hottier, P. (1976). Accuracy of close range analytical solutions. *Photogrammetric Engineering & Romote Sensing*, **42**(3), 345–375.

Kenefick, J.F., Gyer, M.S. and Harp, B.F. (1972). Analytical self calibration. *Photogrammetric Engineering*, **38**, 1117–1126.

Kraus, K. (1994). *Photogrammetrie* (Band 1, Auflage 5), Dümmler, Bonn. 395 pages.

Lerma, J.L. and Cabrelles, M. (2007). A review and analyses of plumb-line calibration. *Photogrammetric Record*, **22**(118), 135–150.

Li, Z. (1988). On the measure of digital terain model accuracy. *Photogrammetric Record*, **12**(72), 873–877.

Lichti, D.D. and Chapman, M.A. (1997). Constrained FEM self-calibration. *Photogrammetric Engineering & Romote Sensing*, **63**(9), 1111–1119.

Lillesand, T.M. and Kiefer, R.W. (1994). *Remote Sensing and Image Interpretation*, John Wiley & Sons, New York. 750 pages.

Luhmann, T., Robson, S., Kyle, S. and Harley, I. (2006). *Close Range Photogrammetry*, Whittles, Caithness. 510 pages.

Maas, H.G. (1999). Ein Ansatz zur Selbstkalibrierung von Kameras mit instabiler inner Orientierung. *Publikationen der Deutschen Gesellschaft für Photogrammetrie und Fernerkundung,* Band 7 (Eds. J. Albertz and S. W. Dech), Weinert, Berlin. 496 pages.

Magill, A. (1955). Variation in distortion with magnification. *Journal of Research of the National Bureau of Standards*, **54**(3), 135–142.

Mills, J.P., Schneider, D., Barber, D.M. and Bryan, P.G. (2003). Geometric assessment of the Kodak DCS Pro Back. *Photogrammetric Record*, **18**(103), 193–208.

Miyatsuka, Y. (1996). Archaeological real-time photogrammetric system using digital still camera. *International Archives of Photogrammetry and Remote Sensing*, **31**(B5), 374–377.

Peipe, J. (1996). Photogrammetric investigation of a 3000 x 2000 pixel high resolution still video camera. *International Archives of Photogrammetry and Remote Sensing*, **31**(B5), 471–474.

Petrie, G. and Kennie, T.J.M. (1990). *Terrain modelling in surveying and civil engineering*, Whittles Publishing in assosiation with Thomas Telford Ltd, Caithness. 351 pages.

Pyle, C.J., Richards, K.S. and Chandler, J.H. (1997). Digital photogrametric monitoring of river bank erosion. *Photogrammetric Record*, **15**(89), 753–764.

Remondino, F. and Fraser, C.S. (2006). Digital camera calibration methods: considerations and comparisons. *International Archives of Photogrammetry, Remote Sensing and Spatial Information Science*, **36**(5), 266–272.

Remondino, F. and Menna, F. (2008). Image-based surface measurement for close-range heritage documentation. *The International Archives of the Photogrammetry, Remote Sensing and Spatial Information Sciences*, vol. XXXVII, Part B5, 199–206.

Schneider, C.T. (1996). DPA-WIN - a PC based digital photogrammetric station for fast and flexible on-site measurement. *International Archives of Photogrammetry and Remote Sensing*, **31**(B5), 530–533.

Shepard, D.C. (1968). A two-dimensional interpolation function for irregulary spaced data. *23rd National Conference ACM*, 517–524.

Shortis, M.R., Robson, S. and Beyer, H.A. (1998). Principle point behaviour and calibration parameter models for Kodak DCS cameras. *Photogrammetric Record*, **16**(92), 165–186.

Shortis, M.R., Bellman, C.J., Robson, S., Johnston, G.J. and Johnson, G.W. (2006). Stability of zoom and fixed lenses used with digital SLR cameras. *IAPRS*, vol. XXXVI, Part 5, 285–290.

Stojic, M., Chandler, J.H., Ashmore, P. and Luce, J. (1998). The assessment of sediment transport rates by automated digital photogrammetry. *Photogrammetric Engineering & Remote Sensing*, **64**(5), 387–395.

TOPCON (2007). *PI-Calib: camera calibration software (30 day trail).* http://www.terrageomatics.com/index.php?option=com_content&task=view&id=43&Itemid=129 [Accessed: 1st October 2007].

WACKROW, R. AND CHANDLER, J.H. (2007). A convergent image configuration for DEM extraction that minimises the systematic effects caused by an inaccurate lens model. *Proceedings of the 2007 Annual Conference of the Remote Sensing & Photogrammetry Society*, TS 4.

WACKROW, R. AND CHANDLER, J.H. (2008a). A convergent image configuration for DEM extraction that minimises the systematic effects caused by an inaccurate lens model. *Photogrammetric Record*, **23**(121), 6–18.

WACKROW, R. AND CHANDLER, J.H. (2008b). Minimising systematic errors in DEMs caused by an inaccurate lens model. *XXI ISPRS Congress, Beijing 2008*.

WACKROW, R., CHANDLER, J.H. AND BRYAN, P. (2007). Geometric consistency and stability of consumer-grade digital cameras for accurate spatial measurement. *Photogrammetric Record*, **22**(118), 121–134.

WOLF, P.R. AND DEWITT, B.A. (2000). *Elements of Photogrammetry* (3rd Edition), McGraw-Hill, London. 663 pages.

ZHENG, Z. AND WANG, X. (1992). A gerneral solution of a closed-form space resection. *Photogrammetric Engineering & Remote Sensing*, **58**(3), 327–338.

ZHIZHUO, W. (1990). *Principles of Photogrammetry (with Remote Sensing)*, Publishing House of Surveying and Mapping, Beijing. 575 pages.

APPENDIX A

Matlab code

Listing A.1: **blob sort plumb**

```
% Authors: Rene Wackrow
% Last modified: 20/02/2007
% Version:1.2

clear, close all

%*********************************************************
%                   PARAMETER TO EDIT                    *
%*********************************************************

%set values for input.plm
%-------------------------------------------------------
standard_x_y=[0.002   0.002]; %standard deviation for image coordinates
estimates_p1_p2_k1_k2_k3=[0.0   0.0   0.0   0.0   0.0]; %initial estimates for
    distortion coefficient
standard_p1_p2_k1_k2_k3=[0.1E-20 0.1E-20 0.1E-2 0.1E-2 0.1E-20]; %standard
    deviation for distortion coefficient

%pixel size in [mm] and resolution in [pixel] of camera
%-------------------------------------------------------
sizex = 0.006095;
sizey = 0.006095;
resox = 3872;
resoy = 2592;

%threshold for objects, lines and columns
%-------------------------------------------------------
tresh_disk=7.6;
```

```
tresh_lines=0.3;
tresh_column=0.8;
tresh_ecc=0.80;

%number of images to process
%-----------------------------------------------------------
num_im=3;

%*********************************************************
%                    MAIN PROGRAM                        *
%*********************************************************

%open output file
%-----------------------------------------------------------
plumb = fopen('F:\Matlab_development\d80_plumbline_medium_range\medium_range\
    plumb.dat','w');
inp = fopen('F:\Matlab_development\d80_plumbline_medium_range\medium_range\input
    .plm','w');
fid = fopen('F:\Matlab_development\d80_plumbline_medium_range\medium_range\row.
    temp','w');
fid_1 = fopen('F:\Matlab_development\d80_plumbline_medium_range\medium_range\
    column.temp','w');

all_rows=0;
all_column=0;
helpplumbprint=0;

%read image
%-----------------------------------------------------------
for pic=1: num_im
    pics=dir('*.jpg');
    nameonly=char([pics(pic).name]);
    I=imread(nameonly);

A = im2double(I);
figure, imshow(A), title(nameonly);

%convert image and label objects
%-----------------------------------------------------------
A=255-A; %**do not invert image for the lab test field****

background = imopen(A,strel('disk',20));
%figure, imshow(background), title('background');

I2 = imsubtract(A,background);
%figure, imshow(I2)

level = graythresh(I2);
```

```
bw = im2bw(I2,level);
figure, imshow(bw), title('grey-scaled');

horizontalKernel = fspecial('disk',tresh_disk);

horizontalBuilding = imfilter(bw, horizontalKernel);

figure, imshow(horizontalBuilding), title('Objects');

[labeled,numObjects_1] = bwlabel(horizontalBuilding,8);

graindata = regionprops(labeled,'Centroid','Eccentricity');

%eliminate rubbish points
%-------------------------------------------------------------
count=1;
PlotX=0;
PlotY=0;
for i=1:numObjects_1
    ecc(i,1)=graindata(i).Eccentricity;
        if ecc(i,1)<tresh_ecc
            coordxy(count,1)=(graindata(i).Centroid(1)-resox/2)*sizex;
            coordxy(count,2)=(graindata(i).Centroid(2)-resoy/2)*sizey;
            PlotX(count)=coordxy(count,1);
            PlotY(count)=coordxy(count,2);
            count=count+1;
        end
end
count=count-1;
 % Now plot
    figure, plot(PlotX, PlotY, '+r'), title('Center_of_objects');
    %image(PlotX, PlotY, C);
    axis ij

%sort x and y values into columns
%-------------------------------------------------------------
 sor=1;
    while sor>0
        sor=0;
        for j=1 : count-1
            if coordxy(j+1,1)<coordxy(j,1)
                help1=coordxy(j,1);
                help2=coordxy(j,2);
                coordxy(j,1)=coordxy(j+1,1);
                coordxy(j,2)=coordxy(j+1,2);
                coordxy(j+1,1)=help1;
                coordxy(j+1,2)=help2;
                sor=sor+1;
```

```
            end
        end
    end

num=100;
numcol=1;
help_num=1;

    for i=numcol : count-1
        if ((coordxy(numcol,1)-coordxy(i+1,1))*(coordxy(numcol,1)-coordxy(i+1,1)
            ))<tresh_column
            coordnumxy(i,1)=num;
            coordnumxy(i,2)=coordxy(i,1);
            coordnumxy(i,3)=coordxy(i,2);
            num=num+1;
        else
        coordnumxy(i,1)=num;
        coordnumxy(i,2)=coordxy(i,1);
        coordnumxy(i,3)=coordxy(i,2);
        numcol=i+1;
        help_num=help_num+1;
        num=100*help_num;
        end
    end
   coordnumxy(i+1,1)=num;
   coordnumxy(i+1,2)=coordxy(i+1,1);
   coordnumxy(i+1,3)=coordxy(i+1,2);

max_column = coordnumxy(count,1)/100;
max_column = int16(max_column);
max_num=200;
min_num=100;

for i=1 : max_column
    sor=1;
    while sor>0
            sor=0;
            for j=1 : count-1
                if coordnumxy(j,1) < max_num && coordnumxy(j,1)>=min_num &&
                    coordnumxy(j+1,1) ~= max_num
                    if coordnumxy(j+1,3) > coordnumxy(j,3)
                        help1=coordnumxy(j,2);
                        help2=coordnumxy(j,3);
                        coordnumxy(j,2)=coordnumxy(j+1,2);
                        coordnumxy(j,3)=coordnumxy(j+1,3);
                        coordnumxy(j+1,2)=help1;
                        coordnumxy(j+1,3)=help2;
                        sor=sor+1;
```

```
                    end
                end
            end
    end
    max_num=max_num+100;
    min_num=min_num+100;
end

for i=1 : count
    column(i,1)=coordnumxy(i,1);
    column(i,2)=coordnumxy(i,2);
    column(i,3)=coordnumxy(i,3);
end

%sort x and y values into rows
%-------------------------------------------------------------

sor=1;
    while sor>0
        sor=0;
        for j=1 : count-1
            if coordxy(j+1,2) > coordxy(j,2)
                help1=coordxy(j,1);
                help2=coordxy(j,2);
                coordxy(j,1)=coordxy(j+1,1);
                coordxy(j,2)=coordxy(j+1,2);
                coordxy(j+1,1)=help1;
                coordxy(j+1,2)=help2;
                sor=sor+1;
            end
        end
    end

num=100;
numrow=1;
help_num=1;

    for i=numrow : count-1
        if ((coordxy(numrow,2)-coordxy(i+1,2))*(coordxy(numrow,2)-coordxy(i+1,2)
            ))<tresh_lines
            coordnumxy(i,1)=num;
            coordnumxy(i,2)=coordxy(i,1);
            coordnumxy(i,3)=coordxy(i,2);
            num=num+1;
        else
        coordnumxy(i,1)=num;
        coordnumxy(i,2)=coordxy(i,1);
        coordnumxy(i,3)=coordxy(i,2);
```

```
        numrow=i+1;
        help_num=help_num+1;
        num=100*help_num;
        end
    end
   coordnumxy(i+1,1)=num;
   coordnumxy(i+1,2)=coordxy(i+1,1);
   coordnumxy(i+1,3)=coordxy(i+1,2);

max_rows = coordnumxy(count,1)/100;
max_rows = int16(max_rows);
max_num=200;
min_num=100;
sor=1;
for i=1 : max_rows
    sor=1;
    while sor>0
            sor=0;
            for j=1 : count-1
                if coordnumxy(j,1) < max_num && coordnumxy(j,1)>=min_num &&
                    coordnumxy(j+1,1) ~= max_num
                    if coordnumxy(j+1,2) < coordnumxy(j,2)
                        help1=coordnumxy(j,2);
                        help2=coordnumxy(j,3);
                        coordnumxy(j,2)=coordnumxy(j+1,2);
                        coordnumxy(j,3)=coordnumxy(j+1,3);
                        coordnumxy(j+1,2)=help1;
                        coordnumxy(j+1,3)=help2;
                        sor=sor+1;
                    end
                end
            end
    end
    max_num=max_num+100;
    min_num=min_num+100;
end

for i=1 : count
    row(i,1)=coordnumxy(i,1);
    row(i,2)=coordnumxy(i,2);
    row(i,3)=coordnumxy(i,3);
end

%print temporary row.dat and column.dat
%-------------------------------------------------------------
for i=1 : count
    fprintf(fid,' %d  %10.4f  %10.4f \n',row(i,1), row(i,2),row(i,3));
end
```

```
for i=1 : count
    fprintf(fid_1,' %d  %10.4f  %10.4f \n',column(i,1), column(i,2),column(i,3))
        ;
end

all_rows=all_rows+max_rows;
all_rows
all_column=all_column+max_column;
all_column
helpplumbprint=helpplumbprint+count;

    pause = input('Pause: for processing next image press [] or press [1] for
        exit!\n');
    if pause == 1;

       break;
    end

    close all
end

fclose(fid);
fclose(fid_1);

%print plumb.dat
%-------------------------------------------------------------

load row.temp
load column.temp

for i=1:helpplumbprint
    fprintf(plumb,' %d  %10.4f    %10.4f \n',row(i,:));
end

for i=1:helpplumbprint
    fprintf(plumb,' %d  %10.4f    %10.4f \n',column(i,:));
end

fclose(plumb)

%print input.plm
%-------------------------------------------------------------

fprintf(inp,' %d  %d \n',all_rows,all_column);
fprintf(inp,' %5.4f  %5.4f \n',standard_x_y);
fprintf(inp,' %2.1f  %2.1f %2.1f  %2.1f %2.1f \n',estimates_p1_p2_k1_k2_k3);
fprintf(inp,' %2.1E  %2.1E %2.1E  %2.1E %2.1E \n',standard_p1_p2_k1_k2_k3);
```

```
fclose(inp);

%*********************************************************
%              CALL EXTERNAL PLUMB LINE PROGRAM           *
%*********************************************************

runplumb = input('Do you want to run the plumb line program (yes=1 or no=[])?\n\
    n');

if runplumb == 1;
    !plumb.exe
end
```

APPENDIX B

Refereed Journal Papers

Wackrow, R., Chandler, J.H. and Bryan, P. (2007). Geometric consistency and stability of consumer-grade digital cameras for accurate spatial measurement. *Photogrammetric Record*, **22**(118), 121-134.

Wackrow, R. and Chandler, J.H. (2008). A convergent image configuration for DEM extraction that minimises the systematic effects caused by an inaccurate lens model. *Photogrammetric Record*, **23**(121), 1-12.

The Photogrammetric Record 22(118): 121–134 (June 2007)

GEOMETRIC CONSISTENCY AND STABILITY OF CONSUMER-GRADE DIGITAL CAMERAS FOR ACCURATE SPATIAL MEASUREMENT

RENE WACKROW (r.wackrow@lboro.ac.uk)
JIM H. CHANDLER (j.h.chandler@lboro.ac.uk)
Loughborough University

PAUL BRYAN (paul.bryan@english-heritage.org.uk)
English Heritage

Abstract

It is known that uncertain internal geometry of consumer-grade digital cameras limits the accuracy of data that can be extracted. These cameras can be calibrated, but the validity of calibration data over a period of time should be carefully assessed before subsequent photogrammetric measurement. This paper examines the geometric stability and manufacturing consistency of a typical low-cost digital camera (Nikon Coolpix 5400) by estimating the degree of similarity between interior orientation parameters (IOP), established over a 1-year period. Digital elevation models (DEMs) were extracted with differing IOP, and accuracies were compared using data obtained from seven identical cameras. An independent self-calibrating bundle adjustment (GAP) and the Leica Photogrammetry Suite (LPS) software were used to provide these data-sets. Results are presented that indicate the potential of these cameras to maintain their internal geometry in terms of temporal stability and manufacturing consistency. This study also identifies residual systematic error surfaces or "domes", discernible in "DEMs of difference". These are caused by slightly inaccurately estimated lens distortion parameters, which effectively constrain the accuracies achievable with this class of sensor.

KEYWORDS: camera calibration, camera stability, close range photogrammetry, digital cameras

INTRODUCTION

THE MAIN ADVANTAGES of consumer-grade digital cameras are their convenience, portability and low cost. These cameras have not been traditionally used for photogrammetric measurements, owing to their uncertain geometry. The uncertainties can be partially resolved by calibration but their temporal stability and manufacturing consistency remain unknown.

During a collaborative project with English Heritage to record rock art in the north-east of England (Chandler et al., 2007), seven identical Nikon Coolpix 5400 digital cameras (Fig. 1) were calibrated. This provided the opportunity to assess their stability over a 1-year period as well as their consistency of manufacture.

FIG. 1. Nikon Coolpix 5400.

Previous work related to calibration of consumer-grade cameras is reviewed, before describing the methodology adopted for the study. The link between the stability analyses strategy and the reconstructed object space is introduced followed by experimental results and discussion. Finally, this paper concludes with a brief summary and recommendations for future work.

PREVIOUS WORK ON CALIBRATION OF CONSUMER-GRADE CAMERAS

Over the past decade, several researchers have assessed the photogrammetric potential of non-metric digital cameras. The Kodak DCS420 and DCS460 have been tested in a variety of photogrammetric applications (Beyer et al., 1995; Brown and Dold, 1995; Fraser et al., 1995; Peipe, 1995; Dold and Peipe, 1996; Miyatsuka, 1996; Schneider, 1996; Shortis et al., 1998; Ahmad and Chandler, 1999) and the use of similar cameras such as the Kodak DC40 has been described in Miyatsuka (1996) and Lichti and Chapman (1997). In addition, the suitability for close range measurement of the Kodak DCS Pro Back used in conjunction with the Mamiya body was reported in Mills et al. (2003). The accuracies in close range surface measurement of three low-cost consumer-grade digital cameras (Sony DSC-P10, Olympus C3030, Nikon Coolpix 3100) and the Kodak DCS460 have been compared in Chandler et al. (2005). All cameras tested revealed potential for use in close range photogrammetry where low to medium accuracy was required. The use of consumer-grade digital cameras for photogrammetric measurements is increasingly accepted in many industrial applications but also in diverse fields ranging from medical and forensic science to architectural work (Fryer et al., 2007).

The stability of non-metric digital cameras has been reported less frequently in the literature. Shortis et al. (2001) introduced a strategy for accessing the stability of a digital camera by using the ratio of the mean precision of target coordinates to the largest dimension of the target array. Habib and Morgan (2005) attributed the lack of literature to the absence of standards for quantitative analyses of camera stability. An approach based on statistical testing of two sets of interior orientation parameters (IOP) was presented and the disadvantages of this strategy were discussed. Due to the drawbacks of this methodology, a new procedure for stability analysis based on the degree of similarity between the reconstructed bundles using two sets of IOP was introduced. The stability of the Olympus C-5050 digital camera was reported in Bosch et al. (2005). This was achieved by comparing the coordinates of check points with coordinates acquired with a total station. This test was not independent because the same points were used to determine the exterior orientation. Three methodologies (ZROT, ROT and SPR) for evaluating the stability of a camera are presented in Habib et al. (2006). The procedures impose constraints regarding the exterior orientation of the bundles compared. Therefore, each is applicable for a specific georeferencing technique which describes the position and orientation of the images relative to a coordinate system.

This review of previous work identified the need for an appropriate method to assess the temporal stability and manufacturing consistency of consumer-grade digital cameras. A suitable approach which achieves this objective is described in this paper.

Stability Analyses of Seven Nikon Coolpix 5400 Cameras

Consumer-grade digital cameras have not been designed for measurement, so their internal geometry is generally considered unstable (Shortis et al., 1998). The aim of stability analyses is to determine whether the interior orientation of a camera changes over time or not. The methodology adopted initially in this study was to evaluate the degree of similarity between two sets of IOP. In addition, the impact of varying IOP on accuracy in the object space was assessed; this is ultimately of more significance to most users.

The Cameras

Seven Nikon Coolpix 5400 digital cameras were purchased by the Northumberland and Durham Rock Art Project in February 2005 (Barnett, 2006). These have been used regularly by teams of volunteers to systematically record 1500 rock art motifs located in the north of England (Chandler et al., 2007). The need to calibrate these seven cameras provided the opportunity to evaluate the stability and consistency of these sensors during normal operation in field conditions. It was judged that there was no further need to simulate disturbing impacts of the camera geometry, such as variations in temperature and moisture, external forces on the camera body or use of the auto-focus device. A benefit of the presence of seven identical cameras was that manufacturing consistency could also be assessed. A detailed overview of the characteristics of the Nikon Coolpix 5400 camera is given in Table I.

The Testfield

It was expected that the seven cameras would mainly be used at an object distance of 1·5 m for rock art recording. Therefore, a 3D and planar testfield was specifically constructed to allow the cameras to be calibrated at this distance. It is an enhancement of the testfield used in Chandler et al. (2005) and consists of a medium density fibreboard (MDF) (1·2 m × 0·9 m) to which eight square blocks of various shapes and heights were added (Fig. 2). These blocks replicate physical structures such as buildings found in normal vertical aerial photography. To provide an appropriate texture for the image-matching algorithm included in the Leica Photogrammetry Suite (LPS) software, the MDF board was painted white and finally splattered

Table I. Characteristics of the Nikon Coolpix 5400 camera.

Feature	*Nikon Coolpix 5400*
Camera body	Compact
Resolution [pixel]	5 million
Image size [pixel]	2592 × 1944
Size of sensor [mm]	7·18 × 5·32
Size of pixel [μm]	2·77 × 2·77
Auto focus	Yes
Manual focus	Yes
Dimensions [mm]	108 × 73 × 69
Weight [kg]	0·4
Cost [£]	240 (January 2005)

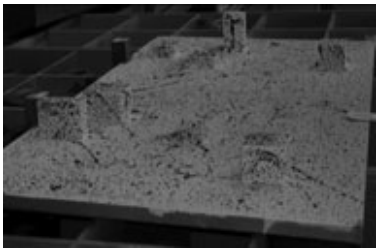

FIG. 2. Test object.

with red and blue paint. This test object provides the opportunity to derive thousands of object measurements; by comparing elevations with their known values, a similar number of check points can be achieved. This allows the accuracy in the object space to be determined with good statistical reliability. In addition, 28 photogrammetric target points were distributed over the testfield (Fig. 3) and coordinated by theodolite intersection using a Leica TC1010 total station (June 2005). The measurements, both horizontal and vertical angles and the distance between the two theodolite stations, were initially computed using basic intersection formulae. The estimates of the coordinates of the target points, the measurements derived using a total station and a subset of distances measured with a steel band were then combined in a least squares ''variation of coordinates'' adjustment to determine the best estimates for the photogrammetric target points. These coordinates were used to create a digital elevation model (DEM) at 1 mm resolution, known as the ''Truth DEM''. Another set of coordinates was derived by repeating the procedure in May 2006. Both sets of coordinates were compared using a 3D similarity transformation. The residuals (maximum 0·5 mm) demonstrate the geometric stability of the testfield over time; thus any deviations between similarly derived IOP cannot be attributed to distortion of the MDF base material.

Camera Calibration

Determination of the geometric conditions of a camera, described by the IOP, is known as camera calibration. Methods of camera calibration have evolved over the past few decades, through the development of computational techniques and because of the increasing use of non-metric digital cameras for photogrammetric measurements. The widely used method of self-calibration, where all image observations from various camera positions are used to determine the unknown interior and exterior orientation parameters (Clarke and Fryer, 1998), was adopted in this research.

Six frames, representing the whole test object, were captured with each of the seven cameras at a camera-to-object distance of approximately 1·5 m (Fig. 4), with the camera focus set on infinity. The same basic configuration was used for each camera at each time.

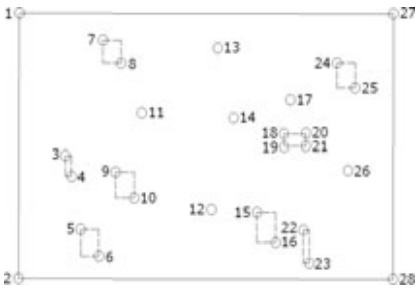

FIG. 3. Position of photogrammetric target points.

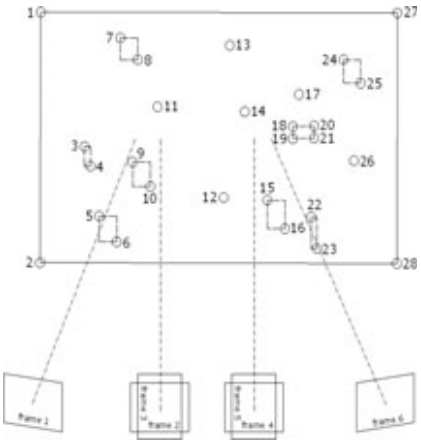

FIG. 4. Image geometry.

For processing the images in the LPS, it was essential initially to define the primary orientation of the sensor. The readily accessible http://www.dpreview.com website was used to identify the physical size of the sensor and consequently the physical size of each pixel of the CCD array in the x and y directions. Once the pixel size and an approximate focal length were defined, the point measurement tool of LPS was used to measure 11 photogrammetric target points manually before 100 tie points were measured using fully automated methods.

Previous work conducted by Chandler et al. (2005) demonstrated that the external self-calibrating bundle adjustment GAP (Chandler and Clark, 1992) can also be used to estimate the camera parameters; this was also used in these studies to provide another approach independent of LPS. A familiar eight-parameter model for the bundle adjustment (Kenefick et al., 1972) was available which includes parameters for principal distance, principal point offset and corrections for radial and decentring distortion. The program can also estimate two additional parameters for affinity and differential scale, but were not found necessary in this study. Avoiding solutions which are overparameterised is important (Granshaw, 1980; Fraser, 1982) and the significance of additional parameters was assessed by comparing them with their stochastic properties. This demonstrated that two parameters (k_1, k_2) were significant for modelling radial distortion. However, k_3 and the parameters (p_1, p_2) used for modelling the decentring distortion proved insignificant and were removed. This five-parameter model for the self-calibrating bundle adjustment was maintained for all seven cameras. The derived inner orientation parameters were then re-established into LPS for the purpose of deriving high-resolution DEMs and check point data.

DEM Generation

The LPS software was used for DEM generation by means of a hierarchical feature-based matching algorithm (ERDAS, 2002). Tests revealed that DEMs with optimum accuracy were produced using the following strategy:

DTM cell size:	0·003 m × 0·003 m
Search size:	7 × 3
Correlation size:	7 × 7
Coefficient limit:	0·80
Topographic type:	Flat terrain
Object type:	Open area
DTM filtering:	High

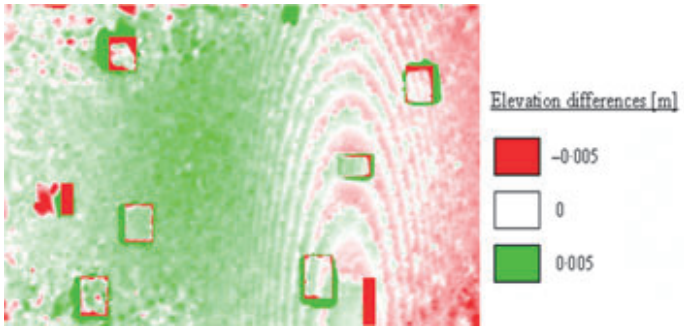

FIG. 5. Elevation differences—IOP: 4th July 2005.

The adaptive capability of LPS to change the search size, correlation size and correlation coefficient limit dynamically during DEM generation was switched off for simplicity.

The automatically extracted DEMs, representing the whole of the physical test object, were compared with the "Truth DEM" by interpolation and subtraction to produce DEMs of difference. As recommended by Li (1988), mean error and standard deviation of error of DEMs of difference were derived using an ERDAS Graphical Model. Tests demonstrated that significant areas of inaccurate DEM are situated adjacent to the wooden blocks, which clearly illustrated the shadowing effect of them (Fig. 5). These effects obviously distorted the accuracy statistics. In order to avoid this distortion, statistics were also computed for an area of interest which represented the central and flat part of the test object and did not include the wooden blocks. The optimum accuracy for each DEM of difference could consequently be quantified.

RESULTS

Temporal Stability

The temporal stability of the Nikon Coolpix 5400 camera can be assessed by comparing the degree of similarity between sets of IOP established at various dates. Seven identical cameras were calibrated on 4th July 2005. This was repeated after 4 days and after a period of approximately 1 year. Table II summarises the accuracy of the calibration procedure in terms of accuracy of fit to the control points (restitution accuracy) of camera 5. Similar results were

TABLE II. Restitution accuracy by using IOP from different dates.

Camera/Imagery date	*IOP date*	*Object rms error [mm]*			*Image rms error [pixel]*	
		X	*Y*	*Z*	*x*	*y*
Camera 5						
4th July 2005	4th July 2005	0·3	0·2	0·4	0·63	0·55
4th July 2005	8th July 2005	0·2	0·2	0·2	0·63	0·57
4th July 2005	12th July 2006	0·5	0·4	0·4	0·68	0·69
8th July 2005	8th July 2005	0·4	0·2	0·3	0·80	0·82
8th July 2005	4th July 2005	0·2	0·2	0·3	0·79	0·85
8th July 2005	12th July 2006	0·4	0·3	0·4	0·90	0·87
12th July 2006	12th July 2006	0·4	0·3	0·4	0·96	0·82
12th July 2006	4th July 2005	0·3	0·2	0·4	0·94	0·83
12th July 2006	8th July 2005	0·3	0·2	0·4	0·97	0·85

TABLE III. DEM accuracy by using IOP from different dates.

Camera/ Imagery date	*IOP date*	*Full area (mean error ± standard deviation) [mm]*	*Central area (mean error ± standard deviation) [mm]*
Camera 5			
4th July 2005	4th July 2005	0·5 ± 7·2	1·8 ± 0·9
4th July 2005	8th July 2005	0·4 ± 5·8	1·1 ± 0·7
4th July 2005	12th July 2006	0·9 ± 7·1	2·5 ± 0·7
8th July 2005	8th July 2005	0·9 ± 6·1	1·4 ± 0·8
8th July 2005	4th July 2005	0·6 ± 6·9	1·3 ± 1·0
8th July 2005	12th July 2006	1·2 ± 5·8	1·9 ± 0·8
12th July 2006	12th July 2006	0·3 ± 6·0	1·6 ± 0·7
12th July 2006	4th July 2005	−0·1 ± 6·6	0·5 ± 0·9
12th July 2006	8th July 2005	−0·2 ± 5·6	0·7 ± 0·7

achieved with the other six cameras; camera 5 will be used as an exemplar. The first column represents the dates of capturing the images of the test object, whilst the second column tabulates the dates of IOP used for restitution. The rms error (mm) in the object space is summarised in columns three to five and the final two columns represent the rms residuals (pixels) in the image space.

The camera achieved sub-millimetre accuracy (average rms error of 0·3 mm), in terms of fit to the control points, whichever combination of image sets and IOP was used. The accuracy statistics indicate no significant variations.

In the image space, accuracies within each set of calibration images varied within the range of approximately 0·1 pixel. However, variations in accuracy at a maximum of 0·4 pixel are noticeable by comparing statistics of different sets of images. This appears to be significant but it must be acknowledged that the automatic tie-point generation tool of LPS was used; this independently creates tie points in each image set. It is plausible that the discrepancies in accuracy are caused by using different sets of tie points in each set of imagery and not by the IOP. This would suggest that there is a high degree of consistency between all sets of IOP for this camera exemplar. A similar result was obtained with the other six cameras.

Table III summarises the accuracy of DEM generation by using different combinations of sets of imagery and IOP at various dates for camera 5 within the two areas of the test object. Similar results were again obtained with the other six cameras. As expected, the cameras achieved poor accuracies for the full test area. These were caused by the small number of gross failures for points adjacent to the wooden blocks. Mean errors for the central area of interest varied from 0·5 to 2·5 mm and did not follow expectations. Even more surprisingly, optimum restitution accuracy was not achieved by generating DEMs using frames and IOP from the same date. This leads to the conclusion that the central area of extracted DEMs was perhaps affected by the same systematic error source, an issue discussed later in this paper.

Consistency of Manufacture

The presence of seven identical Nikon Coolpix 5400 digital cameras provided the opportunity to assess their consistency of manufacture. Three sets of IOP, originally derived with camera 4 in calibration sessions on various dates, were used in conjunction with the six

TABLE IV. Restitution accuracy by using IOP of different cameras/dates.

Camera/Imagery date	*Camera/IOP date*	*Object rms error [mm]*			*Image rms error [pixel]*	
		X	*Y*	*Z*	*x*	*y*
Camera 5	Camera 5					
4th July 2005	4th July 2005	0·3	0·2	0·4	0·63	0·55
Camera 5	Camera 4					
4th July 2005	4th July 2005	0·4	0·2	0·2	0·68	0·75
4th July 2005	8th July 2005	0·4	0·2	0·4	0·78	0·77
4th July 2005	7th June 2006	0·4	0·3	0·4	0·62	0·57

TABLE V. DEM accuracy by using IOP of different cameras/dates.

Camera/Imagery date	*Camera IOP date*	*Full area (mean error ± standard deviation) [mm]*	*Central area (mean error ± standard deviation) [mm]*
Camera 5	Camera 5		
4th July 2005	4th July 2005	0·5 ± 7·2	1·8 ± 0·9
Camera 5	Camera 4		
4th July 2005	4th July 2005	0·5 ± 6·6	1·6 ± 0·6
4th July 2005	8th July 2005	−0·3 ± 6·8	0·6 ± 0·6
4th July 2005	7th June 2006	0·7 ± 7·1	2·1 ± 0·9

calibration frames captured with camera 5 on 4th July 2005. The restitution accuracies achieved for these two cameras, which provide a representative sample for the results obtained from all cameras, are presented in Table IV. In particular, no significant discrepancies were observable in the accuracy statistics (average object rms error of 0·3 mm; variation of image rms error of 0·22 pixel) comparing these configurations. It is notable that there is a high degree of similarity between the sets of IOP which certainly demonstrates remarkable geometric consistency achieved by the manufacturer.

The accuracies in the object space, achieved by extracting DEMs using the configurations presented above, are summarised in Table V. This again indicates a poor DEM accuracy estimated for the whole test object and discrepancies between 0·6 and 2·1 mm for the central test area. By comparing the DEM accuracy statistics presented in Tables III and V, it is notable that camera 5 achieved a similar accuracy level, even though IOP sets derived from a different camera were used. This again demonstrates a high degree of manufacturing consistency for this type of camera.

DISCUSSION

DEM Generation and Accuracy Statistics

Figs. 5 to 7 represent DEMs of difference for the full test object using the imagery from 4th July 2005 and IOP sets derived using the 4th and 8th July 2005 and 12th July 2006 imagery, acquired with camera 5. Sets of IOP were achieved using the GAP calibration approach (Chandler et al., 2005). Areas in DEMs with elevations less than −5 mm are illustrated by solid red, while solid green regions indicate height differences greater than +5 mm and white areas represent regions of no height differences between the ''Truth DEM'' and automatically extracted DEMs.

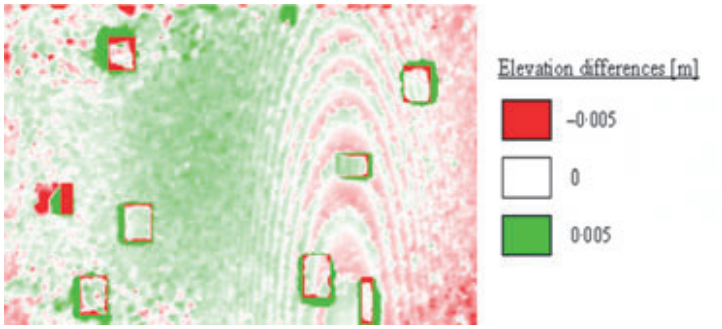

FIG. 6. Elevation differences—IOP: 8th July 2005.

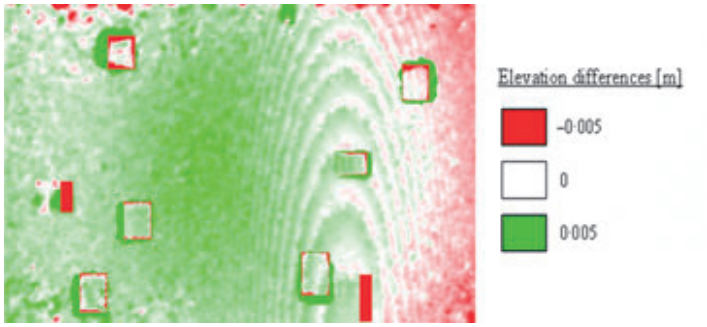

FIG. 7. Elevation differences—IOP: 12th July 2006.

Difference images clearly indicate significant areas of inaccurate DEM which can be classified into four types. Obviously, the DEM generation algorithm of the LPS software has difficulties in extracting information representing the wooden blocks situated on the left and lower right areas of the test object. The dimensions are 70 mm × 30 mm × 100 mm (left block) and 105 mm × 30 mm × 72 mm (lower right block) simulating isolated tall buildings, which perhaps explains these difficulties. Furthermore, areas with gross errors close to the wooden blocks clearly indicate the shadowing effect they cause, which is to be expected. The effect on the numerical statistics can be noticed by comparing the standard deviation (average value 6·3 mm) determined for the full test area with the standard deviation (average value 0·8 mm) for the central region which does not include the wooden blocks. The other obvious areas of inaccurate DEM are the distinctive radial "domes", slightly shifted to the left and the systematic "contour" pattern to the right of the centre of the DEM. These systematic effects will be accounted for in the next section.

Systematic Pattern in Difference Images

A hierarchical feature-based matching algorithm that incorporates both pyramid layers and an epipolar constraint to reduce the search time for conjugate points in image pairs is used by LPS for DEM generation (ERDAS, 2002). This approach generates a systematic "contour" pattern using a base-to-distance ratio of 1:7 for an image pair, illustrated in Figs. 5 to 7. However, tests have shown that changing the base-to-distance ratio to 1:2 reduces this systematic effect, as demonstrated in Fig. 8. The software manufacturer Leica Geosystems was contacted in November 2006 and this unusual effect was reported. However, no explanation accounting for this pattern has been received to date (May 2007). Tests conducted with another

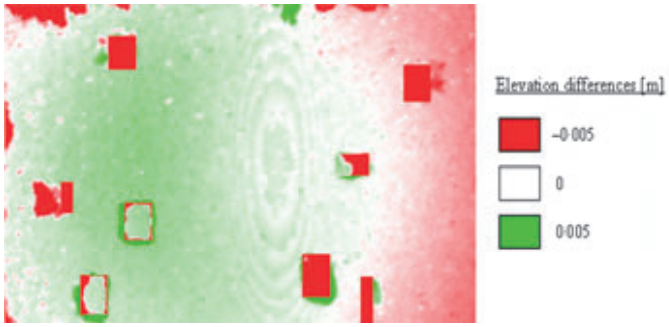

FIG. 8. Difference image with base-to-distance ratio of 1:2.

DEM generation package (ERDAS OrthoMax) created a dome but no such systematic contour pattern.

"Dome" Structure in DEM of Difference

Figs. 5 to 8 represent DEMs of difference for the full test object where distinctive radial "domes" appear to be approximately located to the left of the centre of DEMs. They are caused by residual systematic effects arising from slightly inaccurate radial lens distortion parameters and have also been noted in past work (Stojic et al., 1998; Chandler et al., 2003, 2005). A theoretical proof explaining them was given in Fryer and Mitchell (1987). This confirms that any uncorrected residual x parallaxes will create a systematic offset in computed elevations, causing a flat object to appear curved.

The radial domes (maximum elevation of 2 mm) clearly affect the accuracy statistic estimated for the central test object. The achieved accuracy for the sensors is approximately 1·4 mm (average mean error) for the central area tested. By removing these systematic errors in difference images, the cameras will be certainly capable of achieving an improved accuracy, perhaps approaching the theoretical optimum of 0·5 mm at this camera-to-object distance of 1·5 m.

The variation in radial lens distortion for sensor 5 using various sets of IOP are shown in Fig. 9. The differences between these curves and the mean curve never exceed 7 μm and even these extremes were achieved at the very edges of the image format. These results correspond

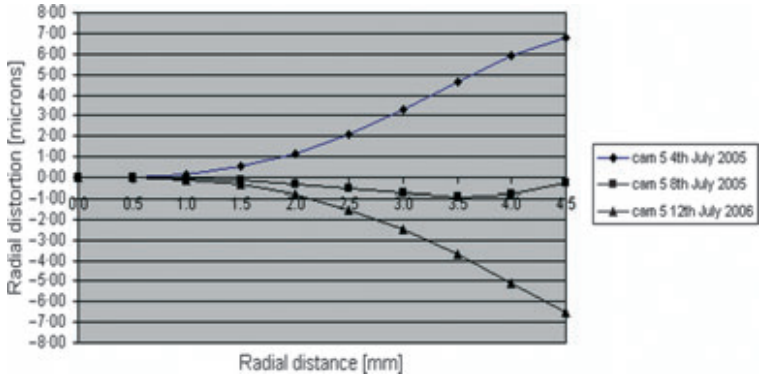

FIG. 9. Radial distortion curves showing differences with respect to a mean curve for camera 5 and three sets of IOP.

closely to the findings of Robson and Gyory (2006) in which the variations in distortion for eight sensors of a panoramic camera cluster have been investigated.

Reviewing the results summarised in Tables II to V and Fig. 9, the cameras achieved similar accuracy whichever combination of camera and IOP was used. This level of accuracy is suitable for routine measurement of textured surfaces and DEM generation to an accuracy of 2 mm. Tests have demonstrated remarkable temporal stability and manufacturing consistency of the cameras. Variations in calibration parameters for these sensors are generally not significant when they are used at the level of accuracy described. This finding agrees with the experimental camera calibration tests carried out by Remondino and Fraser (2006).

Conclusion

The work presented in this paper has explored and successfully identified the temporal stability and manufacturing consistency of the Nikon Coolpix 5400 digital camera over a 1-year period. This type of camera is capable of generating DEMs to an accuracy of 1·4 mm, from a distance of 1·5 m using IOP derived though self-calibration using imagery obtained by any of these cameras. This result is highly significant, as it implies that a ''generic'' distortion curve may well be applicable for all Nikon 5400 cameras (based on the sample of seven). In addition, such accuracies could be suitable for many applications. This paper also identified existing systematic errors in difference images which are caused by slightly inaccurate lens distortion parameters being estimated by the self-calibration approach. These effectively constrain the accuracies achievable. Further experimental work will be conducted to see if it is possible to reduce these effects, and will be reported in a future paper.

Acknowledgements

The authors would like to acknowledge the work of Dr Tertia Barnett, formerly Chair of the Northumberland and Durham Rock Art Project (Northumberland County Council) and also the Engineering and Physical Sciences Research Council (EPSRC) for the first author's studentship.

References

Ahmad, A. and Chandler, J. H., 1999. Photogrammetric capabilities of the Kodak DC40, DCS420 and DCS460 digital cameras. *Photogrammetric Record*, 16(94): 601–615.

Barnett, T., 2006. *Northumberland and Durham Rock Art Project*. http://pscm.northumberland.gov.uk/pls/portal92/docs/2091.pdf [Accessed 10th August 2006].

Beyer, H. A., Uffenkamp, V. and van der Vlugt, G., 1995. Quality control in industry with digital photogrammetry. *Optical 3-D Measurement Techniques III* (Eds. A. Gruen and H. Kahmen). Wichmann, Heidelberg. 533 pages: 29–38.

Bosch, R., Külür, S. and Gülch, E., 2005. Non-metric camera calibration and documentation of historical buildings. *CIPA XX International Symposium*, Torino. 990 pages: 142–147.

Brown, D. C. and Dold, J., 1995. V-STARS—a system for digital industrial photogrammetry. *Optical 3-D Measurement Techniques III* (Eds. A. Gruen and H. Kahmen). Wichmann, Heidelberg. 533 pages: 12–21.

Chandler, J. H. and Clark, J. S., 1992. The archival photogrammetric technique: further application and development. *Photogrammetric Record*, 14(80): 241–247.

Chandler, J. H., Buffin-Bélanger, T., Rice, S., Reid, I. and Graham, D. J., 2003. The accuracy of a river bed moulding/casting system and the effectiveness of a low-cost digital camera for recording river bed fabric. *Photogrammetric Record*, 18(103): 209–223.

Chandler, J. H., Fryer, J. G. and Jack, A., 2005. Metric capabilities of low-cost digital cameras for close range surface measurement. *Photogrammetric Record*, 20(109): 12–26.

Chandler, J. H., Bryan, P. and Fryer, J. G., 2007. The development and application of a simple methodology for recording rock art using consumer-grade digital cameras. *Photogrammetric Record*, 22(117): 10–21.

CLARKE, T. A. and FRYER, J. G., 1998. The development of camera calibration methods and models. *Photogrammetric Record*, 16(91): 51–66.

DOLD, J. and PEIPE, J., 1996. High resolution data acquisition to observe moving objects. *International Archives of Photogrammetry and Remote Sensing*, 31(B5): 471–474.

ERDAS, 2002. *IMAGINE OrthoBASE User's Guide*. Leica Geosystems, Atlanta. 483 pages: 341.

FRASER, C. S., 1982. Film unflatness effects in analytical non-metric photogrammetry. *International Archives of Photogrammetry and Remote Sensing*, 24(5): 156–166.

FRASER, C. S., SHORTIS, M. R. and GANCI, G., 1995. Multi-sensor system self-calibration. *Videometrics IV. SPIE* 2598:2–18.

FRYER, J. G. and MITCHELL, H. L., 1987. Radial distortion and close range stereophotogrammetry. *Australian Journal of Geodesy, Photogrammetry and Surveying,* 46/47: 123–138.

FRYER, J. G., MITCHELL, H. and CHANDLER, J. H., 2007. *Applications of 3D Measurement from Images*. Whittles, Caithness. 384 pages.

GRANSHAW, S. I., 1980. Bundle adjustment methods in engineering photogrammetry. *Photogrammetric Record*, 10(56): 181–207.

HABIB, A. and MORGAN, M., 2005. Stability analysis and geometric calibration of off-the-shelf digital cameras. *Photogrammetric Engineering & Remote Sensing*, 71(6): 733–741.

HABIB, A., PULLIVELLI, A., MITISHITA, E., GHANMA, M. and KIM, E.-M., 2006. Stability analysis of low-cost digital cameras for aerial mapping using different georeferencing techniques. *Photogrammetric Record*, 21(113): 29–43.

KENEFICK, J. F., GYER, M. S. and HARP, B. F., 1972. Analytical self-calibration. *Photogrammetric Engineering*, 38(11): 1117–1126.

LI, Z., 1988. On the measure of digital terrain model accuracy. *Photogrammetric Record*, 12(72): 873–877.

LICHTI, D. D. and CHAPMAN, M. A., 1997. Constrained FEM self calibration. *Photogrammetric Engineering & Remote Sensing*, 63(9): 1111–1119.

MILLS, J. P., SCHNEIDER, D., BARBER, D. M. and BRYAN, P. G., 2003. Geometric assessment of the Kodak DCS Pro Back. *Photogrammetric Record*, 18(103): 193–208.

MIYATSUKA, Y., 1996. Archaeological real-time photogrammetric system using digital still camera. *International Archives of Photogrammetry and Remote Sensing*, 31(B5): 374–377.

PEIPE, J., 1995. Photogrammetric investigation of a 3000×2000 pixel high resolution still video camera. *International Archives of Photogrammetry and Remote Sensing*, 30(5W1): 36–39.

REMONDINO, F. and FRASER, C., 2006. Digital camera calibration methods: considerations and comparisons. *International Archives of Photogrammetry, Remote Sensing and Spatial Information Sciences*, 36(5): 266–272.

ROBSON, S. and GYORY, G., 2006. OpTag—a combined panoramic photogrammetric and radio frequency tagging system for monitoring passenger movements in airports. *International Archives of Photogrammetry, Remote Sensing and Spatial Information Sciences.* http://www.isprs.org/commission5/proceedings06/paper/1262_Dresden06.pdf [Accessed 29th November 2006].

SCHNEIDER, C.-T., 1996. DPA-WIN—a PC based digital photogrammetric station for fast and flexible on-site measurement. *International Archives of Photogrammetry and Remote Sensing*, 31(B5): 530–533.

SHORTIS, M. R., ROBSON, S. and BEYER, H. A., 1998. Principal point behaviour and calibration parameter models for Kodak DCS cameras. *Photogrammetric Record*, 16(92): 165–186.

SHORTIS, M. R., OGLEBY, C. L., ROBSON, S., KARALIS, E. M. and BEYER, H. A., 2001. Calibration modeling and stability testing for the Kodak DC200 series digital still camera. *Videometrics and Optical Methods for 3D Shape Measurements*. *SPIE* 4309: 148–153.

STOJIC, M., CHANDLER, J. H., ASHMORE, P. and LUCE, J., 1998. The assessment of sediment transport rates by automated digital photogrammetry. *Photogrammetric Engineering & Remote Sensing*, 64(5): 387–395.

Résumé

Il est bien connu que la précision des données que l'on peut tirer des caméras numériques du commerce se trouve limitée par l'incertitude de leur géométrie interne. On peut étalonner ces caméras mais il convient de vérifier soigneusement la validité de cet étalonnage dans le temps avant de les utiliser pour des déterminations photogrammétriques. On étudie dans cet article la stabilité géométrique et la reproductibilité de fabrication d'une caméra numérique typique et bon marché (Nikon Coolpix 5400) en estimant le degré de ressemblance des paramètres

d'orientation interne (POI) obtenus sur une période d'un an. En utilisant sept caméras identiques, on a pu calculer des Modèles Numériques d'Elévation (MNE) en utilisant des paramètres d'orientation interne différents et en comparer la précision. Pour obtenir les jeux de données correspondants, on s'est servi du logiciel « suite photogrammétrique » de Leica (LPS) et d'une compensation par faisceaux avec auto-étalonnage. Les résultats que l'on présente montrent l'aptitude de ces caméras à conserver leur géométrie interne en termes de stabilité dans le temps et de reproductibilité dans leur fabrication. Les « MNE des différences » mettent en évidence des erreurs systématiques résiduelles surfaciques en forme de dôme. Elles proviennent de petites inexactitudes dans l'estimation des paramètres de distorsion des objectifs et limitant effectivement la précision que l'on peut attendre avec cette classe de capteurs.

Zusammenfassung

Es ist allgemein bekannt, dass die unsichere innere Geometrie von digitalen Amateurkameras die Genauigkeit der aus den digitalen Bildern extrahierten Daten limitiert. Diese Kameras können zwar kalibriert werden, aber die Gültigkeitsdauer dieser Kalibrierungsparameter sollte vor der Verwendung für photogrammetrische Zwecke sorgfältig überprüft werden. Diese Veröffentlichung betrachtet die geometrische Stabilität und die Fertigungsstabilität einer typischen, kostengünstigen, digitalen Kamera (Nikon Coolpix 5400) durch Beurteilung des Ähnlichkeitsgrades der inneren Orientierungsparameter, welche über einen Zeitraum von einem Jahr ermittelt wurden. Die ermittelten inneren Orientierungen von sieben identischen Kameras wurden benutzt, um Digitale Höhenmodelle zu extrahieren und ihre Genauigkeiten zu vergleichen. Ein unabhängiges Programm zur Bündeltriangulation (GAP) sowie die Leica Photogrammetry Suite (LPS) Software wurden benutzt, um diese Höhenmodelle bereitzustellen. Ergebnisse werden präsentiert, welche das Potential dieser Kameras zeigen, ihre geometrische Stabilität und ihre Fertigungsstabilität beizubehalten. Diese Studie identifiziert aber auch Oberflächen mit systematischen Fehlern oder "Kuppeln", sichtbar in dem Differenzbetrag digitaler Höhenmodelle. Diese werden durch ungenau berechnete radiale Verzeichnungsparameter verursacht und limitieren die erreichbare Genauigkeit mit diesen Kameras.

Resumen

Es conocido el hecho de que lo incierto de la geometría interna de las cámaras digitales de consumo limita la exactitud de los datos que se pueden extraer de ellas. Dichas cámaras pueden calibrarse, pero la validez temporal de los datos de calibración ha de comprobarse concienzudamente antes de realizar medidas fotogramétricas. El artículo examina la estabilidad geométrica y la consistencia de fabricación de una cámara típica de bajo coste (Nikon Coolpix 5400) en base a estimar el grado de similitud entre los parámetros de orientación interna en el periodo de un año. Para ello se calculan Modelos de Elevaciones del Terreno con parámetros de orientación interna que difieren entre sí, y se comparan los resultados de precisión obtenidos para siete cámaras idénticas. Para la generacíon de las pruebas se utilizó un programa independiente de ajuste por haces con autocalibración y el sistema "Leica Photogrammetric Suite (LPS)". Se presentan resultados que muestran el potencial de esas cámaras para mantener su geometría interna en

términos de estabilidad temporal y consistencia de fabricación. El estudio identifica también superficies de errores sistemáticos residuales o "domos" que son discernibles calculando las diferencias entre modelos de elevación. Dichos errores son debidos a estimaciones poco precisas de los parámetros de distorsión de las lentes y delimitan las precisiones alcanzables con esa clase de sensores.

The Photogrammetric Record 23(121): 6–18 (March 2008)

A CONVERGENT IMAGE CONFIGURATION FOR DEM EXTRACTION THAT MINIMISES THE SYSTEMATIC EFFECTS CAUSED BY AN INACCURATE LENS MODEL

RENE WACKROW (r.wackrow@lboro.ac.uk)

JIM H. CHANDLER (j.h.chandler@lboro.ac.uk)
Loughborough University

(Based on a contribution to the Annual Conference of the Remote Sensing and Photogrammetry Society at Newcastle upon Tyne, 12th September 2007)

Abstract

The internal geometry of consumer-grade digital cameras is generally considered unstable. Research conducted recently at Loughborough University indicated the potential of these sensors to maintain their internal geometry. It also identified residual systematic error surfaces or "domes", discernible in digital elevation models (DEMs), caused by slightly inaccurate estimated lens distortion parameters. This paper investigates these systematic error surfaces and establishes a methodology to minimise them. Initially, simulated data was used to ascertain the effect of changing the interior orientation parameters on extracted DEMs, specifically the lens model. Results presented demonstrate the relationship between "domes" and inaccurately specified lens distortion parameters. The stereopair remains important for data extraction in photogrammetry, often using automated DEM extraction software. The photogrammetric normal case is widely used, in which the camera base is parallel to the object plane and the optical axes of the cameras intersect the object plane orthogonally. During simulation, the error surfaces derived from extracted DEMs using the normal case were compared with error surfaces created using a mildly convergent geometry. In contrast to the normal case, the optical camera axes intersect the object plane at the same point. Results of the simulation process clearly demonstrate that a mildly convergent camera configuration eradicates the systematic error surfaces. This result was confirmed through practical tests and demonstrates that mildly convergent imagery effectively improves the accuracies of DEMs derived with this class of sensor.

KEYWORDS: camera calibration, close range photogrammetry, convergent image configuration, digital camera

INTRODUCTION

ACCURATE SPATIAL MEASUREMENT remains an enduring quest in photogrammetry, which is especially important since consumer-grade digital cameras are increasingly used. Convenience, portability and low cost are their main advantages and their potential to maintain their temporal

stability and manufacturing consistency was demonstrated in Wackrow et al. (2007). However, this work also identified residual systematic error surfaces or ''domes'', discernible in digital elevation models (DEMs) of difference.

The purpose of this paper is to assess the relationship between these ''domes'' and an inaccurately specified lens model, as well as to investigate the potential of a mildly convergent image configuration to minimise the systematic error surfaces in DEMs. Previous work related to image configuration is reviewed, before describing the methodology developed to minimise the systematic error surfaces. The relationship between error surfaces, lens model and image configuration is introduced; followed by simulated and experimental results. Finally, this paper concludes with discussion and a brief summary.

Previous Work on Image Configuration

Appropriate network configurations for camera calibration through self-calibration have been well described in many publications (Fraser, 2006; Remondino and Fraser, 2006). Gruen and Beyer (2001) investigated the determinability of self-calibration parameters under various network conditions (one frame up to eight frames). Of all configurations tested in that study, only an eight-frame configuration (convergent, large horizontal base plus vertical base plus additional 90° rotation of frames) produced very good results. This work also indicated that of all interior orientation parameters, the radial distortion is the major source of image deformation.

Karara and Abdel-Aziz (1974) investigated accuracies in object-space coordinates for four non-metric cameras and a metric camera using the direct linear transformation. Image pairs were taken with each of the cameras with the camera axis approximately horizontal and convergence of about 30°. Somewhat surprisingly, Karara and Abdel-Aziz (1974) stated that a strong association between increasing the convergence angle of an image pair and improving precision was not found. These authors concluded that the most desirable configuration is the normal case. Should the normal case not be feasible, the angle of convergence should be kept as small as possible. This result is contrary to the finding described in the present paper.

The use of mildly convergent image configurations for DEM generation is less frequently reported in the literature. The reason might be that the photogrammetric normal case is widely used in automated DEM extraction software. However, an approach using a convergent stereopair for modelling tooth replicas was reported in the field of medical science (Grenness et al., 2005). A semi-metric camera was used to capture multiple convergent images (5, 10, 15, 20 and 25°) of a planar array and used for camera calibration. The estimated camera parameters and digitised images of tooth replicas were imported into a commercial digital photogrammetric software package and DEMs were generated. However, the results are unclear and suggest no association between increasing the convergence angle of the image pairs and increasing precision.

This review of previous work identified some uncertainties, suggesting the need for further investigation in the use of convergent imagery for DEM extraction.

The Relationship between ''Domes'' and Image Configuration

Residual systematic error surfaces or ''domes'' discernible in DEMs of difference were identified in past research conducted by the authors. Metric capabilities of low-cost digital sensors were investigated in Chandler et al. (2005), whilst the geometric stability and consistency of seven identical consumer-grade digital cameras was demonstrated in Wackrow et al. (2007). More recently, research identified a significant dependency between these systematic error surfaces, the lens model and image configuration through the use of simulation.

The Simulation Process

A variety of parameters have to be determined when using a digital camera for accurate photogrammetric measurement, normally derived using self-calibration methods (Fryer, 2001). It was recognised that these parameters needed to be controlled in order to improve understanding, but the variability and uncertainties caused by conducting practical work prevented this. The use of simulated data was considered to be an alternative and more productive approach.

A virtual testfield (1·4 m × 1·3 m) was conceived, composed of evenly distributed X, Y, Z coordinates of hundreds of points. These coordinates were used to create a DEM at 1 mm resolution known as the "Truth DEM". A simulation approach (Fryer et al., 1994) was used to compute perfect photo-coordinates from the X, Y, Z coordinates of each point of the virtual testfield; using predefined interior and exterior orientation. Interior orientation parameters representing a Kodak DCS 460 digital camera were used to provide representative camera information including: principal distance, principal point offset and one parameter (k_1) to model the radial distortion. A vertical stereo-image pair was selected, in which each image covered the whole of the testfield at a camera-to-object distance set to 2·5 m, and a base-to-distance ratio of 1:7. The geometry of this pair was described by two sets of exterior orientation parameters. The derived photo-coordinates and the interior and exterior orientation parameters were then re-established using an external bundle adjustment, GAP (Chandler and Clark, 1992), to compute object coordinates for each point. This provided the opportunity to control each parameter set, representing the interior and exterior orientation, independently. The impact of changing one of these parameters was therefore reflected by the computed object coordinates, which are normally of paramount importance to users. The 3D surfacing tool of the ERDAS IMAGINE 8·7 software was employed to create a DEM through interpolation at 3 mm resolution, which could be compared with the original "Truth DEM". Deviations in the planar surface within the derived DEM of difference could then be related directly to the parameter which had been modified.

The Radial "Domes" and the Lens Model

Initial work in the simulation process focused on confirming the findings of Fryer and Mitchell (1987) in which the systematic error surfaces or "domes" were attributed to an inaccurately estimated lens model. A stereopair configuration was simulated which represents the photogrammetric normal case. This configuration remains important for routine data extraction in photogrammetry, recommended and employed by automated DEM extraction software. The camera base is parallel to the object plane and the optical axes of the cameras intersect the object plane orthogonally. The simulation was employed to calculate photo-coordinates for each point of the virtual testfield using a known interior orientation and the exterior orientation already described. The parameter k_1, modelling radial lens distortion, was changed by ±20% before using the GAP software to calculate object coordinates from the computed photo-coordinates. The significant alteration of ±20% for k_1 was chosen both to illustrate the effect of a significantly inaccurate lens model in the object space and to demonstrate forcibly the capability of the mildly convergent configuration to compensate these effects. The focal length and the parameters for the principal point offset remained unmodified. The computed object coordinates were imported into the ERDAS IMAGINE 8·7 software and a DEM was created at 3 mm resolution. Elevation differences from their theoretical values are visualised in Figs. 1 and 2, exhibiting

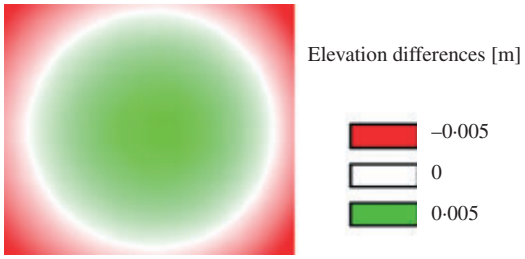

FIG. 1. Elevation differences, k_1 changed by +20% (normal case).

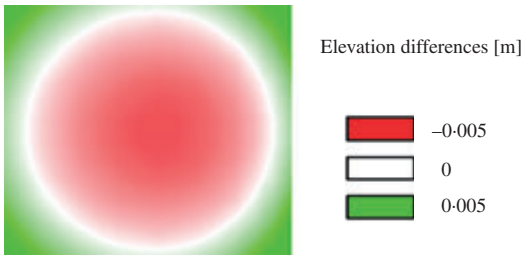

FIG. 2. Elevation differences, k_1 changed by −20% (normal case).

clear evidence of a dome or bowl depending upon the sign of the change. Areas in the DEMs with elevations less than −5 mm are illustrated by solid red, whilst solid green regions indicate height differences greater than +5 mm. White areas represent regions of no elevation difference between the "Truth DEM" and DEMs with a changed lens model. Therefore, the deviations in difference DEMs can be related directly to changes in the lens model.

The Convergent Image Configuration

It was hypothesised that a mildly convergent image configuration could perhaps minimise the systematic error surfaces. The exterior orientation of two photos was derived where the optical camera axes intersect the object plane at the same point, with an angle between these axes of approximately 10°. The parameter k_1 was again changed by +20% which was also used in the normal case configuration (Fig. 1). The simulation process was repeated and a DEM of difference created, illustrated in Fig. 3. It is notable that the "dome" was almost eradicated,

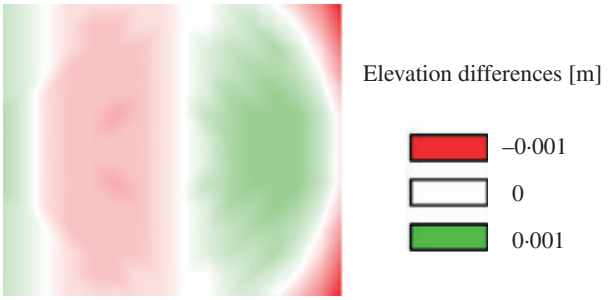

FIG. 3. Elevation differences, k_1 changed by +20% (convergent case).

particularly evident when taking into account that the DEM representation (Fig. 3) was rescaled to ±1 mm. This is significant as the result indicates potential for mildly convergent image configuration to minimise the residual systematic error surfaces caused by an inaccurate lens model.

Practical Test using a Nikon D80 Digital Camera

Two Nikon D80 digital cameras (Fig. 4) were purchased for a research project conducted at Loughborough University to measure flood flows via surface videography and photogrammetry. The need to calibrate these cameras provided the opportunity to validate the findings from the simulation process using real data. A detailed overview of the characteristics of the Nikon D80 camera is given in Table I.

For the calibration process a combined 3D and planar testfield was used, consisting of a medium density fibreboard (MDF) (1·2 m × 0·9 m) to which eight square blocks of various heights and shapes were added. The interior orientation of the camera was determined using the GAP self-calibrating bundle adjustment (Chandler and Clark, 1992). DEMs were extracted by means of the DEM generation tool in the Leica Photogrammetry Suite (LPS) software. The testfield, DEM extraction and the calibration process are described in detail in Chandler et al. (2005) and Wackrow et al. (2007). A vertical image pair, representing the normal case, was used for DEM extraction. Two additional images were captured using a mildly convergent configuration with an angle of approximately 8° between the optical camera axes. DEMs were extracted for both configurations. The automatically generated DEMs were compared with the "Truth DEM" which represents the real shape and geometry of the testfield. The interior orientation remained unmodified for the DEM extraction process and so changes in elevation

FIG. 4. Nikon D80.

TABLE I. Characteristics of the Nikon D80 camera.

Feature	*Nikon D80*
Resolution [pixel]	10 million
Image size [pixel]	3872 × 2592
Size of sensor [mm]	23·6 × 15·8
Size of pixel [μm]	6·095 × 6·095
Auto focus	Yes
Manual focus	Yes
Dimensions [mm]	132 × 103 × 77
Weight [kg]	0·668
Cost [£]	*c*.700

differences in DEMs of difference must be related to the change in image configuration. Figs. 5 and 6 illustrate the DEMs of difference for the normal and convergent image configurations in which the elevation differences were scaled to ±3 mm. The radial dome which is apparent in Fig. 5 was virtually eliminated through using the convergent image configuration (Fig. 6) and similar results were achieved using other test images. This result verifies the findings of the simulation process and demonstrates visually the potential of mildly convergent imaging for minimising errors arising from an erroneous lens model.

Results

DEM Accuracy of the Simulation Process

Although Figs. 1 and 3 and 5 and 6 provide a convincing qualitative argument, it remains necessary to prove the result using quantitative data. The accuracy in the object space is best assessed by deriving mean error and standard deviation of error (Li, 1988) from the DEMs of difference. Systematic effects are represented by mean error, whilst the standard deviation quantifies random effects (Chandler et al., 2005). These statistics were generated using an ERDAS graphical model. Table II summarises DEM accuracy for three tests conducted using the two configurations and simulated data. The first column represents the image configuration used for the simulation, whilst the second column tabulates changes applied to the lens model.

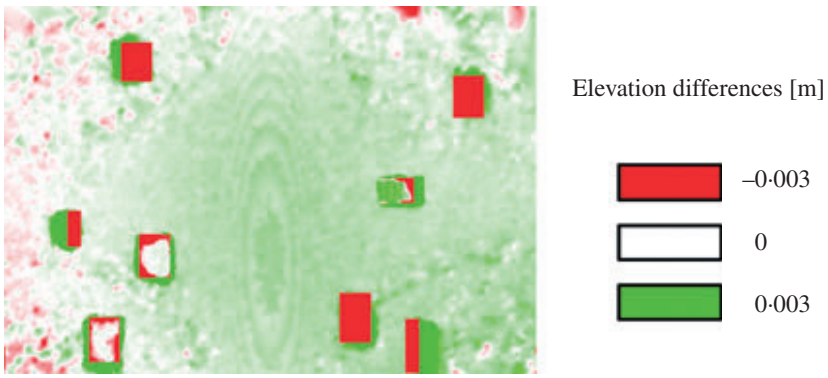

Fig. 5. Elevation differences: normal case.

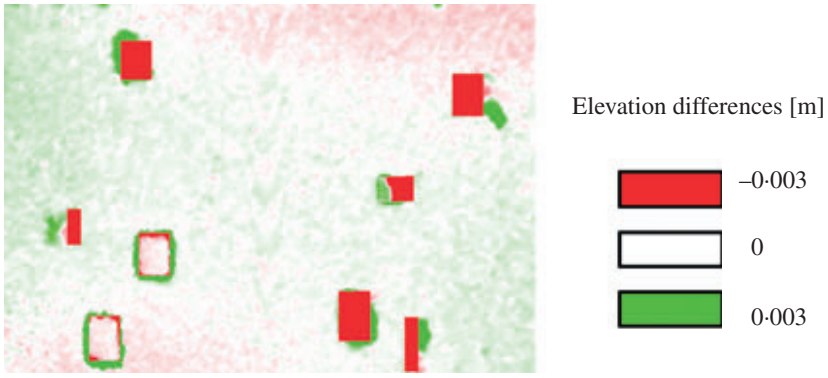

Fig. 6. Elevation differences: convergent case.

TABLE II. DEM accuracy for the simulation process.

Configuration/test	*Changes in lens model*	*Mean error ± standard deviation [mm]*
Normal case	+20%	−0·56 ± 2·1
Normal case	−20%	0·49 ± 1·9
Convergent case	+20%	0·02 ± 0·1

The final column represents the mean error and standard deviation of error for the DEMs of difference. As expected, using the normal case and applying changes to the lens model of ±20%, the mean error changed by 1·05 mm and, as expected, the algebraic sign switched whilst the standard deviation of error remained stable. This symmetrical variation is not of concern because mean error and standard deviation of error followed exactly the theoretical expectations.

Using the mildly convergent configuration and a lens model changed by +20%, a mean error of only 0·02 mm and a standard deviation of error of just 0·1 mm for accuracy of DEM generation were achieved. These results are visualised in Figs. 7(a) and (b), representing cross sections through the DEMs of difference (Figs. 1 and 3) using the normal and convergent configuration, respectively. By comparing these DEM accuracy statistics (normal case versus convergent case), it is notable that accuracy using the mildly convergent configuration improved by a factor of 28. This simulation is highly significant as it implies that a mildly convergent image configuration can eradicate the systematic error surfaces in DEMs extracted, caused by an inaccurate lens model.

DEM Accuracy during Practical Test using the Nikon D80

The presence of a Nikon D80 digital camera and the need to calibrate it provided the opportunity to validate the findings of the simulation in a practical test. DEMs of difference were created using the normal and convergent cases and their mean errors and standard deviations of errors were estimated. These results are summarised in Table III. The first column represents the image configuration used, whilst the second column tabulates mean error and standard deviation of error for the whole of the physical structure of the testfield. The camera may have achieved poor accuracies using both image configurations but this result was predicted. Figs. 5 and 6 clearly indicate that overall accuracies were distorted by significant areas of inaccurate data in the vicinity of the wooden blocks owing to dead ground or occlusion effects (Chandler et al., 2005; Wackrow et al., 2007). In order to exclude these gross errors from the statistics, mean error and standard deviation of error were also computed

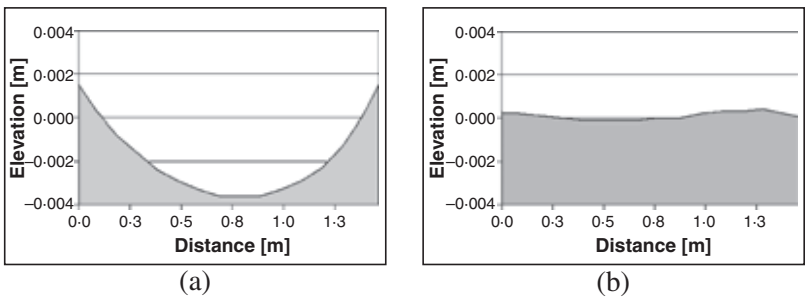

FIG. 7. (a) Cross section for the normal case (lens model +20%).
(b) Cross section for the convergent case (lens model +20%).

TABLE III. DEM accuracy for the Nikon D80 camera.

Configuration/test	*Full area including wooden blocks (mean error ± standard deviation) [mm]*	*Central area (mean error ± standard deviation) [mm]*	*Full area excluding wooden blocks/shadow (mean error ± standard deviation) [mm]*
Normal case	−0·9 ± 9·9	0·9 ± 0·1	0·4 ± 0·4
Convergent case	−1·5 ± 10·0	0·3 ± 0·1	0·1 ± 0·2

for an area of interest situated in the centre of the test object. This represented the flat part of the testfield and did not include the wooden blocks. Statistics are tabulated in column two of Table III for both configurations and demonstrate clear accuracy improvement for the mildly convergent configuration. It should be noticed that this specific area is distorted by a dome which is clearly visible in Fig. 5 and also represented by the mean error (0·9 mm) determined for the normal configuration. A mean error of 0·3 mm estimated for the central area of the test object using the convergent configuration identified an increase of accuracy by a factor of three for this region.

To quantify accuracy for the whole imaging area, data in the vicinity of the wooden blocks (only) was excluded; results are summarised in Table III, column four. The accuracy increased by a factor of four, represented by the mean error for the normal (0·4 mm) and convergent configuration (0·1 mm) and visualised also by the cross sections represented in Figs. 8(a) and (b).

Again, this result is significant. It demonstrated that the disturbing effect, caused by an inaccurate lens model, was almost eradicated using the mildly convergent configuration and verified the results of the simulation.

DISCUSSION

Problems in Recovering the Radial Distortion Parameters

If accurate camera calibration can be achieved, the simulations demonstrated that accurate data can be extracted for all configurations. However, the practical tests using the Nikon D80 digital camera demonstrated the difficulty of recovering perfect lens parameters through self-calibration using the calibration process described in Wackrow et al. (2007). Additional simulation tests were conducted to clarify this difficulty.

A set of interior orientation parameters (focal length, principal point offset and k_1 to model radial lens distortion) was introduced into the simulation and photo-coordinates for the X, Y, Z coordinates of the testfield were estimated using various sets of exterior orientations. These photo-coordinates were then re-established into the external self-calibrating bundle adjustment

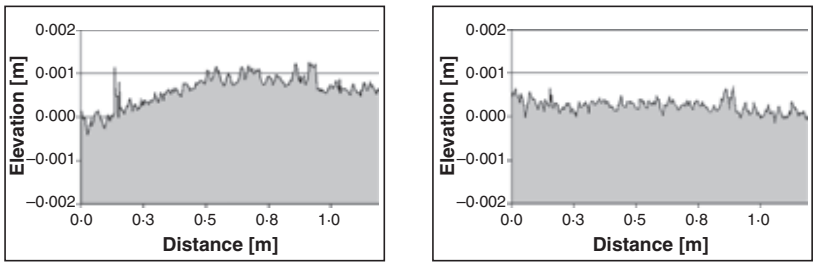

(a) (b)

FIG. 8. (a) Cross section for the normal case. (b) Cross section for the convergent case.

GAP to determine interior and exterior orientation parameters which were treated as unknown. The determinability of these were indicated by comparing the sets of parameters introduced in the simulation and determined by self-calibration.

The configuration (six frames, convergent, two frames rotated) used for camera calibration in Chandler et al. (2005) and Wackrow et al. (2007) was tested initially. The estimated interior orientation parameters were close to their known values but proved inadequate if high accuracy is required. Discrepancies in parameters describing the focal length and principal point offset were not a major concern. These would be compensated by slightly modified exterior orientation parameters because of correlation between interior and exterior orientation parameters, which is well established (Granshaw, 1980; Fraser, 1997; Maas, 1999). However, small discrepancies of the estimated lens distortion parameters relative to their known values remained and consequently degraded the accuracy achievable.

Eleven additional frames were introduced to extend the configuration (convergent, two frames rotated, large horizontal base plus vertical base, two object planes) to examine the possibility of increasing the determinability of the inner orientation parameters. Only a minor improvement was achieved in determining the exact inner parameters, which could only be justified if fully automated measurement methods are available.

Finally, a true multi-station camera configuration (perfect configuration) was described by the exterior orientation in which the camera stations were located all around a wholly transparent testfield and each control point was visible from each camera station. Although the inner camera parameters were determined perfectly, it has to be recognised that such a configuration is impracticable due to target occlusion.

Summarising the results, only the perfect camera configuration was capable of recovering the interior orientation parameters completely. The practicable configuration produced acceptable results; certainly for what may be described as medium accuracy (Fraser, 1997). Unfortunately, the recovered radial distortion parameter differed by 1·5% from its known theoretical value. This characteristic is a feature of self-calibration that is recognised and has been reported in Honkavaara et al. (2006). The uncertainty involved in deriving a completely accurate lens model therefore justifies seeking an alternative approach, which this paper describes. By adopting a mildly convergent image configuration, systematic error surfaces arising from a slightly inaccurate lens model can be eradicated. This suggests that the accuracy of consumer-grade digital sensors can be effectively improved, if a mildly convergent configuration is adopted.

Theoretical Accuracy of the Nikon D80 Camera

The theoretical accuracy in the direction of the camera axis can be expressed using the following mathematical term (Luhmann, 2003):

$$s_z = \frac{h}{b} \times \frac{h}{c} s_{px'} \tag{1}$$

where s_Z is the accuracy in the camera direction, b is the length of the photo base, c is the focal length, h is the camera-to-object distance and $s_{px'}$ is the image precision. The parameters of the stereo-image configuration used in this practical test were: $b = 0{\cdot}229$ m; $c = 0{\cdot}0245$ m; $h = 1{\cdot}6$ m and $s_{px'} = 0{\cdot}6$ μm. Therefore, the theoretical accuracy or predicted precision in depth for the Nikon D80 digital camera was estimated to 0·27 mm.

In order to evaluate the camera accuracies achieved in the practical test, the mean error and standard deviation of DEMs of difference (Table III) can be compared with this theoretical accuracy (0·27 mm).

The statistics, estimated for the full test area including the wooden blocks, indicate that the camera performed poorly for both configurations. This result followed expectations as the gross errors, caused by the wooden blocks, disturbed these statistics. It was also not surprising that the camera could not achieve the theoretical accuracy for the central area of the testfield using the normal case. This area was affected by a dome, caused by an inaccurate lens model. However, a mean error of 0·3 mm and a standard deviation of 0·1 mm estimated for the central testfield area using the convergent case indicated that the dome was significantly minimised and the camera almost achieved the theoretical accuracy of 0·27 mm.

The overall accuracy achieved by the camera in this test is demonstrated by the mean error and standard deviation estimated for the whole test object, in which the gross errors caused by the wooden blocks were excluded from the statistics. The mean error and standard deviation, both of 0·4 mm, estimated using the normal configuration, demonstrated that the camera performed reasonably well, until this is compared with the values achieved using the convergent configuration, $0{\cdot}1\text{ mm} \pm 0{\cdot}2\text{ mm}$. This improvement is highly significant as it demonstrates that the theoretical accuracy of the Nikon D80 camera was achieved when the convergent approach was adopted.

Potential Impact of Findings and Future Work

The mildly convergent image configuration may be suitable for many spatial measurement applications. Current work is focused on further verifying the findings of this paper by conducting tests using a diverse range of case studies.

Accurate modelling of river bed fabric using digital photogrammetry has been investigated in the past (Chandler et al., 2003) and is still of interest in many scientific and industrial areas. The possibility of assessing a model of the bed of a flume (artificial river bed located in a laboratory) provides the opportunity to test the method further in a semi-controlled environment. A non-metric digital camera will be used to acquire a series of images of the flume which describe the normal and convergent configuration. Mosaic DEMs will be extracted and accuracies will be assessed.

Current state-of-the-art computational fluid dynamics (CFD) and, in particular, river flow modelling require accurate estimation of the ‘‘free surface’’ in order accurately to predict the three-dimensional flow field along a river. Accurate water surface elevation data-sets are needed to develop computational flow models but it is extremely difficult and dangerous to acquire such data during floods. A remote water surface measuring technique could be provided using digital photogrammetry and an additional case study is being conducted to measure the dynamic water surface on a small river in Loughborough. A pair of synchronised digital cameras will be used to capture oblique stereoscopic image pairs (normal and convergent configurations) of the water surfaces. DEMs will be extracted and accuracies will be assessed and analysed.

It is hoped that these case studies will demonstrate further that mildly convergent image configuration increases the accuracy of DEMs created using consumer-grade digital cameras.

Conclusion

The work presented in this paper has successfully demonstrated that using a mildly convergent configuration for DEM generation minimises the systematic error surfaces caused by slightly inaccurate lens distortion parameters. In addition, a practical test demonstrated that a Nikon D80 digital camera was capable of achieving its theoretical accuracy, when such a

configuration was adopted. These results are significant for DEM generation using low-cost digital sensors, where a mildly convergent image configuration can reduce the need for an accurate lens model.

ACKNOWLEDGEMENTS

The authors would like to acknowledge the Engineering and Physical Sciences Research Council (EPSRC) for the first author's studentship.

REFERENCES

CHANDLER, J. H. and CLARK, J. S., 1992. The archival photogrammetric technique: further application and development. *Photogrammetric Record*, 14(80): 241–247.

CHANDLER, J. H., BUFFIN-BÉLANGER, T., RICE, S., REID, I. and GRAHAM, D. J., 2003. The accuracy of a river bed moulding/casting system and the effectiveness of a low-cost digital camera for recording river bed fabric. *Photogrammetric Record*, 18(103): 209–223.

CHANDLER, J. H., FRYER, J. G. and JACK, A., 2005. Metric capabilities of low-cost digital cameras for close range surface measurement. *Photogrammetric Record*, 20(109): 12–26.

FRASER, C. S., 1997. Digital camera self-calibration. *ISPRS Journal of Photogrammetry and Remote Sensing*, 52(4): 149–159.

FRASER, C. S., 2006. Evolution of network orientation procedures. *International Archives of the Photogrammetry, Remote Sensing and Spatial Information Sciences*, 36(5): 114–120.

FRYER, J. G., 2001. Camera calibration. *Close Range Photogrammetry and Machine Vision* (Ed. K. B. Atkinson). Whittles, Caithness. 371 pages: 156–179.

FRYER, J. G. and MITCHELL, H. L., 1987. Radial distortion and close range stereophotogrammetry. *Australian Journal of Geodesy, Photogrammetry and Surveying*, 46/47: 123–138.

FRYER, J. G., CHANDLER, J. H. and COOPER, M. A. R., 1994. On the accuracy of heighting from aerial photographs and maps: implications to process modellers. *Earth Surface Processes and Landforms*, 19(6): 577–583.

GRANSHAW, S. I., 1980. Bundle adjustment methods in engineering photogrammetry. *Photogrammetric Record*, 10(56): 181–207.

GRENNESS, M. J., OSBORN, J. E. and TYAS, M. J., 2005. Stereo-photogrammetric mapping of tooth replicas incorporating texture. *Photogrammetric Record*, 20(110): 147–161.

GRUEN, A. and BEYER, H. A., 2001. System calibration through self-calibration. *Calibration and Orientation of Cameras in Computer Vision*, Volume 34 (Eds. A. Gruen and T. S. Huang). Springer, Heidelberg, 34: 163–193.

HONKAVAARA, E., AHOKAS, E., HYYPPÄ, J., JAAKKOLA, J., KAARTINEN, H., KUITTINEN, R., MARKELIN, L. and NURMINEN, K., 2006. Geometric test field calibration of digital photogrammetric sensors. *ISPRS Journal of Photogrammetry and Remote Sensing*, 60(6): 387–399.

KARARA, H. M. and ABDEL-AZIZ, Y. I., 1974. Accuracy aspects of non-metric imageries. *Photogrammetric Engineering*, 40(9): 1107–1117.

LI, Z., 1988. On the measure of digital terrain model accuracy. *Photogrammetric Record*, 12(72): 873–877.

LUHMANN, T., 2003. Analytische Auswerteverfahren. *Nahbereichsphotogrammetrie—Grundlagen, Methoden und Anwendungen* (2. überarbeitete Auflage). Wichmann, Heidelberg. 586 pages: 233–358.

MAAS, H.-G., 1999. Ein Ansatz zur Selbstkalibrierung von Kameras mit instabiler innerer Orientierung. *Publikationen der Deutschen Gesellschaft für Photogrammetrie und Fernerkundung,* Band 7 (Eds. J. Albertz and S. W. Dech). Weinert, Berlin. 496 pages: 47–53.

REMONDINO, F. and FRASER, C. S., 2006. Digital camera calibration methods: considerations and comparisons. *International Archives of the Photogrammetry, Remote Sensing and Spatial Information Sciences*, 36(5): 266–272.

WACKROW, R., CHANDLER, J. H. and BRYAN, P., 2007. Geometric consistency and stability of consumer-grade digital cameras for accurate spatial measurement. *Photogrammetric Record*, 22(118): 121–134.

Résumé

On estime qu'en général la géométrie interne des caméras numériques de qualité courante est instable. Des études récentes menées à l'Université de Loughborough ont montré que ces capteurs avaient la possibilité de conserver leur géométrie interne. On a également pu identifier la cause des erreurs systématiques résiduelles provoquant dans les modèles numériques des altitudes (MNA) des surfaces bombées ou « dômes ». Celle-ci est due à de légères inexactitudes dans l'estimation des paramètres de distorsion de l'objectif. On examine dans cet article ces surfaces résultant d'erreurs systématiques et l'on établit une méthodologie permettant de les rendre minimales. On a commencé par utiliser des données simulées pour s'assurer des effets des variations des paramètres d'orientation interne sur les MNA dérivés, et plus particulièrement des effets des variations du modèle d'objectif. Les résultats obtenus illustrent bien la relation entre l'imprécision des paramètres de distorsion de l'objectif et ces dômes. Le couple stéréoscopique reste fondamental pour l'extraction de données par photogrammétrie, et l'on recourt souvent à des logiciels de production automatique des MNA. C'est la disposition photogrammétrique normale que l'on utilise généralement, dans laquelle la base des caméras est parallèle au plan-objet, tandis que les axes optiques des caméras sont perpendiculaires à ce plan-objet. Dans la phase de simulation, on a pu comparer les « dômes » d'erreur des MNA issus d'une disposition normale avec ceux issus d'une géométrie à axes légèrement convergents. Dans ce dernier cas les axes optiques des caméras se coupent en un même point du plan-objet, contrairement à la disposition normale. Les résultats obtenus avec cette simulation montrent nettement que l'on peut éradiquer ces bombements surfaciques erronés avec une configuration où les caméras sont légèrement convergentes. En effectuant des essais pratiques avec données réelles on a eu la confirmation de ces résultats et l'on a vu que la précision des MNA issus de cette catégorie de capteurs était améliorée avec une géométrie à axes légèrement convergents.

Zusammenfassung

Die innere Geometrie digitaler Amateurkameras wird allgemein als instabil eingeschätzt. Kürzlich durchgeführte Forschungen an der Loughborough University zeigten jedoch das Potential dieser Sensoren ihre innere Geometrie beizubehalten. Die Forschungen identifizierten Oberflächen mit systematischen Fehler oder "Kuppeln", sichtbar in digitalen Höhenmodellen (DEMs), verursacht durch ungenau berechnete Verzeichnungsparameter. Dieser Artikel untersucht die Oberflächen mit systematischen Fehlern und ermittelt eine Methode, diese zu minimieren. Zunächst wurden simulierte Daten verwendet, um den Effekt von Veränderungen der inneren Orientierungsparameter, speziell der Objektverzeichnung, in digitalen Höhenmodellen zu bestimmen. Vorgelegte Ergebnisse zeigen den eindeutigen Zusammenhang zwischen den "Kuppeln" und den ungenau berechneten Verzeichnungsparametern. Das Stereomodell ist in der Photogrammetrie weiterhin von Bedeutung, weil es oft von Software zur automatisierten Erstellung von Höhenmodellen benutzt wird. Meist wird der photogrammetrische Stereonormalfall verwendet, bei welchem die Kamerabasis parallel zur Objektebene ist und die optischen Achsen der Kameras die

Objektebene orthogonal schneiden. In der Simulation wurden die Oberflächen mit Fehlern der Höhenmodelle, extrahiert durch Verwendung des Normalfalls, mit den Oberflächen mit Fehlern der Höhenmodelle, durch Verwendung eines konvergenten Falls, verglichen. Im Gegensatz zum Normalfall schneiden bei konvergenten Aufnahmen die optischen Kameraachsen die Objektebene im gleichen Punkt. Ergebnisse des Simulationsprozesses demonstrieren eindeutig, dass eine konvergente Kamerakonfiguration die Fehler der Oberflächen beseitigt. Dieses Ergebnis wurde durch praktische Tests bestätigt und demonstriert die Bilder die Genauigkeit der Höhenmodelle, dass konvergente mit diesen Sensoren erstellt werden steigern.

Resumen

Por lo general se considera que la geometría interna de las cámaras digitales de consumo es inestable. Los resultados de la investigación realizada recientemente en la Universidad de Loughborough señalan la capacidad de estos sensores para mantener la geometría interna. También identificaron superficies de error sistemático residual o domos, reconocibles en los modelos digitales de elevación (MDE) (Wackrow et al., 2007), causados por una estimación ligeramente inexacta de los parámetros de distorsión de la lente. Este artículo investiga estas superficies de error sistemático y propone una metodología para minimizarlas. Inicialmente se usaron datos simulados para determinar el efecto resultante de cambiar los parámetros de orientación interna en los MDE calculados, particularmente el modelo de la lente. Los resultados presentados señalan la existencia de una relación entre domos y parámetros de la lente que han sido especificados de forma inexacta. El estereopar continúa siendo importante para la obtención de datos en la fotogrametría, en muchos casos usando programas de extracción automática del MDE. El caso normal en la fotogrametría, utilizado comúnmente, es aquél en el que la base de la cámara es paralela al plano objeto y los ejes ópticos de las cámaras intersecan con el plano objeto de forma ortogonal. Las superficies de error del MDE calculado, obtenidas durante la simulación con el caso normal, se compararon con las superficies de error calculadas usando una geometría ligeramente convergente. A diferencia del caso normal, los ejes ópticos de la cámara intersecan el plano objeto en el mismo punto. Los resultados de la simulación demuestran claramente que una configuración de la cámara ligeramente convergente elimina las superficies de error sistemático. Este resultado fue confirmado mediante ensayos prácticos y demuestra que las imágenes ligeramente convergentes mejoran de forma efectiva las exactitudes de los MDE calculados con esta clase de sensor.

